ARISTOTLE UNIVERSITY OF THESSALONIKI
SCHOOL OF GEOLOGY
DEPARTMENT OF GEOPHYSICS

GEORGIOS P. PAPADOPOULOS
Geologist

CONTRIBUTION OF APPLIED GEOPHYSICS TO SOIL CHARACTERIZATION AND EVALUATION IN STATIONS OF THE NATIONAL ACCELERATION-SENSOR NETWORK

MASTER THESIS

POSTGRADUATE STUDIES PROGRAMME 'APPLIED AND ENVIRONMENTAL GEOLOGY', DIRECTION: 'APLPIED GEOPHYSICS AND SEISMOLOGY'

THESSALONIKI
2022

GEORGIOS P. PAPADOPOULOS
ΓΕΩΡΓΙΟΣ Π. ΠΑΠΑΔΟΠΟΥΛΟΣ
Πτυχιούχος Γεωλόγος

CONTRIBUTION OF APPLIED GEOPHYSICS TO SOIL CHARACTERIZATION AND EVALUATION IN STATIONS OF THE NATIONAL ACCELERATION-SENSOR NETWORK

ΣΥΜΒΟΛΗ ΜΕΘΟΔΩΝ ΕΦΑΡΜΟΣΜΕΝΗΣ ΓΕΩΦΥΣΙΚΗΣ ΣΤΟΝ ΕΔΑΦΙΚΟ ΧΑΡΑΚΤΗΡΙΣΜΟ ΚΑΙ ΤΕΚΜΗΡΙΩΣΗ ΣΕ ΘΕΣΕΙΣ ΤΟΥ ΕΘΝΙΚΟΥ ΔΙΚΤΥΟΥ ΕΠΙΤΑΧΥΝΣΙΟΓΡΑΦΩΝ

Υποβλήθηκε στο Τμήμα Γεωλογίας στα πλαίσια του Προγράμματος Μεταπτυχιακών Σπουδών 'Εφαρμοσμένη και Περιβαλλοντική Γεωλογία', Κατεύθυνση 'Εφαρμοσμένη Γεωφυσική και Σεισμολογία'

Ημερομηνία Προφορικής Εξέτασης: 27/05/2022
Oral Examination Date: 27/05/2022

Three-member Examining Board

Fikos Ilias, Staff Member, Aristotle University of Thessaloniki, Supervisor
Theodoulidis Nikolaos, Researcher A', ITSAK, Board Member
Vargemezis Georgios, Assoc. Professor, Aristotle University of Thessaloniki, Board Member

Τριμελής Εξεταστική Επιτροπή

Φίκος Ηλίας, Ε.ΔΙ.Π., Α.Π.Θ., Επιβλέπων
Νικόλαος Θεοδουλίδης, Διευθυντής Ερευνών (Ερευνητής Α'), ΙΤΣΑΚ, Μέλος Τριμελούς Εξεταστικής Επιτροπής
Βαργεμέζης Γεώργιος, Αν. Καθηγητής, Α.Π.Θ., Μέλος Τριμελούς Εξεταστικής Επιτροπής

CONTRIBUTION OF APPLIED GEOPHYSICS TO SOIL CHARACTERIZATION AND EVALUATION IN STATIONS OF THE NATIONAL ACCELERATION-SENSOR NETWORK – *Master Thesis*

ΣΥΜΒΟΛΗ ΜΕΘΟΔΩΝ ΕΦΑΡΜΟΣΜΕΝΗΣ ΓΕΩΦΥΣΙΚΗΣ ΣΤΟΝ ΕΔΑΦΙΚΟ ΧΑΡΑΚΤΗΡΙΣΜΟ ΚΑΙ ΤΕΚΜΗΡΙΩΣΗ ΣΕ ΘΕΣΕΙΣ ΤΟΥ ΕΘΝΙΚΟΥ ΔΙΚΤΥΟΥ ΕΠΙΤΑΧΥΝΣΙΟΓΡΑΦΩΝ – *Μεταπτυχιακή Διπλωματική Εργασία*

Citation:

Papadopoulos G., (2022) – Contribution of applied geophysics to soil characterization and evaluation in stations of the national acceleration-sensor network. Master Thesis, School of Geology, Aristotle University of Thessaloniki.

Παπαδόπουλος Γ., (2022). – Συμβολή μεθόδων εφαρμοσμένης γεωφυσικής στον εδαφικό χαρακτηρισμό και τεκμηρίωση σε θέσεις του εθνικού δικτύου επιταχυνσιογράφων – Μεταπτυχιακή Διπλωματική Εργασία, Τμήμα Γεωλογίας Α.Π.Θ.

ABSTRACT

The strong correlation of earthquake damage and local geological conditions is clearly depicted in several studies. This correlation is the basis of the subsurface exploration studies for site characterization since adequate knowledge of the geophysical and/or geotechnical subsurface structure leads to realistic mitigation of the seismic risk. The estimation of the S-waves velocity of the topmost 30m of the subsurface (V_{S30}) has been recognized as the main parameter for site characterization. While its use has been incorporated into several building codes, obtaining V_S estimates remains a challenging task, especially in urban environments. Most V_S estimation methods use active source acquisition techniques either in boreholes (downhole/crosshole methods) or surface methods (e.g., seismic refraction, MASW etc.). In each case, the time and cost of the application is large, especially when using boreholes and significant limitations apply in demanding environments. In the last decades, ambient noise is greatly utilized in site characterization by estimating the V_S profile and providing information regarding the seismic response of the shallow formations. The main aim of this dissertation is the examination of single-station HVSR curve inversion to estimate 1D V_S structures for the calculation of the VS30.Inversion of HVSR was based on the diffuse field assumption (DFA) (Sánchez-Sesma, F.J. et al., 2011a.) which implies the connection between the HVSR and the elastodynamic Green's function. While ambient noise data acquisition is immensely cost-effective, HVSR inversion is subject to the solution non-uniqueness issue providing ambiguous results. To provide a possible solution for this matter, geophysical methods are applied to derive information regarding the shallow subsurface structure and incorporate it in the inversion. Tests were conducted with and without this information to explore how it facilitates the inversion procedure. The proposed methodology was applied at 6 accelerometric sites in the city of Thessaloniki, northern Greece, with different geological conditions. The electrical resistivity tomography method (ERT) was applied to distinguish subsurface layers based on their electrical resistivity. Active-source seismic data were acquired to estimate the shallow 1D VS profile and were analyzed with the seismic refraction and multichannel analysis of surface waves (MASW) methods. The ambient noise array technique was implemented to provide a large number of ambient noise recordings for selective HVSR curve computation. The passive data were also processed with the f-k method to extract the Rayleigh wave dispersion curve which was then inverted to provide a robust V_{SZ} profile. The reliability of the obtained 1D V_{SZ}

profiles was validated by direct comparison with the existing downhole measurements (available at 3 sites) and the ambient noise array results at each site. Moreover, the V_{S30} was calculated to classify the investigation sites according to the Eurocode 8 regulations. Finally, synthetic ambient noise recordings were generated based on the final V_{SZ} profiles derived from HVSR inversion and were analyzed with the HVSR method. Synthetic HVSR was compared with observed ambient noise HVSR and single-station earthquake HVSR at each site, validating the adopted structures.

ΠΕΡΙΛΗΨΗ

Η ισχυρή συσχέτιση μεταξύ του καταστροφικού αποτελέσματος ενός σεισμού και των τοπικών γεωλογικών συνθηκών αποτυπώνεται ξεκάθαρα σε αρκετές μελετών. Η συσχέτιση αυτή αποτελεί τη βάση για τη διερεύνηση της υπεδάφιας δομής με σκοπό τον εδαφικό χαρακτηρισμό, καθώς η επαρκής γνώση της γεωφυσικής ή/και γεωτεχνικής δομής του υπεδάφους μπορεί να οδηγήσει σε αντιμετώπιση του σεισμικού κινδύνου ως ένα βαθμό. Η μέση ταχύτητα των S-κυμάτων των πρώτων 30m του υπεδάφους (VS30) θεωρείται η κύρια παράμετρος για την κατηγοριοποίηση των εδαφών. Παρά την αξιοποίηση της παραμέτρου αυτής από πληθώρα αντισεισμικών κανονισμών, ο υπολογισμός προφίλ ταχυτήτων S-κυμάτων με το βάθος (V_{SZ}) παραμένει μια απαιτητική διαδικασία, ειδικότερα σε αστικά περιβάλλοντα. Οι πιο συνήθεις μέθοδοι για τον υπολογισμό των V_{SZ} περιλαμβάνουν τη χρήση τεχνητών πηγών για τη λήψη σεισμικών καταγραφών είτε μέσα σε γεωτρήσεις (downhole, crosshole) ή στην επιφάνεια της Γης (π.χ. σεισμική διάθλαση, MASW κλπ). Σε κάθε περίπτωση, η εφαρμογή των μεθόδων αυτών είναι δαπανηρή και χρονοβόρα, ειδικά όταν πραγματοποιούνται σε γεωτρήσεις, και η εφαρμογή της σε αστικά περιβάλλοντα περιορίζεται σημαντικά. Τις τελευταίες δεκαετίες, αξιοποιείται όλο και περισσότερο ο εδαφικός θόρυβος στον εδαφικό χαρακτηρισμό με υπολογισμό των V_{SZ} μέσω της ανάλυσης επιφανειακών κυμάτων παρέχοντας επίσης πληροφορίες για την απόκριση των επιφανειακών σχηματισμών στη σεισμική κίνηση. Ο κύριος στόχος αυτής της διπλωματικής εργασίας είναι ο προσδιορισμός συγκεκριμένης μεθοδολογίας για εκτίμηση 1D V_{SZ} προφίλ από αντιστροφή καμπυλών HVSR, και τον προσδιορισμό της V_{S30} για χρήση στον εδαφικό χαρακτηρισμό. Για το σκοπό αυτό πραγματοποιήθηκε διερεύνηση της αντιστροφής καμπύλης HVSR εδαφικού θορύβου από καταγραφές ενός σταθμού για 1D δομή V_{SZ}. Η αντιστροφή των καμπυλών HVSR βασίστηκε στη θεωρία Diffuse Field Assumption (DFA) που προτάθηκε από τους Sánchez-Sesma, et al., 2011 στην οποία βασίζεται η συσχέτιση μεταξύ του HVSR και των συναρτήσεων Green του μέσου διάδοσης. Ενώ η συλλογή καταγραφών εδαφικού θορύβου είναι σημαντικά οικονομική, η αντιστροφή HVSR εμπίπτει στο πρόβλημα της μη-μοναδικότητας της λύσης. Για την αντιμετώπιση του οποίου πραγματοποιήθηκε εφαρμογή γεωφυσικών μεθόδων επιφανείας για τη δημιουργία ενός αξιόπιστου αρχικού μοντέλου. Στη συνέχεια πραγματοποιήθηκε διερεύνηση αξιοποίησης αυτού του μοντέλου και η επινόηση στρατηγικής αντιστροφής. Η μεθοδολογία εφαρμόσθηκε σε 6 θέσεις του εθνικού δικτύου επιταχυνσιογράφων στην πόλη

της Θεσσαλονίκης (Β. Ελλάδα), με διαφορετικές γεωλογικές συνθήκες. Οι γεωφυσικές μέθοδοι που εφαρμόσθηκαν είναι η Τομογραφία Ηλεκτρικής Αντίστασης (ERT) για την αναγνώριση υπεδάφιων στρωμάτων βάσει της ειδικής ηλεκτρικής αντίστασης, καθώς και οι μέθοδοι της σεισμικής διάθλασης και της Πολυκαναλικής Ανάλυσης Επιφανειακών Κυμάτων (MASW) για την απόκτηση επιφανειακών προφίλ σεισμικών ταχυτήτων. Η τεχνική δικτύου εδαφικού θορύβου εφαρμόσθηκε για να παράξει μεγάλο αριθμό καμπυλών HVSR και να αποτελέσει μια αξιόπιστη σύγκριση με το τελικό αποτέλεσμα της αντιστροφής HVSR. Η αξιοπιστία των 1D V_{SZ} προφίλ επιβεβαιώθηκε συγκρίνοντας τα με προφίλ V_{SZ} από υπάρχουσες downhole και από το δίκτυο εδαφικού θορύβου. Επιπλέον, εξάχθηκαν τιμές V_{S30} για την κατηγοριοποίηση κάθε θέσης με βάση του κανονισμούς του Ευρωκώδικα 8. Τέλος, δημιουργήθηκαν συνθετικές καταγραφές εδαφικού θορύβου με βάση την τελική δομή που προέκυψε από την αντιστροφή HVSR σε κάθε θέση. Συνθετικές καμπύλες HVSR συγκρίθηκαν επιτυχώς με καμπύλες εδαφικού θορύβου και HVSR καταγραφών σεισμών σε κάθε θέση, επιβεβαιώνοντας την τελική δομή.

Preface

The present dissertation is the capstone of the Research and Analysis in the field of HVSR inversion subject to the "Applied and Environmental Geology" Postgraduate Studies Programme of the School of Geology of the Aristotle University of Thessaloniki. Its main goal was to investigate the inversion of HVSR curves for reliable estimations of 1D V_{SZ} profiles for the subsequent calculation of the V_{S30} parameter, utilized in site characterization. For this purpose, single-station ambient noise HVSR curves are computed. Since HVSR inversion is heavily subjected to the solution non-uniqueness problem, we applied surface geophysical methods to mitigate this issue and investigated the incorporation of a priori information (thickness and number of layers, V_S) in the inversion. The aforementioned methodology was applied at 6 accelerometer station sites in the city of Thessaloniki, northern Greece. The final V_{SZ} profiles are evaluated with the generation synthetic ambient noise recordings that are processed with the HVSR technique, as well as earthquake HVSR curves.

The first chapter is an introduction to site characterization and the V_{S30} parameter, accompanied by Greek and international literature on its applications, mainly with combined geophysical methodologies and HVSR applications.

Chapter 2 recalls the basic principles of the geophysical methods that were used during this research, namely the Electrical Resistivity Tomography, active seismic methods such as the Seismic Refraction and the Multichannel Analysis of Surface Waves (MASW) and passive seismic methods such as the Horizontal to Vertical Spectral Ratio (HVSR) and the Ambient Noise Array. Next, the theoretical background of the Diffuse Field Assumption, that is the basis of HVSR inversion that is conducted in this research, is thoroughly described. Finally, the two methods that were used in the validation of the final V_{SZ} profiles are described, that is the Numerical Simulation of Ambient Noise with the generation of synthetic recordings (Hisada 1D) and the single-station earthquake HVSR.

In Chapter 3, we present the investigation sites and the combined methodology that was followed. A brief presentation of the equipment that was used for the geophysical data acquisition is also conducted. For each investigation site, the field planning of the combined geophysical methods, is presented.

Chapter 4 is separated in two parts. The first part is devoted to the data processing for each individual geophysical method as well as the HVSR analysis of ambient noise and earthquake recordings. Emphasis is given to the appropriate computation of the HVSR curves in order to be compatible with the inversion under the Diffuse Field Assumption theory. A parametric investigation of the HVSR inversion is also presented. In the second part of Chapter 4, we present the methodology for the construction of the initial model for the HVSR inversion that is based on the local geophysical model derived from the geophysical methods as well as on features exhibited by the HVSR curve itself. Additionally, comparisons between V_{SZ} profiles from the HVSR inversion and the ambient noise array and downhole results, where available, are presented. Finally, V_{S30} parameters are computed from each method, discussing possible deviations, and are utilized to classify each site accordingly to the Eurocode 8 regulations. Lastly, the final subsurface structures are validated by directly comparing synthetic ambient noise HVSR curves with observed ambient noise and earthquake HVSR curves.

In Chapter 5 comes the epilogue of this dissertation along with the conclusions of the application of the HVSR inversion as well as the methodology for the construction of the local initial model. A thorough discussion is also conducted presenting the final methodology along with specific guidelines and the arisen problems as well as ways to overcome these problems. Finally, alternative processing methods and prospects of the HVSR inversion are discussed.

This work was supported by the project HELPOS – Hellenic System for Lithosphere Monitoring" (MIS 5002697), which is implemented under the Action "Reinforcement of the Research and Innovation Infrastructure", funded by the Operational Programme "Competitiveness, Entrepreneurship and Innovation" (NSRF 2014-2020) and co-financed by Greece and the European Union (European Regional Development Fund).

Words cannot express my gratitude to my supervisor Dr. Fikos Ilias for entrusting me with this project. His invaluable patience, guidance, feedback, continuous encouragement, and faith in my abilities gave me all the extra motivation needed to overcome any difficulties I faced along the way. His epistemic way of thinking and methodicalness are among the most important things instilled in me.

I am deeply indebted to Dr. Theodoulidis Nikolaos, who generously provided knowledge and expertise, for showing trust in me and for the financial support through professional work and projects.

Also, I am extremely grateful to the third member of my defense committee, Associate Professor Vargemezis Georgios, for his consultation and interpretation of the results.

I am also thankful to Professor Antonio Garcia-Jerez from the University of Almeria for this critical guidance and consultation on HVSR inversion.

I would also like to extend my thanks to Dr. Panou Areti for her instructions and guidance during the processing of ambient noise simulation which is a pivotal part of my dissertation and dealing with any technical issues that occurred.

Thanks should also go to PhD Candidate, Mr. Chatzis Nikolaos for being always available in answering all my questions regarding the theoretical background of ambient noise and the technical issues during data processing.

I would also like to extent my sincere thanks to all the members of the Department of Geophysics, to whom I owe the acquisition of my geological and geophysical knowledge through their excellent training.

Special thanks to my dear friends Tokmaktsi Eleni, Mavros Serafeim and the rest of my classmates for their help during the data acquisition phase, encouragement, and fun times we had together.

I owe my deepest gratitude to Maria for her implicit moral support, patience, and continuous encouragement.

Finally, I could not have undertaken this journey without the support of my family, so I dedicate this work to them with all my love and gratitude…

Georgios Papadopoulos,

May 2022

Table of Contents

1. Introduction

Striking with no warning, earthquakes are among the most devastating natural disasters with great negative impact on the natural and anthropogenic environment, caused by the movement of tectonic plates along faults, on the earth's surface. The level of seismic damage on a construction depends on properties of both the seismic ground motion and the constructions itself. The characteristics of seismic ground motion at an area are related to properties of the earthquake focus (magnitude, focal mechanism, seismic energy radiation etc.), to properties of the propagation medium of the seismic waves (travel distance, attenuation of the seismic energy etc.) and to properties of the local ground conditions of the examined site (local geological conditions, shear wave velocity of the surface layers etc.).

The characteristics of seismic motion, meaning, amplitude, frequency, and duration of both horizontal and vertical components of seismic waves arriving at a site may be drastically affected by the local geological conditions. Hence, the assessment of the effects of local site conditions on seismic motion, especially in urban environments, is important to rationally estimate seismic hazard and mitigate the respective seismic risk and consequences of seismic excitation.

A basic requirement for the seismic hazard assessment at a site is the knowledge of the geophysical properties of the uppermost sedimentary formations. The geophysical structure consists of the distribution of the values of several parameters with depth, such as seismic waves velocities, mass density, and elastic parameters. Knowledge of the subsurface geophysical structure leads to the extraction of information regarding the subsurface geological formations such as the depth of the bedrock, the existence of fault zones, the mechanical properties of the formations and so on. This information contributes to the estimation of the effects of the local geological conditions to the seismic motion.

One of the most important issues regarding local site conditions effects is that seismic motion is amplified with seismic energy propagating from the geological and/or seismic bedrock into the surficial sedimentary formations. The amplification of the seismic motion depends heavily on the shear-wave velocity contrast which is related to the impedance contrast between the bedrock and the less coherent sedimentary formations. The greater the contrast the higher the amplification. The direct relation between the seismic amplification and the S-wave velocity of the surficial geological formations led to the necessity of the classification of the ground (or site characterization) based on the S-wave velocity. For this purpose, site characterization is performed at areas of interest, providing subsurface information useful to engineers in designing low vulnerability constructions. According to the proposed provisions by the Eurocode 8 (CEN, 1994, EN 1998-1 – Table 1.1), five standard ground types are specified, A, B, C, D, and E for sites with stiffer to sites with softer uppermost soil layers, depending on the stratigraphic profile and the parameters described below. Two special soil classes are also defined (S_1 and S_2) which require special investigation for the seismic site response. More specifically, for the S_1 class special studies regarding site amplification and soil-structure interaction effect is required since at least 10m thick, soft clays of high plasticity index and high water-content exist, while for the S_2 class also special studies are required due to their liquefaction potential under seismic loading.

The shear-wave velocity of the top 30m (i.e., V_{S30}) is the main parameter used for soil classification, followed by the N_{SPT} (number of blows for the Standard Penetration Test of 30cm thickness) and c_u (undrained shear strength of soil) if V_{S30} is not available. If the subsurface structure consists of *i* (=1, …, N) different soil layers up to the depth of 30m and h_i, v_i correspond to their thicknesses (in meters) and shear-wave velocities (in m/s) for each layer, then the average V_{S30} velocity is defined as:

$$V_{S30} = \frac{\sum_{i=1}^{N} d_i}{\sum_{i=1}^{N} \frac{d_i}{v_i}} \qquad (1)$$

where $\sum_{i=1}^{N} d_i = 30m$.

The methods used for site response assessment are generally grouped in three main categories. The first category includes the numerical simulation of seismic excitation based on utilization of geophysical and/or geotechnical data. Application of conventional geophysical methods (e.g., seismic reflection, seismic refraction, multichannel analysis of surface waves) and use of geotechnical data (boreholes, laboratory tests etc.) can adequately provide reliable information on required parameters of site response investigation based on 1D/2D/3D soil profile models (e.g., thickness of each geological layer, seismic velocities, densities etc.). as input to numerical simulation

Table 1.1. Soil classification based on the regulations of Eurocode 8 (EC8 § 3.1.2 Table 3.1).

Ground Type	**Description of stratigraphic profile**	**Parameters**		
		V_{S30} (m/s)	**N_{SPT} (blows/30cm)**	**c_u (kPa)**
A	Rock or other rock-like geological formation, including at most 5 m of weaker material at the surface.	>800	-	-
B	Deposits of very dense sand, gravel, or very stiff clay, at least several tens of meters in thickness, characterized by a gradual increase of mechanical properties with depth.	360-800	>50	>250
C	Deep deposits of dense or medium-dense sand, gravel, or stiff clay with thickness from several tens to many hundreds of meters.	180-360	15-50	70-250
D	Deposits of loose-to-medium cohesionless soil (with or without some soft cohesive layers), or of predominantly soft-to-firm cohesive soil.	<180	<15	<70
E	A soil profile consisting of a surface alluvium layer with vs values of type C or D and thickness varying between about 5 m and 20 m, underlain by stiffer material with vs > 800 m/s.			
S_1	Deposits consisting, or containing a layer at least 10m thick, of soft clays/silts with a high plasticity index (PI > 40) and high water-content.	<100 (indicative)	-	10-20
S_2	Deposits of liquefiable soils, of sensitive clays, or any other soil profile not included in types A - E or S1.			

The second category includes methods that contribute to the direct assessment of the local site effects on the seismic motion with the analysis of earthquake motion recordings. These methods include the widely applied Standard Spectral Ratio (SSR) (Borcherdt 1970; Steidl et al. 1996; Field and Jacob, 1995; Mittal et al., 2013) and the Receiver Function (RF) method

(Langston, 1979; Lermo et al., 1993; Field and Jacob 1995). A significant disadvantage of these methods is their inability to effectively apply in low to moderate seismicity regions due the long time required for seismic data acquisition with an adequate signal-to-noise ratio.

Finally, the third category includes methods that are based on the analysis of ambient noise recordings that offers a practical and low-cost tool for applications in urban environment. Ambient noise recordings are analyzed mainly by four techniques for local site effects assessment (Bard, 1999): (a) the power spectra method (Kanai method) (Kanai and Tanaka, 1954), (b) the horizontal-to-vertical spectral ratio (HVSR) method (Nakamura 1989, 1996, 2000), (c) the Standard spectral ratio method (SSR) (Lermo and Chavez-Garcia, 1994) and (d) the array technique (Wathelet, 2005). The first three techniques contribute to the estimation of site response (fundamental frequency and amplification under certain limitations) of the surficial sedimentary formations, while the array technique is a geophysical method used for the 1D estimation of S-wave velocity with depth, Vsz. A basic drawback of the array technique is that a large number (>7) of seismometers is required.

Below, some of the most important and recent literature on site characterization using ambient noise methods and/or other non-invasive geophysical methods is presented. Hunter et al. (2010) in the context of seismic site characterization for the city of Ottawa, capital of Canada, used seismic geophysical methods on the ground surface and in boreholes in combination with geological information available from existing boreholes in the survey area. The main goal was the construction of a seismic site classes map based on the V_{S30}, as well as a map of fundamental period of the surficial sedimentary layers based on shear-wave velocities and depths to fundamental impedance interfaces. The latter was compared with experimental fundamental period values from HVSR measurements providing good agreement. Hunter et al. (2012) proposed updated guidelines on site characterization based on V_{S30} values derived by a combination of passive and active seismic data with non-invasive and invasive techniques, validated with a number of case studies in Canada. Yong et al. (2013), conducted geophysical site characterization in 191 strong-motion stations in California and Central-Eastern United States, using a combination of passive and active seismic methods, including the HVSR, ambient noise array and MASW techniques, among others. The authors compared the NEHRP programme for Site Classes based on V_{S30} values with the Site Classes expected from analysis of the surficial geology. The NEHRP Site Classes based on V_{S30} ranged from being consistent with Site Class expected from analysis of surficial geology, to being one or two Site Classes below expected. In a few cases where differences between the observed and expected Site Class occurred, the authors stated that it was the consequence of inaccurate or coarse geologic mapping, as well as considerable degradation of the near-surface rock. Additionally, several sites mapped as rock had Class D velocities due to extensive weathering of the surficial rock. Mohamed et al. (2016), performed site characterization at the Suez Canal, northeastern Egypt using a combination of active seismic MASW measurements for the computation of V_{S30} values and ambient noise HVSR measurements for the extraction of the fundamental frequency values. Martin et al. (2017), used non-invasive geophysical methods consisting of seismic refraction and MASW methods, to obtain V_S profiles for site characterization at 33 seismic station sites in the US with ranging topographic conditions, based on the knowledge acquired by Yong et al., 2013. The researchers used either the Rayleigh or Love waves for the MASW based on the success level of each method. Stephenson et al. (2021), explored a multimethod approach for V_{SZ} site characterization acquiring active and passive seismic data at seismograph stations in Oklahoma that recorded earthquakes of at least M>4.0, by modeling in a non-linear least-squares joint inversion also exploring application of least-squares and Simulated Annealing joint inversion to obtain a best fit 1D Vs profile for each site.

Anthymidis et al. (2012) conducted ambient noise measurements in the town of Grevena (Greece) using the single-station and array techniques, for the identification of the response of the surficial sedimentary formations and the surficial geophysical structure for site characterization. The HVSR analysis of the ambient noise data let the researcher to delimit areas with common response characteristics. The processing of ambient noise data with the array technique led to the recognition of the contact interface of the recent Quaternary deposits and the deeper Neogene sediments at selected sites. Double peaks observed in the HVSR curves were attributed to interfaces between sedimentary formations and the geologic bedrock (maximum at low frequencies) as well as to the interface between Quaternary and Neogene deposits (maximum at high frequencies). This interpretation was theoretically validated with the generation of synthetic ambient noise recordings and appropriate 1D numerical simulation.

Loupasakis et al. (2015), combined geotechnical and geophysical methods for site characterization in 13 selected sites of the Hellenic Accelerometric Network (HAN) in Crete Island, Greece. The researchers constructed guidelines based on their experience regarding limitations of the methodology and its accuracy in urban sites. Comparison of seismic site classes of the EC8 provisions, of analyses from geological maps and V_{S30} values derived from geophysical methods led to the conclusion that V_{S30} values for sites with shallow depth (10 to 20m), loose to medium dense deposits, overlaying stiffer or rock like formations, the ground type category seems to be overestimated. The researchers agreed that in these cases the V_{S30} is radically influenced by the velocity of the stiffer underlying formations upgrading the ground type and verified their conclusions with geotechnical investigation identifying layers with reduced mechanical properties.

Chatzis et al. (2018), explored the applicability of HVSR curve inversion to retrieve the local 1D VS structure. The researchers performed single-station ambient noise measurements at 73 calibration sites for which a database containing geophysical and geological information was existent. HVSR curve inversions were performed by constraining the average S-wave velocity of the first 5m (V_{S5}) as provided by the database information. The 1D V_{SZ} models were validated with geological information from their database (e.g., depth of the bedrock). Moreover, they compared V_{S30} results from the HVSR inversions with V_{S30} values from the database, as well as estimates from V_{S5} proxies. The authors concluded that constraining the HVSR curve inversions with V_{S5} values significantly improves the V_{S30} estimates for stiffer formations (ground type B, by EC8) providing also improved V_{S30} values for several softer (ground type C, by EC8) sites. The above methodology suggested that inversion of HVSR curves can be considered as a supplementary tool for efficient, large scale and low cost V_{S30} estimations.

Utilizing much simpler and practical methods has become a necessity, hence leading to methods based on ambient noise for the estimation of the S-wave profile without employing a large number of seismometers as in array technique. In this thesis, this issue is examined with the inversion of HVSR curves that result from single station ambient noise measurements, as well as the implementation of additional information derived from the application of a group of geophysical methods to facilitate the inversion procedure and deal with the solution non-uniqueness issue of the HVSR to a certain extent. The applied geophysical methods consist of a geophone array to collect active source Rayleigh-wave data for P-wave travel-time modeling and multichannel analysis of surface waves (MASW) and the electrical resistivity tomography (ERT) for subsurface layer geometry recognition based on the electrical resistivity distribution.

The inversion of HVSR curves is based on the diffuse field assumption (DFA) theory (Sánchez-Sesma et al., 2011; Piña-Flores et al., 2021) which proposes that the ambient noise wavefield contains all types of body and surface waves whose associated energy participation stabilizes in fixed proportions. This methodology provides significant advantages, being relatively low-cost and typically implementable in a single working day. The main goal of this dissertation is to study the reliable implementation of HVSR inversion through the DFA theory for site characterization and its applicability in urban environment and propose simple and straightforward guidelines towards its effective implementation.

2. Methods Used

2.1 Introduction

In this study active and passive geophysical methods are used to obtain one-dimensional V_S profiles for geotechnical site characterization though the V_{S30} proxy parameter, that is the time-averaged shear wave velocity of the uppermost 30 meters. To this goal, surface wave analysis of ambient noise was conducted with the array technique and the computation of the HVSR curves at each receiver position. Inversion of HVSR was conducted based on the Diffuse Field Assumption (DFA) theory. As all surface wave methods, the HVSR inversion is subject to the solution non-uniqueness issue. To facilitate the inversion procedure and to obtain more reliable results it was deemed necessary to acquire geophysical data and use as *a priori* information in the HVSR inversion. For this purpose, the electrical resistivity tomography method (ERT) was employed to obtain information regarding the subsurface structure and determine a possible number of geological layers and/or detect possible lateral variations in the subsurface structure. Non-invasive active methods such as the 1D multichannel analysis of surface waves (MASW) and the seismic refraction were employed to acquire shallow 1D V_S and V_P profiles (up to 30m) in the vicinity of the ambient noise measurements. Estimated V_{SZ} profiles from the ambient noise array dispersion curves inversion as well as from available geophysical information (downhole measurement) and other geological information (borehole stratigraphy) were used to evaluate the final results of the HVSR inversion. Earthquake motion HVSR curves were computed from accelerometric data for the validation of the fundamental frequency value (f_0) derived from HVSR based on ambient noise at the investigation area. Finally, synthetic ambient noise HVSR curves computed from synthetic recordings based on the final velocity profile (ambient noise simulation, Hisada 1D), are directly compared to observed ambient noise and earthquake HVSR curves to validate the 1D V_{SZ} profile derived from the HVSR inversion. The flow-chart of the followed methodology is shown in Figure 2.1.

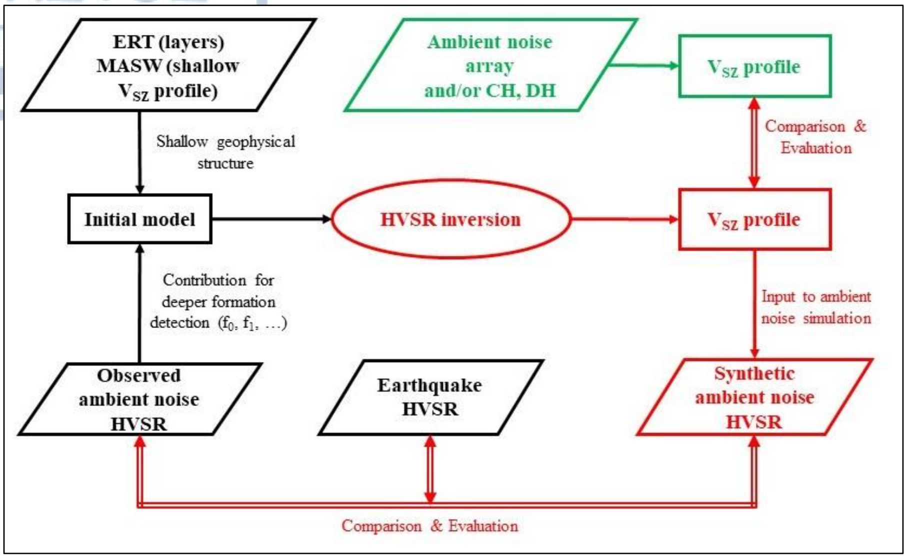

Figure 2.1. Flow-chart of the methodology followed towards HVSR inversion and the validation of the derived V_{SZ} profiles.

The aforementioned methodology for site characterization was applied and tested at six accelerometric sites in the city of Thessaloniki, northern Greece, for a variety of geological conditions ranging from rock to sedimentary sites. Some external factors, such as limited space availability and high anthropogenic noise provided useful experience for the implementation of the methodology in urban and metropolitan areas.

The purpose of this chapter is to give a brief insight of the geophysical methods that compose the methodology and are used in this applied research enhancing to the overall understanding of the joint geophysical data processing and analysis. More specifically, the next sections are devoted to describing the theoretical background regarding the electrical resistivity method (ERT) and its basic principles. Moreover, the principles of the surface wave methods such as the multichannel analysis of surface waves (MASW), the HVSR analysis and the ambient noise array method as well as the principles of the Rayleigh waves are described. Finally, the analysis of earthquake motion recordings with the HVSR technique, as well as the ambient noise simulation method for the validation of the final V_S profile are described.

2.2 Electrical Resistivity Tomography

The electrical resistivity tomography (ERT) is one of the most popular geophysical methods employed in a plethora of geological problems such as, among others, the detection of metalliferous zones, groundwater exploration and fault zone mapping and finds application in the environmental, geothermal, geotechnical, and archaeological research. It belongs to the category of active electrical methods, that during their application, artificial electrical fields are generated, and induced into the ground.

The ERT method is mainly used to reveal the 2D distribution of the electrical resistivity of the subsurface and belongs to the general category of electrical resistivity methods. With these methods we measure the potential difference between two points due to the current injected in two different points, either on the ground surface or inside boreholes, aiming to calculate the electrical resistivity of the subsurface geological formations. Electrical resistivity is a fundamental property of a material that measures how strongly it resists electric current. Electrical resistivity is typically represented by the Greek letter 'ρ' and is measured in Ohm-m (Table 2.1).

Table 2.1Measured ranges of resistivity for some typical materials (Styles, 2012, modified).

Material	**Resistivity (Ohm-m)**	**Material**	**Resistivity (Ohm-m)**
Igneous rock	10^2-10^6	Alluvium and sand	10-8*10^2
Altered granite	1-10^2	Clay	10-10^2
Limestone	10-10^4	Soil	1-10
Sandstone	10-10^3	Fresh water	3-10^2
Dry gravel	6*10^2-10^4	Copper	2*10^{-7}

Some other factors that also affect the values of the electrical resistivity besides the material, are the porosity of the formation, the humidity, the chemical composition of the water and temperature.

2.2.1 Electrical Resistivity Data Acquisition

During common applications of the ERT method, steel electrodes are placed on the ground surface in a line and equally spaced. The length of the electrode array (L) is related to the maximum investigation depth according to the equation,

$$z_{max} = \frac{L}{m} \tag{2}$$

where 3≤m≤5.

The spacing of electrodes depends on the desired resolution and the length of the ERT line. During measurements electrical current is injected into the ground through a pair of electrodes (A^+ and B^-) and the potential difference due to the current flow is measured at a second pair of electrodes (M and N). The quantity calculated is called the apparent resistivity, ρ_α and is given by:

$$\rho_a = 2\pi \frac{\Delta V}{I}\frac{1}{G} = 2\pi \frac{R}{G} \quad (3)$$

where ΔV is the potential difference, I the current intensity, R the ohmic resistance and G the geometrical factor that is given by:

$$\left(G = \frac{1}{AM} - \frac{1}{BM} - \frac{1}{AN} + \frac{1}{BN}\right) \quad (4)$$

Of all the possible ways to place the four electrodes and all the possible combinations between the current and potential electrodes (quadripoles) the acquisition of the measurements depends on the chosen electrode array configuration. Some of the most popular inline arrays are the dipole-dipole and the multi-gradient array (Figure 2.2). In the dipole-dipole array configuration the spacing of the source electrodes and the receiver electrodes is constant (a). The distance between the two dipoles is increasing as n*a. In the multi-gradient array configuration, the distance between the source electrodes is longer and the receiver electrodes are moving as a dipole of various distance between the source electrodes.

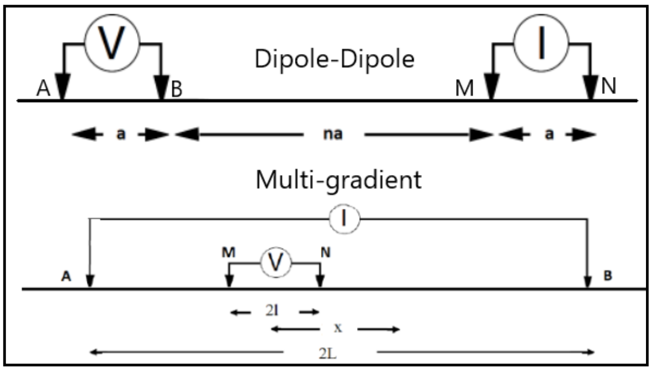

Figure 2.2 Schematic representation of the dipole-dipole and multi-gradient electrode array configurations.

2.2.2 Processing and inversion of geoelectrical data

Apparent resistance is considered as a kind of average resistance of the subsurface formations (Robinson and Coruh, 1988) and not the specific resistivity. The complex mathematical procedure of inversion is implemented to convert the apparent values to specific resistance. In the case of ERT data the aim of inversion is to generate a 2-D resistivity model as close to the real resistivity structure as possible. The first step involves solving the forward problem, namely the calculation of the apparent resistivity. For this purpose, a finite element algorithm is used to solve the differential equations that describe the electrical current flow in heterogeneous subsurface structure (Pain et al. (2002), Pridmore et al. (1981), Sasaki (1994), Tsourlos and Ogilvy (1999), Yi et al. (2001)). Due to the non-linear relationship between the geoelectric parameters and the measured data, iterative inversion algorithms are implemented. During the inversion procedure, the under-investigation area is divided to a network of parameters which are given an initial value of specific resistance (initial model). The synthetic data are generated based on the initial model. A first estimation of the error is calculated as dy= (measured data – synthetic data). The initial model is adjusted with each iteration until the error (dy) is minimum. The final model represents the true resistance structure and can be interpreted to identify the geological structure of the subsurface.

2.3 Seismic Refraction

The seismic refraction (SR) is an active seismic method that utilizes the refraction of generated seismic waves on the interfaces between geological formations to characterize the subsurface geological conditions. Seismic refraction has application in geotechnical problems, in the estimation of the depth of the bedrock, as well as in underground water and other geological exploration. The method involves a geophysical principle governed by Snell’s law, which is a formula used to describe the behavior of seismic waves, concerning the relationship between seismic wave angles when passing through an interface between two different isotropic media.

The seismic refraction method depends on the principle that the compression (P) and shear (S) seismic waves travel with different velocities within differing types of soil and rock material. Seismic waves are refracted when they cross over between different geological formations of differing seismic velocities. The seismic wave is generated at the source point at the surface of the ground by a seismic impact source, typically an 8kg sledgehammer (Igboekwe and Ohaedgbuchu, 2011). The generated seismic energy propagates directly through the surficial layer (direct arrivals) or travels downwards and is refracted through the subsurface layers (refracted arrivals). Assuming that the propagation velocity increases with depth, the refracted wave travels back to the surface and is recorded by geophones, aligned with the seismic source. After specific distance from the seismic source the refracted wave is recorded earlier than the direct wave. In the seismic refraction method, both P-waves and S-waves can be utilized to estimate the depth of the various interfaces between layers but also the S-waves are utilized to provide additional information concerning the mechanical properties of the subsurface media (Ayolabi et al., 2009; Igboekwe and Ohaegbuchu, 2011; Gabr et al., 2012).

The recorded seismic data are subject to selected inversion technique which for this work was the time-term inversion. The time-term inversion is a combination of the least-squares method and the travel time analysis of the seismic waves. The inversion provides a 2D profile of the P-wave velocities with depth that are then attributed to geological formations depending on the available data for the site.

2.4 Multichannel Analysis of Surface Waves

The Multichannel Analysis of Surface Wave (MASW) is an active seismic method introduced by Park et al., 1999. It analyzes the dispersion of surface waves, mainly the fundamental mode of the Rayleigh waves, to generate a one-dimensional S-wave velocity (V_S) profile. It is noteworthy that, during the generation of surface waves with a compressional source, more than $2/3$ of the total seismic energy is carried by Rayleigh waves (Richart et al., 1970).

2.4.1 Characteristics of the Rayleigh surface waves

The Rayleigh waves are created by the interference of the generated P-waves and SV-waves due to incident SV-waves to a free surface (Aki and Richards, 1980) and propagate parallel to the free surface (Lay and Wallace, 1995). The interfering waves propagate with the same frequency but with different phase (Telford et al., 1990), hence the Rayleigh waves cause an elliptical particle motion, producing both a horizontal and vertical component of motion at the free surface, with retrograde direction (Figure 2.3). For $(V_P/V_S)^2 = 3$ (Poisson's ratio v=0.25) the propagation velocity of the Rayleigh waves corresponds approximately to 92% of the V_S (Sheriff and Geldart, 1995) while the ratio of the vertical over the horizontal component on the free surface equals to 1.465:1 (Kritikakis, 2010). At greater depths, the particle motion is converted to prograde. In homogeneous media the associated motion decays exponentially with depth, becoming negligible within about one wavelength (λ) from the surface, while in the case of vertically heterogeneous media, the decay of the ground particles motion cannot be predicted a-priori without knowledge of the subsurface structure (Foti et al., 2018).

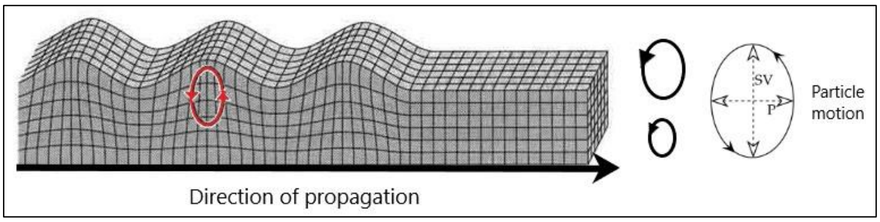

Figure 2.3 Elliptical particle motion during the propagation of fundamental mode Rayleigh waves, whose amplitudes decrease exponentially with depth. The vertical component is dominated by SV waves while the horizontal component by P waves with significantly lower amplitudes (http://allshookup.org/quakes/wavetype.htm, modified).

Since Rayleigh waves are confined near the ground surface, their in-plane amplitude decays only as $1/\sqrt{r}$, where r is the radial distance while body waves amplitudes decay as $1/r$ meaning that Rayleigh wave amplitudes are larger (on the ground surface) compared to body wave amplitudes.

In the case of heterogenous media, such as the subsurface of the Earth, the Rayleigh velocity varies with depth and every different frequency of the Rayleigh waves propagates with different phase velocity, meaning that different wavelengths exist for each frequency. This phenomenon is called dispersion and is utilized to study the elastic properties of the surficial formations (Nazarian et al., 1983; Stokoe et al., 1994; Park et al., 1998). Dispersion mainly depends on the V_S of each geological formation.

The Rayleigh wave propagation velocity is either studied by analyzing the phase velocity, $c = \omega/k$, or by analyzing the group velocity, U, (Lay and Wallace, 1995), which are related through the following equation:

$$U = \frac{d\omega}{dk} = c - \lambda\frac{dc}{d\lambda} = c + k\frac{dc}{dk} \tag{5}$$

where ω is the angular frequency, λ the wavelength, and k the wavenumber (Figure 2.4).

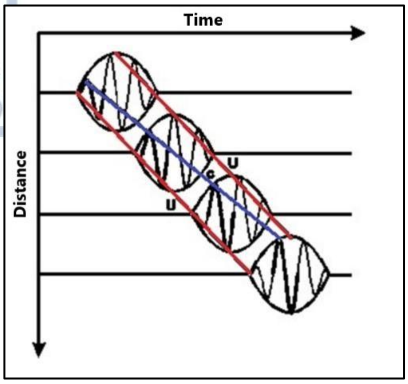

Figure 2.4 Typical propagation way of Rayleigh surface waves. The total seismic energy propagates with group velocity while each harmonic frequency propagates with phase velocity (Papazachos and Papazachos, 2013, modified).

The Rayleigh wave propagation is a complex, multimodal phenomenon. In the case of propagating in a horizontally layered medium, the surface wave propagation equations do not possess a unique solution, but finite discrete k values exist for a given ω, meaning that different modes of vibration exist. Each mode is defined by its own propagation velocity, which always increases from the fundamental to the higher modes. The fundamental mode is characterized by the lowest phase velocity. The depiction of the seismic energy in one of the following domains: phase velocity – frequency, phase velocity – wavelength or phase velocity – wavenumber, is necessary to identify the fundamental and the higher modes (Yilmaz, 1987).

2.4.2 Seismic Data Acquisition

To acquire the Rayleigh wave data, multiple evenly spaced vertical geophones are aligned with the seismic source on the ground surface (Figure 2.5). A wave is generated with an impact at the source point (usually a sledgehammer striking on a metal plate) at the one end of the array and the resulting ground motion is recorded as a function of time by the geophones which are connected via a multichannel cable with a portable seismograph.

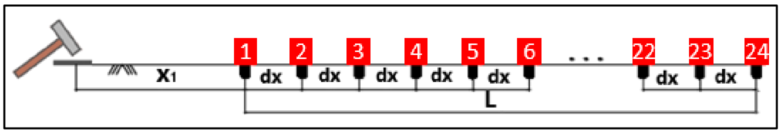

Figure 2.5 Array of 24 geophones with equal spacing (dx) aligned with a seismic source (sledgehammer striking on a metal plate). The source offset is x_1.

The investigation depth and resolution of the data depend on the geometry of the geophone array. The maximum investigation depth (Z_{max}) depends on the longest wavelength (λ_{max}) recordable (Park and Carnavele, 2010) and is approximately equal to:

$$Z_{max} = \frac{\lambda_{max}}{2} \tag{6}$$

The geophone array aperture (L) is twice the length of the longest wavelength recordable (λ_{max}) and therefore also related to the maximum investigation depth. Thus, the geophone spread should be 2-3 times longer than the desired investigation depth:

$$L/3 \leq z_{max} \leq L/2 \tag{7}$$

The resolution is related to the shortest wavelength recordable (L_{min}) that depends on the geophone spacing (dx) and is equal to 2dx (Nyquist's theorem) (Yilmaz, 1987). Thus, determining the shallowest resolvable investigation depth:

$$0.3dx \leq z_{min} \leq dx \tag{8}$$

The minimum source offset required to eliminate the near-field effects depends on the λ_{max}. Park and Carnavare, 2010, Park et al., 1999 and Stokoe et al., 1994 suggest that:

$$x_1 \geq 0.5L, \qquad \lambda_{max} \approx L \tag{9}$$

2.4.3 Seismic data processing and dispersion curve inversion

The MASW data processing is a two-phase procedure. The first phase involves data acquisition as already described as well as the extraction of the dispersion curve while the second phase involves the inversion of the dispersion curve (Figure 2.6).

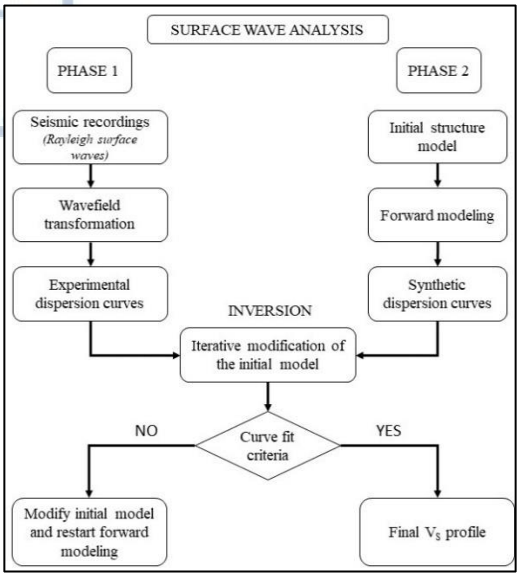

Figure 2.6 Flow-chart of the surface wave analysis procedure followed during the MASW data processing.

The most widespread technique to process active seismic data is based on the picking of amplitude maxima in 2D spectral depictions of the wavefield. A 2D Fourier transformation is applied to convert the wavefield from the time – distance (t – x) domain (Figure 2.7a) to the frequency – phase velocity (f – c) domain (Figure 2.7b) (McMechan and Yedlin, 1981, Yilmaz, 1987). The dispersion curves correspond to local maxima of the seismic energy that exist in the f – c domain and they represent the variation of the phase velocity (c) of the Rayleigh surface waves with frequency (f) (Kritikakis, 2010).

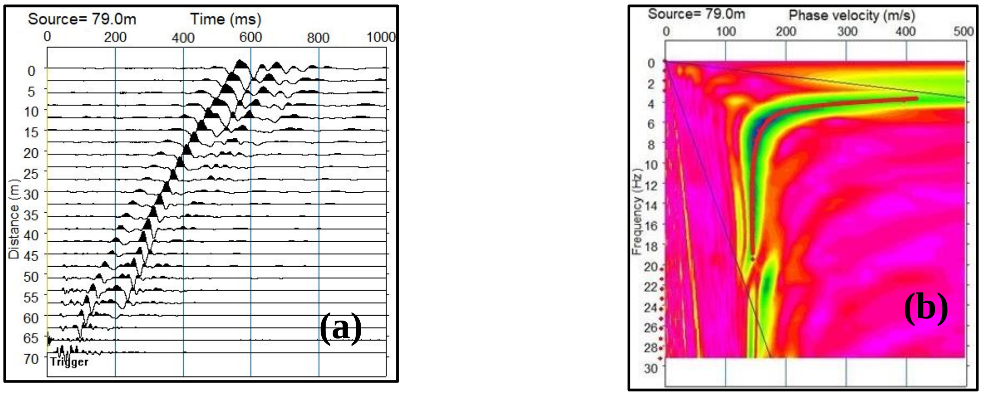

Figure 2.7 Transformation of the distance – time (x – t) domain to the frequency – phase velocity (f – c) domain (a) and selection of the fundamental mode dispersion curve (red curve) (b). Cooler colors indicate a high concentration of the seismic energy that propagates with a given velocity and frequency.

The inversion procedure of the experimental dispersion curves is similar to the geoelectrical data inversion, described in Section 2.2.2. The main goal is to search for the best subsurface model whose forward response fits well the experimental data, based on the misfit function that is minimized during the inversion. The misfit function is a norm of the distance between the experimental and the synthetic dispersion curves associated with a given subsurface velocity model. The inversion procedure is described in the next sequential steps:

1. Initial model definition: In this step, the parameters of the initial model are defined (number of layers, thickness, V_S, V_P).
2. Computation of the synthetic dispersion curves: Forward modeling allows the generation of synthetic dispersion curves corresponding to the initial model.
3. Comparison of experimental and synthetic dispersion curves and inversion of the linear system of the residuals: In this step, the root mean square (RMS) error of the current model is calculated, and a new model is found by the linearized inversion of the residuals.
4. Procedure iteration: The procedure is iterated multiple times until a satisfactory fit between the synthetic and experimental dispersion curves is achieved.

2.5 Ambient noise and ambient noise interpretation techniques

2.5.1 Nature and origin of ambient noise

Ambient noise can be described as the superposition of low-amplitude ambient vibrations of the Earth’s crust. These vibrations exhibit a stochastic spatio-temporal variation, with amplitudes ranging from 0.1 – 10μm, are imperceptible to humans and cause no damage to infrastructure. Ambient noise consists mainly of surface waves, as shown in the pioneering work of Aki (1957), and hence their decay with depth is significant as is considered for surface waves. Therefore, the maximum penetration depth depends heavily on their wavelength, which varies with the nature of the surface waves generated by ambient noise sources.

Ambient noise recordings are acquired with high sensitivity seismometers and are usually used in studies of the Earth’s structure. The techniques utilizing ambient noise measurements (typically referred to as passive seismic techniques) have recently seen significant development, because of their low cost and null environmental impact. The origin sources of ambient noise are either natural such as the ocean waves, tides, wind, and changes in the atmospheric pressure or anthropogenic such as industrial activity, road traffic etc. Despite dispute in the scientific community, the correlation between ambient noise and specific natural origins has been demonstrated in several cases (Figure 2.8). Rhie and Romanowicz (2004) have proven a strong relation between stacked amplitudes of daily recorded ambient noise with a small number of earthquakes and significant ocean wave heights for the winter and summer seasons of the year 2000 for the northern hemisphere. The authors concluded that more than 85% of the maximum amplitude recordings depends on the interaction between ocean surface, bottom, and atmosphere for winter periods (northern and southern hemisphere, respectively).

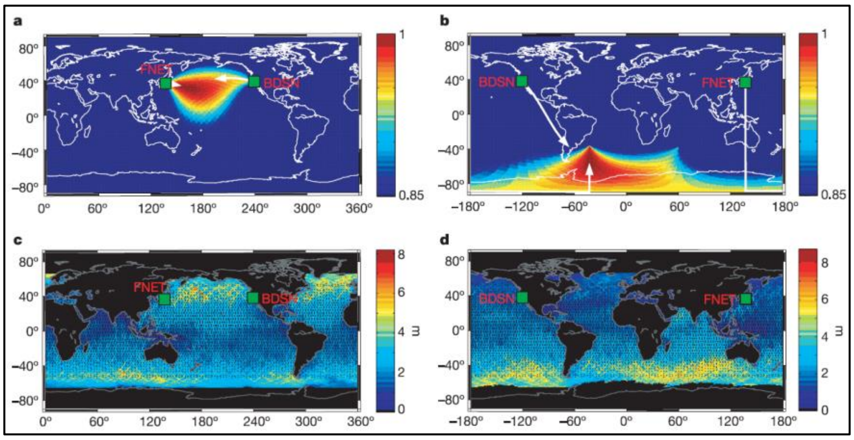

Figure 2.8 Correlation of stacked amplitudes of ambient noise recordings for winter (a) and summer (b) periods and significant ocean wave height for the same time period (c and d, respectively) for the year 2000 (Rhie and Romanowicz 2004).

Vibrations with frequencies lower than 1Hz are usually referred to as microseisms whereas above 1Hz they are referred to as microtremors (Seo, 1997). Moreover, anthropogenic noise tends to generate waves that cause high frequency vibrations, while noise that originated from natural sources propagates with low frequencies (Gutenberg, 1958; Asten, 1978; Asten and Henstridge, 1984; Bennefoy-Claudet et al., 2006). Seo (1997) suggested that the frequency band of the generated ambient noise is affected by the source depth, the recording time (day or night), the variation of recorded amplitudes and the area of the recording. The amplitudes of the microseisms are varied with natural phenomena, while the amplitudes of the microtremors exhibit daily and weekly fluctuations. Frequency bands of recorded signals from different noise sources are summarized in Table 2.1 (Bonnefoy-Claudet et al., 2006). According to this classification, ambient noise with natural origin produces waves with a low frequency content, close to 1 Hz threshold, while anthropogenic ambient noise sources generate waves with higher frequencies.

Table 2.2 Summary of ambient noise sources according to their frequency (Bennefoy-Claudet et al., 2006).

Ambient noise sources	Gutenberg (1958)	Asten (1978, 1984)
Ocean waves striking along coasts	0.05 – 0.1 Hz	0.5 – 1.2 Hz
Monsoon/Large scale meteorological perturbations	0.1 – 0.25 Hz	0.16 – 0.5 Hz
Cyclones over the oceans	0.3 – 1 Hz	0.5 – 3 Hz
Local scale meteorological conditions	1.4 – 5 Hz	-
Volcanic tremor	2 – 10 Hz	-
Urban	1 – 100 Hz	1.4 – 30 Hz

The ambient noise wavefield is complex, consisting of body (P and S) and surface waves (Rayleigh and Love) with random spatio-temporal variations. As mentioned already, ambient vibrations consist mainly of surface waves (Aki, 1957) and therefore decay greatly with depth, penetrating only the shallow layers. The related research (Douze, 1964, 1967, Toksöz and Lacoss, 1968, Li et al., 1984, Horike, 1985, Yamanaka et al., 1994, Bonnefoy-Claudet, 2004, Bonnefoy-Claudet et al., 2006) suggests that body waves phases (P, SV, and SH) contribute lower amounts of energy in the total wave-field, while vertical and horizontal components seem to be dominated by Rayleigh and Love waves. Several researchers (Ohmachi and Umezono (1998), Chouet et al. (1998), Okada (2003), Yamamoto (2000), Arai and Tokimatsu (1998, 2000), Schmidt (1981), Cornou (2002) and Cornou et al. (2003a, b)) studied the wave content of ambient noise, in an attempt to distinguish the contribution of Rayleigh and Love waves. These studies suggest that Rayleigh waves dominate the noise wave-field of signals for frequencies lower than 1 Hz, while Love waves tend to dominate higher frequencies. Also, Tokimatsu (1997) showed that Rayleigh wave higher modes are also present (and sometimes dominate) in the ambient noise wavefield and are highly affected by the V_S structure.

Bonnefoy-Claudet et al. (2006) compiled all published results regarding the composition of the ambient noise wavefield (Rayleigh and Love waves) for a wide variety of geological settings. The authors concluded that for shallow sedimentary formations (with depths <100m) and for frequencies lower than 1Hz, the wavefield is dominated by Rayleigh waves. On the other hand, for higher frequencies and greater depths the wavefield is dominated by Love waves. Although this approach provides useful information on the composition of the noise wavefield, the results are limited to sedimentary deposits and do not cover a significant range of possible site geologic conditions (weathered rocks, presence of water, igneous / metamorphic bedrock etc.).

Table 2.3 Relative proportion of surface waves in the ambient noise wavefield for different frequency bands and a variety of geological conditions (Bennefoy-Claudet et al., 2006).

Study	**Freq. Band**	**Geology**	**Rayleigh**	**Love**
Chouet et al (1998)	>2Hz	Volcanics	23%	77%
Yamamoto (2000)	3 - 8Hz	Sediments (thickness <100m)	<50%	>50%
Arai and Tokimatsu (1998)	1 - 12Hz	Sediments (thickness <100m)	40%	60%
Cornou (2002)	0.1 - 1Hz	Sediments (thickness ~500m)	50%	50%
Okada (2003)	0.4 - 1Hz	Sediments (thickness ~50m)	<50%	≥50%
Kohler et al (2004)	0.5 – 1.3Hz	Sediments (thickness ~200m)	10– 35%	65-90%

2.5.2 Horizontal to Vertical Spectral Ratio (HVSR) technique

The Horizontal to Vertical Spectral Ratio (HVSR or H/V) has been proposed and thoroughly studied by Nakamura (1989, 1996, 1997, 2000, 2014, 2019). Based on the results of local site effects to earthquake excitation, he suggested the applicability of the HVSR method using single-station, three-component seismometers for ambient noise recording. Local site effects attributed to the local geology can be modelled based on the HVSR of ambient noise recorded on the surface (Nakamura 1989, 1996). According to the same researcher, the horizontal (H_f) and vertical (V_f) spectra recorded on the surface of a sedimentary basin (Figure 2.9) dominated by body and surface waves, provides the transfer function of the sedimentary formations given by the Quasi Transfer Spectra (QTS) equation:

$$QTS = \frac{H_f}{V_f} = \frac{A_h * H_b + H_s}{A_v * V_b + V_s} = \frac{H_b}{V_b} * \frac{\left[A_h + \frac{H_s}{H_b}\right]}{\left[A_v + \frac{V_s}{V_b}\right]} \quad (10)$$

where A_h, A_v are the amplification of horizontal and vertical spectra respectively due to vertically incident body waves, H_b, V_b are the horizontal and vertical spectra of the bedrock beneath the sedimentary formations and Hs, Vs are the spectra of the horizontal and vertical motion respectively of the Rayleigh surface waves (Nakamura 2000).

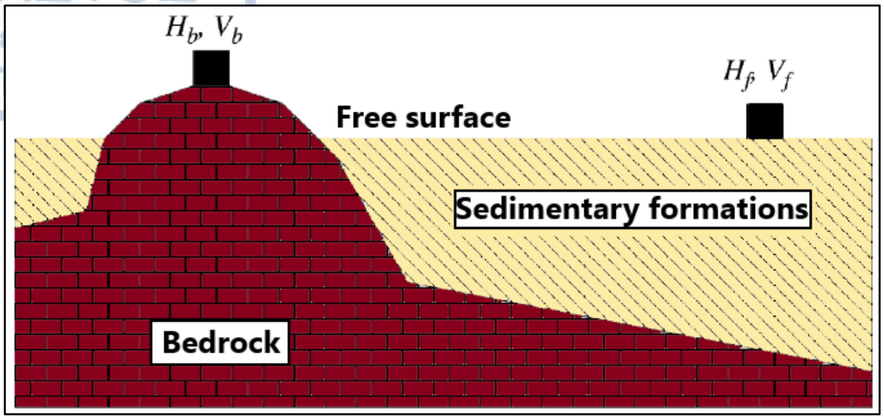

Figure 2.9 Typical geological structure of a sedimentary basin. H_f, V_f refer to the horizontal and vertical spectra of the ground motion at the surface of the sedimentary formation and Hb, V_b, to the respective spectra at the bedrock (Nakamura 2000, modified).

According to Moisidi et al (2012), the interpretation is based in the following assumptions: (1) the effects of surface Rayleigh waves are equal for vertical and horizontal component at the basement, (2) the horizontal component of the ambient noise is amplified by scattering of the S-waves and the vertical component is amplified by scattering of the P-waves, (3) the Rayleigh wave effect exists only in the vertical spectrum at the surface and not in vertical spectrum at the bedrock, (4) for the frequency band 0.2 – 20 Hz, the amplification is close to unity ($H_b/V_b \approx 1$). Ambient noise near the ground surface is dominated by surface waves, hence

$$QTS = {}^{H_S}/_{V_S} \tag{11}$$

The HVSR curve due to the Rayleigh waves effect exhibits a steep maximum peak at the fundamental frequency (f_0) (Figure 2.10) at locations where high contrast of mass density (ρ) and S-wave velocities (V_S) between the bedrock and the overlying sedimentary formations exists (Nogoshi and Igarashi 1971, Field and Jacob 1993, Lachet and Bard 1994, Ansary et. al 1995, Horike 1996, Tokimatsu et. al 1996, Konno and Ohmachi 1998, Bard 1999; among others).

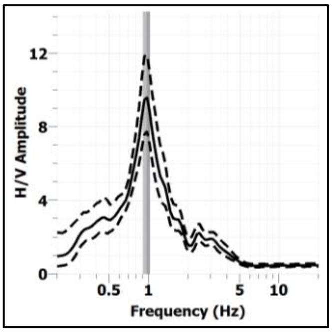

Figure 2.10 The HVSR curve with its standard deviation. The maximum peak at approximately 1Hz is related to the fundamental frequency (f_0) of the surficial formations at the measurement point.

Nakamura (1989, 1996, 2000) concluded that the HVSR method:

- provides the fundamental frequency (f_0) of the surficial formations,
- allows for the estimation of the amplification factor of seismic motion at the measurement point, despite the level of the Rayleigh effect,
- can provide an estimation of the depth of the bedrock according to the following equation:

$$H = \frac{V_S}{4f_0} \tag{12}$$

where V_S is the average S-wave velocity of the surficial formations. Bonnefoy-Claudet et al, (2008) proved that this equation works both if ambient noise is composed of mostly body and/or surface waves.

In general, the scientific community is still debating on the theoretical background and the importance of the HVSR method for the local site assessment, mostly because the HVSR method was empirically developed. The SESAME research project (**S**ite **E**ffect**S** assessment using **AM**bient **E**xcitations, SESAME 2004) was an attempt to study the validity of the ambient noise methods and their robustness in local site effect assessment (Bard et al., 2004). The main conclusions regarding the HVSR method are that it can provide a reliable estimation of the fundamental frequency (f_0) of the surficial formations (HVSR curve peak) but cannot provide a reliable value of the amplification, A_0, corresponding to the HVSR peak. Haghshenas et al., (2008) compared the f_0 and A_0 values derived from a large database using the HVSR method with corresponding values by the SSR (Standard spectral Ratio) technique. Despite a very good agreement of the f_0 values from both techniques, the comparison of the A_0 values showed that the HVSR method significantly underestimates the true amplification. Therefore, the A_0 value extracted by the HVSR method can be considered as a minimum threshold of the true amplification of the seismic motion due to local site effects.

2.5.3 Ambient noise array technique

The analysis of ambient noise measurements acquired by implementing the ambient noise array technique is an attractive tool for the estimation of a 1D V_S profile (Aki 1957, Asten 1978). The application of this technique is based on the assumption that the ambient noise is dominated by surface waves and that the subsurface structure is one-dimensional (Tokimatsu, 1997). In such 1D, heterogeneous structures, the surface waves exhibit the dispersion phenomenon (see Section 2.4.1). The dispersive characteristics of the surface waves depend mainly on the body waves velocities (both P and S waves), the mass density and the thickness of each layer of the subsurface structure (Murphy and Shah 1988, Aki and Richards 2002). The Rayleigh and Love surface waves coexist in the horizontal component of the seismic motion, while the vertical component is affected only by the Rayleigh waves. Typically, the surface wave analysis is conducted by utilizing only the vertical component, hence the extracted information regards the dispersion of the Rayleigh waves.

In the ambient noise wavefield, the source positions are generally unknown, and energy radiates from many directions at unknown angles to the receivers. For this reason, recording stations are installed typically at 2D concentric circular arrays with symmetrical geometries (Figure 2.11), as they provide a similar sensitivity of the array to wavefields impinging from different directions (Foti et al., 2018). It is common practice that the distribution of the stations is equal at each circle, with 60^o angle for the first circle and 120^o for the second and third circle) (Figure 2.11). It is common that small deviations may apply to the field locations (and angles) due to free field restrictions. The locations are pre-planned before field deployment and if the locations change, the new coordinates are recorded with a GPS system.

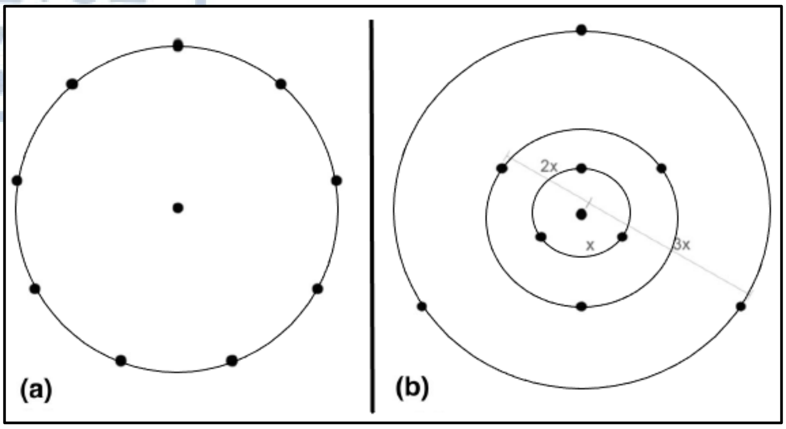

Figure 2.11 Commonly used array geometries for passive data acquisition, (a) circular shape, (b) nested triangles. These examples are given with a total number of 10 sensors.

The aperture of the array (maximum distance between sensors) affects the maximum measurable wavelength and therefore the depth of the investigation (Foti et al., 2018). The minimum spacing between sensors is related to the shortest wavelength measurable and therefore to the resolution of the shallow depths. Given the number of the available sensors, arrays from small to larger apertures are usually deployed successively (typically 3 circles) to sample over a wide wavelength range. An empirical relation regarding the depth of investigation is that its value is three times lower than the diameter of the bigger circle (or practically, the maximum distance between two stations). The value of the fundamental frequency (f_0) is crucial since the energy of the vertical component (Rayleigh waves) vanishes in the vicinity of and below the f_0 value and the extraction of the part of the dispersion curve below that limit becomes difficult (resolution problem) (Wathelet et al. 2008).

The processing techniques of ambient noise data usually derive the dispersion characteristics from statistics computed on a large number of narrow windows extracted from the long duration recorded signals. The length of these time blocks is adapted to the analyzed frequency. There are mainly three techniques to process passive data. The frequency – wavelength (f-k) method (Lacoss et al. 1969, Kvaerna and Ringdahl 1986), the high-resolution frequency – wavelength method (Capon 1969, Asten and Henstridge 1984, Wathelet et al., 2018) and the spatial autocorrelation method (SPAC) (Aki 1957, Ohori et al. 2002, Roberts and Asten 2004). The results of the aforementioned methods are generally in good agreement taking into consideration the generated V_{SZ} profile (Wathelet et al., 2008). In the present work, the processing of all ambient noise recordings for the extraction of the dispersion curve of the Rayleigh waves is conducted using the f – k method (Figure 2.12).

The f – k method allows the use of relatively high energy elastic waves that compose the complex ambient noise wavefield (Okada, 2003). Although, it cannot determine the composition of these waves, namely the proportion of body and surface waves and the existence of fundamental or higher modes, it is considered that the f – k method provides the dispersion curve of the surface waves because of the assumption that ambient noise is dominated by them.

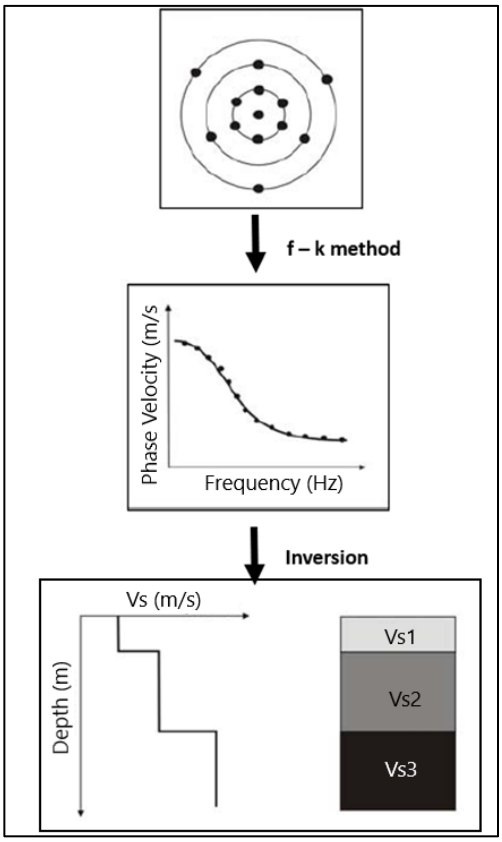

Figure 2.12 Surface wave analysis of ambient noise data with the application of the ambient noise array technique. The data are acquired by seismometer arrays to extract the surface waves dispersion curve. The inversion of the dispersion curve generates the one-dimensional V_S profile of the subsurface structure (Okada 2003, modified).

The processing of ambient noise data with the f – k method is based on the assumption that the ambient noise sources are remotely situated, hence the incoming wavefield at the array location consists of plane waves. Let’s consider a wave with frequency f, which propagates in a homogeneous medium with arbitrary velocity and direction (or with wavenumbers k_x and k_y), then the arrival times can be calculated at each recording station. The arrival times at each station are shifted in accordance with the time residuals, viz the delay of the arrival time compared to the arrival time in the reference station (seismometer at the center of the array). All shifted signals are summed and divided into small time windows. The f – k spectrum and the f – k cross spectrum are computed for each time window and the data are transferred to the f – k field (Okada 2003. Ohrnberger et al., 2004). The value of the f – k cross spectrum is called the array output and is plotted on the k_x, k_y field for each frequency. The location of the array output for a particular frequency provides an estimation of the velocity and the azimuth of the propagated waves with the maximum energy entering the seismometer array.

The dispersion curve of the surface waves can be reliably extracted inside frequency limits that depend mainly on the geometry and the maximum aperture of the array as well as on characteristics of the wavefield that can be altered due to the effect of the local geology. According to Woods and Lintz (1973) these limits also depend on the spatial distribution of the seismometers and the correlation of the incoming waves. They suggested that the evaluation of the ability of an array to provide a dispersion curve in the desired limits should be conducted using the theoretical array response (array transfer function) in the k_x, k_y field. The theoretical array response is computed with the coordinates (x_i, y_i) of each station according to the equation by Woods and Lintz (1973) and Asten and Henstridge (1984).

$$R_{th}(k_x, k_y) = \frac{1}{n^2}\left|\sum_{i=1}^{n} e^{-j(k_x x_i + k_y y_i}\right|^2 \qquad (13)$$

where n is the number of the recording stations of the array. An example of the theoretical array response is presented in Figure 2.13d, for the array geometry of Figure 2.13a.

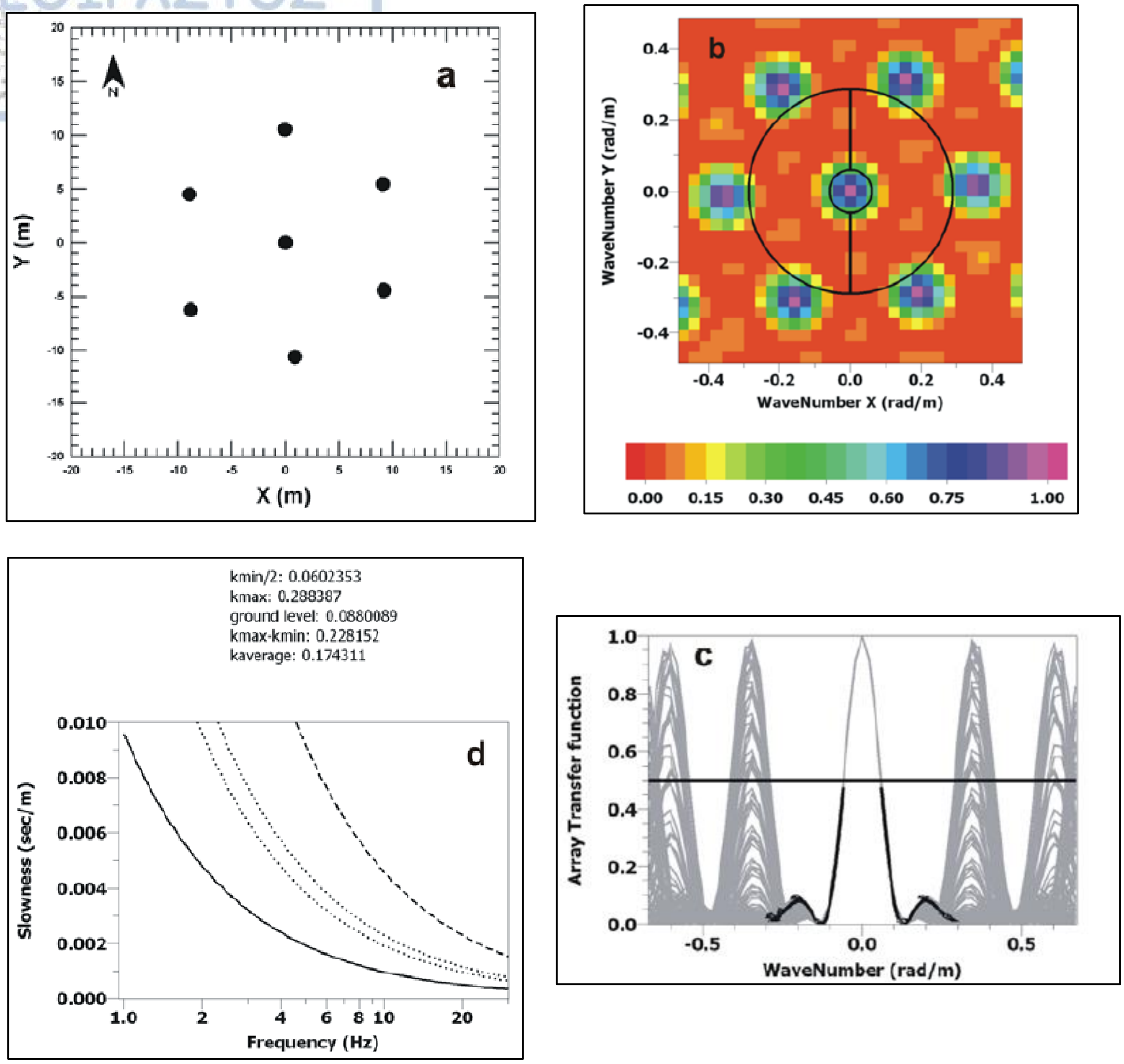

Figure 2.13 Theoretical array response example for a circular array geometry (a). The black circles at (b) correspond to wavenumber values $k_{min}/2$ (inner circle) and k_{max}(outer circle). (c) Dashed lines to the wavenumber diagram for different azimuths (grey curves). The black curve represents the direction of the black line in (b). (d) The 4 exponential curves are calculated for the constant wavenumber values $k_{min}/2$ (continuous black line), k_{min}, $k_{max}/2$, (dotted lines) and k_{min} (dashed line) and define the reliability part of the dispersion for the array geometry in (a) (Anthymidis, 2008).

The dispersion curve that is extracted using the f – k method is inverted to generate a 1D velocity structure profile. The inversion is based on a neighborhood algorithm, which also gives the possibility to add a priori information regarding ground parameters (thickness, V_P, V_S, mass density, Poisson’s ratio). To exhaustively explore the parameter space, a great number of models and corresponding dispersion curves (typically a few thousands) are generated. The theoretical (synthetic) curves and the experimental dispersion curve are compared with the misfit calculation according to the following equation:

$$misfit = \sqrt{\sum_{i=0}^{n_F} \frac{(x_{di} - x_{ci})^2}{\sigma_i^2 n_F}} \tag{14}$$

where x_{di} is the velocity at the experimental dispersion curve at frequency f_i, x_{ci} is the velocity of the theoretical dispersion curve at frequency f_i, σ_i is the uncertainties of the points of the experimental dispersion curves for each f_i frequency and n_F is the number of points that compose the experimental dispersion curve. The resulting value of equation 14 reveals how "far" is each one of the theoretical dispersion curves from the experimental one.

The geometry obtained is purely one-dimensional and is averaged across the seismometer array, implying that the array technique is not suitable when strong lateral variations exist in the investigation area (Wathelet M., 2005). The 1D structure of the investigation area is checked through the HVSR for every station of the array. The similarity among the shape of the HVSR curves of all the stations can be stated as a consistency control.

2.6 Inversion of HVSR

As already mentioned, the HVSR is a simple way to evaluate local site effects on seismic motion by retrieving the fundamental frequency of the surficial formations, utilizing ambient noise measurements. Additionally, to the previously described physical interpretations of the HVSR (section 2.5.1), Sánchez-Sesma et al., 2010, 2011a have recently proposed that ambient noise is a diffuse wavefield that contains all types of body (P, S) and surface waves (Love and Rayleigh). The authors named this model of ambient noise wavefield the diffuse field assumption (DFA).

The DFA theory is based on a diffuse field illumination enhanced by multiple scattering and has strong theoretical links with deterministic problems (Sánchez-Sesma et al., 2011b). It is assumed that the relative power of each seismic wave that composes the illumination emerges from the principle of equipartition of energy. Theory asserts that within a diffuse elastic wavefield, the autocorrelation in frequency domain, at any point of the medium, is proportional to the imaginary part of the Green's function when source and receiver coincide (Sánchez

Sesma et al., 2008, 2011a; Perton et al, 2009). Then, the ambient noise HVSR can be expressed in terms of directional energy densities (DEDs) that are then proportional to the imaginary part of the Green's functions, as expressed in the following equations:

$$[H/V](\omega) = \sqrt{\frac{E_{EW}(x,\omega) + E_{NS}(x,\omega)}{E_V(x,\omega)}} = \sqrt{\frac{Im[G_{11}(x,x;\omega)] + \mathrm{Im}[G_{22}(x,x;\omega)]}{Im[G_{33}(x,x;\omega)]}} \quad (15)$$

where, E_{EW}, E_{NS} are the DEDs of the horizontal and E_V of the vertical component (Arai and Tokimatsu, 2004). This equation (Sánchez-Sesma et al., 2010) links "average" measurements expressed on the left part of the equation with an intrinsic property of the medium on the right part of the equation. Therefore, the equation naturally allows for the inversion of HVSR accounting for all types of elastic waves.

In this work, inversion of HVSR was conducted with HV-Inv program (Garcia-Jerez et al, 2016) which allows separate computation of the contributions of SH, P-SV and Rayleigh, Love surface waves.

2.7 Numerical Simulation of Ambient noise

The numerical simulation of ambient noise by generating synthetic recordings contributes to better identifying the subsurface structure in an area and therefore leads to a better interpretation of the results of the ambient noise analysis methods such as the HVSR inversion method.

It is possible to estimate the response of the surficial sedimentary formations to seismic motion at a site by generating synthetic ambient noise recordings if geophysical and geotechnical properties of the subsurface structure are known. Each synthetic recording that is computed at receiver location depends on a specific subsurface structure model, as well as on the ambient noise sources. The HVSR analysis of the synthetic recordings allows for the estimation of the fundamental frequency (f_0) and the corresponding amplitude (A_0) of the seismic motion for the theoretical 1D structure used, regardless of the location and the signal type of the ambient noise sources. The closer the theoretical structure is to the real subsurface structure, the more the synthetic HVSR curve approaches the experimental one. Therefore, the main idea behind this approach is to compare the synthetic and experimental HVSR curves to indirectly assess the validity of the velocity models as representative of the subsurface geophysical structure in the study site. The generation of synthetic ambient noise recordings is the result of a combination of factors which contain: the source, the subsurface structure that serves as the propagation medium of seismic waves, and the seismometer (Stein and Wysession, 2003). Hence, a recording, $u_{(t)}$, may be considered as the convolution of the time series of each factor:

$$u_{(t)} = S_{(t)} * G_{(t)} * I_{(t)} \tag{16}$$

where $S_{(t)}$ is the source function, $G_{(t)}$ represents the local site effects, and $I_{(t)}$ describes the response of the seismometer. The G(t) factor is analyzed with the Green's functions that describe the signal that arrives at the seismometer if the source time function is a delta function. Hence, the generation of synthetic recordings is based on the simulation of these parameters: the source function and the response of the surficial geological formations computed with the Green's functions. The response of the seismometer is known by its manufacturer.

The ambient noise simulation consists of the three following steps:

- modeling of ambient noise sources for a specific volume of space around the examined site
- computation of the Green's functions for a horizontally layered subsurface structure to compose the synthetic ambient noise recordings.
- HVSR analysis of the synthetic ambient noise recordings

Modeling of the ambient noise sources is conducted using the RANSOURCE code (Moczo and Kristek, 2002). The RANSOURCE code generates random ambient noise point sources with normal spatial and temporal distribution in a predefined 3D space (Figure 2.14). The spatial distribution of the sources is constrained by the defined minimum distance between two neighboring sources and by the minimum and maximum distance between a point source and a receiver. The temporal distribution is constrained by the defined minimum and maximum number of point sources that radiate energy simultaneously. Hence, the generated ambient noise sources are mostly surficial point forces with the following characteristics:

- the position at space (x, y, z),
- the direction and the amplitude of the force vector,

- the activity duration,
- the source time function.

The time function of the source may be either a delta-like (Figure 2.15 – left) or a pseudomonochromatic type signal (Figure 2.15 – right) with random activity duration and dominant frequency.

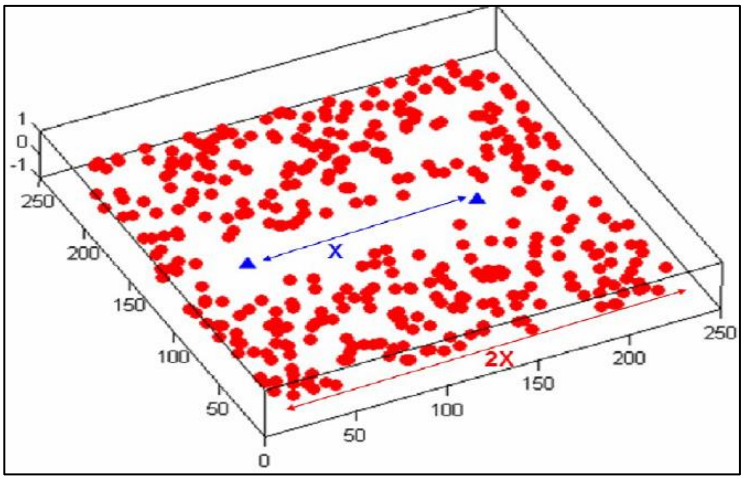

Figure 2.14 Example spatial distribution of ambient noise point sources (circles) and receivers (triangles) in predefined 3D space (Panou, 2007).

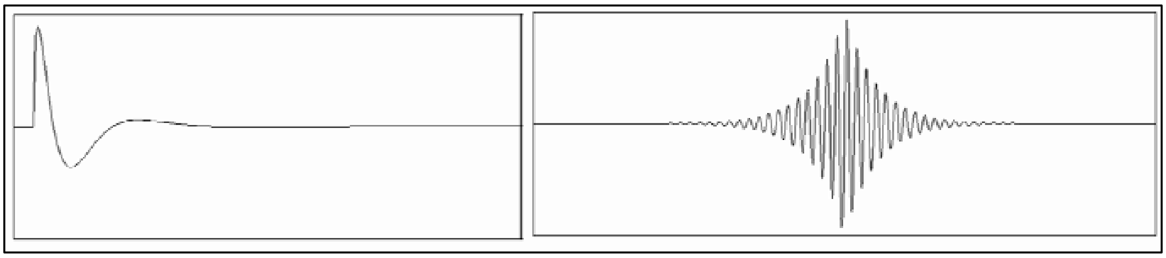

Figure 2.15 Example of source time function with a delta-like signal (left) and a pseudomonochromatic type signal (right) (Panou, 2007).

The response of the propagation medium to the seismic waves that radiate from the ambient noise point sources is calculated with the method proposed by Hisada (1994, 1995). Generalizing the reflection and transmission (R/T) coefficient method (Luco and Apsel, 1983), Hisada (1994) defined a solution to compute the Green functions in a heterogenous viscoelastic, horizontally layered structure with sources and receivers located in shallow depth. The free surface of the structure is considered flat, without topography, while the intrinsic properties of the medium vary only with depth (1D simulation) (Figure 2.16). Q_P and Q_S correspond to the attenuation factors for the P and S waves, respectively. Relatively low Q_P and Q_S mean that the seismic waves are being attenuated. If they are high the waves travel almost undisturbed through the region. Particularly in areas where Q_P and Q_S are low, several competing effects such as intrinsic attenuation or scattering may affect the amplitude of the waves (Hauksson and Shearer, 2006).

This methodology was improved in Hisada (1995) by deriving analytical asymptotic solutions for both the direct wave and the reflected/transmitted waves from the boundaries. This methodology can compute the ground motion at a particular time, caused by a 3D defined force. The originality of this methodology lies in the fact that it assumes receivers and sources at the same (close) depth. In this case, convergence of the Green functions is a difficult task. The more the receiver depth approaches the source depth, the more the Green function oscillates with increasing amplitude.

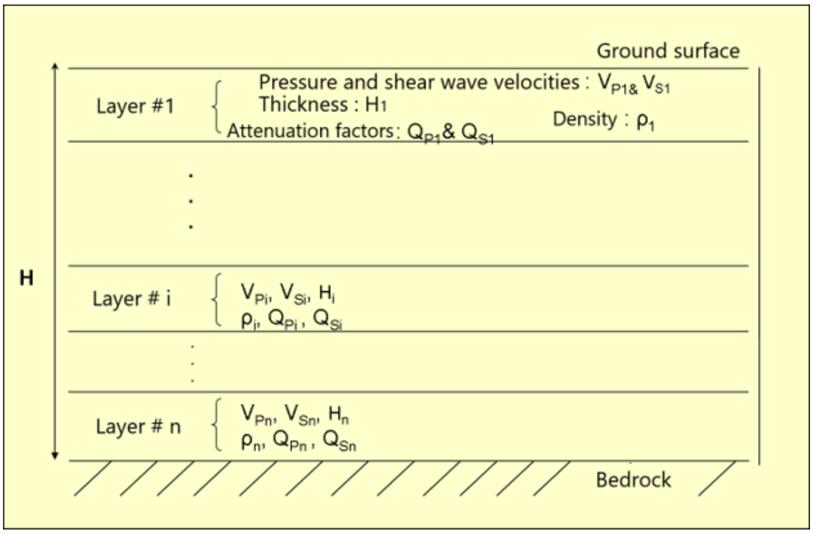

Figure 2.16 Horizontal stratigraphy of surface deposits over hard bedrock (Panou, 2007).

2.8 Earthquake Horizontal to Vertical Spectral Ratio

The methods based on ambient noise measurements such as the HVSR method and the ambient noise array method, extract important information regarding local geological structure and its theoretical response during an earthquake event. The most reliable approach to estimate local site effects is the simultaneous recording of the ground motion in sites with different geological conditions (rigid rock, deposits) during an earthquake event (Standard Spectral

Ration – SSR method introduced by Borcherdt, 1970). Therefore, the analysis of seismic motion recordings can be used to assess the validity of the ambient noise methods (directly for the HVSR method and indirectly for the inverted velocity profile that is derived from the HVSR inversion), as well as, for the computation of the true amplification of the seismic motion of the surficial geological formations.

A simpler method to estimate the transfer function using the HVSR of earthquake recordings without a reference station is introduced in Lermo and Chavez-Garcia, 1993. The authors used the intense S-wave part in all 3 components of earthquake recordings to compute the HVSR which they compared to ambient noise HVSR from the same site with encouraging results. For the purpose of this thesis, we used the part of the seismic recording corresponding to the arrival of the S-waves to the end of coda waves which is the most energetic part of an earthquake recording, to compute the earthquake HVSR. The produced earthquake HVSR is compared with the observed ambient noise HVSR and synthetic HVSR curves.

3. Geophysical Data Used

3.1 Introduction

The methodology for site characterization that was described in the previous chapter is applied at six accelerometric sites in the metropolitan area of the city of Thessaloniki, northern Greece. The geological conditions observed at each site vary from rock to thick sedimentary formations. Another important characteristic of the approach of this research is that the application sites exhibit different levels of anthropogenic noise (transient signals, machinery operation, car traffic etc.). A few sites were located at a very close proximity to the sea which by theory provides low frequency ambient vibrations. Each site exhibited different spatial variations for the deployment of the geophysical methods rendering the implementation of the methodology a quite difficult task in the urban environment. The space availability depended upon the urban infrastructure (buildings etc.) and human activities (car traffic, passers-by etc.) and defined the scale of the geophysical methods (ambient noise aperture, length of the ERT and the active seismic methods) and therefore the investigation depth. An important part of the methodology is the available information at each site (existing boreholes, downhole measurements etc.) as they complement the acquired geophysical data and provide constraints at models with greater depths. The methodology required a relatively small number of personnel, mainly for the supervision of the seismometers during the ambient noise array deployment and the application of the geophysical methods and it was typically manageable in one day, per site.

This chapter is devoted to describing in detail the field planning and geometry of the individually applied geophysical methods and how the spatial design of each method (i.e., the aperture of ambient noise array) affected the others' at each site also given the locations of the permanently installed accelerometers and the existing boreholes. The difficulties that emerged dealing with the anthropogenic factor (transient signals from passers-by, car traffic etc.) are also thoroughly described. Problems that arose from data loss due to defective power supplies or seismometers as well as a case of seismometer theft and how they affected data processing and results, are also described to enhance the knowledge and experience gained, and to mitigate or prevent future similar phenomena.

A brief reference of the equipment used for the implementation of each method (instruments, receivers, connectivity, power supply etc.) is also mentioned as well as photographs of the field operation in an attempt to demonstrate the difficulties and particularities that were dealt with at each accelerometer station.

3.2 Data acquisition equipment

This section is devoted to giving a brief description of the instruments and equipment used in data acquisition as well as the very important procedure of the seismometers huddle-testing before fieldwork.

3.2.1 Ambient Noise Recording Equipment

The ambient noise data acquisition with the ambient noise array and the single station (HVSR) techniques was conducted with the use of triaxial broadband seismometers. The seismometers used in this study are Guralp CMG-6TD. A complete recording system consists of:

1. A Guralp CMG-6TD seismometer with a built-in 24-bit digitizer to convert ground motion to digital data and an internal flash memory storage of 2GB.
2. A GPS receiver for geographical coordinates and accurate absolute timing.
3. A power supply unit (e.g., 12V battery).
4. A junction box that connects all the above and provides PC serial RS232 connectivity.
5. Appropriate communication and power cables for the connection between the seismometer and power supply/ PC.

Data acquisition can be monitored during recording with a laptop PC through serial connection. The data are retrieved with the usage of an external firewire disk directly connected to the seismometer. A complete recording system configuration is shown in Figure 3.1.

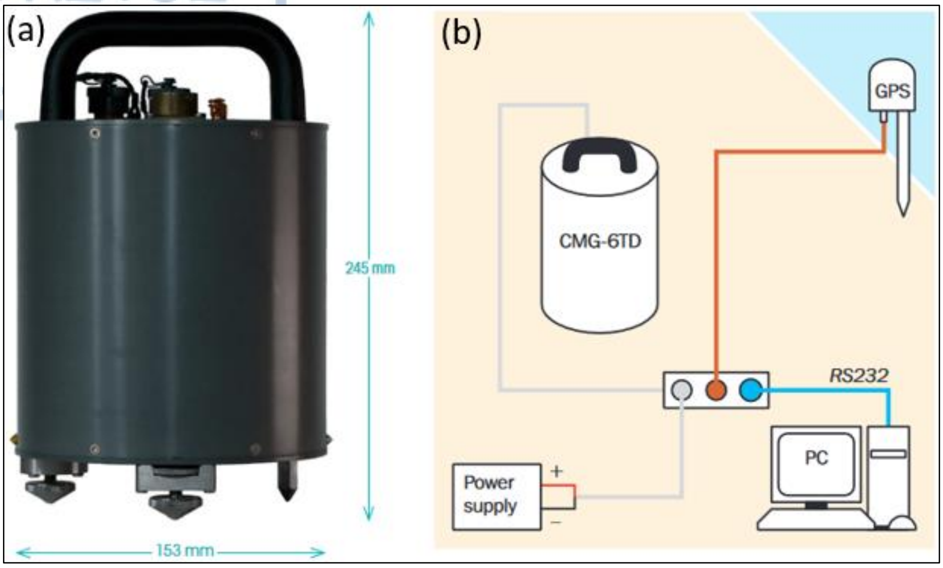

Figure 3.1 Guralp seismometer CMG-6TD (a) and schematic representation of proper connection between components (b) (https://www.guralp.com).

Huddle-testing of the seismometers before field deployment is a key part of any seismic experiment. It involves a simultaneous in the same site testing of all the recording stations' components to be used in the experiment. During huddle-testing the recording stations are also visually inspected to identify physical damage (e.g., during their transportation) and the compatibility between components is ensured. The huddle-testing can be conducted either in free-field on soil or on the ground floor (if in a building). The stations are placed at a minimum distance of 10 cm from each other whereas other heavy objects or walls abstain appropriately, and no requirement actual orientation is needed but similar among the seismometers. (Figure 3.2). The GPS receivers (antennas) are placed properly to receive satellite signals. All the available recording stations are set to record ambient noise, mostly overnight when anthropogenic noise is at a minimum level. Finally, the Fourier spectra of both horizontal and vertical components as well as the HVSR curves of each seismometer are computed and compared between all the seismometers. An example of a successful huddle-test is shown in Figure 3.3. The consistency between the resulted FAS of each component or the HVSR curves is used to assess the effectiveness of the seismometers. In Figure 3.3 the greatest inconsistency is exhibited by the seismometer with serial number 6701 (yellow curve) which was excluded from the finally chosen seismometers for fieldwork.

Figure 3.2 Huddle-testing of the recording stations in parallel before field deployment.

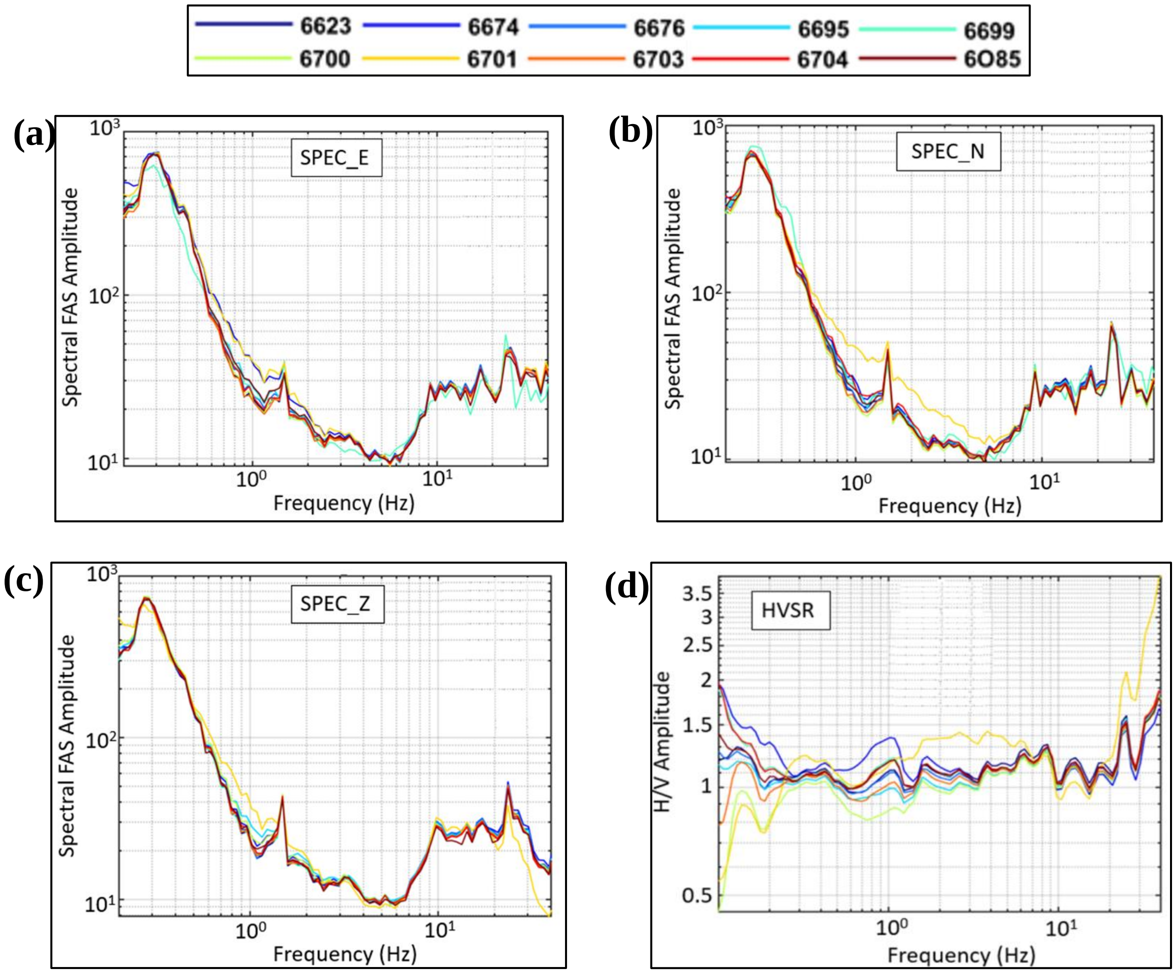

Figure 3.3 The results of a huddle-test for 10 seismometers before field operation. The results include the Fourier amplitude spectra for the Easting (a), Northing (b) and Vertical (c) components of the ground motion as well as the HVSR curves (d), for each seismometer.

3.2.2 Electrical Resistivity Tomography Equipment

The electrical resistivity investigation was conducted utilizing the Electrical Resistivity Tomography technique. The geoelectrical data acquisition was conducted utilizing the Syscal Pro Switch 48 system (Figure 3.4). It is a fully automated, all-in-one, multi-node resistivity sounding and profiling system for environmental and engineering geophysical studies, supplied by IRIS Instruments. The system is equipped with a 10-channel receiver and a 250W internal transmitter with a maximum voltage of 800 Vpp. The generated current intensity can go as high as 2500 mA. The Syscal Pro allows the connection of up to 48 electrodes (nodes) via multi-channel cables. Features such as the digital superposition for signal enhancement and live measurement error monitoring during resistivity measuring ensure high quality measurements.

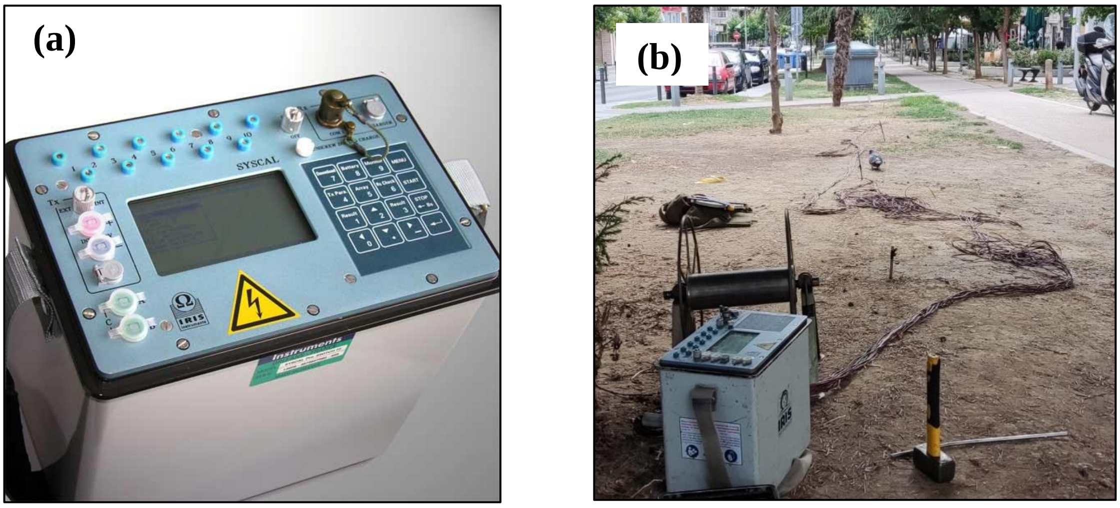

Figure 3.4 The geoelectrical data acquisition system, Syscal Pro (a) and the connection with the electrodes via multichannel cables in the field (b).

3.2.3 Active Seismic Methods Equipment

The active seismic investigation with the MASW and refraction methods was conducted using the 48-channel StrataView portable seismograph, provided by GEOMETRICS. The seismograph connects with up to 48 geophones via multichannel cables and power is supplied by an external 12V battery (Figure 3.5a). The recordable frequency content ranges from 3 to 14 kHz. For this research, vertical component geophones with 4.5 Hz eigenfrequency from Racotech company were placed into the ground. At some sites, placing the geophones on paved road required the use of metallic tripods (Figure 3.6). An 8 kg sledgehammer (Figure 3.5b) with an integrated triggering system, striking on a metallic plate (for an optimal ground coupling) was used as a seismic source.

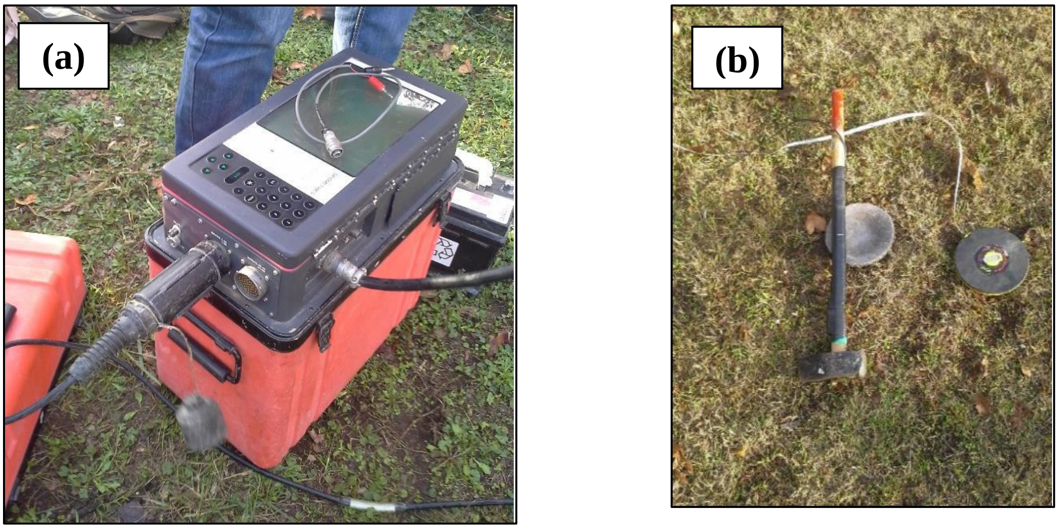

Figure 3.5 The StrataView portable seismograph from GEOMETRICS (a) and the sledgehammer along with the metallic plate used as a seismic source (b).

Figure 3.6 The.4.5 Hz eigenfrequency vertical geophones from Racotech, connected to a 24-channel cable (a). In the case of pavement or paved road, the spikes are replaced by metallic tripods for a proper ground coupling (b).

3.3 Fieldwork planning and data acquisition

In this section, the application of the aforementioned methodology is thoroughly described separately for each accelerometric site, giving a complete and spherical insight of the urban conditions that affected the in-field implementation as well as the arisen problems. The description concerns the design geometry of the larger scale applied methods (i.e., ambient noise array) in accordance with the smaller scale ones (MASW and ERT methods) as well as how the existing boreholes and accelerometer locations (if any) affected the field planning.

As already mentioned, the aim of this thesis is to test the implementation of the combined methodology in the assessment of local site effects in the seismic motion. For this purpose, we had to choose an adequate number of test sites that would fit the following criteria:

- Sites with permanently installed accelerometer stations to validate the results of the methodology with earthquake motion data.
- Sites in the metropolitan urban area of the city of Thessaloniki for an easy access.
- Sites with adequate space to effectively apply the geophysical methods.

Finally, the methodology was applied at six accelerometric sites in the metropolitan area of the city of Thessaloniki, northern Greece (Figure 3.7). All six accelerometer stations are operated by the Institute of Engineering Seismology and Earthquake Engineering (ITSAK) and are part of a free field strong motion network that spans the whole Greek territory consisting of more than 200 accelerometers installed mainly within Greek cities and towns.

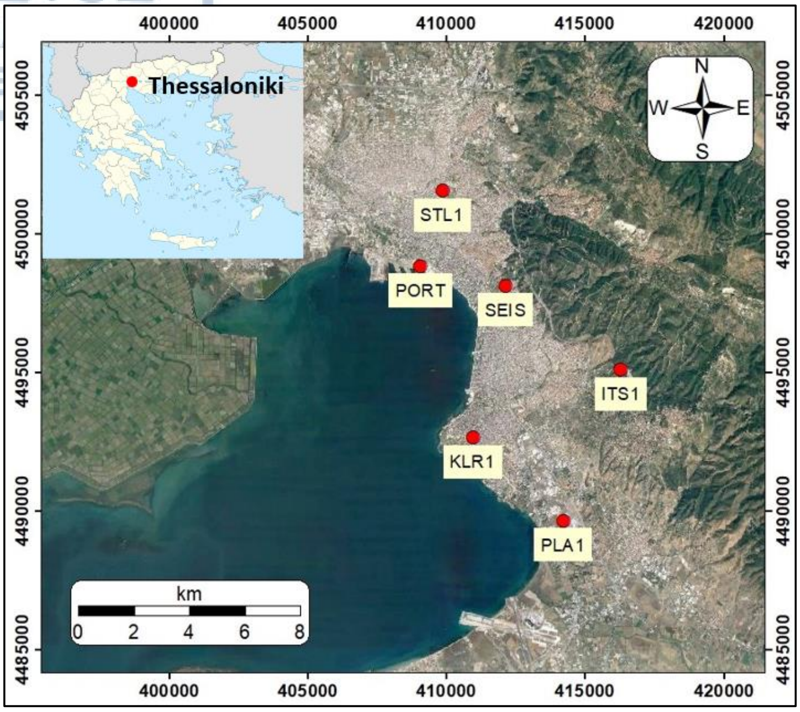

Figure 3.7 Locations of the accelerometer station sites where the methodology was applied within the metropolitan area of Thessaloniki.

As already mentioned, the methodology applied at each one of the test sites combines the following methods: the ambient noise array, the Electrical Resistivity Tomography (ERT) and the Multichannel Analysis of Surface Waves (MASW). The application of the methods was conducted as close to the permanently installed accelerometer station as possible, given the spatial restrictions per site. The installation positions of the recording stations, as well as the ERT and MASW survey lines were pre-planned before the in-situ experiment day. For each seismic line, three seismic shots with a sledgehammer were conducted.

The apertures of the ambient noise arrays were determined based on 3 criteria, by order of significance: (a) adequate depth of investigation to provide the V_{S30} (at least 30m penetration depth), meaning an aperture of about 90m, (b) depth of investigation comparable to other available information (e.g., stratigraphic logs, downhole measurement etc.), (c) available space to deploy the array. The recording stations were positioned in circumferences of circles with specific radii depending on the local restrictions of planning and deployment. Circles with relatively great radii (matching the aperture of the array of each site) were deployed to retrieve the low frequency part of dispersion curves. Circles with smaller radii (usually 10 to 15m radius) were deployed to retrieve the high frequency part of local dispersion curve. The coherency of the dispersion curve of the two different datasets was theoretically checked and validated based on the geometry of each ambient noise array (theoretical array response). Some slight variations from the pre-planned positions of the stations were due to *in situ* restrictions (e.g., building, trees, non-appropriate installation surfaces, etc.). An attempt was made to not install stations close building or walls to avoid artificial data to be introduced into the energy spectra. Also, the positions of the stations of the outer circles were considered as the limits of the study area in which the retrieved average 1D profile is limited to. Moreover, the HVSR at each station, are used to check whether the test site is characterized by 1D structure.

The ERT and MASW methods were performed in such a way so that their focus would coincide with the center of the ambient noise array, where it was possible. The main reason for this is so that the retrieved geophysical data might correspond to a vertical 1D "column" beneath the center of the ambient noise array. The survey lines were designed so that the investigation depth would be at close to 30m (where possible) and in all cases both methods used shared a common investigation line.

Finally, stratigraphic logs and downhole data from available boreholes at each site were taken into consideration and were used for the comparison of the methodology results with the actual subsurface structure.

3.3.1 Data acquisition at PORT accelerometer site – Site 1

An interesting feature at this investigation site is its proximity to the sea, which is an important source for ambient noise measurements. The local stratigraphic log as well as, a downhole measurement down to approximately 80m were available from a nearby borehole (Figure 3.8), at the location of the permanently installed accelerometer. The downhole data were acquired the database of the Institute of Engineering Seismology and Earthquake Engineering (ITSAK). Therefore, by using this information, the possible depth of investigation was determined at 100m given the widely available space. For this purpose, the maximum aperture of the ambient noise array was set to 300m (150m radius – red circle). The configuration of the application of the geophysical methods is presented in Figure 3.9.

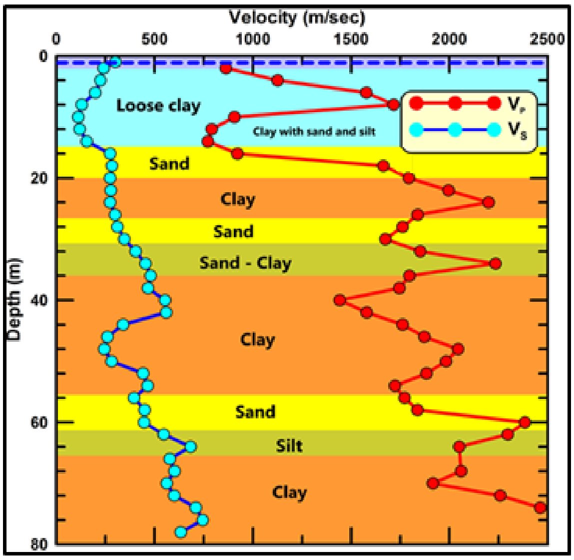

Figure 3.8 Stratigraphic log and downhole results from the available borehole at PORT site. The colored layers correspond to the subsurface geological formations. The watertable depth is indicated with the blue dashed line (at -1m). The cyan and red curves represent the V_S and V_P distribution with depth, respectively (Institute of Engineering Seismology and Earthquake Engineering – ITSAK, 2008).

Ambient noise recording with the array technique was conducted in two phases, as it is described in Section 2.5.3. In the first phase, 7 stations recorded ambient noise simultaneously at the locations of the black circles (15m radius) (Figure 3.9 and Figure 3.11) for about 40 minutes. At the second phase, the 6 stations of the circumference were moved at proper locations of the blue (45m radius) and red circle (150m radius) where they recorded for about 3 hours. Hence, 13 station locations were used for data acquisition. As it is already mentioned, the data extracted from the two datasets (one dataset regarding measurements at the black circle and one dataset regarding measurements at the blue and red circles) correspond to different parts of the dispersion curve. The smaller radius circle (black) extracts information regarding the high frequency part of the dispersion curve and the combination of the larger circles (blue and red) extracts information regarding the lower frequencies. The frequency limits of each part of the curve are defined by the theoretical response of the array (Figure 3.10). To protect the seismometers from rain drops, they were preemptively covered with pots as seen in Figure 3.12a. After the installation and before the starting time of the experiment, the seismometers were checked with a laptop via the “Scream!” software for possible malfunctioning components and proper power supply (Figure 3.12b).

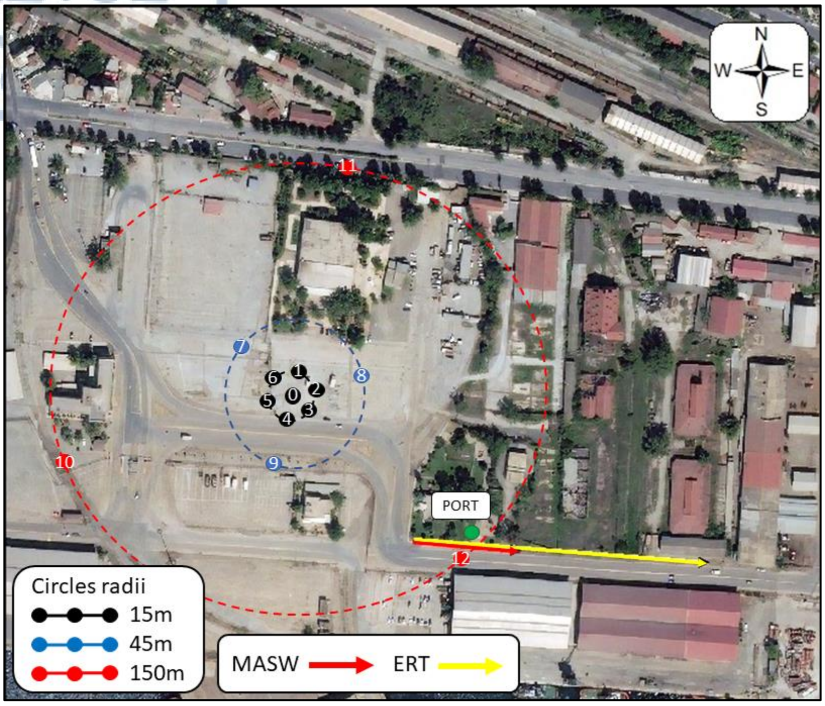

Figure 3.9 Geophysical methods configuration at the PORT accelerometer site (green circle). The green circle is the location of the permanently installed accelerometer and the borehole. The red and yellow lines represent the investigation lines of the MASW and ERT methods respectively. The black circles represent the locations of the stations during the first phase of ambient noise recording, while the blue and red circles represent the locations to which the stations were moved at during the second phase.

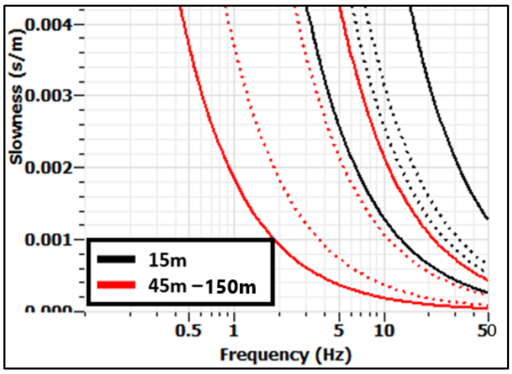

Figure 3.10 Theoretical array response for the configuration at PORT site, based on the geometry of the array. The solid exponential curves delimit the reliability zone of the dispersion curve for the 15m radius circle (zone delimited by the black curves) and the 45m – 150m radii circles (zone delimited by the red curves). The dotted lines represent the k_{min} and $k_{max}/2$ values for each data group.

Figure 3.11 Configuration of the black circle (see Figure 3.9) with the stations positioned at a 15m radius from the center of the array.

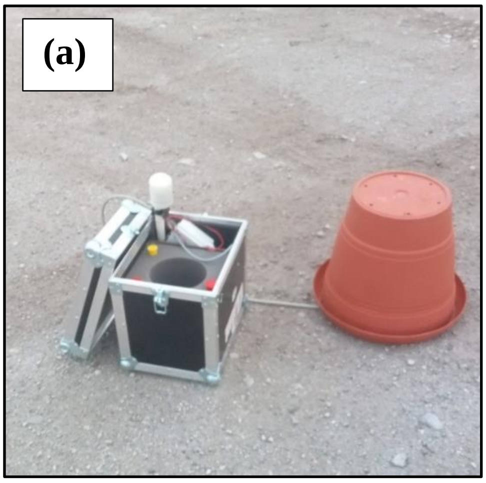

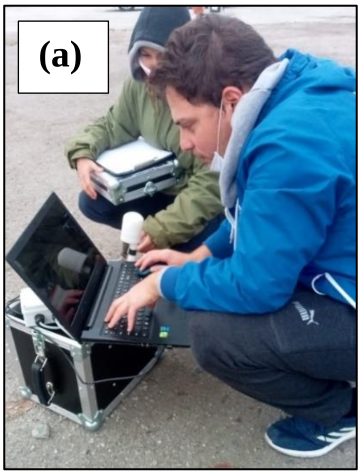

Figure 3.12 The seismometers were covered with pots in order to be physically protected from rain drops as they cause transient signals (a). Before defining the start time of the experiment, the correct functionality of all 3 components is monitored through the appropriate software (Scream!) (b).

The ERT was conducted in the south-eastern part of the ambient noise array, where unpaved ground was available, very close to the borehole and the accelerometer station PORT. The ERT configuration consisted of 48 electrodes with 4m spacing, resulting in a total length of 188m of the investigation line and therefore setting the maximum depth of the investigation at 60-70m (Figure 3.13). The geoelectrical data was acquired using both the dipole-dipole and the multigradient electrode array configurations.

Figure 3.13 (a) The ERT survey line conducted with 48 channels at an unpaved location near the vicinity of the ambient noise array. (b) Two 24-channel cables are connected to the Syscal Pro at the center of the tomography line.

The geophone array for the MASW technique was configured on the same line as the ERT method, using a common starting point (western side). The seismic measurements were conducted using 24 geophones with a 3m spacing (Figure 3.14), resulting in a 69m investigation line and approximately 30m depth of possible investigation. Stacked seismic shots were conducted at both ends of the geophone array with an offset of 10m (at -10m and 79m) and at the middle point (34.5m).

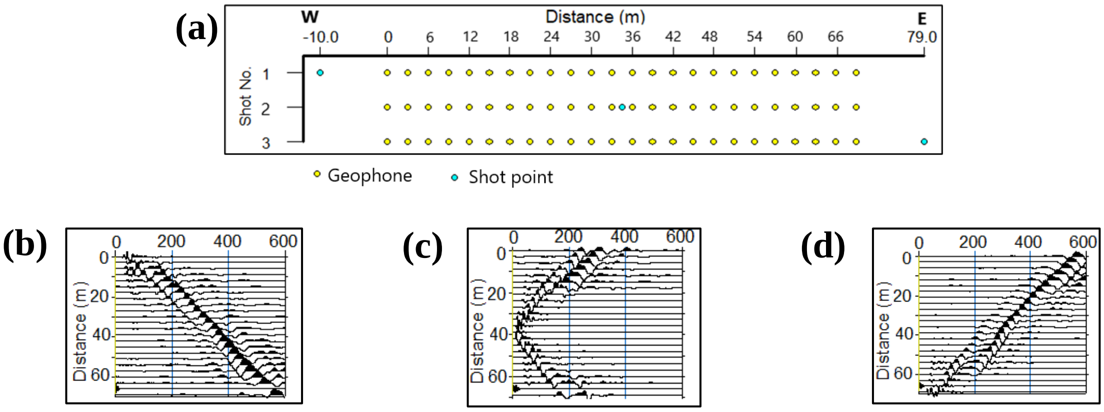

Figure 3.14 (a) Schematic representation of the MASW and Seismic Refraction layout including the geophone and shot point positions and seismogram examples at PORT site used for the refraction analysis from shots at (b) -10m, (c) 34.5m, and (d) 79m.

3.3.2 Data acquisition at STL1 accelerometer site – Site 2.

The ambient noise array aperture at this site, was determined given the available space west of the permanent accelerometer station (Figure 3.15, green circle). The stations recorded ambient noise for about 2 hours in the pre-planned locations of the black circle (15m radius). The large recording duration was due to the suspicion of transient signals in the area. Then, the 6 stations of the circumference were moved to the appropriate locations of the blue and red circles (45m and 85m radii, respectively) where they recorded for about 2 hours and 30 minutes. As already mentioned, the diameters of the circles are determined so that the theoretical limits of the response functions of each circle cover a different part of the frequency range, ideally with a small amount of overlap (Figure 3.16). It is noteworthy that the 15m ambient noise array was positioned in a football field with no ability to create ground coupling by properly anchoring the seismometers (Figure 3.17). Grassy surfaces along with the effects of wind may perturb results in the low frequencies negatively impacting the HVSR, as is suggested by the SESAME Guidelines (2004). In attempt to mitigate those effects the seismometers were covered by pots and were placed as steady as possible to ensure a desired ground coupling.

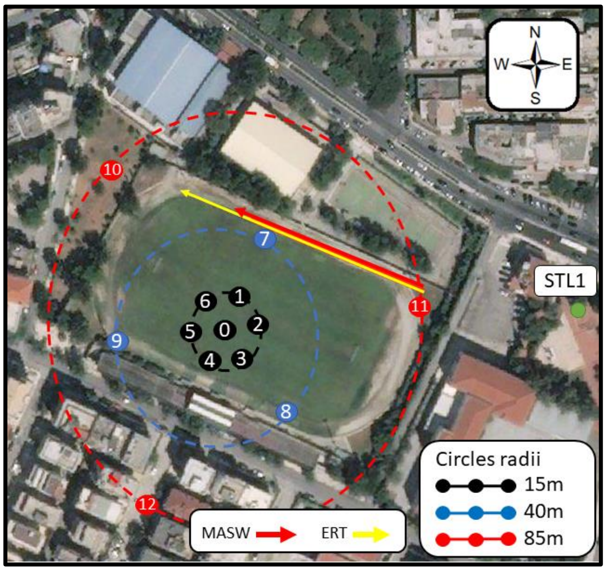

Figure 3.15 Geophysical methods configuration at the STL1 permanent accelerometer site (green circle). The red and yellow lines represent the survey lines of the MASW and ERT methods respectively. The black circle represents the positions of the stations with 15m radius, and the blue and red circles represent the positions of the stations with 45m and 85m, respectively.

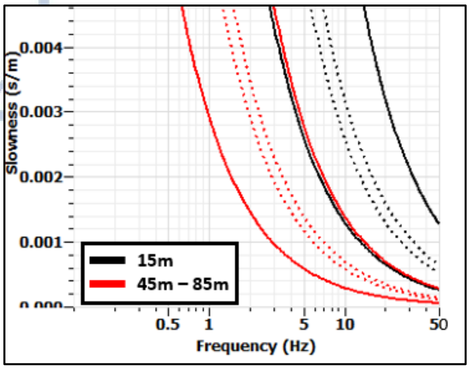

Figure 3.16 Theoretical array response for the ambient noise array configuration at STL1 site, based on the geometry of the array. The solid exponential curves delimit the reliability zone of the dispersion curve for the 15m radius circle (zone delimited by the black curves) and the 45m – 85m radii circles (zone delimited by the red curves). The dotted lines represent the k_{min} and $k_{max}/2$ values for each data group.

Figure 3.17 The 15m radius ambient noise array positioned on a grassy football field.

The ERT survey was conducted using 24 electrodes with 5m spacing, resulting in a tomography of 115m total length. The maximum depth of investigation is determined at approximately 40m. The 1D MASW survey was conducted using 24 4.5 Hz geophones at 4m spacing resulting in a 92m survey line providing an estimated depth of investigation of at least 30m. Stacked seismic shots were conducted at both ends of the geophone array, with a 10m offset (at -10m and 102m) and at the middle point (46m). The MASW shot – geophone map is presented at Figure 3.18.

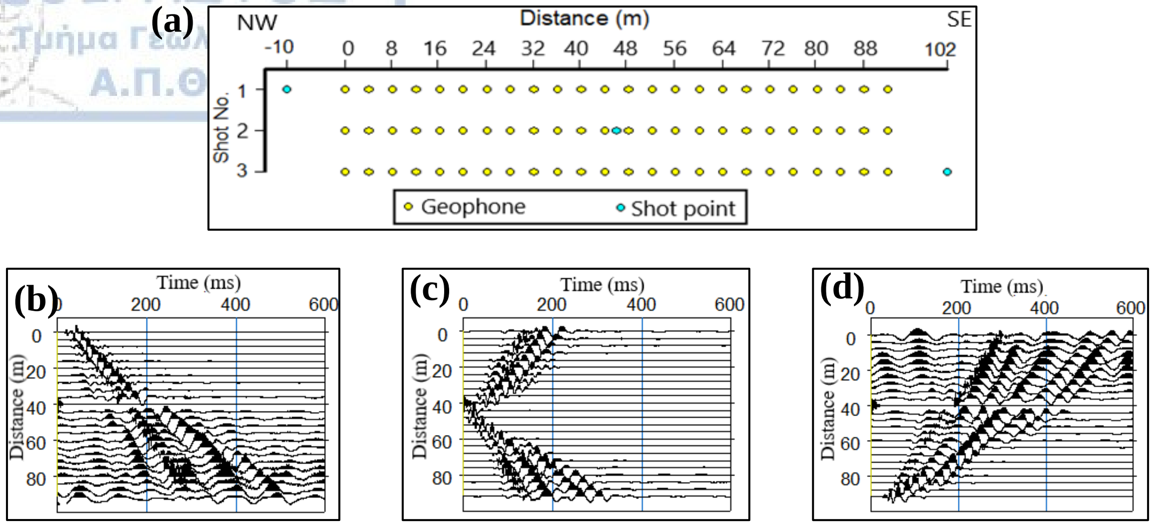

Figure 3.18 (a) Schematic representation of the MASW and Seismic Refraction layout including the geophone and shot point positions and seismogram examples at STL1 site used for the refraction analysis from shots at (b) -10m, (c) 46m, and (d) 102m.

3.3.3 Data acquisition at KLR1 accelerometer site – Site 3.

Due to limited available space in this accelerometer station site, the main goal was set estimation of the V_{S30}. An existing borehole in the vicinity of the KLR1 accelerometer provided the stratigraphic log and a downhole measurement (Figure 3.19). The maximum array aperture was determined about 90m, to achieve an investigation depth of at least 30m. The stations recorded ambient noise for about 2 hours at the positions of the red and black circles (positions 0, 1, 3, 5, 7, 8 and 9, Figure 3.20). Then, the three stations of the red circle were moved to locations of the same azimuthal angle of the black circle (15m radius) and the 7 stations at the black circle recorded for 1 hour (positions 0 – 6). The ambient noise array configuration as well as the ERT and MASW survey lines are presented in Figure 3.20 The theoretical array response is shown in Figure 3.21. An important feature of this accelerometric site, is that it is a very densely populated area with the Town Hall of Kalamaria, a public square as well as a church nearby. This was the reason of very high anthropogenic noise that generated transient signals making the ambient noise analysis a difficult task. For this purpose, the recording time for the ambient noise array was relatively increased (1hour for the 15m array versus 30 minutes for the PORT array), despite its small radius due to expected transient signals.

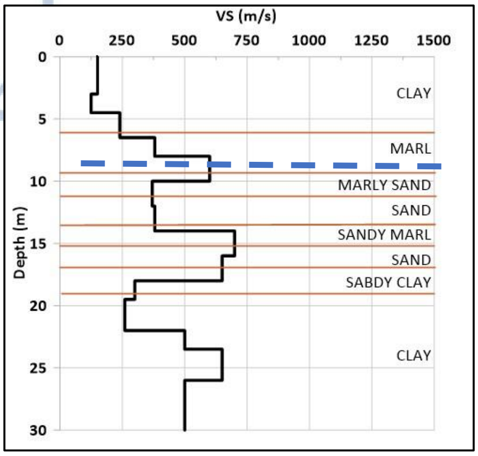

Figure 3.19 Stratigraphic log and downhole results from an existing borehole at the vicinity of KLR1 site. The watertable depth is indicated with the blue dashed line (at -7.5m). The black curve represents the measured V_S variation with depth (Lontzetidis, 1993).

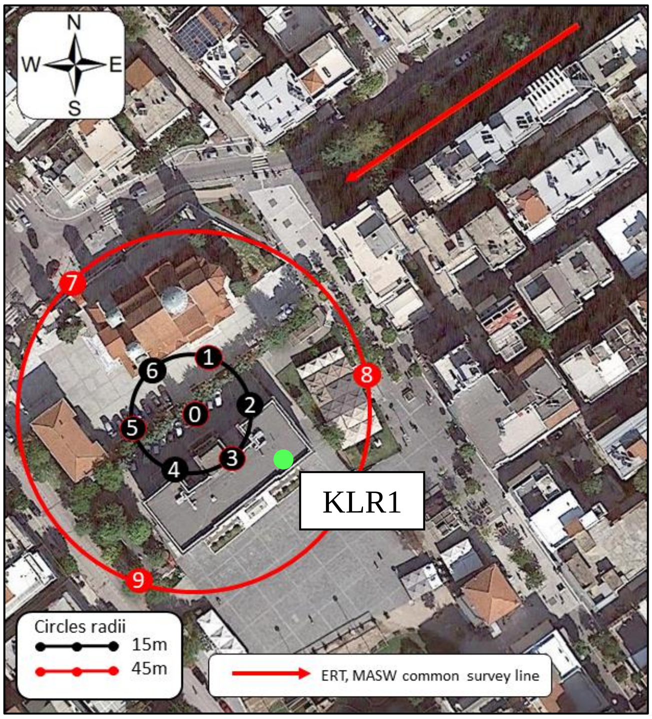

Figure 3.20 Geophysical methods configuration at the KLR1 accelerometer site. The green circle represents the location of the permanently installed accelerometer. The red line represents the common survey line of the MASW and ERT methods. The black circle includes the positions of the stations at a 15m radius, and the red circle represents the positions of the stations at 45m radius from the position 0.

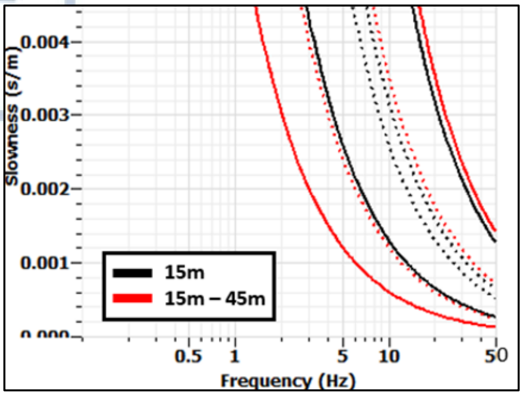

Figure 3.21 Theoretical array response for the ambient noise array configuration at KLR1 site, based on the geometry of the array. The solid exponential curves delimit the reliability zone of the dispersion curve for the 15m radius circle (zone delimited by the black curves) and the 45m – 85m radii circles (zone delimited by the red curves). The dotted lines represent the k_{min} and $k_{max}/2$ values for each data group.

The ERT and MASW techniques shared a common survey line. For the geoelectrical data acquisition, 24 electrodes were used with a 3m spacing resulting in 69m total length survey line. The depth of investigation was determined at approximately 25m. Both dipole – dipole and multi – gradient acquisition techniques were used. The 1D MASW survey line was configured with 24 vertical geophones evenly spaced at 3m setting up a 69m survey line. The estimated depth of investigation was set at least 25m. Due to free field restrictions, only one seismic shot was conducted at the southwestern end of the geophone array, with a 10m offset (at -10m). The MASW array configuration is presented at Figure 3.22.

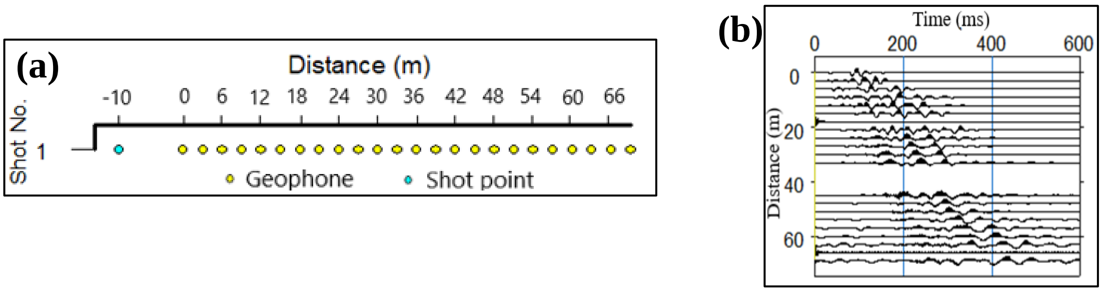

Figure 3.22 (a) Schematic representation of the MASW and Seismic Refraction layout including the geophone and shot point positions and seismogram examples at KLR1 site used for the refraction analysis from shots at (b) -10m.

3.3.4 Data acquisition at SEIS accelerometer site – Site 4.

The SEIS accelerometer is installed in the basement of the Seismological Station of the Aristotle University of Thessaloniki, which is located on a high velocity gneiss bedrock and is considered a reference rock station. The local stratigraphic log and a downhole measurement are available by a 30m depth borehole (Figure 3.23), located right next to the building of the Seismological Station. The downhole data were acquired from the database of the Institute of Engineering Seismology and Earthquake Engineering (ITSAK). The center of the ambient noise array was placed a few meters away from the borehole.

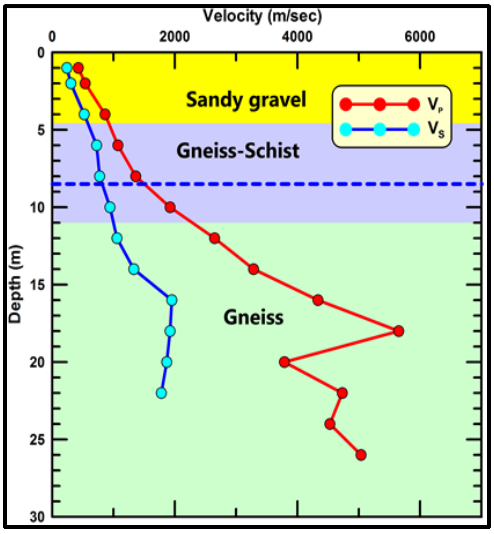

Figure 3.23 Stratigraphic log and downhole measurement from an existing borehole at the SEIS accelerometric site. The colored layers correspond to the subsurface geological formations. The water table depth is indicated with the blue dashed line (at -8.5m). The cyan and red curves represent the V_S and V_P distribution with depth, respectively (Institute of Engineering Seismology and Earthquake Engineering – ITSAK, 2008).

Figure 3.24 shows the ambient noise array configuration at the SEIS site. The available space due to the intense topographic morphology determined the ambient noise array aperture to be 180m. The stations recorded ambient noise for 2 hours at the positions of the red and blue circles (positions 7-12, Figure 3.24). Then, the stations were moved to the locations of the same azimuthal angle in the black circle (15m radius) and recorded for 1 hour (positions 0 – 6). Due to free field restrictions, some positions deviate from the initial plan, as for example the 30m radius circle (blue circle at Figure 3.24). A significant feature of this case is the existence of high transient noise inside the bounds of the ambient noise array due to densely populated area, due to civilian activity, passing cars, swimming pool etc. For this purpose, the recording time of the 15m array (Figure 3.24 and 3.26) was increased to 1 hour. The problem that occurred during the ambient noise data acquisition at this site is the data loss at position 7 due to the theft of the seismometer at this position. The lost seismometer was replaced, and the total recording duration was expanded for 1 hour. The theoretical array response for this configuration is presented at Figure 3.25.

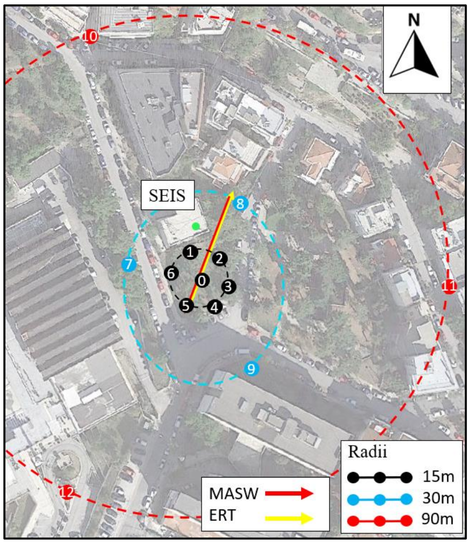

Figure 3.24 Geophysical methods configuration at the SEIS permanent accelerometer station and the respective borehole (green circle). The red and yellow lines represent the MASW and ERT survey, respectively. The black circles include the positions of the stations at a 15m radius, the blue circles include the positions of the stations at a 30m radius, and the red circles include the positions of the stations at 45m radius from the center of the array (position 0).

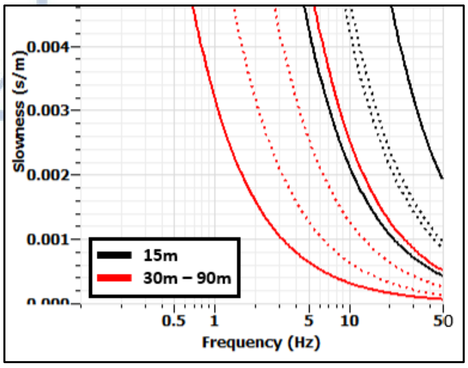

Figure 3.25 Theoretical array response for the ambient noise array configuration at SEIS site, based on the geometry of the array. The solid exponential curves delimit the reliability zone of the dispersion curve for the 15m radius circle (zone delimited by the black curves) and the 30m – 90m radii circles (zone delimited by the red curves). The dotted lines represent the k_{min} and $k_{max}/2$ values for each data group.

Figure 3.26 The configuration of the 15m ambient noise array at the SEIS site.

Due to practical reasons, the MASW and ERT survey lines faced the opposite direction (Figure 3.27a). Due to limited space availability, the survey line length was shorter compared to the configuration at the other investigation sites. For the geoelectrical data acquisition, 24 electrodes were used with a 2m spacing resulting in 46m total length survey line (Figure 3.27b) and both dipole – dipole and multi – gradient acquisition techniques were used. The depth of investigation was determined at approximately 15m.

Figure 3.27 (a), (b) The configuration of the ERT and MASW geophysical methods.

The 1D MASW survey line was configured with 24 vertical geophones evenly spaced at 2m setting up a 46m survey line. The investigation depth was set to at least 15m. Due to free field restrictions, two seismic shots were conducted, one at the southern end of the geophone array, with 5m offset (at 51m) and one more at the middle point (23m). The MASW array configuration is presented at Figure 3.28.

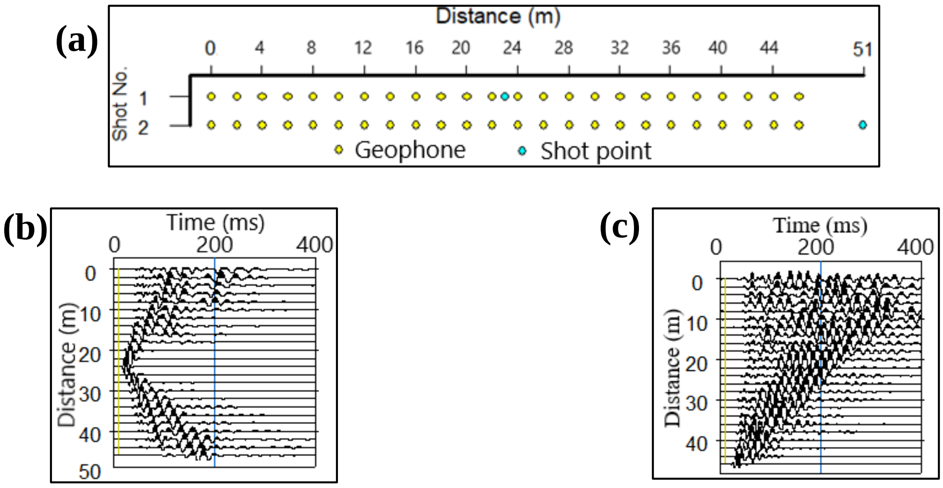

Figure 3.28 (a) Schematic representation of the MASW and Seismic Refraction layout including the geophone and shot point positions and seismogram examples at SEIS site used for the refraction analysis from shots at (b) 23m and (c) 51m.

3.3.5 Data acquisition at ITS1 accelerometer site – Site 5.

The ambient noise array at the ITS1 accelerometer site was designed with an aperture of 600m. To extract the high frequency part of the dispersion curve of the uppermost surficial layers, the stations were positioned at the circumference of a circle with a 15m radius, and one station was positioned at the center of the circle (Figures 3.29a and 3.30). The recording time was approximately one hour. In order to test whether a two-circle array (e.g., 10m and 20m radii) would introduce any differences to the theoretical array response, a second small array was conducted. For this purpose, the circumferential stations were moved at distances of 10m and 20m, keeping the central station stationary as shown in Figure 3.29b. The recording time was 30 minutes. As is shown in Figure 3.32. the two small arrays (15m and 10m-20m) provided similar theoretical array responses. For the extraction of the lower frequency part of the dispersion curve, the stations were moved at the appropriate positions of the blue, red, and yellow circles with 60m, 180m, 300m radii, respectively for simultaneous recording. The recording time was 2 hours. The configuration is shown in Figure 3.31.

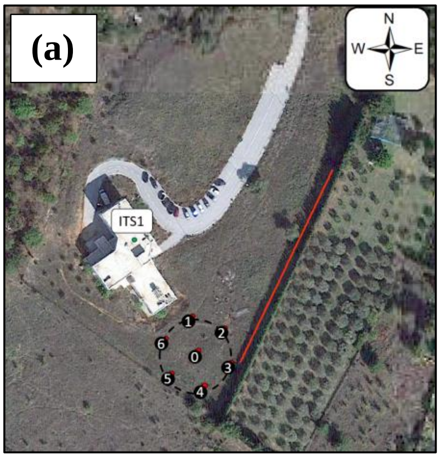

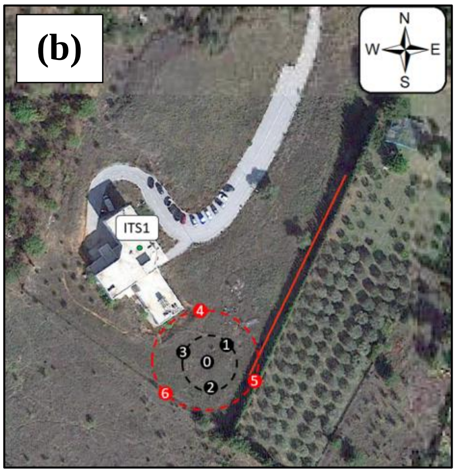

Figure 3.29 Configuration of the short radius ambient noise arrays for the extraction of the dispersive characteristics of the surficial layers at high frequencies at the ITS1 accelerometer station (green circle). (a) the stations are positioned at the circumference of a 15m radius circle and (b) the stations are positioned at 10m (black circle) and 20m radii (red circle) with the same central station and the same azimuthal angles for both configurations. The red line represents the shared survey line of the MASW and the ERT methods.

Data loss was dealt with again at this site due to a defective power supply. The affected seismometer had been placed at position 0 of the big (60m – 180m – 300m) array (see Figure 3.31). This incident was expected to directly affect the theoretical array response and will be described in Chapter 4 - Data processing and results.

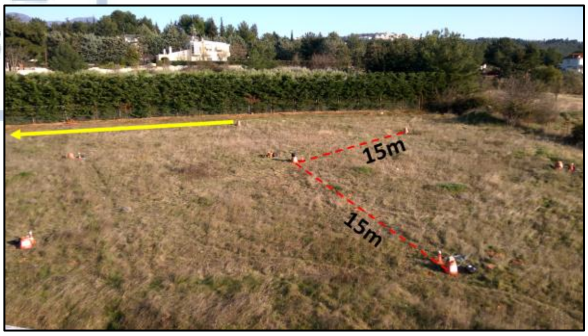

Figure 3.30 The configuration of the 15m radius ambient noise array. The yellow line represents the southern end of the ERT and MASW common survey line.

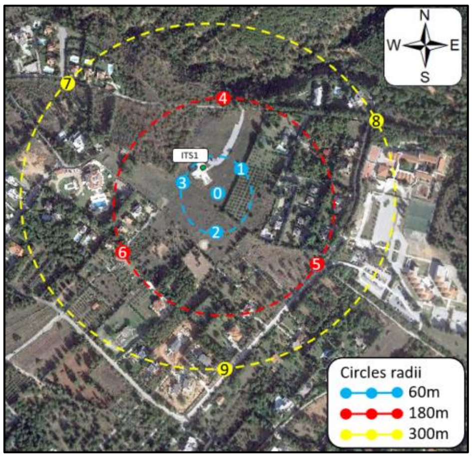

Figure 3.31 Geophysical methods configuration at the ITS1 accelerometer site. The green circle represents the location of the permanently installed accelerometer. The blue circle includes the positions of the stations at a 60m radius (0 – 3), the red circle includes the positions of the stations at a 180m radius (4 – 6), and the yellow circle includes the positions of the stations at 300m radius (7 – 9) from the center of the array (position 0).

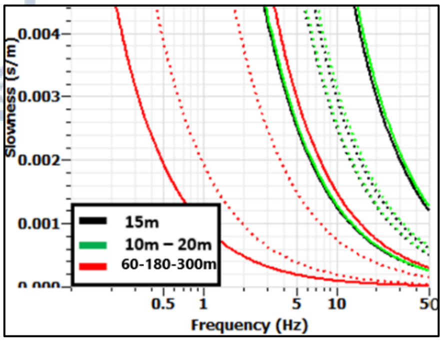

Figure 3.32 Theoretical array response for the ambient noise array configuration at ITS1 site, based on the geometry of the array. The solid exponential curves delimit the reliability zone of the dispersion curve for the 15m radius circle (zone delimited by the black curves), the 10m – 20m radii circles (zone delimited by the green curves) and for 60m-180m-300m radii circles (zone delimited by the red curves). The dotted lines represent the k_{min} and $k_{max}/2$ values for each data group.

The ERT and MASW survey lines were deployed near the center of the ambient noise array (Figure 3.29). For the geoelectrical data acquisition, 24 electrodes were used with 4m spacing resulting in 92m total length survey line. The estimated maximum depth of investigation was determined at approximately 30-35m. Both dipole – dipole and multi – gradient acquisition techniques were used. The 1D MASW survey line was configured with 24 vertical geophones evenly spaced at 4m setting up a 92m survey line. The investigation depth was set to at least 30-35m. Two seismic shots were conducted at either end of the geophone array with an offset of 6m at the northern end, and a 10m offset at the southern end. One shot was also conducted at the middle point (46m). The MASW shot – geophone map is presented at Figure 3.33.

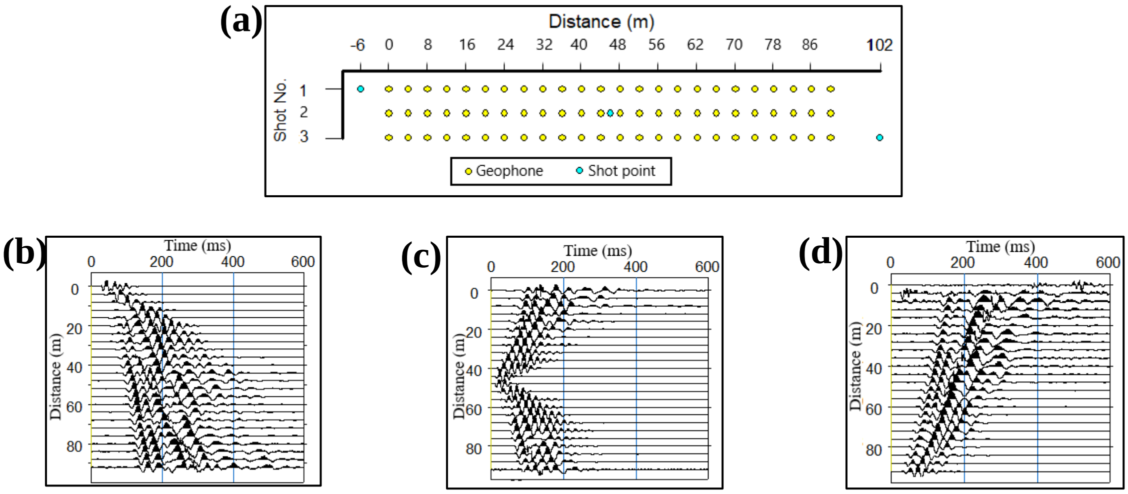

Figure 3.33 (a) Schematic representation of the MASW and Seismic Refraction layout including the geophone and shot point positions and seismogram examples at ITS1 site used for the refraction analysis from shots at (b) -6m, (c) 46m, and (d) 102m.

3.3.6 Data acquisition at PLA1 and PLA2 accelerometer site – Site 6.

The main characteristic of this accelerometric site is its location on a thick package of sedimentary formations. Due to the proximity to the sea (~850m) this site is provided with low frequency noise energy, including potentially greater wavelengths of surface waves. Anthropogenic noise was also expected to be lower than at the other sites, due to its suburban location.

The ambient noise array was designed with an aperture of 240m, aiming for an investigation depth of approximately 80m. The stations were positioned at the circumference of the black circle (Figure 3.34) with a 15m radius (positions 0 – 6). The theoretical array response is presented in Figure 3.35. The recording time was one hour. Then, the stations were moved to the circumferential positions of the blue (40m radius) and red circles (120m radius) with the same azimuthal angles. The recording time was 2 hours and 30 minutes. The long recording time of the second dataset was needed to record longer wavelengths and acquire information from deeper geologic structures.

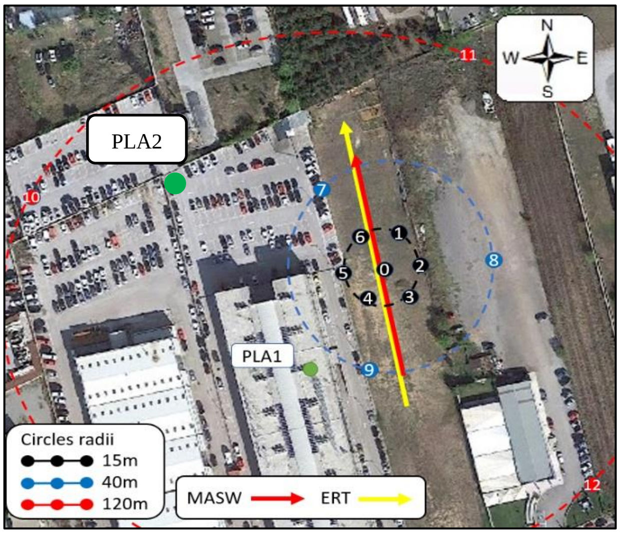

Figure 3.34 Geophysical methods configuration at the PLA1, PLA2 permanent accelerometer stations site (green circles). The black circle includes the positions of the stations at a 15m radius (stations 0 – 6), the blue circle includes the positions of the stations at a 40m radius (stations 7 – 9), and the red circle includes the positions of the stations at 120m radius (stations 10-12) from the center of the array (station 0). The red and yellow lines represent the MASW and ERT survey lines, respectively.

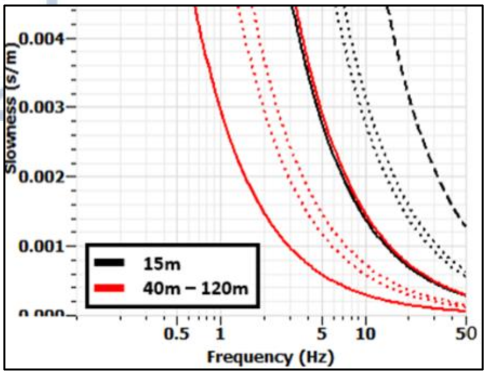

Figure 3.35 Theoretical array response for the ambient noise array configuration at SEIS site, based on the geometry of the array. The solid exponential curves delimit the reliability zone of the dispersion curve for the 15m radius circle (zone delimited by the black curves) and the 30m – 90m radii circles (zone delimited by the red curves). The dotted lines represent the k^{min} and $k^{max}/2$ values for each data group.

Due to the malfunction of the seismometers at positions 1, 4, 9 and 11, data loss resulted in narrowing the reliability zones of the theoretical array response for the selection of the dispersion curve.

The ERT and MASW survey lines were deployed so that the center of each line would coincide with the center of the ambient noise array (see Figure 3.34). The ERT survey was deployed with 24 electrodes with a 5m spacing. The total length of the line was 115m and the estimated maximum depth of investigation close to 40m. Both dipole – dipole and multi – gradient acquisition techniques were used. The 1D MASW survey line was configured with 24 P-wave geophones evenly spaced at 4m setting up a 92m survey line. The depth of investigation was at least 30-35m. Two seismic shots were conducted at either end of the geophone array with an offset of 10m and one shot was also conducted at the middle point (46m). The MASW array configuration is presented at Figure 3.36. The seismic data are indicative of noise – free signals in high frequency content due to the low anthropogenic noise in this site.

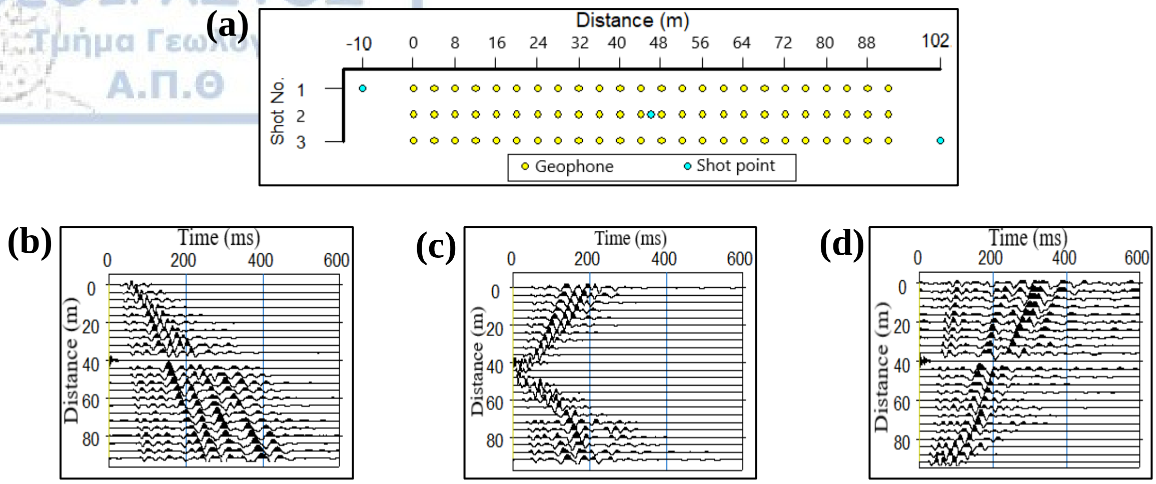

Figure 3.36 (a) Schematic representation of the MASW and Seismic Refraction layout including the geophone and shot point positions and seismogram examples at PLA1 site used for the refraction analysis from shots at (b) -10m, (c) 46m, and (d) 102m.

4. Data processing and results

4.1 Data processing

The first part of this chapter is devoted to present the data processing for each one of the methods that comprise the methodology as has been described in the previous chapters. The data processing is described per method highlighting the issues arose in problematic cases of data acquisition and how the processing procedure was affected as well as workarounds in these cases. Some cases that demanded different approaches in the pre-processing of the data are also mentioned. The second part of this chapter is devoted to presenting the methodology results per site and the combined interpretation with respect to site characterization through the V_{S30} parameter.

4.1.1 Electrical Resistivity Tomography

This section is devoted to the processing procedure of the geoelectrical data. This process is typical for every ERT survey line. Any different approach regarding the pre-processing of the geoelectrical data is thoroughly mentioned.

The Prosys II software is used to download the geoelectric data to a PC. Prosys II is a program distributed by IRIS Instruments, free of charge, that allows the transfer, editing, processing, visualization and exporting of resistivity data from the IRIS Instruments resistivity-meters (www.iris-instruments.com) (Figure 4.1).

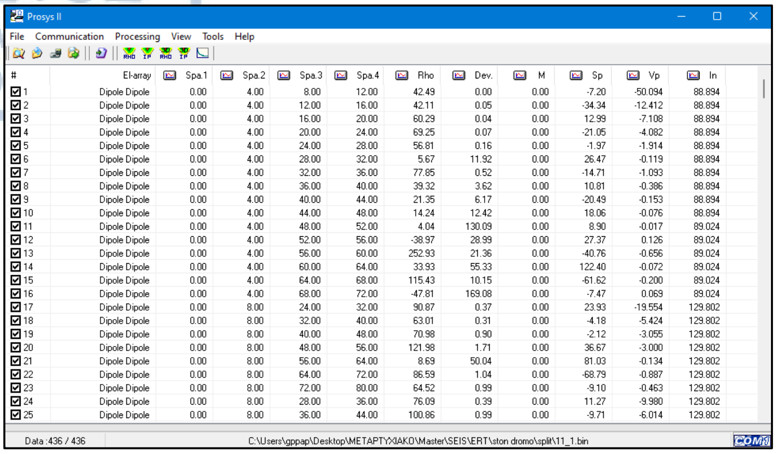

Figure 4.1 The Prosys II environment. Each line represents a single geoelectrical measurement.

Prosys II was used to separate datasets acquired with different acquisition techniques (e.g., dipole – dipole and multi – gradient) and to perform an initial filtering of the data by rejecting outliers or rejecting data from problematic electrodes (bad ground coupling etc.) (Figure 4.2). Finally, the filtered data are exported in appropriate format, compatible with the inversion software.

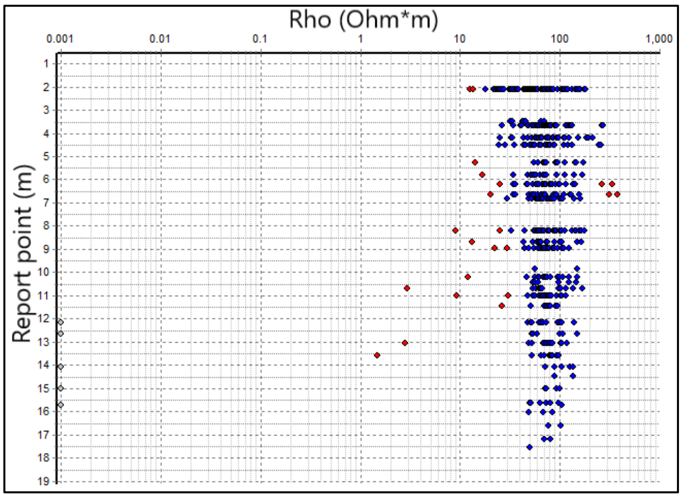

Figure 4.2 Rejection of data with large deviation (red points) using Prosys II.

Further pre-processing was required for the data acquired at PORT site. The ERT detected a very resistive volume at the eastern end of the tomography which is attributed to unwanted noise possibly introduced by buried constructions or other utilities. Also, a low resistivity anomaly was introduced at the electrodes around the 48m of the tomography most probably due to the metallic casing of the existing borehole. The pre-processing involved the removal of data acquired by the electrodes at these two parts of the ERT. The results, after the inversion of the geoelectrical data that is described below, are presented in Figure 4.4.

The exported geoelectrical data are subject to 2D inversion to acquire the subsurface resistivity distribution (Tsourlos et al., 1998; Tsourlos and Ogilvy, 1999). The software used for the inversion of the data is the DC2D_PRO (Kim 2010). This program uses the Occam technique (Constable et al., 1987) to conduct a nonlinear 2D inversion of the geoelectrical data. The algorithm performs a set number of iterations and for each iteration it employs the finite element technique for forward modelling.

The first step involves the parameterization of the initial model by defining the investigation depth of the ERT survey line and setting up the finite element mesh (Figure 4.3a). The second step involves the inversion of the geoelectrical data and the retrieval of the 2D resistivity distribution (Figure 4.3b).

(a)

(b)

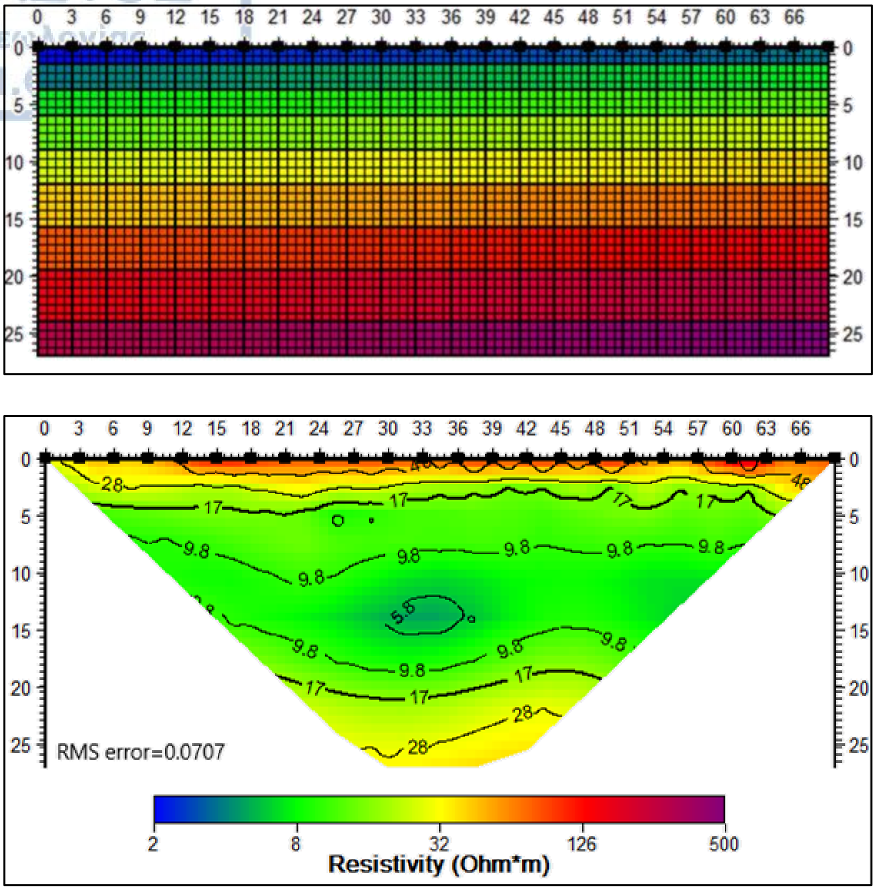

Figure 4.3 . Inversion procedure example. (a) Finite element mesh structure with an investigation depth defined by the user at 25m before the inversion and (b) the final inverted resistivity model of the subsurface after 7 iterations with a satisfactory 7% RMS error.

The inverted resistivity models were edited by rejecting data based on the RMS error (%) between the measured and the synthetic data (Figure 4.5) and the remaining dataset was inverted again until a resistivity model with a satisfactory RMS error (%) was achieved (typically RMS error <10%). The 2D resistivity distribution in the final inverted profile is depicted in a rainbow color scale, where cooler colors (blue) depict lower resistivity values and warmer colors (red) depict higher resistivity values (Figure 4.3b).

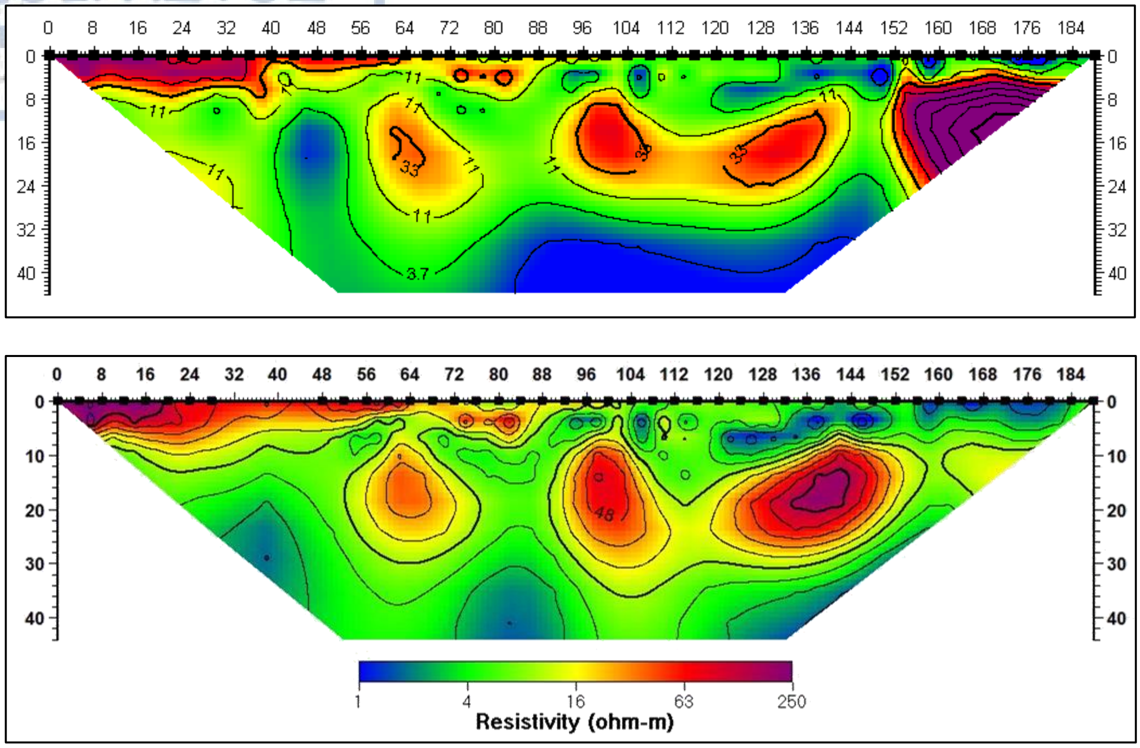

Figure 4.4 The results of further pre-preprocessing of the geoelectrical data. The possible effect of the borehole introduced at 48m of the tomography and the very resistive body at the right end of the ERT (top) are suppressed by removing data acquired by the neighboring electrodes (bottom).

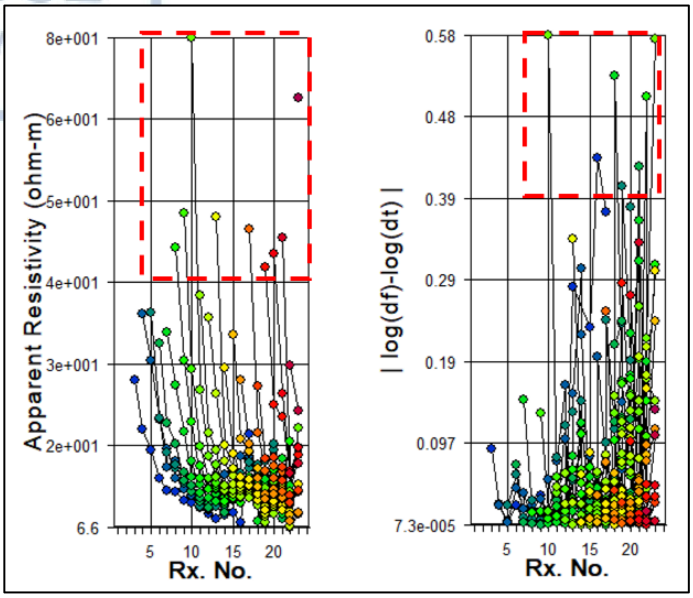

Figure 4.5 Rejection of erroneous data (outliers) at (a) the absolute resistivity values and (b) the error between the true and synthetic data.

4.1.2 Multichannel Analysis of Surface Waves

The SeisImager software suite from Geometrics Inc (www.geometrics.com) was used for the active seismic data processing and interpretation. This software suite is composed of multiple modules, each one for a different seismic data process. The Pickwin module was used to import the seismic waveforms which are viewed as a time – distance plot and bad recordings from faulty geophones or loose connections were removed (Figure 4.6). For the MASW analysis only one out of the three shots was used for the extraction of the dispersion curve since all of them exhibited similar characteristics.

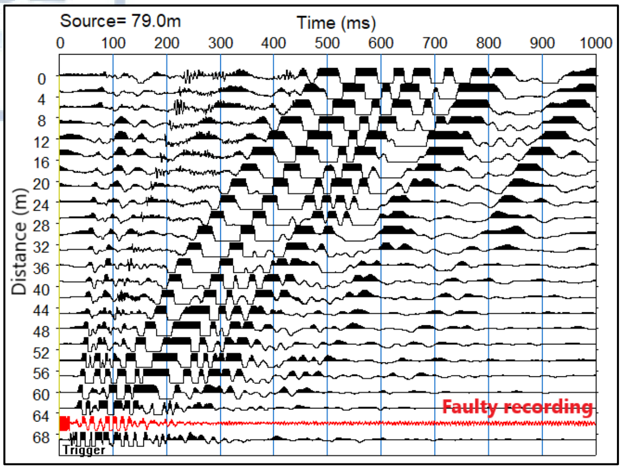

Figure 4.6 The time – distance plot generated by a single shot at 79m. The red trace is flagged as faulty due to a malfunctioning receiver.

The next step involves the transformation of the seismic energy into the phase velocity – frequency domain. The local energy maxima (dark blue colors in figure 4.8) between the black dashed lines were manually picked to form the corresponding dispersion curve. The maximum investigation depth (z_{max}) was determined based on equation (6). (Figure 4.7). Each selected dispersion curve is characterized by a quality line. The quality line is a relative indicator of the quality of the points that define the dispersion curve. High quality points will correlate with peaks and low-quality points with valleys on the quality line. If all data points were high quality, the line would be flat.

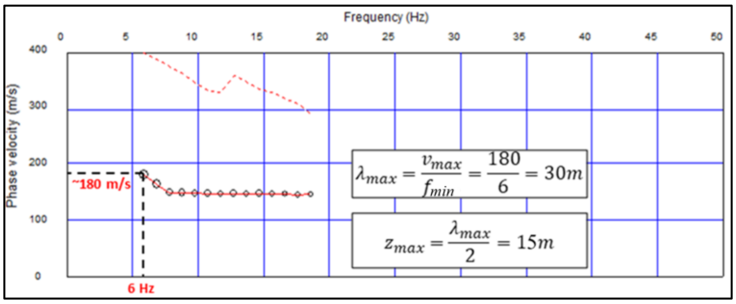

Figure 4.7 Example of the investigation depth computation from the dispersion curve (red line). The red line solid represents the dispersion curve and the red dashed line the corresponding quality.

The selected dispersion curve was inverted (in 10 iterations) in accordance with the procedure described in Section 2.4.3 to generate the 1D V_S velocity structure for each site. The generated phase velocity – frequency diagram, as well as each selected dispersion curve for each site are shown in the Figures 4.8 to 4.13.

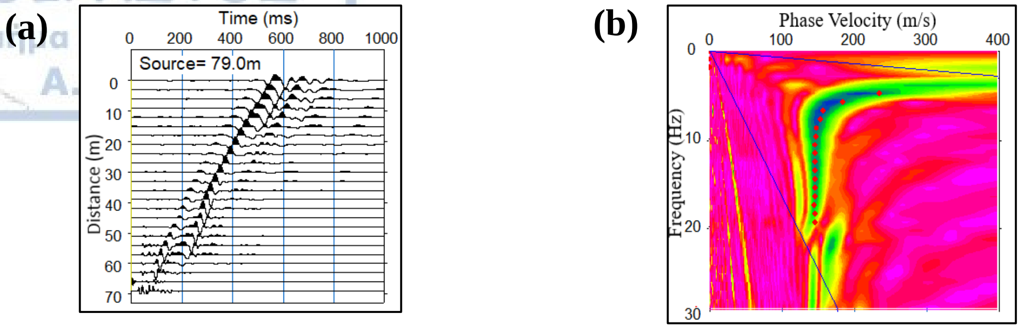

Figure 4.8 (a) Time – distance plot generated from shot at 79m at PORT site and the corresponding phase velocity – frequency diagram. (b) Cooler colors indicate high concentration of the seismic energy. The dotted line represents the selected dispersion curve. The black solid lines delimit the stable velocity range with slopes that correspond to the minimum and maximum wavelengths.

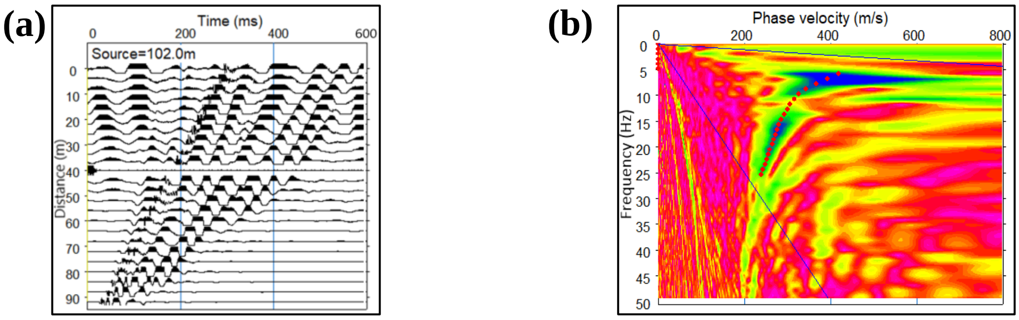

Figure 4.9 (a) Time – distance plot generated from shot at 102m at STL1 site and the corresponding phase velocity – frequency diagram. (b) Cooler colors indicate high concentration of the seismic energy. The dotted line represents the selected dispersion curve. The black solid lines delimit the stable velocity range with slopes that correspond to the minimum and maximum wavelengths.

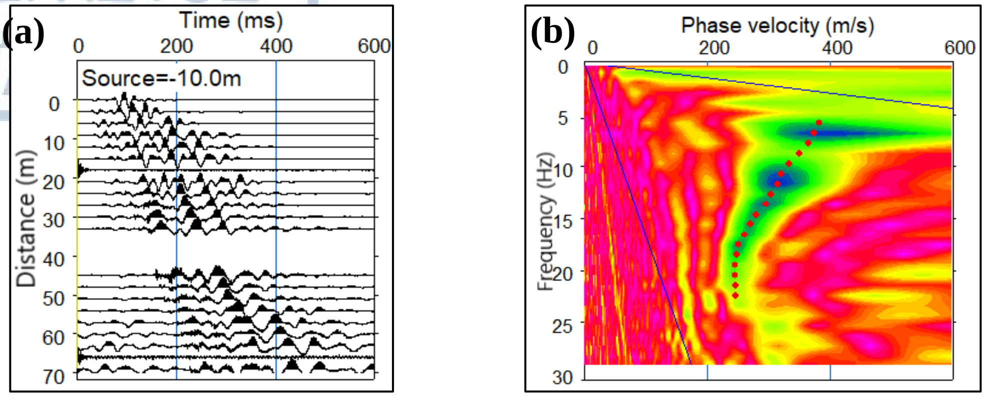

Figure 4.10 (a) Time – distance plot generated from shot at -10m at KLR1 site and the corresponding phase velocity – frequency diagram. (b) Cooler colors indicate high concentration of the seismic energy. The dotted line represents the selected dispersion curve. The black solid lines delimit the stable velocity range with slopes that correspond to the minimum and maximum wavelengths.

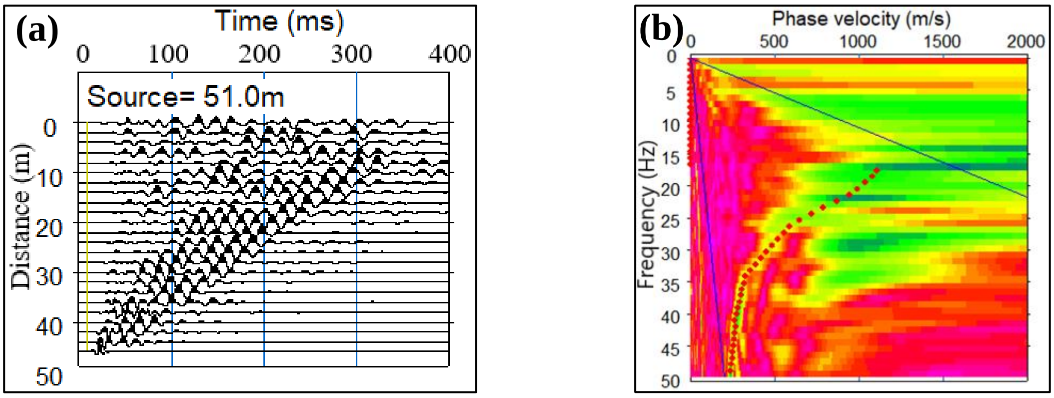

Figure 4.11 (a) Time – distance plot generated from shot at 51m at SEIS site and the corresponding phase velocity – frequency diagram. (b) Cooler colors indicate high concentration of the seismic energy. The dotted line represents the selected dispersion curve. The black solid lines delimit the stable velocity range with slopes that correspond to the minimum and maximum wavelengths.

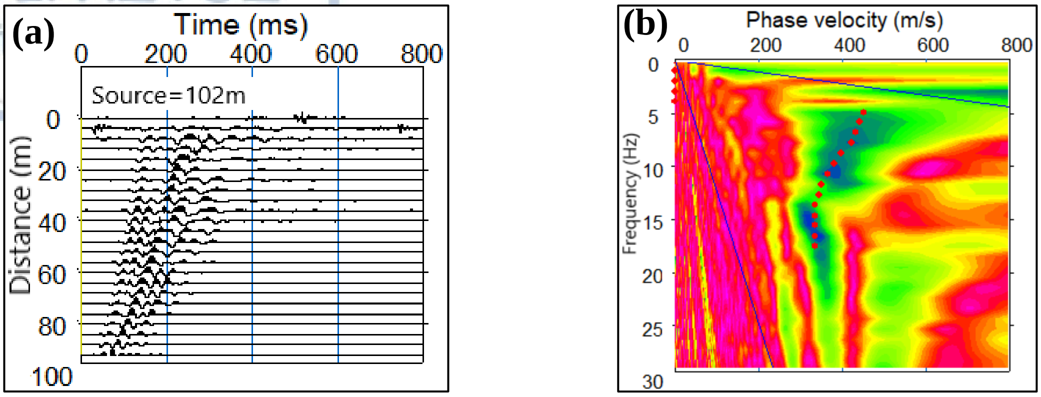

Figure 4.12 (a) Time – distance plot generated from shot at 102m at ITS1 site and the corresponding phase velocity – frequency diagram. (b) Cooler colors indicate high concentration of the seismic energy. The dotted line represents the selected dispersion curve. The black solid lines delimit the stable velocity range with slopes that correspond to the minimum and maximum wavelengths.

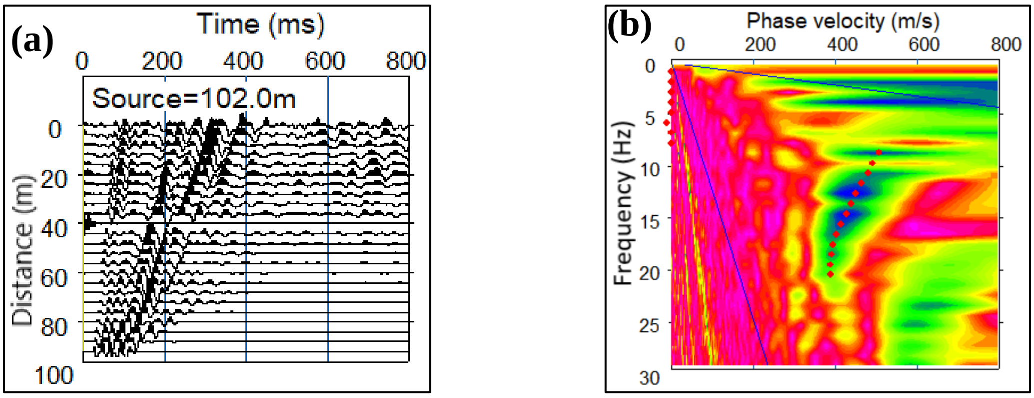

Figure 4.13 (a) Time – distance plot generated from shot at 102m at PLA1 site and the corresponding phase velocity – frequency diagram. (b) Cooler colors indicate high concentration of the seismic energy. The dotted line represents the selected dispersion curve. The black solid lines delimit the stable velocity range with slopes that correspond to the minimum and maximum wavelengths.

4.1.3 Seismic Refraction

The active seismic data were also analyzed with the refraction method using the SeisImager software suite (Pickwin and Plotrefa modules). In this section, the processing of the seismic data gathered at the PLA1 site will be demonstrated, because they had the best signal to noise ratio compared to the other sites.

The first arrivals of the P waves were selected for all traces of each waveform. Figures 4.14a to 4.14c show the picking of the first arrivals of the waveforms generated from the source points at -10m, 46m and 102m. Noisy traces (far away receivers) or noisy traces due to faulty connection with the receiver (e.g., trace at 40m of Figures 4.14a to 4.14c) were removed. The travel-time curves that were picked from the waveforms of Figure 4.14 are plotted together in the travel-time – distance domain (Plotrefa module) (Figure 4.14b). Change at the inclination of a travel-time curve indicate the transition to a new layer. In Figure 4.14b a three-layer model is suggested. Finally, the travel-time curves are inverted with the Time-Term inversion method to produce the 2D distribution of the P-wave velocities (Figure 4.15).

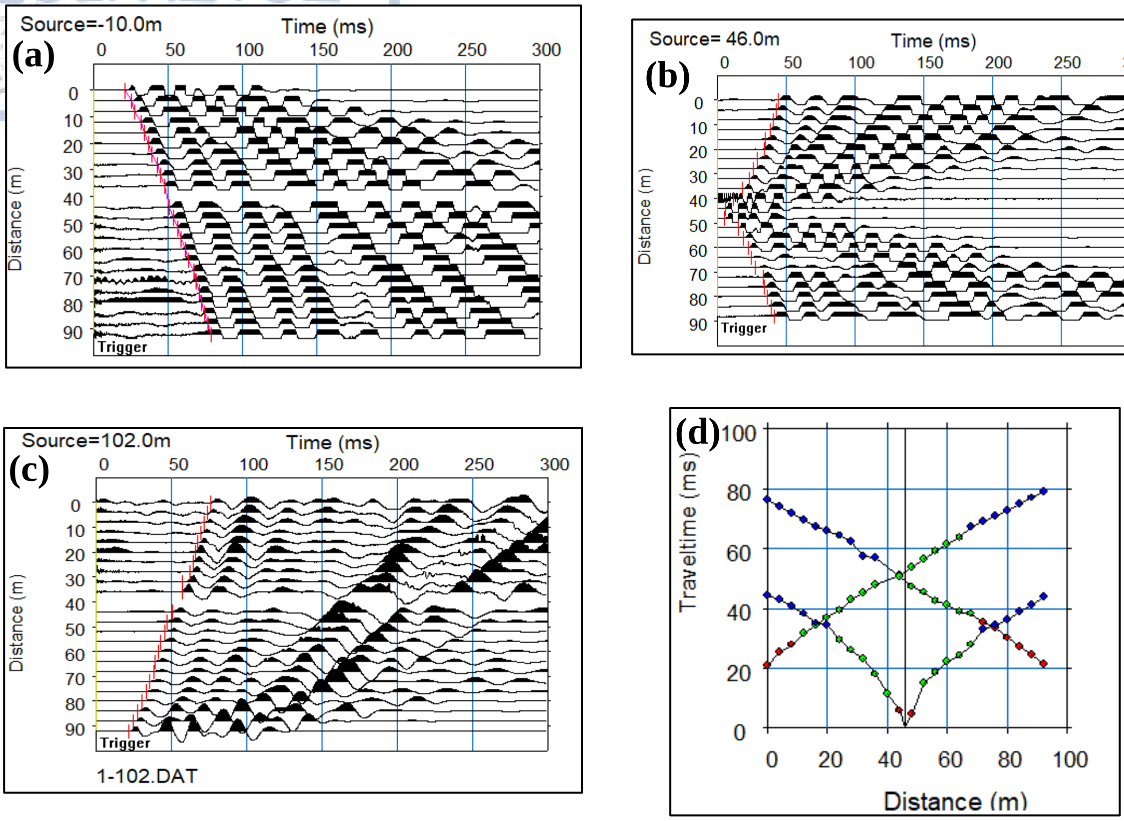

Figure 4.14 The waveforms generated at source points (a) -10m, (b) 46m and (c) 102m at the PLA1 site and the selected first arrivals for each trace (red lines). The trace at 40m was removed. (d) The travel-time curves that were formed from the selection of the first arrivals. The consecutive red points correspond to the first layer, while the green and blue points correspond to the second and third layer, respectively.

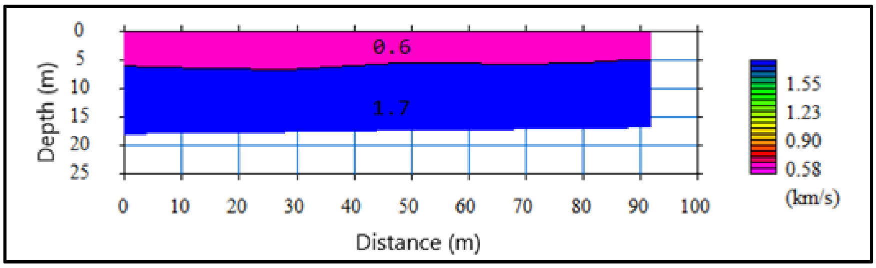

Figure 4.15 The final V_P model derived from the analysis of the active seismic data with the refraction method.

4.1.4 Horizontal to Vertical Spectral Ratio (HVSR)

Processing of the ambient noise data was conducted with the Geopsy software suite (www.geopsy.org). Geopsy software suite is a graphical desktop application dedicated to seismic signal processing (both active and passive seismic data) available for a wide variety of platforms (Windows, Unix/Linux, and MacOS) (Wathelet et al, 2020). The Geopsy software suite was selected for three main reasons. The first reason is that it is an open-source, user-friendly tool that provides easiness and flexibility to the user for managing the output files in graphical and computational level. The second reason is that besides the HVSR analysis, Geopsy also provides the ability to process passive seismic data acquired with the ambient noise array technique. Finally, the third reason is that Geopsy is completely compatible with seismic data downloaded from most seismic data loggers (including the Guralp 6TD instruments used in the present study), and no format conversion is required.

Generally, the HVSR analysis of ambient noise data consists of three stages. The first stage is the selection of the appropriate time-windows, the second stage involves the computation of the power spectra (power spectral density plot) for each component and the third stage is the computation of the spectral ratios.

In the first stage, after importing the 3-component recordings to Geopsy, a bandpass filter 0.2 to 20 Hz is applied. This frequency band selection is based on the response of the seismometer to ground velocity (flat in the frequency range 0.2-50 Hz). For frequencies f>20Hz there is no engineering interest for our specific study. Next, parts of the digital recording (i.e., time-windows) are selected in order to isolate undesirable transient signals (near-field anthropogenic noise sources) (Figure 4.16). An example is the transient signals caused by passing cars providing short duration signals but with large amplitude local maxima. The duration of each time-window was decided at 60 seconds, with no overlapping between two consecutive time-windows. The number of windows was kept to at least 20 at all sites. The number of the selected time-windows is an important parameter because it ensures the reliability of the spectral ratio (SESAME Guidelines, 2004). Each one of the selected time-windows is common for all three components. The time-windows are automatically selected by implementing an “anti-triggering” algorithm or manually by the user.

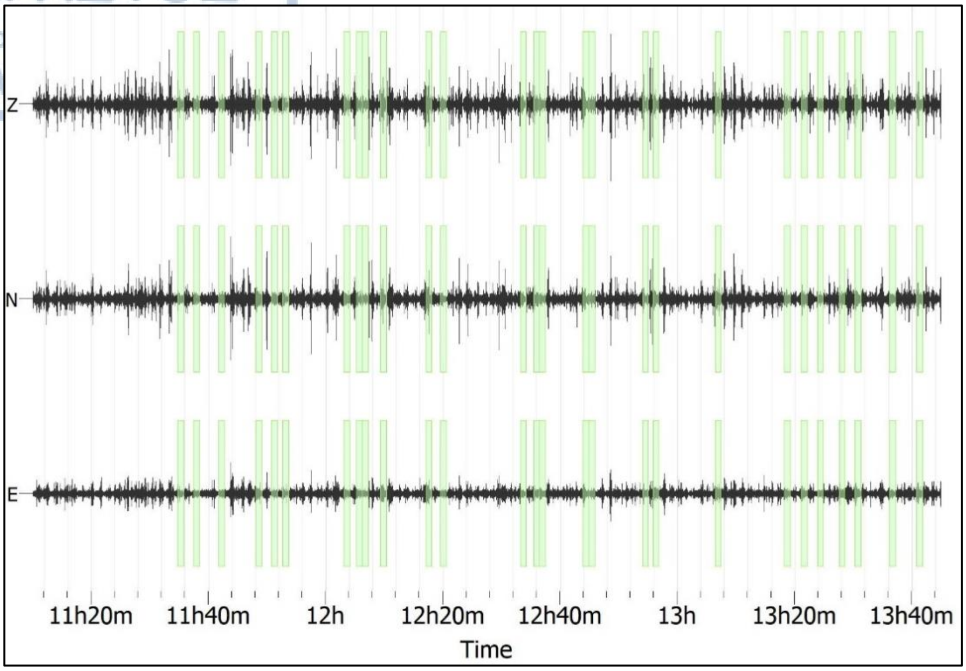

Figure 4.16 Example of digital ambient noise recordings for three components at STL1 accelerometer site with the automatically selected time windows (green rectangles).

The second stage of the HVSR analysis involves the computation of the amplitude spectra for each component. Geopsy uses a Fast Fourier Transform (FFT) algorithm for the spectral analysis. Power spectra are computed for each time-window based on the total energy for both horizontal components, as proposed by Sanchez-Sesma et al, (2011) and Garcia-Jerez et al, (2016). The mean average of all the computed curves composes the final spectral curve for each component. A cosine taper function of 5% width was applied to all the selected time-windows. For the Spectrum computation, the Fourier spectrum from each selected time window is smoothed according to the methodology suggested by Konno and Ohmachi, (1998), with a smoothing constant β=0.4 (40%) and then the averaged curve is computed. Smoothing is strongly recommended because it ensures a constant number of points at low and high frequency.

The third and final stage of the HVSR analysis is the subsequent computation of the spectral ratio (Figure 4.17) according to equation (15) in Section 2.6. The final HVSR curve is the result of the geometrical average of all curves that result from the analysis of each individual window of the ambient noise time history.

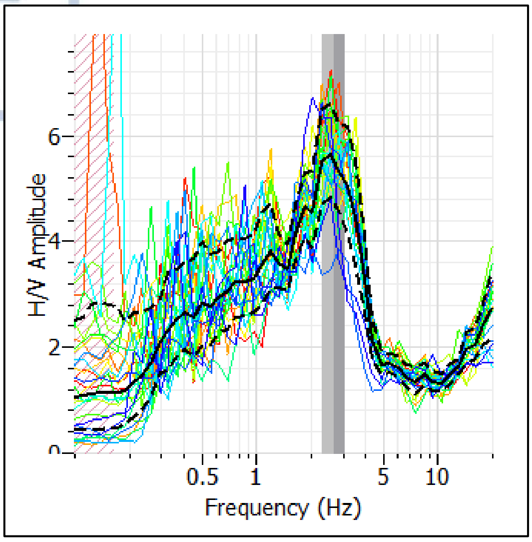

Figure 4.17 Example of a H/V spectral ratio at STL1 accelerometer site. The colored lines represent the spectral ratio for each individual time-window. The black curve represents the H/V geometrically averaged over all colored individual H/V curves, and the dashed lines represent the H/V ± 1 standard deviation. The grey area represents the averaged fundamental frequency and its ± 1 standard deviation. The red sketched area at the low frequency part (<0.18 Hz) marks a low reliability area in which the data should not be interpreted.

It is important to highlight that the HVSR curves do not always possess simple shapes. In an ideal case, a single maximum peak, easily distinguishable from the rest of the curve exists. In many cases the shape of the HVSR curve is not a simplistic one. Some examples may involve (see SESAME 2004):

- the existence of multiple (more than two) peaks,
- the existence of peaks that appear in a broad frequency band,
- peaks that correspond to industrial noise and cannot provide information concerning the subsurface structure and,
- HVSR flat curves that maintain a constant H/V amplitude value between 1 to 2 along all frequency range.

In most cases the interpretation of the HVSR curve is not an easy task. Additional information regarding the subsurface structure of an investigation site, such as geological, geotechnical, and geophysical data etc., greatly assist in the interpretation of HVSR analysis results. Piña-Flores et al. (2016) suggested that the number of main peaks is an indicator of minimum number of subsurface layers on the half-space. This is also useful information when considering HVSR curve inversion to acquire the V_{SZ} profile at a site.

A significant assistance towards the interpretation of the HVSR analysis results are the guidelines provided by the European research project SESAME (2004). These practical guidelines recommend procedures for field experiment design, data processing and interpretation of the results for the implementation of the HVSR technique using ambient noise excitations. The interpretation guidelines are based on strict mathematical criteria (Figure 4.18) that contribute to the minimization of subjectivity. The criteria concern the reliability of the HVSR curve and are linked to the "clear" and "single" concepts of the H/V peak (or peaks) frequency value (fundamental or and dominant frequency).

Criteria for a reliable H/V curve

i) $f_0 > 10 / l_w$

and

ii) $n_c (f_0) > 200$

and

iii) $\sigma_A(f)<2$ for $0.5f_0<f<2f_0$ if $f0>0.5Hz$
or $\sigma_A(f)<3$ for $0.5f_0<f<2f_0$ if $f0<0.5Hz$

Criteria for a clear H/V peak
(at least 5 out of 6 criteria fulfilled)

i) $\exists f^- \in [f_0/4, f_0] \mid A_{H/V}(f^-) < A_0/2$
ii) $\exists f^+ \in [f_0, 4f_0] \mid A_{H/V}(f^+) < A_0/2$
iii) $A_0 > 2$
iv) $f_{peak}[A_{H/V}(f) \pm \sigma_A(f)] = f_0 \pm 5\%$
v) $\sigma_f < \varepsilon(f_0)$
vi) $\sigma_A(f_0) < \theta (f_0)$

- l_w = window length
- n_w = number of windows selected for the average H/V curve
- $n_c = l_w \cdot n_w \cdot f_0$ = number of significant cycles
- f = current frequency
- f_{sensor} = sensor cut-off frequency
- f_0 = H/V peak frequency
- σ_f = standard deviation of H/V peak frequency ($f_0 \pm \sigma_f$)
- $\varepsilon (f_0)$ = threshold value for the stability condition $\sigma_f < \varepsilon(f_0)$
- A_0 = H/V peak amplitude at frequency f_0
- $A_{H/V} (f)$ = H/V curve amplitude at frequency f
- f^- = frequency between $f_0/4$ and f_0 for which $A_{H/V}(f^-) < A_0/2$
- f^+ = frequency between f_0 and $4f_0$ for which $A_{H/V}(f^+) < A_0/2$
- $\sigma_A (f)$ = "standard deviation" of $A_{H/V} (f)$, $\sigma_A (f)$ is the factor by which the mean $A_{H/V}(f)$ curve should be multiplied or divided
- $\sigma_{logH/V} (f)$ = standard deviation of the $logA_{H/V}(f)$ curve, $\sigma_{logH/V} (f)$ is an absolute value which should be added to or subtracted from the mean $logA_{H/V}(f)$ curve
- $\theta (f_0)$ = threshold value for the stability condition $\sigma_A(f) < \theta(f_0)$
- $V_{s,av}$ = average S-wave velocity of the total deposits
- $V_{s,surf}$ = S-wave velocity of the surface layer
- h = depth to bedrock
- h_{min} = lower-bound estimate of h

Threshold Values for σ_f and $\sigma_A(f_0)$

Frequency range [Hz]	< 0.2	0.2 – 0.5	0.5 – 1.0	1.0 – 2.0	> 2.0
$\varepsilon (f_0)$ [Hz]	0.25 f_0	0.20 f_0	0.15 f_0	0.10 f_0	0.05 f_0
$\theta (f_0)$ for $\sigma_A (f_0)$	3.0	2.5	2.0	1.78	1.58
$\log \theta (f_0)$ for $\sigma_{logH/V} (f_0)$	0.48	0.40	0.30	0.25	0.20

Figure 4.18 The SESAME guidelines that concern the reliability of the HVSR curve and the "clarity" of the maximum peak (SESAME, 2004).

The first requirement before any extraction of information and any interpretation, concerns the reliability of with the HVSR curve. Reliability implies stability, i.e., the fact that actual HVSR curve obtained the selected recordings, be representative of HVSR curve that could be obtained with other ambient noise recordings and/or other physically reasonable time-window selection. Such a requirement demands the fulfillment of the three suggested criteria of Figure 4.18. In case one particular set of processing parameters does not lead to satisfactory results in terms of stability (some criteria are not fulfilled), the data must be reprocessed testing other sets of parameters or measurements must be repeated for a longer duration.

The clear peak case is met when the HVSR curve exhibits a clear, single H/V peak. The "clarity" of the peak is related to several characteristics such as the amplitude of the H/V peak and its relative value with respect to the H/V amplitude value in other frequency bands as well as the relative value of the standard deviation σ_A (f), and σ_f of f_0 estimates from individual windows. To interpret a maximum peak as "clear" at least 5 out of 6 criteria of Figure 4.18 must be fulfilled. The "single" concept of the maximum peak is related to the fact that no other peak exists in any other frequency band that satisfies the same criteria.

When the HVSR curve and the maximum peak satisfy the aforementioned criteria, then the f_0 value is considered a reliable estimation of the fundamental frequency. Additionally, if the amplitude value of the maximum (A_0) is greater than 4 – 5, then the existence of a geological interface with large seismic velocity contrast exists.

All the HVSR curves and the corresponding maxima that resulted from the processing of ambient noise measurements with the HVSR method and are presented in the current thesis, were inspected for their reliability and "clarity" according to the criteria of Figure 4.18.

4.1.5 Ambient noise array

The ambient noise data processing with the ambient noise array technique was conducted by the Geopsy software suite (Wathelet, 2005 and 2020). This software suite includes modules besides Geopsy, that are used in different stages during data processing such as warangps (theoretical array response), Geopsy (f – k method), max2curve (dispersion curve selection) and dinver (inversion).

At each site the ambient noise data are divided into two datasets corresponding to different circles of the array configuration with a different total recording duration. The analysis of each dataset provides a different part of the surface waves dispersion curve, but the processing stages and parameters are common for both datasets. The next paragraphs are devoted into thoroughly describing the processing procedure that was followed for every recording station group that was designed for the array technique.

The first stage involves the creation of a database consisting of the ambient noise recordings. The database includes the vertical component of each recording station; hence the extracted dispersion curve is related to the Rayleigh wave propagation. Besides the seismic waveforms, the database holds some additional information, such as the absolute start and end recording time, the recording duration, the sampling frequency, and the station coordinates.

The second stage involves the creation of cartesian coordinate system the origin of which (point 0, 0) coincides with the central station. Therefore, each recording station, depending on its position at space, has its own pair of coordinates on the aforementioned cartesian system. The theoretical array response is computed with the coordinates (x_i, y_i) of each station using equation (13).

The distribution of the theoretical array response values at plane (k_x, k_y) is calculated for wavenumber values in the range of $k_{min}/2$ to k_{max} which are typical for every array configuration. Surface waves that propagate with wavenumber values lower than $k_{min}/2$ cannot provide reliable information regarding the dispersion curve, while for wavenumber values greater than k_{max} aliasing effects emerge in the processing results. The exponential curves for constant wavenumbers $k_{min}/2$, k_{min}, $k_{max}/2$ and k_{max} are plotted in the slowness – frequency diagram, demarcating the reliable area for the selection of the dispersion curve (see Figure 2.11).

The next stage involves the application of the f – k method to the ambient noise database. The recordings are segregated in time-windows and the array output is computed for each frequency. The range of the frequency values is estimated at the reliable area of the slowness – frequency diagram, according to the theoretical array response (previous stage). The duration of the time-windows is frequency dependent and is scaled to the center frequency of each frequency to be processed. The duration of the time-windows equals to 250T, with the value “250” corresponding to a window length in number of cycles for each frequency band and “T” to the center period of the band. For each time-window, the surface wave velocity at a frequency point is calculated from the position of the maximum value of the array output at the plane (k_x, k_y) for wavenumber values <1.5 rad/m and for velocity values >100 m/sec. Therefore, multiple velocity estimations are calculated for each frequency point, their number being equal to the number of time-windows. The grouping of the velocity values is conducted with the construction of a histogram for each frequency, as suggested by Ohrnberger et al. (2004). The probability density function (PDF) is applied at each histogram. The final velocity value and its standard deviation, for each frequency, is the median value of the PDF.

At the next stage, the f – k method results are presented graphically with the *max2curve* module (Figure 4.19). The mean dispersion curve that is computed by the f – k method may diverge from the desirable because, the velocity selection from the frequency histograms is conducted taking into account all computed velocity values although some of these values lie outside the reliable area or/and exhibit small PDF value. Figure 4.19 shows the f – k method results for the geometry of the ambient noise array conducted at the STL1 site pointing out the spurious data that affect the seismic energy depiction. The black line with the error bars represents the mean dispersion curve (DC) computed by the f – k method. The solid red line represents the $k_{min}/2$ curve, while the red dashed line represents the k_{max} curve which demarcate the reliability zone for the DC selection. In Figure 4.19 it can be observed that the right part of the DC is led by velocity values that lie outside of the reliable zone and is affected by data aliasing (higher from the k_{max} curve) while the left part of the dispersion curve also lies outside the reliable zone, lower from the $k_{min}/2$ curve. The lack of reliability at this part is due to the limited resolution of the particular array configuration and its inability to identify low velocity surface waves that propagate at lower frequencies. By removing unwanted velocity values from the histograms, the computed mean dispersion curve is shifted inside the reliable zone. In the case of an experienced user the correct DC can be easily picked manually.

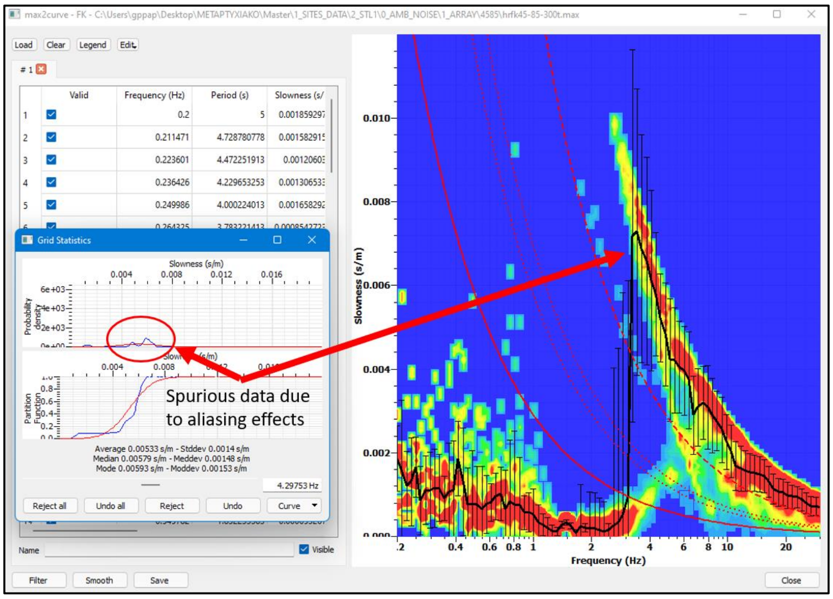

Figure 4.19 Environment of the max2curve module showing an example of the f – k method results for the geometry of the STL1 ambient noise array. The black line represents the mean dispersion curve computed by the f – k method. The red exponential curves demarcate the reliable zone for the selection of the dispersion curve.

The slowness – frequency diagrams resulted from the application of the f – k method to the ambient noise data for each site are shown in Figures 4.20 through 4.25. The exponential black curves represent the theoretical response of each array, based on its geometry. The black lines with the error bars represent the selected dispersion curve extracted for each array inside the reliable zone. The two dispersion curves at each site are unified to form the final dispersion curve that is used in the inversion at the next step. As mentioned in chapter 3, data loss cases were experienced with the ambient noise arrays at ITS1, SEIS, and PLA1 sites, introducing changes at the geometry of each array and thus, at their theoretical responses. If data were lost from a seismometer at the outer circles, then the higher limit of the theoretical response was shifted to lower frequency. Analogously, if data were lost from a seismometer close to the center of the array, the lower limit was shifted to higher frequencies, narrowing the reliable section for the selection of the dispersion curve. These cases introduced gaps between the dispersion curves of each dataset for each array (Figures 4.25c, 4.26c). The dispersion curves were left unconnected in order to let the inversion algorithm "determine" the best mathematical model.

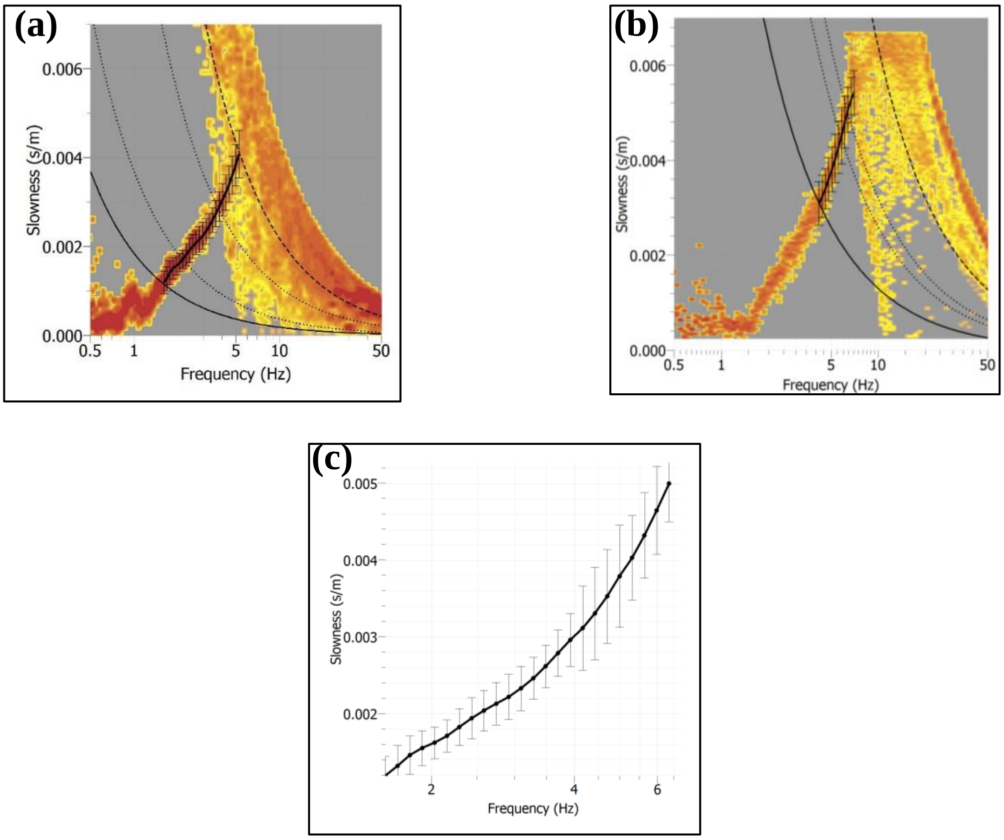

Figure 4.20 The slowness – frequency diagrams derived from the ambient noise array at **PORT** site for (a) the 45m – 150m array and (b) the 15m array. The exponential curves (theoretical array response) demarcate the reliability zone in which the dispersion curve is selected across the zone with the highest energy (red colors). The two dispersion curves are unified (c) to form the final Rayleigh-waves dispersion curve that is used in the inversion and are smoothed through resampling.

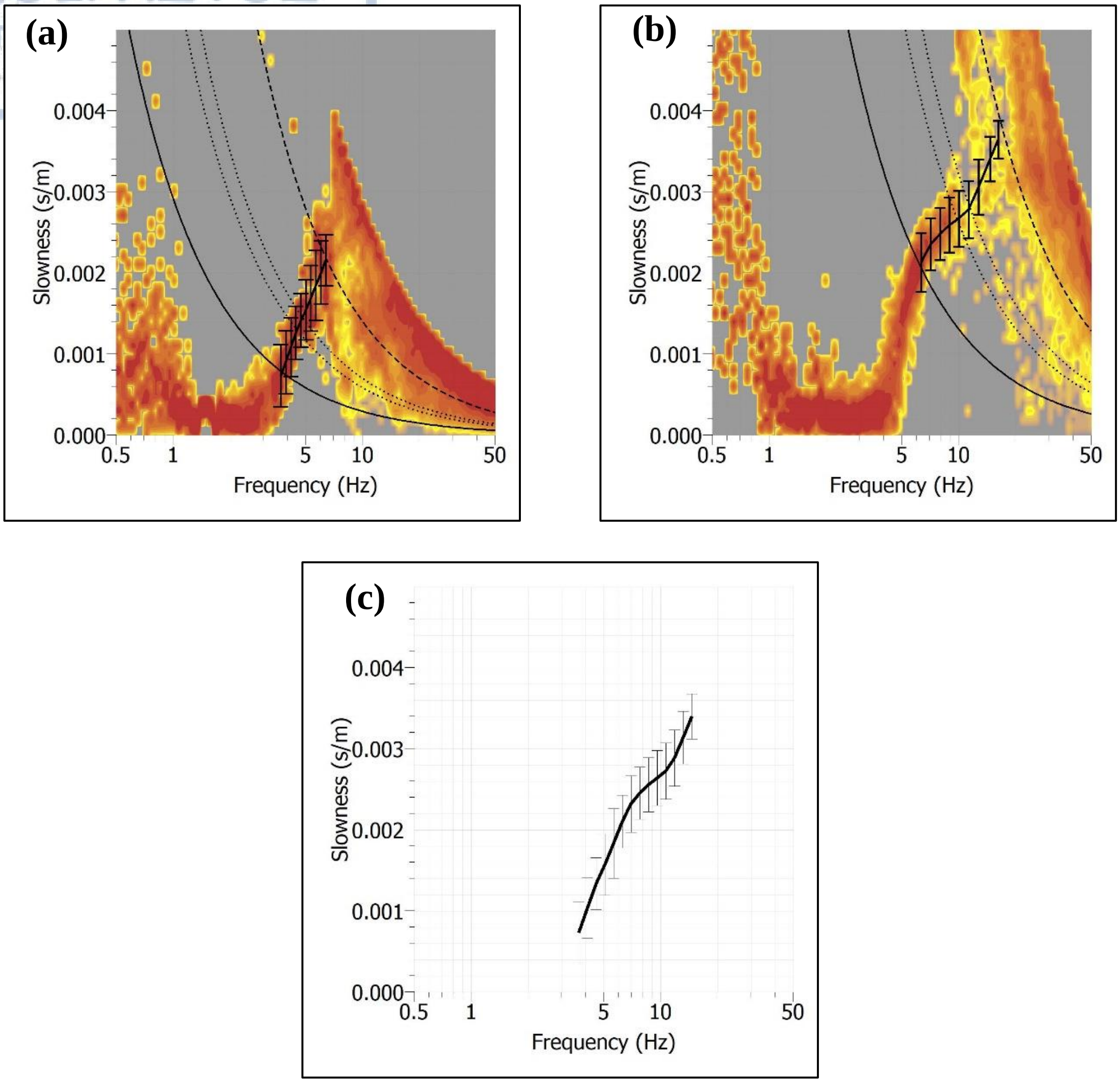

Figure 4.21 The slowness – frequency diagrams derived from the ambient noise array at **STL1** site for (a) the 45m – 85m array and (b) the 15m array. The exponential curves (theoretical array response) demarcate the reliability zone in which the dispersion curve is selected across the zone with the highest energy (colder colors). The two dispersion curves are unified (c) to form the final Rayleigh-waves dispersion curve that is used in the inversion and are smoothed through resampling.

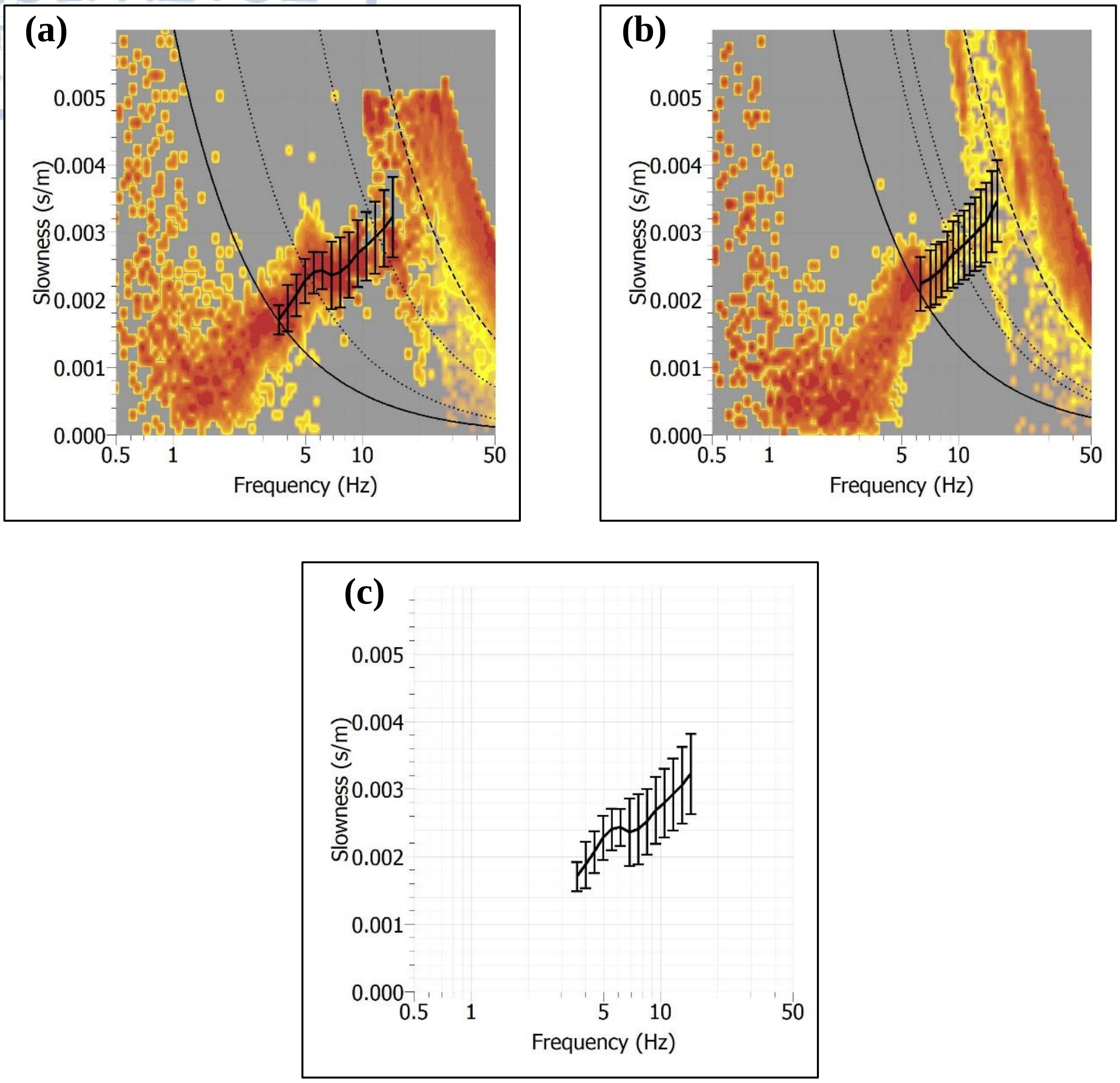

Figure 4.22 The slowness – frequency diagrams derived from the ambient noise array at **KLR1** site for (a) the 15m – 45m array and (b) the 15m array. The exponential curves (theoretical array response) demarcate the reliability zone in which the dispersion curve is selected across the zone with the highest energy (colder colors). The two dispersion curves are unified (c) to form the final Rayleigh-waves dispersion curve that is used in the inversion and are smoothed through resampling.

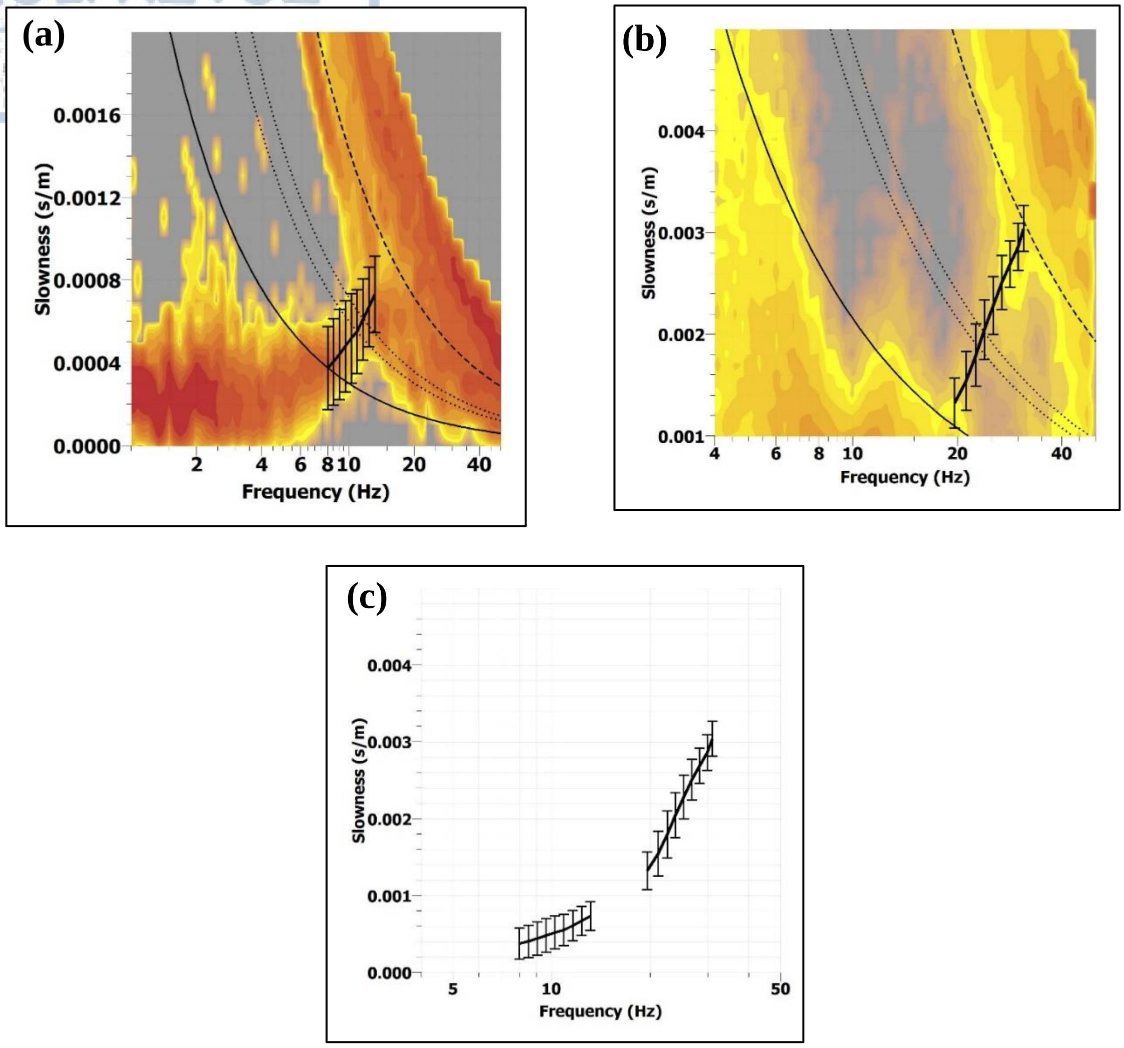

Figure 4.23 The slowness – frequency diagrams derived from the ambient noise array at **SEIS** site for (a) the 30m – 90m array and (b) the 15m array. The exponential curves (theoretical array response) demarcate the reliability zone in which the dispersion curve is selected across the zone with the highest energy (colder colors). The two dispersion curves are unified (c) to form the final Rayleigh-waves dispersion curve that is used in the inversion and are smoothed through resampling.

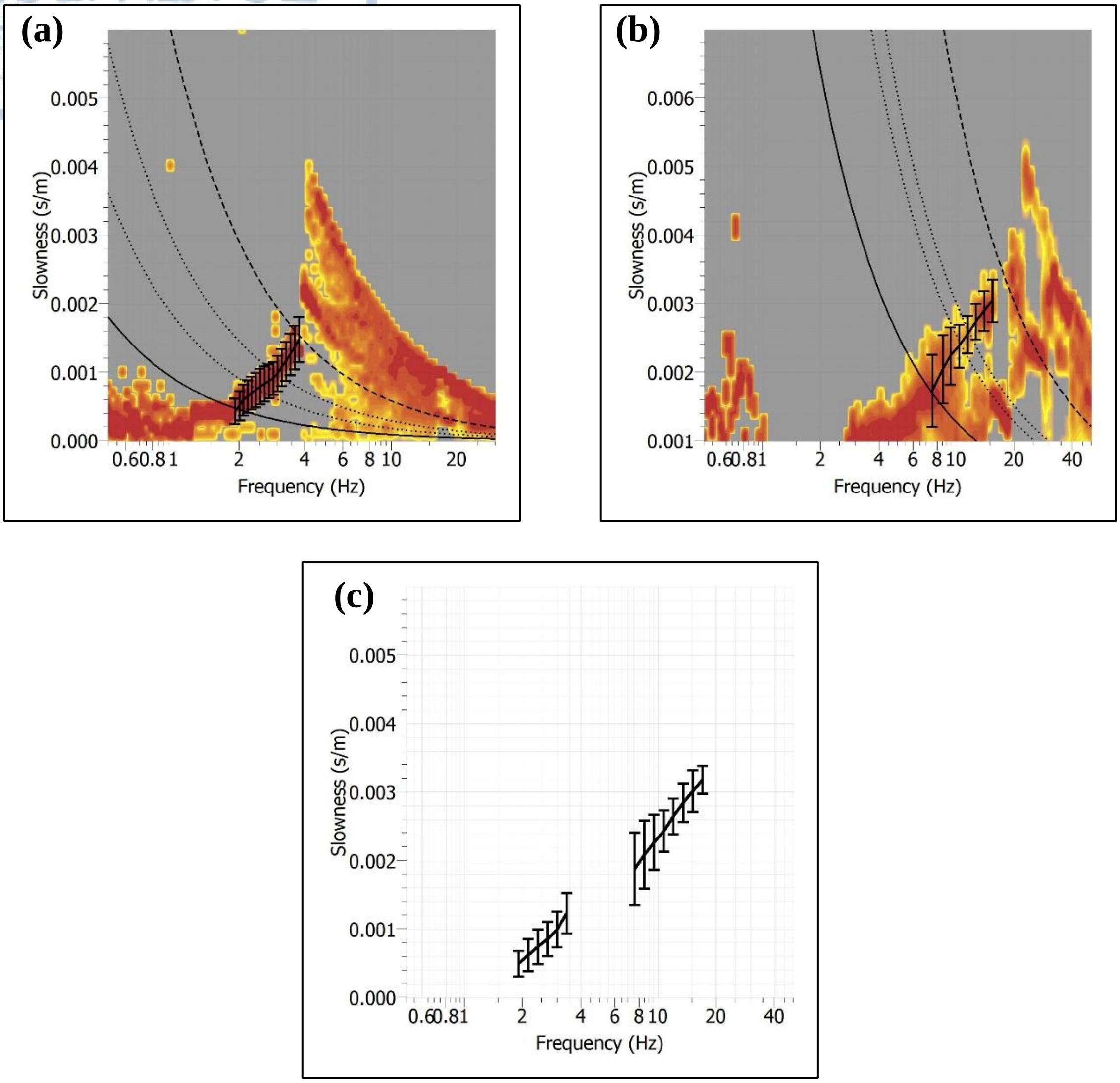

Figure 4.24 The slowness – frequency diagrams derived from the ambient noise array at **ITS1** site for (a) the 60m – 180m – 300m array and (b) the 10m - 20m array. The exponential curves (theoretical array response) demarcate the reliability zone in which the dispersion curve is selected across the zone with the highest energy (colder colors). The two dispersion curves are unified (c) to form the final Rayleigh-waves dispersion curve that is used in the inversion.

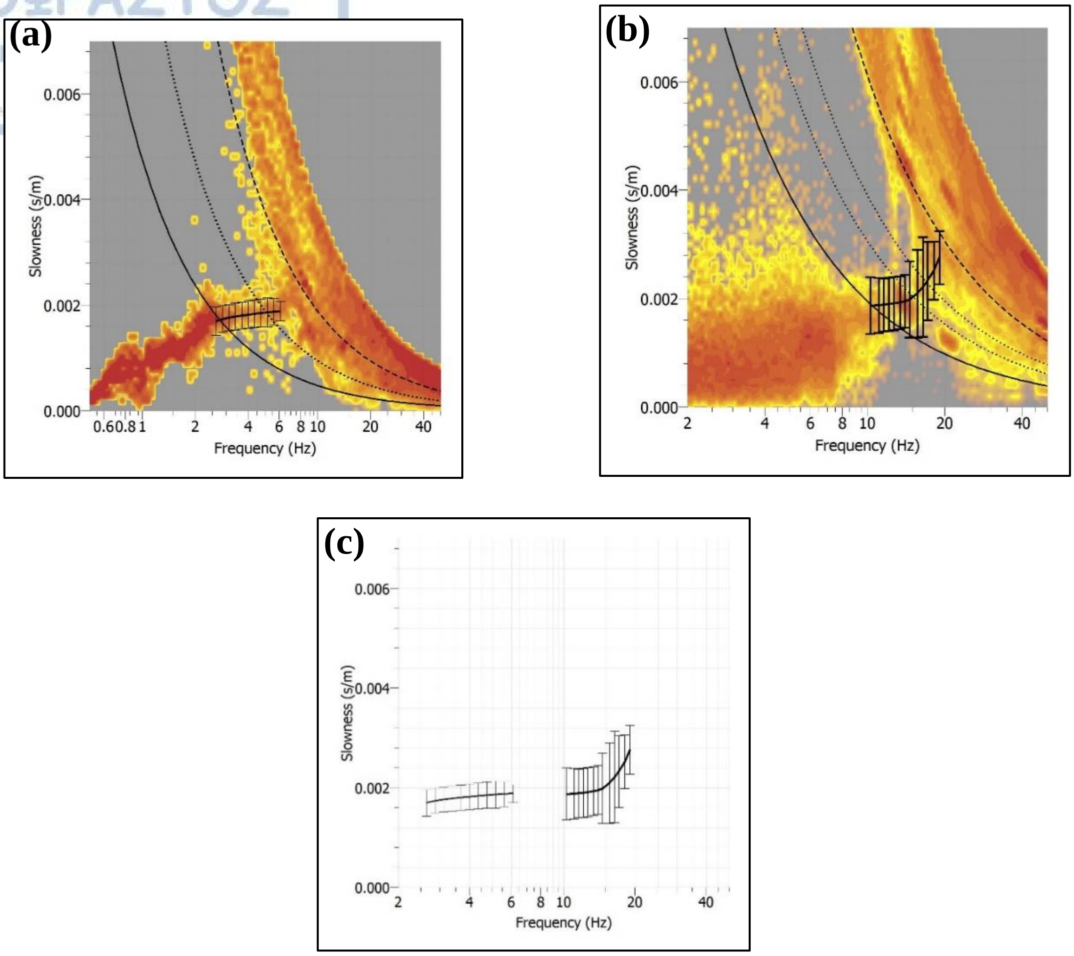

Figure 4.25 The slowness – frequency diagrams derived from the ambient noise array at **PLA1 and PLA2** site for (a) the 40m – 120m array and (b) the 15m array. The exponential curves (theoretical array response) demarcate the reliability zone in which the dispersion curve is selected across the zone with the highest energy (colder colors). The two dispersion curves are unified (c) to form the final Rayleigh-waves dispersion curve that is used in the inversion.

The investigation depth of each extracted dispersion curve is based on the recordable wavelength and thus is determined as in the MASW processing and is shown in Figure 4.7. The final processing stage involves the inversion of the Rayleigh wave dispersion curve for the estimation of the 1D Vs profile and was conducted with the dinver module of the Geopsy software package. Dinver uses a neighborhood algorithm originally proposed by Sambridge, 1999 and improved by Wathelet et al., 2004 and Wathelet, 2005, 2008. As already mentioned, each ambient noise array was divided in two datasets, with each dataset providing a part of the total dispersion curve at a different frequency band, depending on the array geometry. The f – k method results of each dataset are combined for the construction of the total dispersion curve and the final curve for each site was smoothed through resampling. Smoothing before inversion is necessary for two main reasons: firstly, it facilitates the mathematical prerequisites of the inversion and secondly, an unsmoothed, with intense variations dispersion curve cannot provide a theoretical structure model. Before the inversion of the smoothed dispersion curve, the initial values for the velocities of the seismic waves (V_S) and (V_P), the mass density, the number of layers, the Poisson's ratio, and the thickness of each layer of the subsurface structure are defined to construct the initial parameter space. Typically, these parameters can vary freely between a wide range of values, however in our work the initial model defined before the inversion is different for each site and the values ranges are based on the geophysical information acquired by the ERT and MASW methods. The inversion algorithm constructs theoretical models with a random selection of values (random seed) for each parameter. A theoretical dispersion curve is computed for each theoretical model (forward modeling) as well as the corresponding misfit value according to the Equation (14).

The inversion procedure stops when the misfit value is at a minimum. The inversion algorithm produced a great number of theoretical structure models. If the results were not satisfactory (bad correlation between experimental and theoretical dispersion curves) the initial parameter space was redefined, and the inversion algorithm was reapplied. For each application site, the inversion algorithm was applied for several parameter spaces for the best possible results (minimum misfit). The inversion results, that is the 1D V_S profiles represent as best as possible the true subsurface structure and are presented per site in the next section.

4.1.6 Inversion of HVSR for 1D V_S profile

The inversion of the HVSR curves has been conducted using the open-source HV-Inv program developed by Garcia-Jerez et al., (2016). This program allows for the forward modeling of the HVSR under the Diffuse Field Assumption (DFA) theory, by considering the connection between the HVSR of ambient noise measurements and the elastodynamic Green's function which arises from the ambient noise interferometry theory. The reliability of HVSR inversion obtained under the diffuse field assumption has been already stated by Sánchez-Sesma et al. (2011) and Salinas et al. (2014), among others.

HV-Inv is equipped with a variety of global (heuristic) inversion methods (Monte Carlo - MC (Hastings, 1970), Simulated Annealing - SA (Kirkpatrick, 1983), Modified Simulated Annealing – MSA (Lee et al. 2019) and local inversion methods (Interior Point - IP (Waltz et al., 2006) and Simplex Downhill -SD (Nelder and Mead, 1965)).

A parametric investigation of how a priori information is incorporated and facilitates the HVSR inversion was deemed necessary. For this purpose, various tests were conducted, classified in 3 main groups with different options each time (number of layers, low velocity layers). All inversion methods implemented in HV-Inv were used and were combined with 3 different initial models (Table 4.1).

Table 4.1 Test groups conducted for the parametric investigation of the HVSR inversion.

Test Group	Number of Layers	Velocity inversions
1st	Small - 5	NO
2nd	Small - 5	YES
3rd	Large - 20	YES

The HVSR measurement that is used in these tests was conducted at PORT accelerometer station site along with the MASW and ERT methods. The existing borehole at the site revealed the geologic stratigraphy down to 80m while a downhole measurement provided a detailed Vs profile for the same depth. The shallow layers are formed by anthropogenic infill while a thick package of recent geologic sediments consisting of clay, sandy clay, sand, sandy silt, among others, is underlain and a very cohesive sandy clay exists near the bottom of the borehole. The ERT revealed the existence of a 1D subsurface structure, down to about 34m, consisting of 3 layers of approximate thicknesses of 8m, 16m and a layer of at least 10m, from top to bottom (Table 4.2). Additionally, the 1D MASW method revealed the V_S profile. The geophysical method results and construction of the local 1D subsurface model of the PORT area is explained in Section 4.2.1. The HVSR curve was computed with the procedure described in Section 4.1.4 and is characterized by respective standard deviation for each frequency. However, based on the assumption that it is highly time-dependent and not a property of the site we decided to use one representative standard deviation value to describe the HVSR curve. At A_0 amplitude, a standard deviation of ±20% is considered in the HVSR uncertainty in terms of amplification.

Table 4.2 Information compiled from geophysical investigation in the vicinity of the HVSR measurement point at PORT accelerometer station site.

Layers	Thickness (m) (from ERT)	V_S (m/s) (from MASW)
1	8	100-200
2	16	150-300
3	≥10	250-350

The first step involved the computation of the three initial models for each test group, generated by the respective parameter spaces through the Random Search method described in Garcia-Jerez et al., (2016). Test groups 1 and 2 shared the same initial models (A, B and C) (Table 4.3). Initial model A describes a parameter space (thickness, V_S) with generally broad parameter intervals (unconstrained) while initial model B constrains only thickness based on information from the ERT. Additionally, the initial model C constrains V_S values based on the results of the MASW method. The investigation depth was kept at a maximum of 100m in all tests.

Table 4.3 Initial models used in test groups 1 and 2.

Initial model		**A**		**B**		**C**	
Parameter		**t (m)**	**Vs(m/s)**	**t (m)**	**Vs(m/s)**	**t (m)**	**Vs(m/s)**
Constrained		✗	✗	✓	✗	✓	✓
Layers	1	1-20	200-3400	8	200-3400	8	100-200
	2	1-20	200-3400	16	200-3400	16	150-300
	3	1-20	200-3400	10-40	200-3400	10-40	200-3400
	4	1-20	200-3400	10-40	200-3400	10-40	200-3400
	5 (HS)	-	200-3400	-	200-3400	-	200-3400

In test group 3 the initial models (Table 4.4) are constructed similarly to the ones used for Test Groups 1 and 2 introducing additional layers (20 layers including half-space) in an attempt to improve the resolution of the resulting V_S profiles. These initial models were expected to facilitate and improve the fit of the respective HVSR due to higher number of layers and their individual settings.

Table 4.4 Initial models used in test group 3.

Initial model		**A**		**B**		**C**	
Parameter		**t (m)**	**Vs(m/s)**	**t (m)**	**Vs(m/s)**	**t (m)**	**Vs(m/s)**
Constrained		✗	✗	✓	✗	✓	✓
Layers	1	1-5	200-3400	3	200-3400	3	100-200
	2	1-5	200-3400	5	200-3400	5	100-200
	3	1-5	200-3400	5	200-3400	5	150-300
	4	1-5	200-3400	3	200-3400	3	150-300
	5	1-5	200-3400	5	200-3400	5	150-300
	6	1-5	200-3400	3	200-3400	3	150-300
	7	1-5	200-3400	1-5	200-3400	1-5	200-3400
	…						
	20 (HS)	-	200-3400		200-3400		200-3400

As seen in Table 4.1 for the test group 1, HV-Inv rejects profiles where Vs decreases with depth. A relatively large number of iterations was conducted for each test. The correlation coefficient, r, of theoretical and observed HVSR curves was calculated for each test based on the following equation:

$$r(d_{obs}, d_{the}) = \frac{\sum\left(d_{obs} - \overline{d_{obs}}\right)\left(d_{the} - \overline{d_{the}}\right)}{\sqrt{\sum\left(d_{obs} - \overline{d_{obs}}\right)^2 \sum\left(d_{the} - \overline{d_{the}}\right)^2}} \tag{17}$$

where d_{obs} and d_{the} correspond to amplitude values of the observed and theoretical HVSR curves, respectively and $\overline{d_{obs}}$, $\overline{d_{the}}$ correspond to the mean value of each one of the samples. Also, to evaluate the convergence of the f_0 values from theoretical and observed HVSR curves the ratio f_{0calc}/f_{0obs} is computed, where f_{0calc} is the theoretical f_0 value and f_{0obs} is the observed f_0 value. Calculations of this ratio close to unity are indicative of a good convergence between observed and HVSR theoretical curves.

Test group 1 results are shown in Table 4.5 and Figure 4.26. Figure 4.27 shows a combined plot of the r and f_{0calc}/f_{0obs} values for each test. Tests with initial model A show bad convergence results. It is evident (Figure 4.27) that tests conducted with initial model B (thickness constrained) and C (constrained thickness and V_S) exhibit good positive correlation (r close to +1), and f_{0calc}/f_{0obs} values close to 1 meaning good convergence of the theoretical HVSR curves to the observed one. However, bad convergence is observed at the high frequency part (≥5Hz) (Figures 4.26b, 4.26c) which is characterized by low HVSR amplitude (<1) relatively to the rest of the HVSR curve. According to Garcia-Jerez, (personal communication, 2021), low HVSR amplitude at high frequencies might correspond to a thin, surficial layer of high velocity (e.g., pavement, cement). This assumption was considered in test group 2 by allowing velocity inversions (V_S decreasing with depth).

Table 4.5 V_S profiles derived from HVSR inversions conducted in Test group 1.

Test	r	Layer 1		Layer 2		Layer 3		Layer 4		Half-space	
		t(m)	Vs (km/s)	t(m)	Vs (km/s)	t(m)	Vs (km/s)	t(m)	Vs (km/s)	t(m)	Vs (km/s)
MC-A	-0.6	3.4	3.3	1.6	3.4	7.1	3.4	10.9	3.4	-	3.4
MC-B	0.9	8.0	0.2	16.0	0.2	38.3	0.2	30.4	1.3	-	2.6
MC-C	1.0	8.0	0.1	16.0	0.2	33.9	0.2	11.3	0.7	-	0.8
SA-A	-0.7	2.9	3.0	1.9	3.1	7.2	3.2	17.0	3.2	-	3.2
SA-B	0.2	8.0	0.6	16.0	0.6	16.4	0.7	33.1	1.0	-	1.0
SA-C	0.6	8.0	0.2	16.0	0.2	37.9	0.2	26.3	0.4	-	0.7
MSA-A	-0.5	2.3	3.4	1.2	3.4	8.5	3.4	1.1	3.4	-	3.4
MSA-B	0.9	8.0	0.3	16.0	0.3	32.0	0.3	30.3	0.4	-	1.4
MSA-C	0.9	8.0	0.2	16.0	0.2	33.8	0.2	15.7	0.4	-	0.8
SD-A	-0.6	1.7	2.6	2.0	3.2	2.2	3.2	2.5	3.2	-	3.2
SD-B	0.9	8.0	0.2	16.0	0.2	40.0	0.3	27.7	1.0	-	2.4
SD-C	0.9	8.0	0.1	16.0	0.2	37.0	0.2	16.0	0.8	-	0.8
IP-A	-0.6	1.0	1.9	2.7	2.5	2.6	2.6	19.6	2.8	-	2.8
IP-B	0.9	8.0	0.2	16.0	0.2	38.1	0.2	34.1	1.1	-	1.9
IP-C	0.9	8.0	0.2	16.0	0.2	28.2	0.2	26.0	0.3	-	1.6

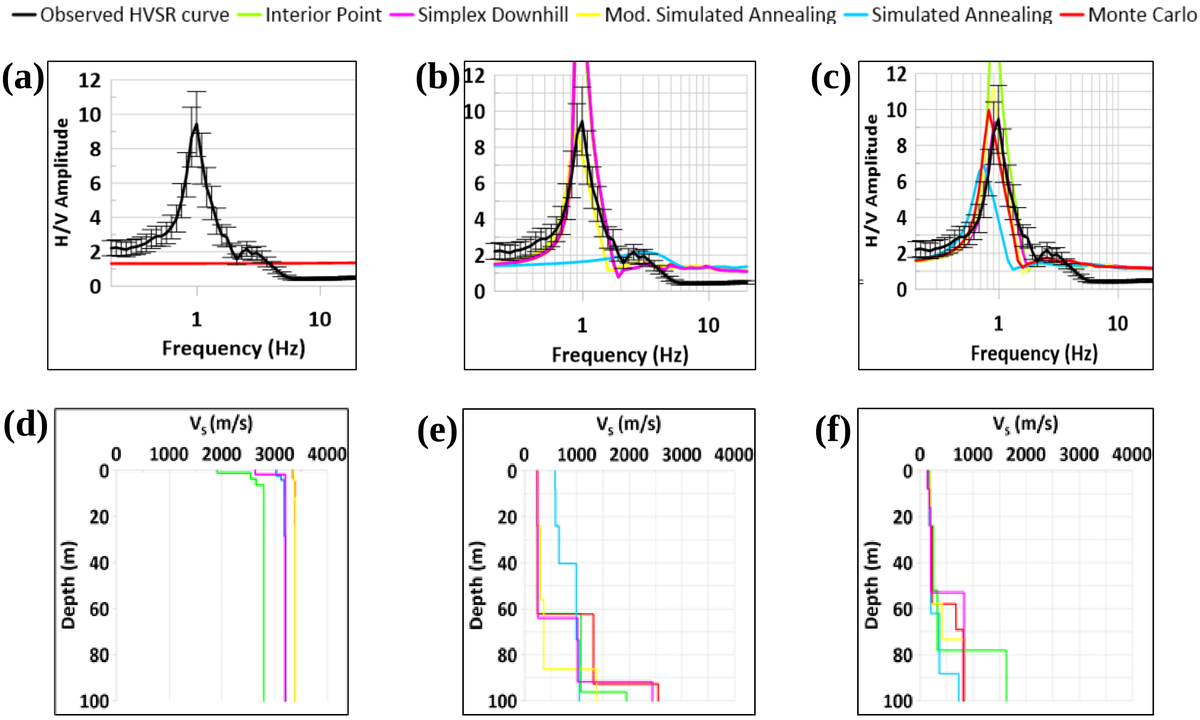

Figure 4.26 Test group 1 results. Inversion of the observed HVSR curve (black curve) using PS_A (a), PS_B (b), PS_C (c) and corresponding Vs profiles (d), (e) and (f).

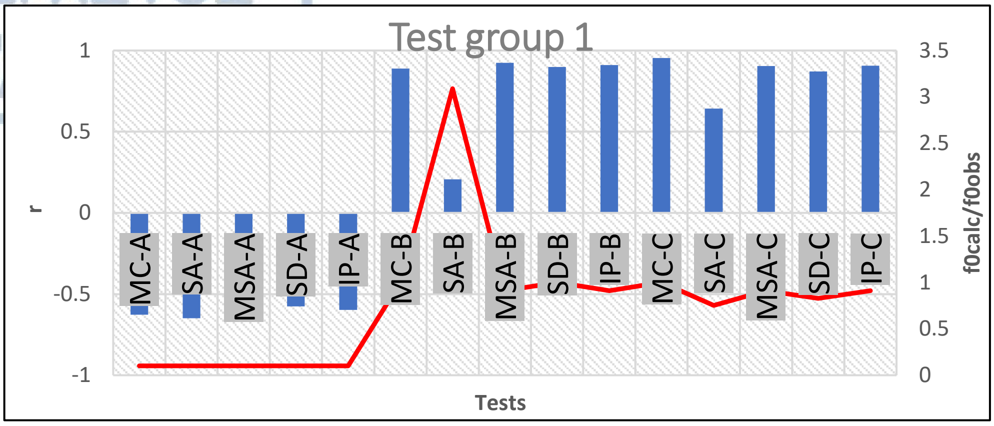

Figure 4.27. Combined plot of the correlation coefficient, r, (bars) and the f_{0calc}/f_{0obs} values (red curve) for each test in Test group 1.

Test group 2 used the same initial models as in test group 1 (Table 4.3). The corresponding results are presented in Table 4.6. Inversion outcomes derived from the use of initial models A and B exhibit low r values (0.4 – 0.5) and bad f_{0calc}/f_{0obs} values (Figure 4.29), although it is noteworthy that a very good convergence is achieved at the high frequency part (≥5Hz) (Figures 4.27a and 4.27b). The corresponding V_S profiles (Figures 4.28d and 4.28e and Table 4.6) show that a high velocity surficial layer led to the successful convergence at the high frequency part. Inversion outcomes derived from the use of initial model C achieved greater correlation and simulated well the observed f_0 value (f_{0calc}/f_{0obs} close to 10), however convergence is bad at the ≥5Hz part. This is due to the constraints applied from initial model C that does not allow the generation of a surficial high velocity layer.

Table 4.6 V_S profiles derived from HVSR inversions conducted in Test group 2.

Test	r	Layer 1		Layer 2		Layer 3		Layer 4		Half-space	
		t(m)	Vs (km/s)	t(m)	Vs (km/s)	t(m)	Vs (km/s)	t(m)	Vs (km/s)	t(m)	Vs (km/s)
MC-A	0.4	5.6	2.9	18.7	0.6	18.9	1.9	17.3	0.6	-	2.9
MC-B	0.5	8.0	3.1	16.0	0.5	39.8	0.5	38.1	1.3	-	3.1
MC-C	0.9	8.0	0.1	16.0	0.3	29.6	0.2	29.7	0.5	-	0.9
SA-A	0.4	3.0	1.7	9.1	0.3	8.9	1.3	17.4	0.5	-	1.7
SA-B	0.5	8.0	3.1	16.0	0.5	39.9	1.3	34.6	1.2	-	3.1
SA-C	0.9	8.0	0.2	16.0	0.2	37.6	0.2	19.4	1.0	-	1.1
MSA-A	0.4	5.3	2.2	8.5	0.3	17.0	1.6	18.5	0.6	-	2.2
MSA-B	0.5	8.0	3.4	16.0	0.5	33.0	2.2	36.5	1.0	-	3.4
MSA-C	0.8	8.0	0.2	16.0	0.2	36.4	0.2	38.1	0.7	-	1.0
SD-A	0.5	4.1	1.9	12.3	0.4	13.7	1.3	19.6	0.6	-	1.9
SD-B	0.9	8.0	2.7	16.0	0.3	38.9	1.7	32.1	1.1	-	2.7
SD-C	0.9	8.0	0.2	16.0	0.2	29.2	0.2	11.4	0.4	-	0.9
IP-A	0.4	9.4	3.0	15.3	3.0	10.5	1.7	10.4	0.9	-	3.0
IP-B	0.5	8.0	2.5	16.0	0.5	38.7	1.0	39.0	1.4	-	2.5
IP-C	0.9	8.0	0.2	16.0	0.2	33.2	0.2	21.3	0.8	-	0.9

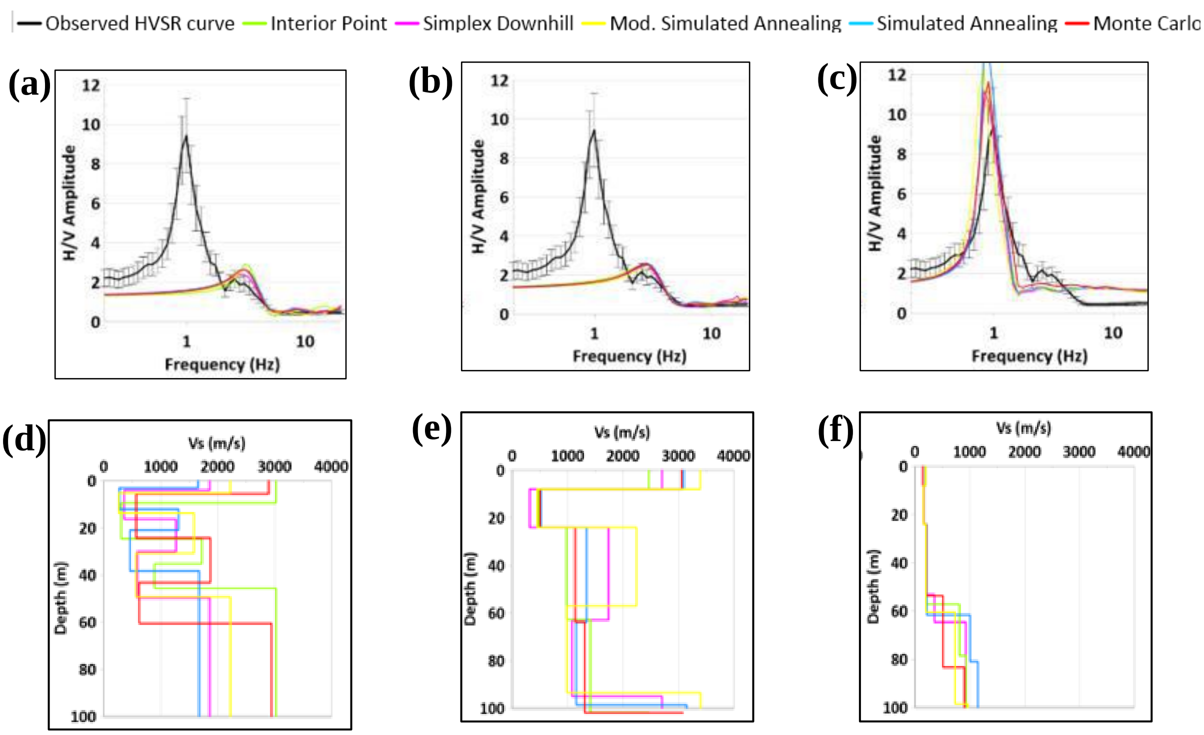

Figure 4.28 Test group 2 results. Inversion of the observed HVSR curve (black curve) using PS_A (a), PS_B (b), PS_C (c) and corresponding VS profiles (d), (e) and (f).

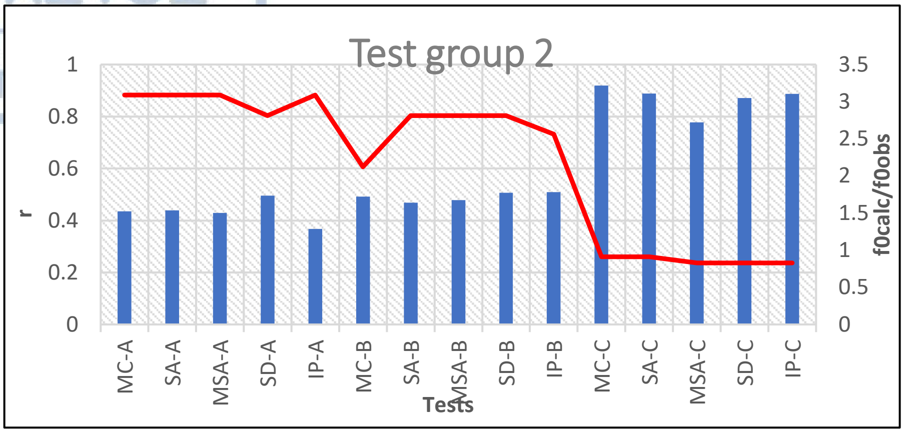

Figure 4.29 Combined plot of the correlation coefficient, r, (bars) and the f_{0calc}/f_{0obs} values (red curve) for each test in Test group 2.

Inversions performed in Test group 3 were conducted with the parameter spaces in Table 4.4. Inversion outputs (Table 4.7 and Figure 4.30) conducted with the use of initial model A (20 layers) and B led to velocity models that exhibit alternating adjacent layers with low and high velocities. Such profile could hardly correspond to a real soil structure. However, in Figures 4.30a and 4.30b very good convergence at frequencies ≥5Hz is observed. Inversion profiles based on initial model C generated velocity models with high deviation between the corresponding theoretical and observed HVSR curve over the entire frequency range with bad f_{0calc}/f_{0obs} and r values (Figure 4.31).

Table 4.7 V_S profiles derived from HVSR inversions conducted in Test group 3.

Test	r	Layer 1		Layer 2		Layer 3		Layer4		Layer 5		Layer 6		Layer 7		HS	
		t(m)	VS (km/s)	t(m)	VS (km/s)	t(m)	VS (km/s)	t(m)	VS (km/s)	t(m)	VS (km/s)	t(m)	VS (km/s)	t(m)	VS (km/s)	t(m)	VS (km/s)
MC-A	0.4	5.0	2.8	1.0	1.2	5.0	0.3	2.0	2.4	3.0	1.5	2.0	0.3	4.0	2.1	-	2.9
MC-B	0.4	3.0	2.9	5.0	0.3	5.0	0.9	3.0	2.8	5.0	0.4	3.0	1.3	2.0	2.6	-	2.9
MC-C	0.1	3.0	0.2	5.0	0.1	5.0	0.2	3.0	0.2	5.0	0.2	2.0	0.2	1.0	0.6	-	3.2
SA-A	0.4	3.0	3.1	3.0	0.4	4.0	2.2	5.0	2.9	4.0	0.2	5.0	1.1	4.0	1.2	-	3.3
SA-B	0.5	3.0	3.3	5.0	0.4	5.0	3.2	3.0	0.5	5.0	0.7	3.0	2.6	3.0	1.6	-	3.3
SA-C	0.3	3.0	0.2	5.0	0.1	5.0	0.2	3.0	0.2	5.0	0.2	3.0	0.2	4.0	0.2	-	3.1
MSA-A	0.4	2.0	2.7	4.0	3.0	2.0	0.6	4.0	0.3	4.0	0.3	4.0	1.3	1.0	2.6	-	3.1
MSA-B	0.4	3.0	3.0	5.0	2.5	5.0	0.3	3.0	3.1	5.0	0.3	3.0	2.1	1.0	0.7	-	3.3
MSA-C	0.2	3.0	0.2	5.0	0.1	5.0	0.2	3.0	0.2	5.0	0.2	3.0	0.2	1.0	0.6	-	3.4
SD-A	0.5	3.0	2.8	2.0	0.3	4.0	0.0	5.0	0.5	3.0	2.9	4.0	1.4	4.0	1.1	-	3.2
SD-B	0.5	3.0	2.8	5.0	1.0	5.0	0.3	3.0	2.5	5.0	1.2	3.0	0.3	4.0	2.7	-	2.8
SD-C	0.1	3.0	0.2	5.0	0.1	5.0	0.2	3.0	0.2	5.0	0.2	3.0	0.2	1.0	0.8	-	3.4
IP-A	0.4	3.0	2.4	2.0	0.3	4.0	3.2	5.0	0.6	3.0	2.9	4.0	1.6	4.0	1.1	-	3.4
IP-B	0.4	3	3.3	5.0	1.9	5.0	0.2	3.0	2.2	5.0	2.7	3.0	1.5	3.0	1.3	-	3.3
IP-C	0.1	3	0.1	5.0	0.1	5.0	0.2	3.0	0.2	5.0	0.2	3.0	0.2	3.0	0.8	-	3.2

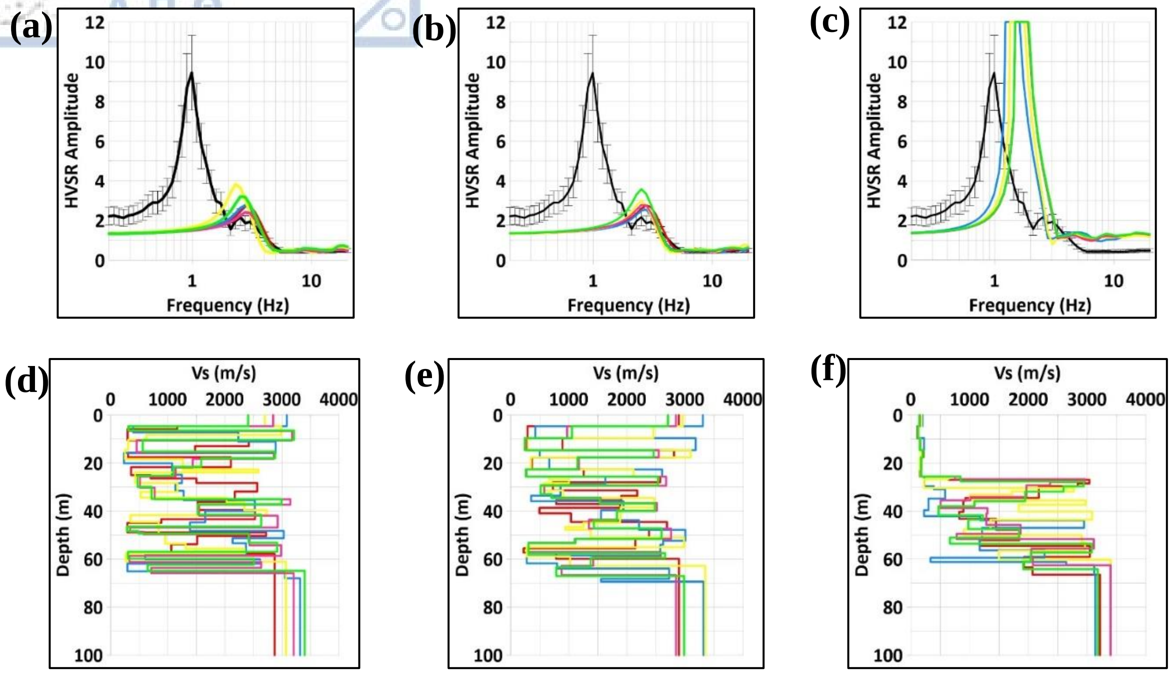

Figure 4.30 Test group 3 results. Inversion of the observed HVSR curve (black curve) using PS_A (a), PS_B (b), PS_C (c) and corresponding Vs profiles (d), (e) and (f).

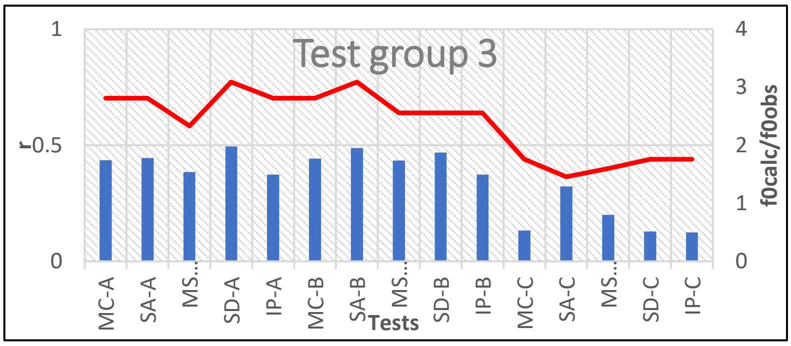

Figure 4.31 Combined plot of the correlation coefficient, r, (bars) and the f_{0calc}/f_{0obs} values (red curve) for each test in Test group 3.

Test group 1 showed that constraining Vs and thickness is pivotal to deal with the solution non-uniqueness issue of the HVSR inversion to some extent. In particular, a global trade-off between velocities and thicknesses exists in any interpretation of the HVSR (if all velocities and thicknesses are scaled by the same factor, the curve shape doesn't vary). It is also insensitive to absolute density values (only contrasts matter). Allowing the decrease of Vs with depth in test group 2 showed that low amplitudes at high frequencies are due to a surficial high velocity layer possibly corresponding to very cohesive most probably hard infill material. Usage of high complexity initial models might generate unexpected velocity profiles of alternating layers with low and high velocities. According to Garcia-Jerez (personal communication, 2021) HV-Inv does not include algorithms intended to force a degree of smoothness between velocities of adjacent layers. Therefore, inversions using a large number of layers should be done and interpreted with caution.

Blind inversions (unconstrained V_S, thickness) imply huge search within the parameter space and the convergence of the theoretical to the experimental H/V curve may require long time and/or may not satisfactorily achieved. In order to facilitate the inversion procedure, it is preferable to constrain target values with available *a priori* information and/or by analyzing the shape of the experimental HVSR curve itself (Piña-Flores et al., 2016). According to Piña-Flores et al., 2016 and Garcia-Jerez et al., 2016, when either no information or a little *a priori* information is available, global methods such as the Monte Carlo or Simulated Annealing methods must be used (Hastings 1970; Holland 1975; Kirkpatrick et al. 1983; Goffe et al. 1994; Goffe 1996; Iglesias et al. 2001). When the misfit is minimized to an *a priori* acceptable value, or when adequate *a priori* information is available, the inversion can be based on a local optimization scheme (e.g., Byrd et al. 1999; Waltz et al. 2006).

HVSR inversion at the 6 accelerometer station sites was performed considering the above conclusions and the following guidelines for the construction of the initial model:

- The surficial layers were based on the acquired geophysical data at each site, regarding the subsurface layer thicknesses and Vs values.
- If the high frequency part (≥5Hz) of the HVSR curve is characterized by low amplitude (<1), then it is attributed to a surficial layer of hard infill material and high velocity (e.g., cement or pavement).
- The shape of the HVSR, that is fundamental frequency, f_0, and its higher modes (if available) are also considered in the initial model since they may be related to high contrast interfaces between geological formations. An estimation of the corresponding interface minimum depth is calculated through Equation 12, assuming an average top layer shear wave velocity.

- The final selection of inversion methods for this thesis was based on the findings of our assessment as described earlier and, on the methodology, followed in Garcia-Jerez et al. 2016 and Piña-Flores et al., 2016. First, a global inversion method (i.e., Monte Carlo) is used to generate about 1000 models. Once an acceptable fitting of the data was obtained (HV-Inv misfit <100) then a local inversion method is used. Finally, a global inversion method is applied at the end to compute the mean model and its standard deviation. At this step the Simulated Annealing method was preferred because it can produce models in parallel computing (CPU based) and is time efficient.

4.1.7 Earthquake HVSR

As already mentioned in Section 2.8, processing of the earthquake motion data was based on the methodology suggested by Lermo and Chavez-Garcia, (1993). Geopsy software suite (Wathelet 2005 and 2020), was used for the analysis of the earthquake recordings. The aim of the methodology is the computation of the spectral ratio of the horizontal to vertical component of the whole earthquake recording except for the P-wave part, at an accelerometer station. Therefore, in this HVSR method, earthquake recordings instead of ambient noise are used. The entire analysis and processing procedure of the earthquake motion data is analogous to the ambient noise data and is analytically described in Section 4.1.4. The only difference lies in the selection of the time-windows of the signals which was based on the duration of the seismic recording. Therefore, the length of the windows varied from 10 seconds for local seismic events, to 40 seconds for regional distant events providing long duration recordings. An example of an earthquake recording, and the appropriate selection of the time-window (25s) is shown in Figure 4.32.

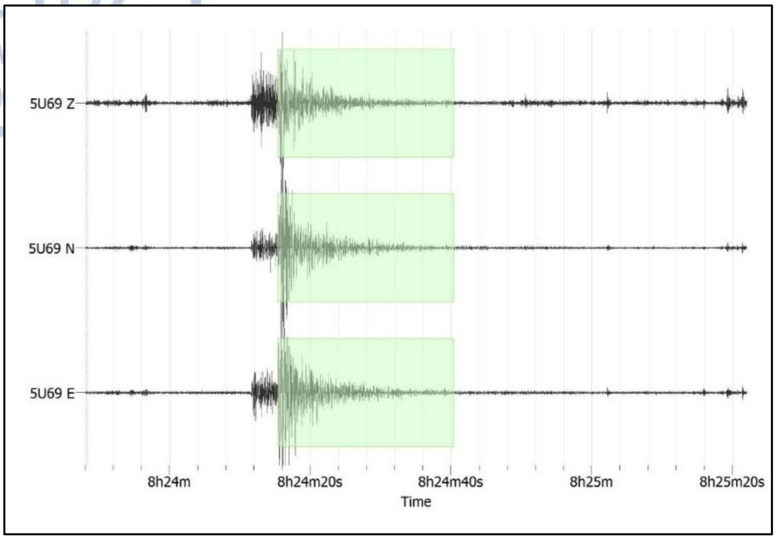

Figure 4.32 Example of an earthquake motion recording and the selection of part to be processed with Geopsy software suite. The part following the arrival of the S-waves is selected. One time-window with a duration of 25s has been selected (green selected area).

Earthquake data recorded by the accelerometers of the ITSAK National Accelerometric Network, at which the methodology of this thesis is applied are presented in Table 4.8. The information regarding the earthquake events was acquired from the database of the Permanent Regional Seismological Network operated by the Aristotle University of Thessaloniki. Distance and the source type barely affect the results; hence the earthquake events can be used in the estimation of the local site effects (Lozano et al., 2008; Bard et al. 2010).

Table 4.8 Earthquake events data recorded by accelerometers of the ITSAK National Accelerometric Network (database of the AUTh Seismological Station). Distance is calculated to the location of the SEIS accelerometer station and is also indicative for the other 5 accelerometric sites.

Events	Date	Time (GMT)	Lat (^{0})	Lon (^{0})	Depth (km)	M	Distance (km)
1	1/1/2018	22:13:52	41.192	22.875	10	3.9	62.7
2	1/2/2018	4:24:17	41.182	22.892	13	4.7	61.5
3	1/2/2018	17:36:34	41.182	22.860	11	4	61.8
4	1/4/2018	10:45:51	35.768	27.461	3	3.3	668.4
5	1/4/2018	10:46:12	42.605	19.992	0	4.9	330.3
6	1/15/2018	20:24:14	38.169	23.852	11	4.5	284.3
7	1/23/2018	23:14:04	35.065	23.153	7	4.3	619.2
8	1/28/2018	14:48:34	37.191	23.805	8	4.2	389.5
9	2/3/2018	12:53:14	42.905	16.748	19	4.4	573.9
10	2/11/2018	13:05:22	42.944	19.719	31	4.4	372.0
11	2/20/2018	3:52:54	39.294	23.915	11	4.2	169.5
12	2/21/2018	23:42:00	41.953	24.942	9	4.4	221.2

Events	Date	Time (GMT)	Lat (^{0})	Lon (^{0})	Depth (km)	M	Distance (km)
13	2/25/2018	15:21:15	38.605	25.632	13	4.2	321.0
14	3/13/2018	11:02:31	37.358	20.954	0	4	403.3
15	3/28/2018	13:28:10	37.753	20.360	1	4	390.8
16	4/10/2018	15:56:20	36.678	26.169	13	4.7	520.3
17	4/21/2018	0:20:07	39.947	23.717	10	4.6	99.5
18	5/3/2018	2:04:34	39.964	26.881	7	4.4	340.5
19	5/16/2018	22:30:03	36.519	22.921	5	4.6	457.3
20	5/19/2018	18:14:42	40.329	19.801	8	4.2	269.5
21	6/5/2018	8:52:40	36.615	22.627	6	4.6	447.6
22	6/25/2018	5:14:46	36.651	21.350	1	5.2	464.3
23	6/25/2018	8:21:55	40.712	23.323	7	4.2	31.7
24	6/25/2018	8:23:09	40.705	23.294	7	3.4	29.1
25	6/25/2018	8:24:05	40.694	23.325	5	3.7	31.3
26	6/27/2018	1:00:49	38.832	26.376	4	4.1	353.9
27	7/4/2018	9:01:09	41.496	19.581	8	4.8	299.3
28	7/4/2018	9:08:57	41.575	19.554	0	4.1	304.2
29	7/5/2018	21:39:04	37.976	21.296	1	4.4	328.3
30	7/5/2018	22:49:02	41.484	19.584	10	4	298.7
31	7/8/2018	20:32:12	35.352	22.917	1	4.1	587.1
32	7/13/2018	12:42:40	34.977	25.997	0	4.7	682.8
33	7/14/2018	2:50:59	38.785	16.559	11	4.8	584.8
34	7/17/2018	13:05:10	41.072	19.863	6	4	265.3
35	7/18/2018	6:49:47	39.791	20.701	0	4.1	213.6
36	7/23/2018	2:40:26	37.751	30.124	25	4.7	695.0
37	8/2/2018	6:56:54	36.755	21.290	4	4.2	454.8
38	8/11/2018	15:38:33	41.579	20.245	0	4.6	250.9
39	8/31/2018	7:12:24	39.279	21.619	11	5.2	189.1
40	8/31/2018	8:26:22	39.362	21.597	6	4.2	183.0
41	10/3/2019	4:57:38	40.005	22.392	9	3.7	84.9
42	10/19/2019	19:54:06	40.725	23.091	9	2.1	15.0
43	10/22/2019	21:37:16	40.304	24.062	10	3.2	99.9
44	10/29/2019	15:20:18	40.706	23.300	9	2.3	29.6
45	10/30/2019	11:45:38	40.510	23.520	7	2.8	49.0
46	11/1/2019	5:25:44	40.463	20.756	4	4.7	187.4
47	11/23/2019	3:30:37	40.841	23.172	6	2.4	29.2
48	3/21/2020	0:49:52	39.304	20.621	6	5.4	248.2
49	4/15/2020	12:20:37	40.538	21.794	12	4	99.2
50	5/2/2020	12:51:11	34.551	25.614	10	6	715.3
51	5/14/2020	16:23:36	40.572	23.139	9	3	16.3
52	5/19/2020	14:05:36	40.578	22.236	2	2.9	61.6

Events	Date	Time (GMT)	Lat (^{0})	Lon (^{0})	Depth (km)	M	Distance (km)
53	5/20/2020	23:43:22	35.318	20.453	30	5.8	630.4
54	5/29/2020	6:32:35	40.597	22.214	5	3.8	63.3
55	10/21/2020	23:00:56	37.230	20.517	2	5.2	433.4
56	10/30/2020	11:51:25	37.911	26.815	10	6.7	448.8
57	11/5/2020	22:16:27	39.922	23.972	9	4.2	116.4
58	12/2/2020	21:10:17	40.542	23.510	12	2.4	47.3
59	12/3/2020	11:00:12	40.776	23.434	2	2.6	42.8
60	12/8/2020	17:12:42	40.546	23.520	10	2.2	48.0
61	12/8/2020	19:16:45	40.543	23.520	9	2.4	48.1
62	12/12/2020	2:29:09	40.502	23.091	11	2.3	18.0
63	1/3/2021	16:11:35	40.077	22.702	6	2.9	65.5
64	1/10/2021	16:27:11	40.5441	22.5558	10	2.3	35.7
65	2/17/2021	3:36:05	38.358	21.957	11	4.9	267.2
66	7/14/2021	15:05:17	38.8893	21.7937	8.7	3.2	218.0
67	7/16/2021	19:28:02	38.2494	22.5938	10.9	3.5	266.8
68	7/17/2021	13:23:17	39.8085	22.0711	9.8	3	118.8
69	7/18/2021	22:21:44	40.6357	20.8713	2	3.5	176.5
70	7/22/2021	15:49:34	39.7888	19.574	7.4	3	302.6
71	7/22/2021	16:49:38	39.9051	20.7175	13.2	4.3	206.9
72	7/25/2021	20:57:01	39.63	22.2496	8.8	3.4	126.8
73	7/25/2021	22:36:04	39.7842	22.0944	12.1	2.9	119.7
74	7/26/2021	11:09:16	38.7318	20.5724	14.1	3	294.1
75	7/26/2021	19:23:19	40.9415	22.7664	14.7	2.7	38.2
77	8/1/2021	4:31:26	36.3821	27.0895	15.6	5.4	593.3
78	8/3/2021	12:38:19	36.3515	27.0992	11.5	5	596.6
79	8/7/2021	1:38:44	36.3029	27.0296	16.9	4.7	597.4
80	8/11/2021	5:59:31	38.7181	22.9527	11	3.8	212.8
81	8/21/2021	18:42:32	39.0056	22.0198	11.3	4	198.0
82	8/21/2021	19:09:46	38.9781	22.0097	13.9	3.3	201.1

4.1.8 Structure Models for The Numerical Simulation of Ambient Noise

To compute the synthetic ambient noise recordings at the investigation sites it is required to define the subsurface model of each site for which the Green functions are computed (Hisada 1994, 1995). Each model is defined by the number and thickness (in m) of layers (including half-space) and corresponding parameters such as mass density (in gr/m^3), P-wave and S-wave velocities (in m/s) and attenuation factors, Q_P for P-waves and Q_S for S-waves (Figure 4.33). A general rule of thumb for the calculation of Q_P and Q_S is the following (Kramer, 1997):

$$Q_P = \frac{V_P}{10}, Q_S = \frac{V_S}{10} \tag{18}$$

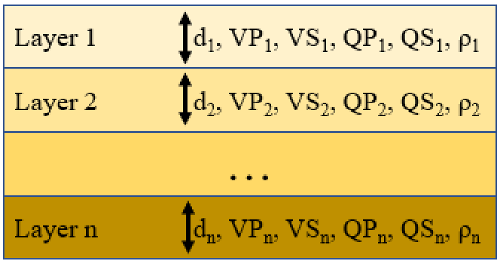

Figure 4.33 Theoretical subsurface structure with properties that define the input structure model for the numerical simulation of ambient noise.

4.2 Combined Results and Interpretation

In this section the results of the present study methodology are described per site. The important aspects described herein is the composition of the initial models for the HVSR inversion, the construction of the local 1D subsurface structure at each site and its validation.

4.2.1 PORT accelerometer station site – Site 1

The configuration of the surface geophysical methods together with the positions of the temporary seismometer and the borehole are presented in Figure 3.8. The result of the Electrical Resistivity Tomography for this site is presented in Figure 4.34a. Despite the complexity of the model revealed by the ERT, the geoelectric formations can be roughly grouped and provide a 1D underground model, down to about 40m depth. This simplified model consists of 3 layers of approximate thicknesses of 8m, 16m and a layer of at least 10m, from top to bottom.

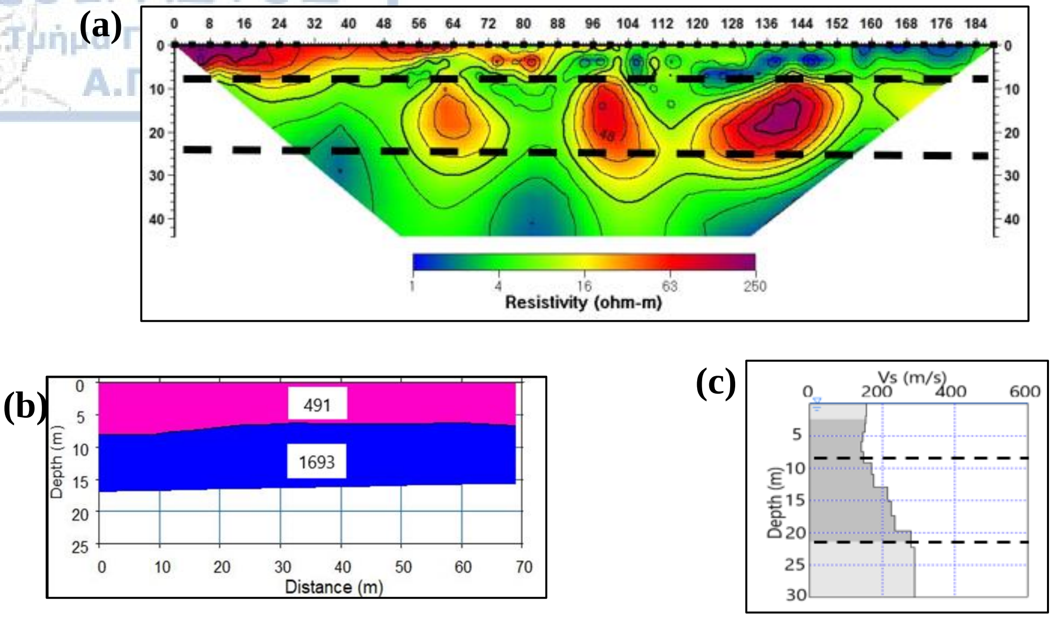

Figure 4.34 Geophysical investigation at the PORT accelerometer station site. (a) The ERT method result, (b) P-wave travel-time modeling (seismic refraction). (c) The 1D V_S profile, generated by the MASW method.

The 1D MASW method revealed almost similar number of layers with Vs equal to 140 m/sec for the first 6-meters from surface. At this depth Vs gradually increases until it reaches the value of 250 m/sec at around 22m depth. For greater depths and at least down to 30 meters from the surface the Vs appears constant (Figure 4.34c). V_P velocities calculated by the refraction method, although didn't reach the same investigation depth, seem to verify the assumption of a 1D model (Figure 4.34b). The suggested 1D local structure model that was used for the PORT area is presented in Table 4.11.

Table 4.9 Properties (number of layers, seismic velocities) regarding the subsurface layers according to the results of the geophysical methods.

Layers	Thickness (m)	VP (m/s)	VS (m/s)
1	8	450-650	100-200
2	16	1500-2500	150-300
3	≥10	1500-2500	250

HVSR analysis of the ambient noise recordings was conducted individually at all temporary station positions of the ambient noise array to verify the 1D subsurface structure for the investigation area. As shown in Figure 4.35b and 4.35c the $f_0 \approx 1$Hz value of all computed HVSR curves is consistent, indicating a horizontally layered structure. The high frequency part of the HVSR curve (5Hz – 20Hz) exhibits very low amplitude, almost flat, that may correspond to a thin high velocity layer, possibly due to hard anthropogenic infill or cement as shown in the preliminary testing of HVSR inversion (see Section 4.1.6, Inversion of HVSR for 1D VS profile).

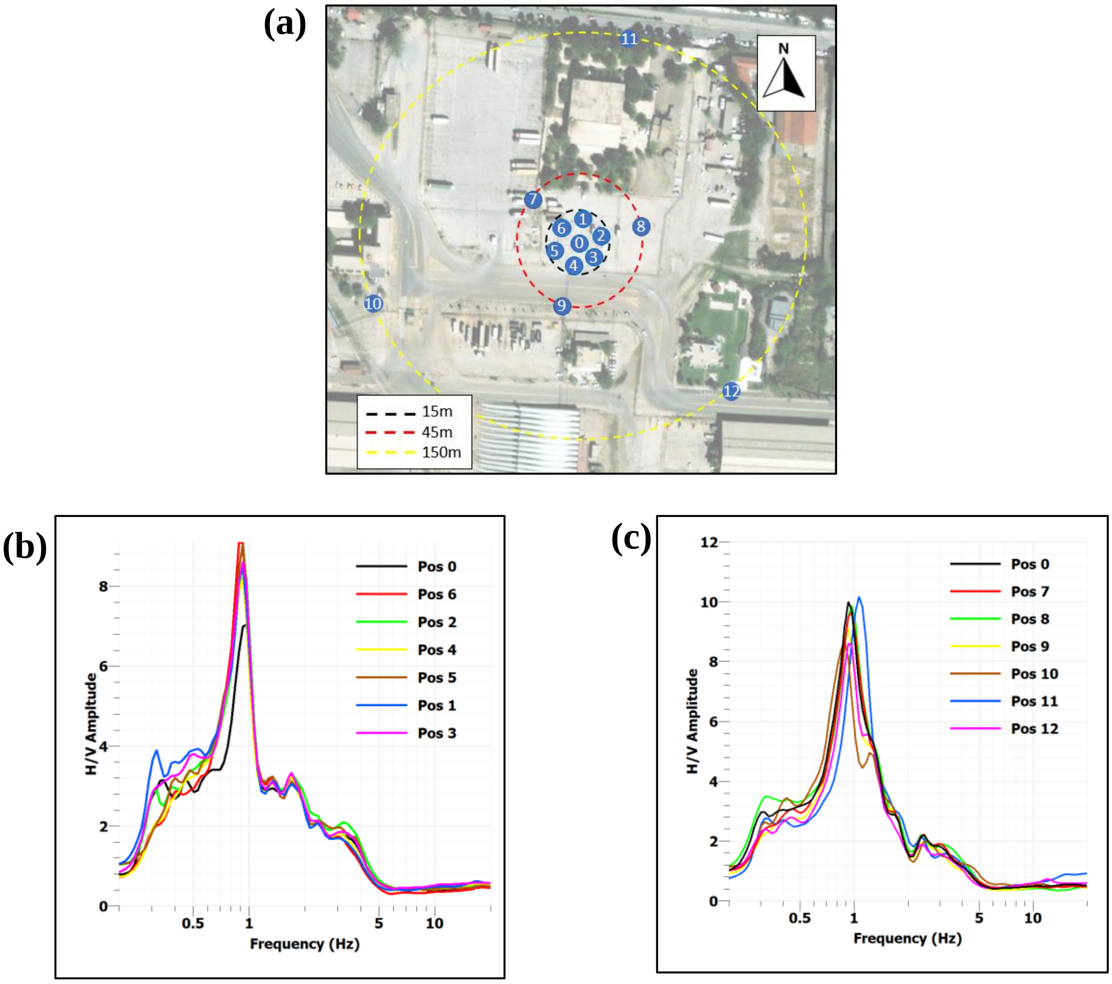

Figure 4.35 (a) Positions of the temporary seismometers. (b) HVSR computed at positions 0-6 and (b) HVSR computed at positions 7-12 of the ambient noise array at PORT site.

Analyzing the shape of the HVSR curve and given a mean Vs=310m/s at least for 80m depth from downhole result, the fundamental frequency peak at ~1Hz suggests an interface at a minimum 77m according to Equation (12). This information along with the 1D structure model retrieved by the geophysical methods was used in the inversion of the dispersion curve of the ambient noise array and the HVSR curve. The initial model for the HVSR inversion is presented in Table 4.12 and the results in Figure 4.36. Also, a surficial layer with broad V_S interval is added because of the low amplitude – high frequency part that was described above.

Table 4.10 HVSR inversion initial model for PORT accelerometer station site.

Layers	Thickness (m)	VP (m/s)	VS (m/s)
1	1-5	400-6000	200-3400
2	5-10	400-6000	150-300
3	10-20	400-6000	200-350
4	10-50	400-6000	350-750
5	10-50	400-6000	700-850
6 (HS)	-	400-6000	1500-2500

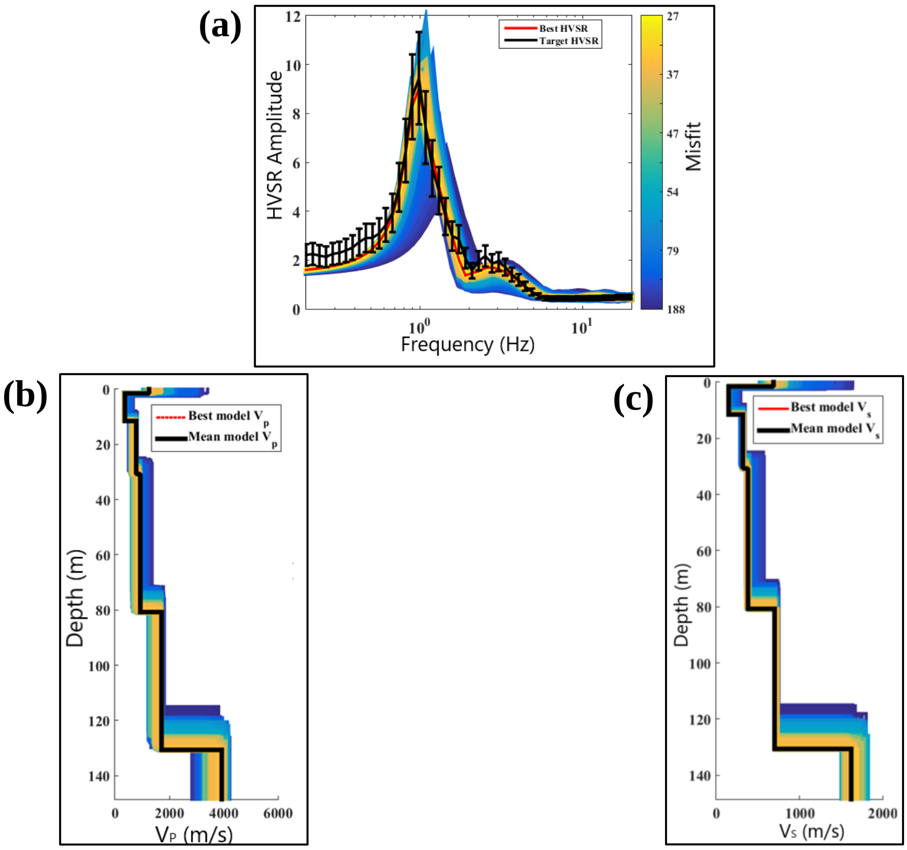

Figure 4.36 Inversion of the HVSR curve (position 8 at Figure 4.35c) at the PORT accelerometer station. site. Black line and black error bars in (a) represent the experimental average HVSR curve ±1sd. The colored curves in (a) show the forward calculations for the corresponding velocity models shown in (b) and (c). Red lines show the best fitting model for V_P, V_S, (b and c) and the corresponding theoretical HVSR (a).

The initial model that was used for the ambient noise dispersion curve is presented at Table 4.13. The dispersion curve inversion results are presented in Figure 4.37.

Table 4.11 Initial model for the dispersion curve inversion for PORT1 accelerometer station site.

Layers	Thickness (m)	VP (m/s)	VS (m/s)
1	5-10	200-5000	150-300
2	10-20	200-5000	200-350
3	10-50	200-5000	350-750
4	10-50	200-5000	350-3500
5	10-80	200-5000	350-3500
6 (HS)	-	200-5000	1500-3500

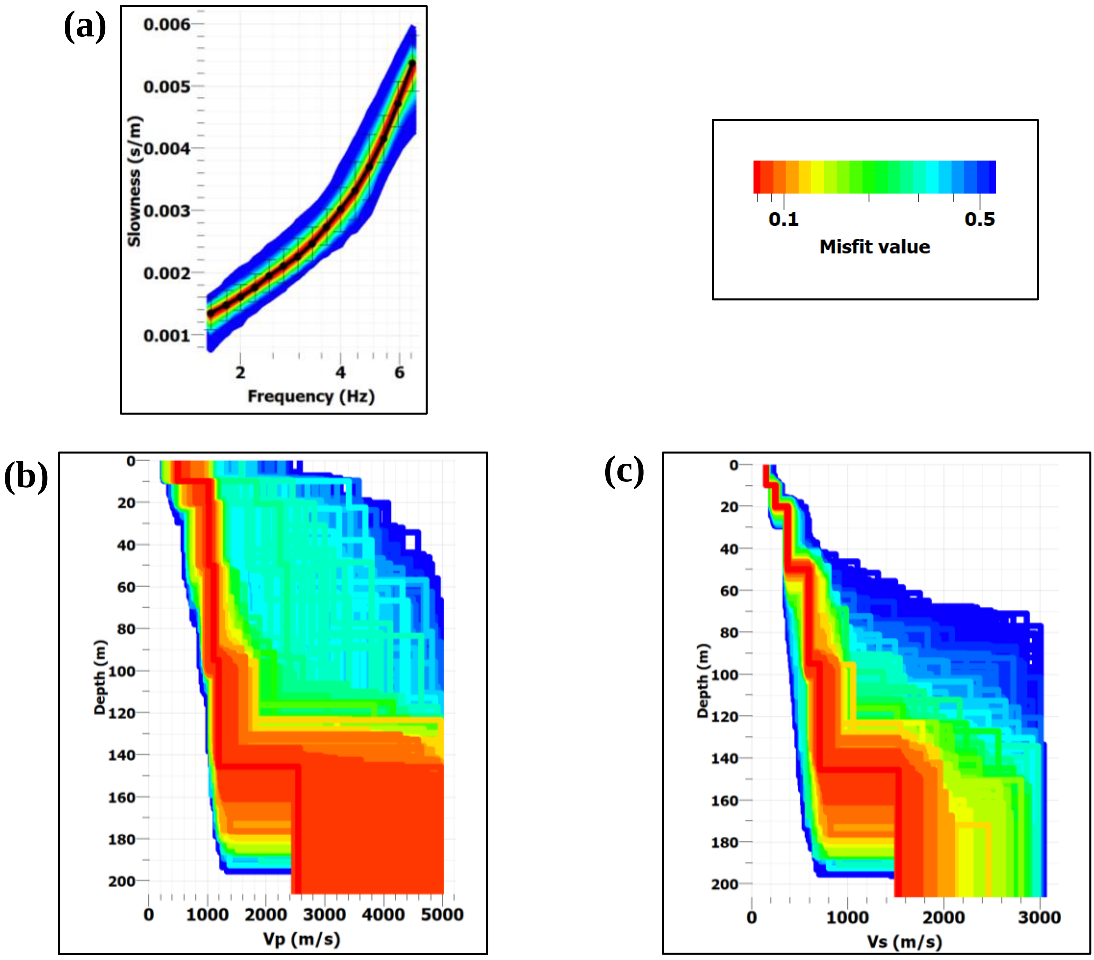

Figure 4.37 Ambient noise array dispersion curve inversion at the PORT accelerometer station site. (a) Forward modeling of the observed dispersion curve. (b) V_P and (c) V_S profiles.

The final structure model that resulted from the HVSR curve inversion (Table 4.14) was used as the theoretical model for the numerical simulation of ambient noise. Figure 4.38 shows the HVSR curves for the measured ambient noise (black curve), the synthetic ambient noise (red curve) and the earthquake motion recordings (blue curve).

Table 4.12 Final structure model that resulted from the HVSR curve inversion at PORT accelerometer station site.

Layers	Thickness (m)	VP (m/s)	VS (m/s)	QP	QS
1	1.5	1255	690	125	69
2	10	367	150	37	15
3	19	781	320	78	32
4	50	932	383	93	38
5	50	1715	701	171	70
6 (HS)	-	3931	1623	393	162

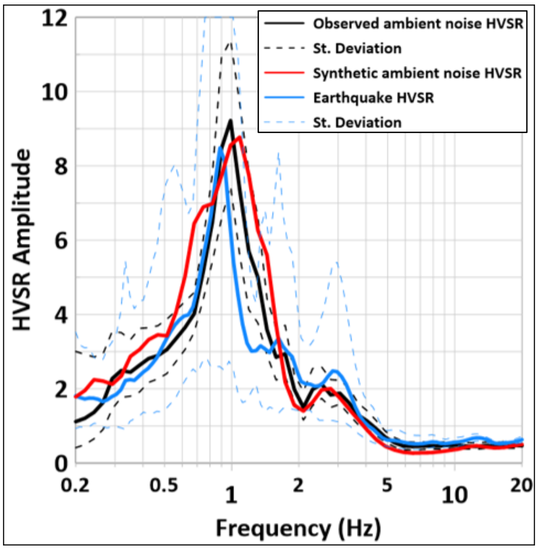

Figure 4.38 The ambient noise HVSR curve (position 8 at Figure 4.35c) (black curve), earthquake HVSR curve (blue curve) and the synthetic ambient noise HVSR curve (red curve). The synthetic ambient noise HVSR has been computed based on the theoretical structure of Table 4.17.

It is noteworthy that the thin high velocity layer that was related to frequencies f ≥5Hz of the HVSR, is not observed in the dispersion curve of the ambient noise array through velocity inversion. A possible explanation is that due to the large array aperture and thus larger recordable wavelength, the array method is unable to detect such thin layer in contrast with the HVSR, being a point measurement.

As already observed, the ambient noise HVSR curve exhibits a maximum at the f_0=1Hz which suggests a deep interface with high velocity contrast formations. This assumption has been validated by the dispersion and HVSR curves inversions. This high contrast is also verified by the numerical simulation of ambient noise, because the synthetic HVSR curve exhibits approximately equal f_0 value and a similar shape in general. Evidently, the earthquake HVSR curve (blue line in Figure 4.38) is in excellent agreement with the observed ambient noise HVSR exhibiting the same f_0 value (=1Hz) as well as the minor peak at around 3Hz. It is notable, that both earthquake and synthetic ambient noise HVSR curves are in excellent agreement with the experimental HVSR curve at the very low amplitude high frequency part (≥5Hz), due to the introduction of a high velocity surficial thin layer. Additionally, the V_{SZ} profile derived from the HVSR inversion (Figure 4.36c) is in good comparison with the V_{SZ} derived from the ambient noise array (Figure 4.37c). Therefore, the velocity model derived from the HVSR inversion is reliable for the V_{S30} parameter estimation and is in very good agreement with the existing downhole measurement (Figure 3.8). Based on the Equation (1) and from the final model of Table 4.12, the V_{S30} is estimated for each one of the available methods and are presented in Table 4.13. The V_{S30} values from all methods classify the PORT site as Ground Type C (Eurocode-8).

Table 4.13 Computation of the V_{S30} parameter from all the available methods at the PORT accelerometer station site.

Method	**V_{S30} (m/s)**
HVSR inversion	233
Ambient noise array	223
Downhole (existing)	208

4.2.1 STL1 accelerometer station site – Site 2

The ERT method at STL1 site (Figure 4.39a) has revealed the resistivity distribution of the subsurface, showing a relatively low resistivity surficial layer with a ranging depth of 5m – 10m. This layer corresponds to the Holocene sediments that cover the investigation area. At the depth of 10m – 25m a more resistive zone (>70 Ωm) possibly corresponds to coarse-grained materials. A significant decrease of the resistivity below the depth of 25m is possibly related to increase of clay content (10-15 Ωm) in the sediments. The 1D VS profile derived from the MASW method shows a gradual increase of the S-wave velocities with depth (Figure 4.39b). This velocity increase is stabilized at the depth of 20-25m possibly due to the transition to the more cohesive clay formation. This result is partly verified also by the seismic refraction results (Figure 4.39c). Comparing the results of the ERT and MASW methods, it is obvious that both methods suggest a similar 1D structure that can be distinguished in 3 surficial layers as presented in Table 4.14.

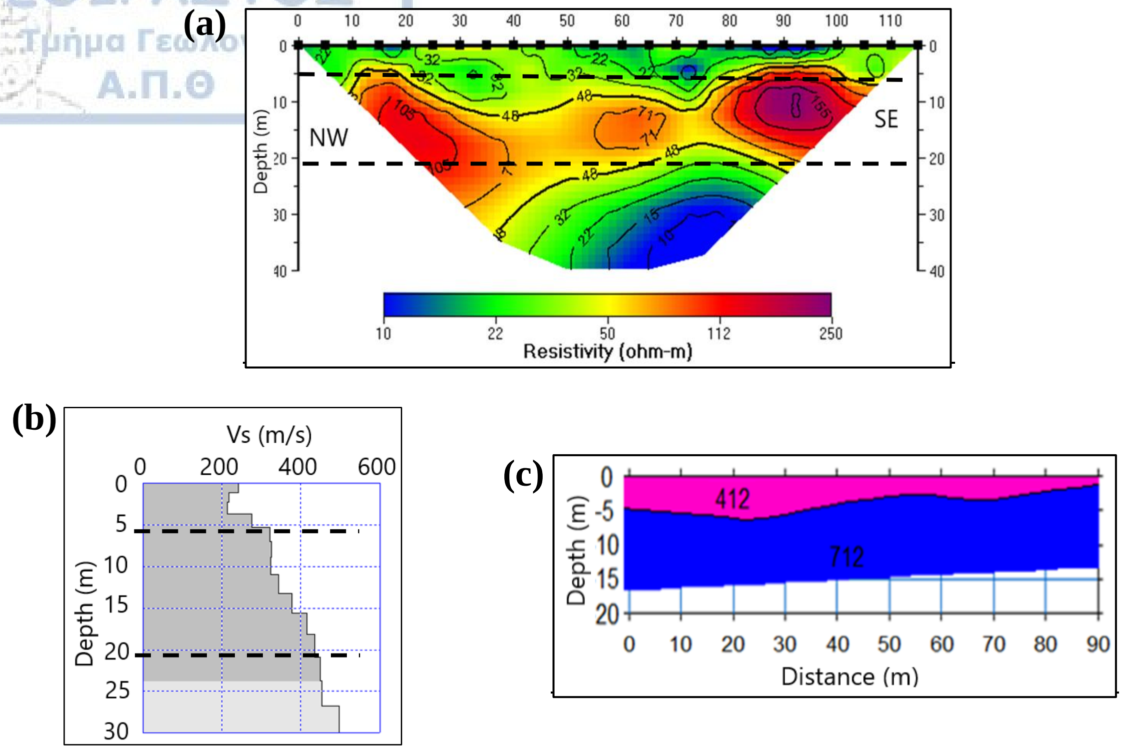

Figure 4.39 Geophysical investigation at the STL1 accelerometer station site. (a) The ERT method result. (b) The 1D V_S profile, generated by the MASW method. (c) P-wave travel-time modeling (seismic refraction).

Table 4.14 Properties regarding the subsurface layers based on the geophysical investigation at STL1 accelerometer station site.

Layers	Thickness (m)	V_P (m/s)	V_S (m/s)
1	5	300-500	200-400
2	15	400-1000	300-500
3	≥20	800-5000	400-3400

The HVSR curves computed at the positions of the ambient noise array are shown in Figures 4.40b and 4.40c. Due to limited available space the seismometers for the smaller circle were placed on grass (positions 0 – 6) introducing artificial peaks below 1Hz. The HVSR curves at positions 7, 8, 10 and 11 (Figure 4.40c) exhibited a clear peak around 3Hz that can also be observed at the rest of the curves as well, regardless of the perturbed results below 1Hz. However, the HVSR computed position 12 also exhibits a possible artificial peak at 0.4Hz. Therefore, the fundamental frequency f_0 = 3Hz is considered reliable and is also observed in the earthquake HVSR as well (Figure 4.43). As mentioned above, most of the HVSR curves included perturbed results for frequency lower than 1Hz (positions 0 – 6). Therefore, the only HVSR curves eligible for inversion were the ones computed at positions 7, 8, 10 and 11. The one closer to the permanently installed accelerometer (position 11) was preferred. Analyzing the HVSR curve shape useful information regarding the relatively shallow interface associated with the $f_0 \approx 3$Hz peak is extracted. According to the Equation (12) and given an average V_S of the surficial sedimentary formations of 350m/s, the depth of the interface related to the f_0 is roughly calculated at 30m. The initial model for the HVSR inversion is shown in Table 4.15. The inversion results are show in Figure 4.41.

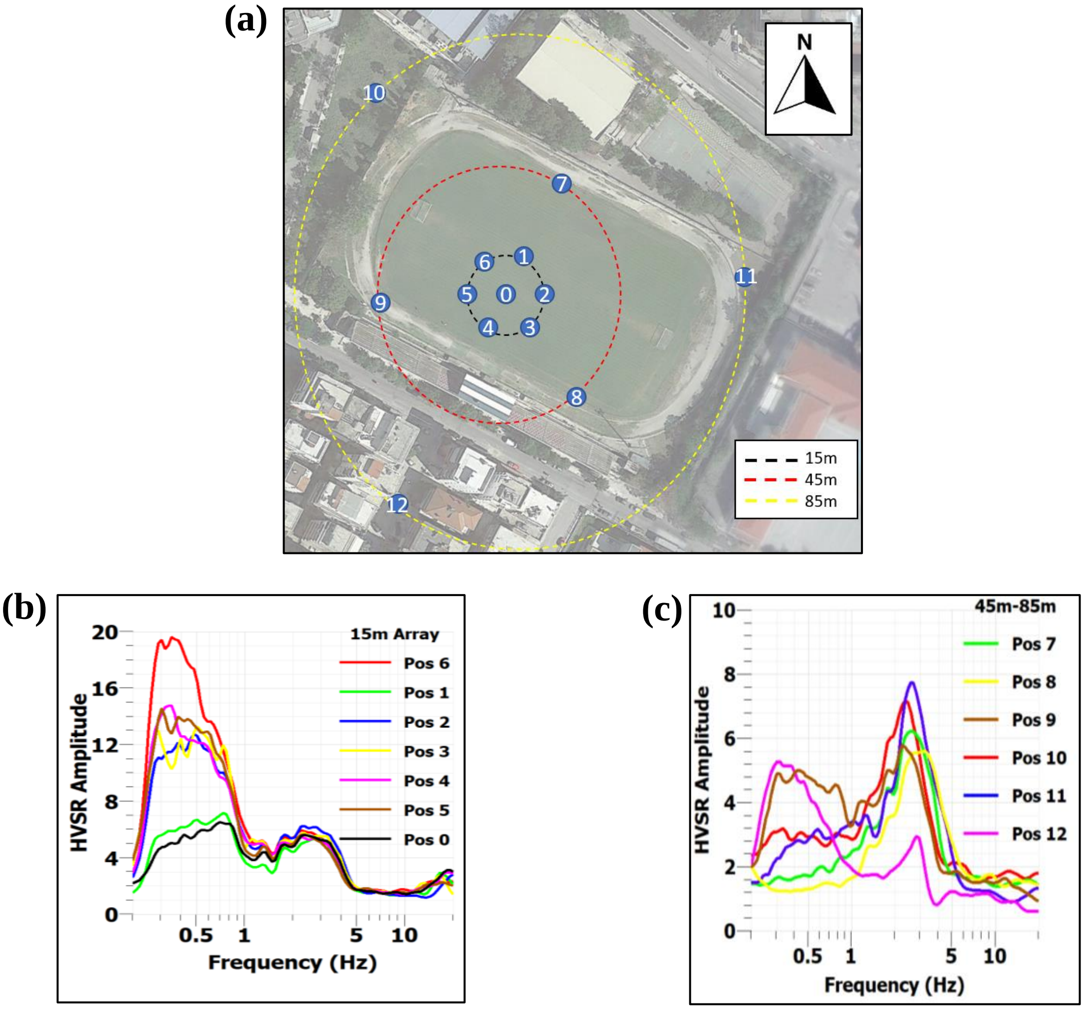

Figure 4.40 HVSR computed at all stations of the ambient noise array at **STL1** site. The consistency between the f_0 values is an indication of the 1D subsurface structure at the investigation area. The perturbed results below 1Hz are discussed in the document.

Table 4.15 Initial model for the inversion of the HVSR curve at STL1 accelerometer station site.

Layers	Thickness (m)	V_P (m/s)	V_S (m/s)
1	1-12	400-500	200-400
2	10-20	500-1000	300-500
3 (HS)	-	1000-5000	500-3400

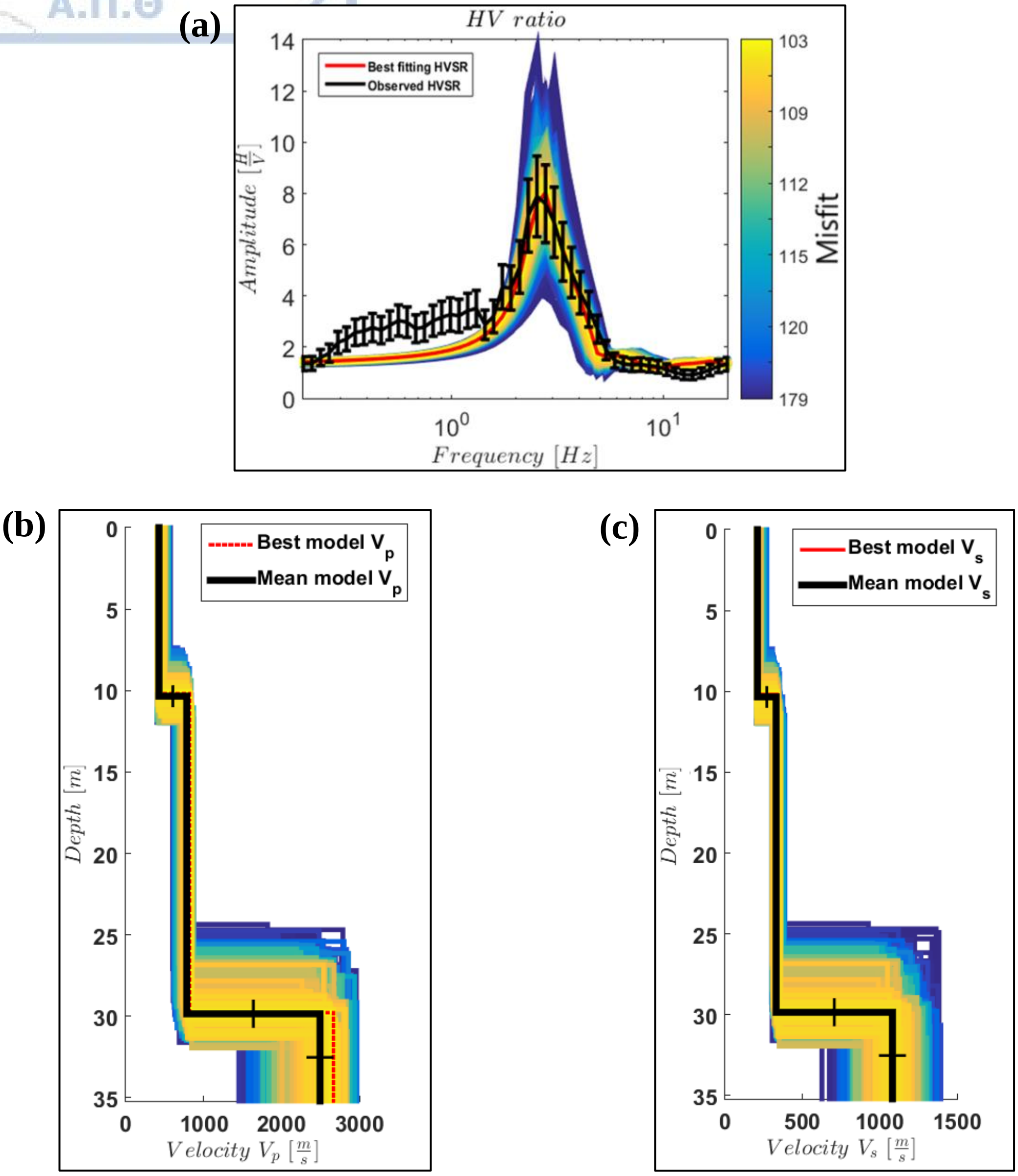

Figure 4.41 Inversion of the HVSR curve (position 11 at Figure 4.40c) for STL1 accelerometer station site. Black line with black error bars in (a) represent the experimental average HVSR curve $\pm$1sd. The colored curves in (a) show the forward calculations for the corresponding velocity models shown in (b) and (c). Red lines show the best fitting model for V_P, V_S, (b and c) and the corresponding theoretical HVSR (a).

Inversion of the ambient noise array dispersion curve was conducted using a slightly different initial model than the HVSR inversion. The difference is the addition of a third layer due to the deeper investigation depth based on the experimental dispersion curve (approximately 120m) (Table 4.16). The results of the ambient noise array dispersion curve are presented in Figure 4.42.

Table 4.16 Initial model for the dispersion curve inversion for STL1 accelerometer station site.

Layers	Thickness (m)	V_P (m/s)	V_S (m/s)
1	1-12	300-500	200-400
2	10-20	400-1000	400-500
3	20-100	800-5000	400-3400
4 (HS)	-	3000-5000	400-3400

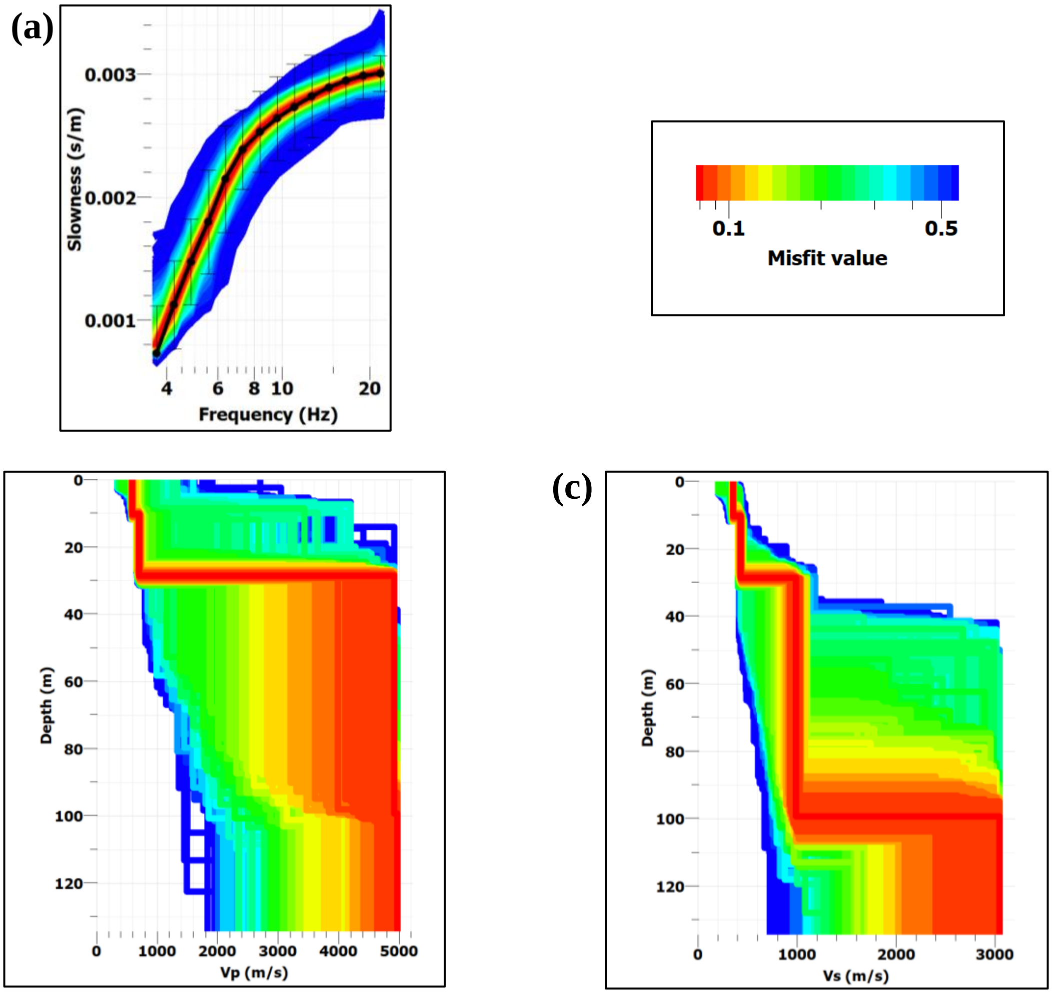

Figure 4.42 Ambient noise array dispersion curve inversion for STL1 accelerometer station site. (a) Forward modeling of the observed dispersion curve. (b) V_P and (c) V_S profiles.

The final structure model that resulted from the HVSR curve inversion (Table 4.18) was used as the theoretical model for the numerical simulation of ambient noise. The HVSR analysis of the synthetic recordings were compared with the HVSR analysis of observed ambient noise and earthquake recordings (Figure 4.43).

Table 4.17 The final structure model that resulted from the HVSR curve inversion at STL1 accelerometer station site.

Layers	Thickness (m)	V_P (m/s)	V_S (m/s)	Q_P	Q_S
1	10	418	200	42	20
2	19	821	335	82	34
3	-	2668	1089	267	109

As already noted, the ambient noise HVSR curve exhibits a maximum at the f_0=2.5Hz which correlates with a relatively shallow interface between high velocity contrast formations. This assumption has been validated by the dispersion and HVSR curves inversions. This high contrast is also recognized by the numerical simulation of ambient noise, because the synthetic HVSR curve exhibits approximately equal f_0 value and a similar shape in general.

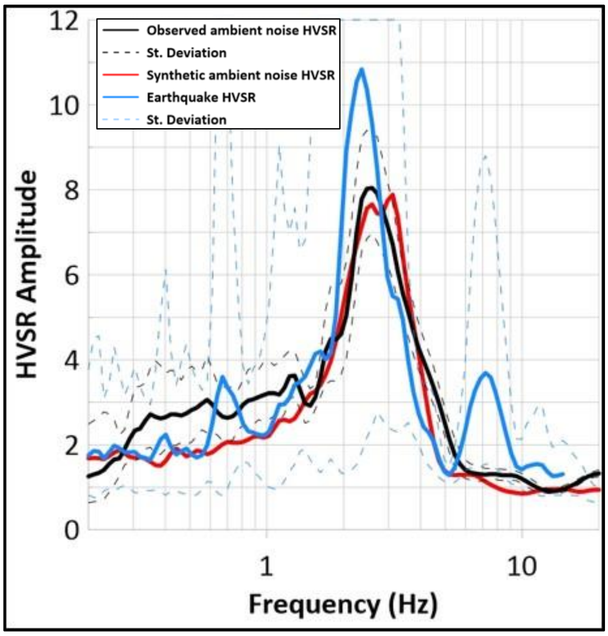

Figure 4.43 The ambient noise HVSR curve (position 11 at Figure 4.40c) (black curve), earthquake HVSR curve (blue curve) and the synthetic ambient noise HVSR curve (red curve). The synthetic ambient noise HVSR has been computed based on the theoretical structure of Table 4.17.

Evidently, the earthquake motion HVSR curve (blue line in Figure 4.43) is in good agreement with the measured ambient noise HVSR exhibiting the same $f_0 \cong 2.5$Hz. The earthquake HVSR exhibits additional peaks at 0.7Hz and 7Hz that are not observed in ambient noise HVSR. These are possibly related to subsurface structures with relatively low V_S contrast and are only observed with earthquake HVSR due to the higher energy carried by earthquakes. The synthetic HVSR curve is also in satisfactory agreement with the HVSR curves from the measured ambient noise, meaning that the HVSR inversion provided a reliable velocity model. Additionally, the V_{SZ} profile from the HVSR inversion (Figure 4.41c) overestimated the V_S values in comparison with the ambient noise array results (Figure 4.42c). The V_{S30} parameter was calculated from both methods and the results are shown in Table 4.18. Therefore, the results range at the threshold of C-B classes and the site is classified as Ground Type C (Eurocode 8).

Table 4.18 Computation of the V_{S30} parameter from all the available methods at the STL1 accelerometer station site.

Method	**V_{S30} (m/s)**
HVSR inversion	274
Ambient noise array	408

4.2.3 KLR1 accelerometer station – Site 3

The electrical resistivity distribution of the subsurface (Figure 4.44a) revealed a relatively less conductive top layer (20Ωm – 40Ωm) consisting of coarse-grained materials down to the depth of 5m. Deeper, a slight decrease in the resistivity values is probably due to the existence of clay. At the depth of ~20m the resistivity values increase probably because of greater sand proportion.

The 1D V_S profile that was retrieved with the MASW method shows a gradual velocity increase below 5m and down to the depth of 20m (Figure 4.44b). Then, velocity appears stable probably related to the transition to a homogenously compacted formation. The V_P model suggests that a surficial layer of approximately 8m thickness exists over a higher velocity layer. The high VP value of the second layer might be explained by the watertable depth at 8m (Figure 3.19). Therefore, both the ERT and seismic methods suggest a horizontal three-layer structure model, presented in Table 4.19.

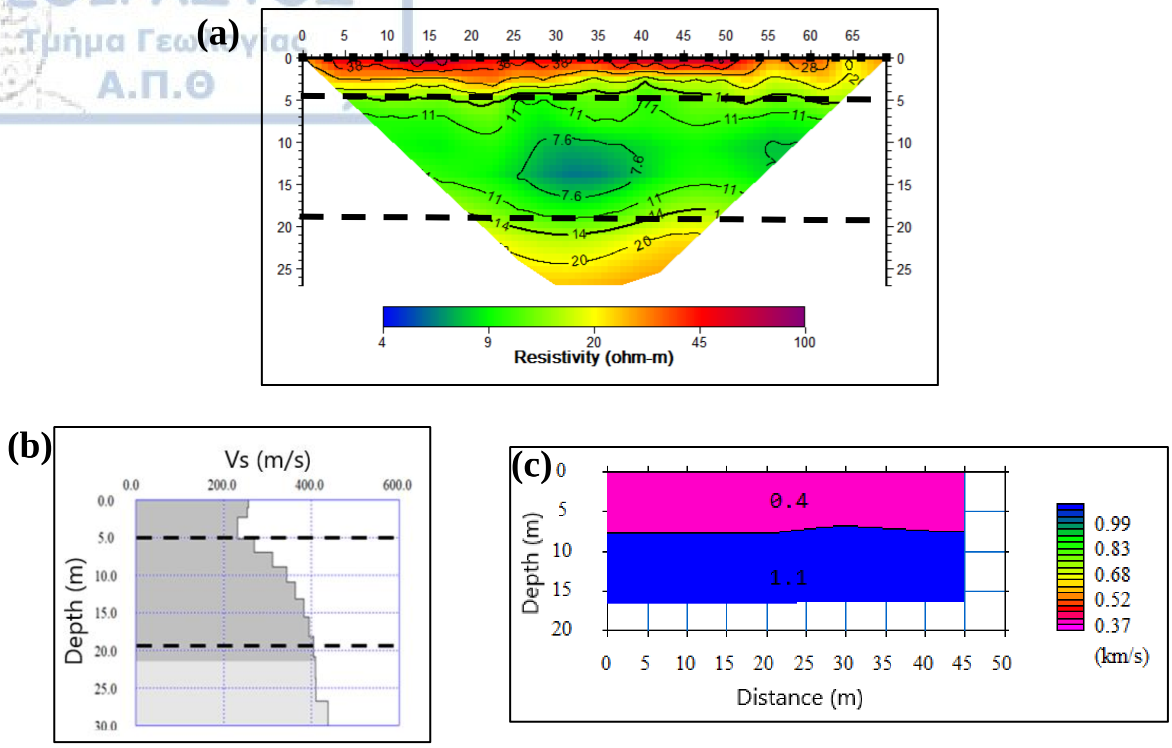

Figure 4.44 Geophysical investigation at the KLR1 accelerometer station site. (a) The ERT method result. (b) The 1D V_S profile, generated by the MASW method. (c) P-wave travel-time modeling (seismic refraction).

Table 4.19 Properties regarding the subsurface layers according to the geophysical investigation at ITS1 site, including the number of layers, their approximate thicknesses, and the velocity ranges of the seismic waves.

Layers	**Thickness (m)**	**V_P (m/s)**	**V_S (m/s)**
1	5	500-1000	200-300
2	15	1500-5000	250-500
3	≥10	1500-5000	≥400

The computed HVSR at all temporary seismometer positions is shown in Figure 4.45. The HVSR results are indicative of the transient signals polluted data due to the high anthropogenic noise during the field measurements. This high-level noise introduced an underestimation of the HVSR amplitudes. Despite the highly perturbed results, the HVSR curves exhibit amplification, approximately at the fundamental frequency f_0 = 0.3Hz, that is sharper at the computation positions 1, 6, 7, 9 (Figures 4.45b and 4.45c). Therefore, the homogeneous f_0 value is an indication of the 1D structure of the investigation area. The very low amplitudes (<1) at the high frequency part of the HVSR curves (≥5Hz) is possibly due to a thin, high velocity layer at the surface, that can be attributed to the pavement and/or anthropogenic. The HVSR computed at position 1 was selected for inversion, because it exhibited the sharpest f_0

indication and a smooth curve in general. The shape of the HVSR curve exhibits a clear peak at f_0 = 0.3Hz which is most probably related to a very deep interface, possibly with the geological bedrock (schist – gneiss). With increasing frequency, the curve becomes generally flat which is indicative of an overlain thick package of sediments. Given an average S-wave velocity of 340m/s (MASW results), using the Equation (12) and for f_0 = 0.3Hz, a rough estimation of the corresponding interface depth is approximately at 280m. Using this assumption, and the information derived from the application of the geophysical methods, a more general and deeper initial model for the HVSR inversion was used (Table 4.20). The results of the HVSR inversion are presented in Figure 4.46.

(a)

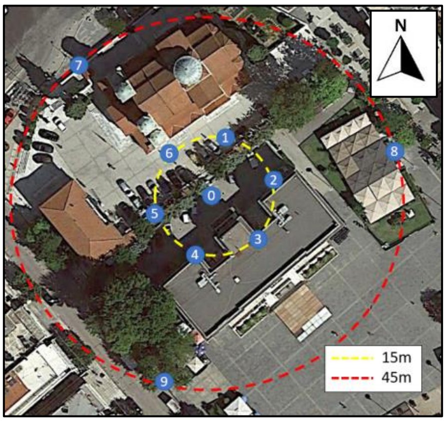

(b)

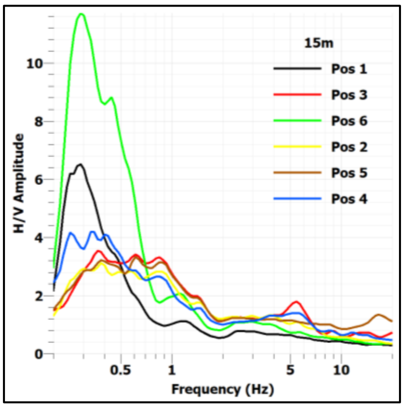

(c)

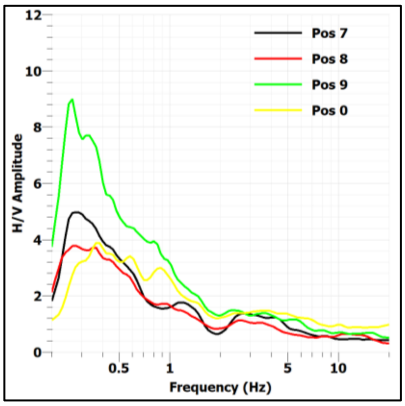

Figure 4.45 The HVSR was computed at all seismometer positions from the ambient noise array data at the KLR1 accelerometric site. The f_0=0.3Hz fundamental frequency value is sharper at positions 1, 3, 4, 7, 9 due to less noisy data.

Table 4.20 The initial model that was used in inversion of the HVSR curve.

Layers	Thickness (m)	V_P (m/s)	V_S (m/s)
1	1-5	400-5000	200-3500
2	1-5	400-5000	200-300
3	10-20	1500-5000	300-400
4	300-500	1500-5000	400-3400
5 (HS)	-	1500-5000	1000-3400

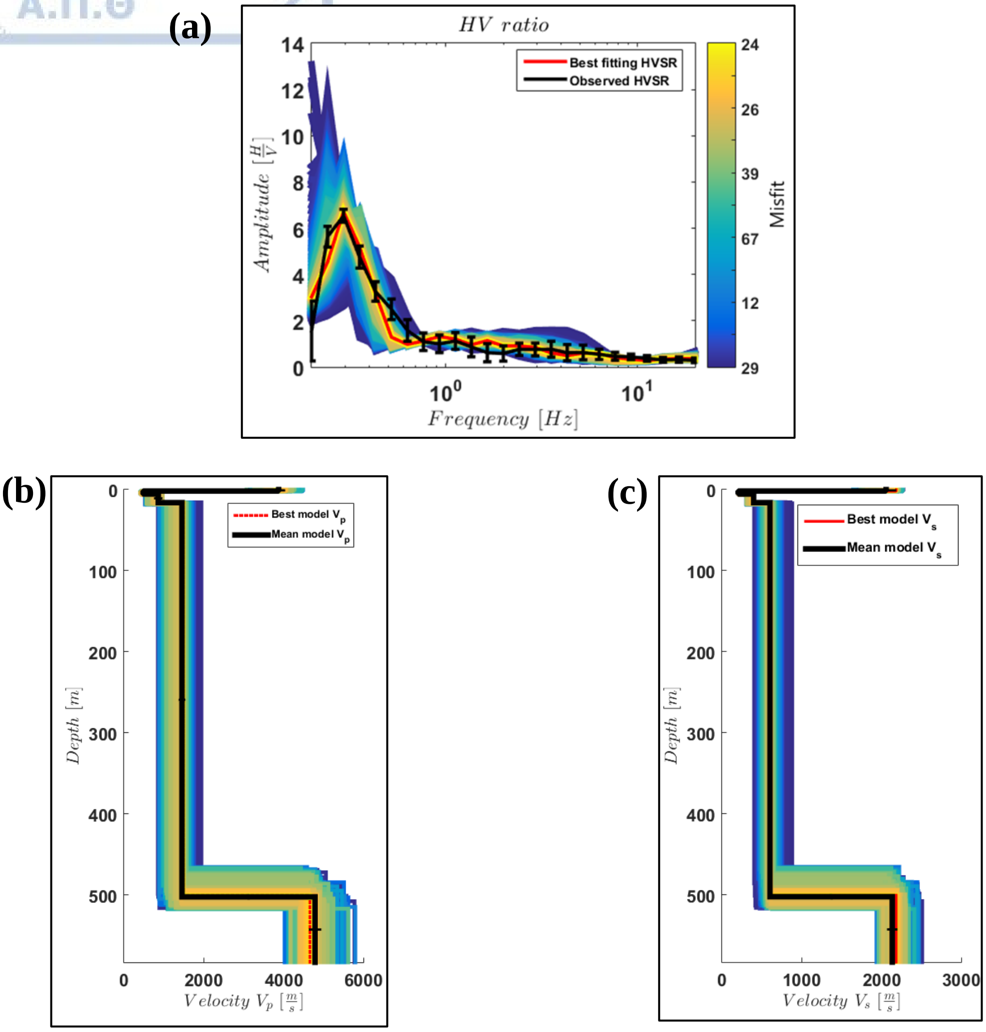

Figure 4.46 Inversion of the HVSR curve (position 1 at Figure 4.45b) for KLR1 accelerometer station site. Black line with black error bars in (a) represent the experimental average HVSR curve ±1sd. The colored curves in (a) show the forward calculations for the corresponding velocity models shown in (b) and (c). Red lines show the best fitting model for V_P, V_S, (b and c) and the corresponding theoretical HVSR (a).

The initial model for the dispersion curve inversion is presented at Table 4.21 and the inversion results at Figure 4.47.

Table 4.21 Initial model for the dispersion curve inversion for STL1 accelerometer station site.

Layers	Thickness (m)	V_P (m/s)	V_S (m/s)
1	1 – 10	200-700	100-250
2	5 - 30	1500-5000	200-400
3	20 – 60	1500-5000	300-600
4 (HS)	-	200-5000	500-1500

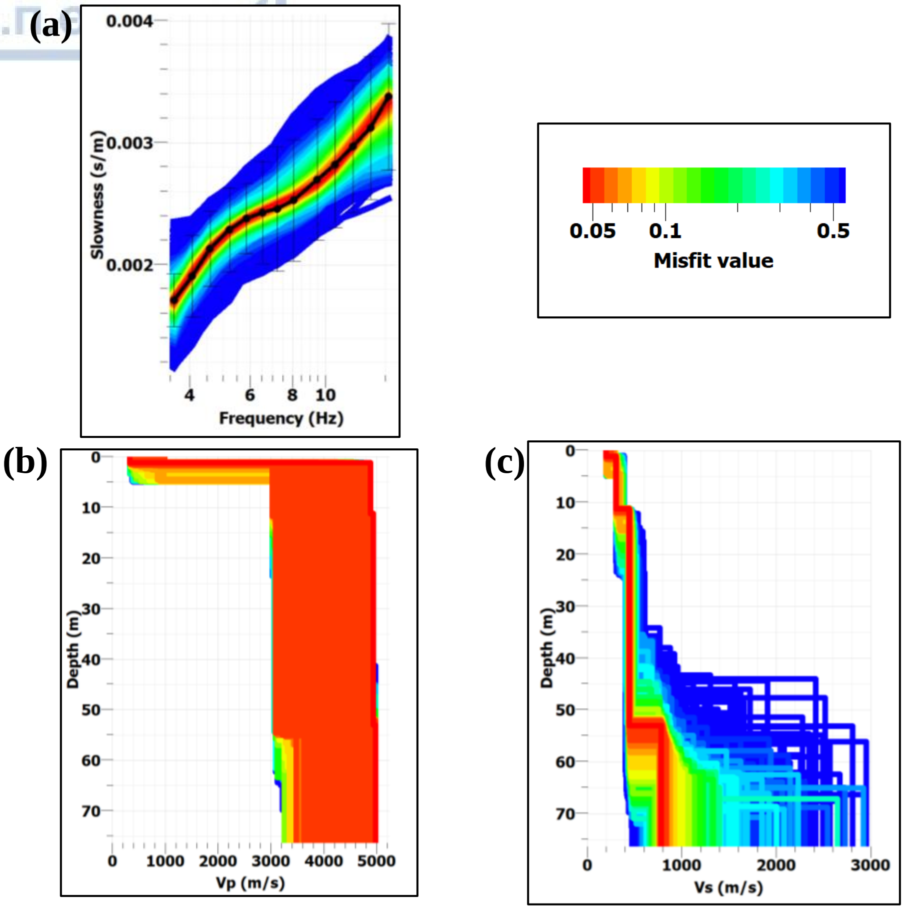

Figure 4.47 Ambient noise array dispersion curve inversion for KLR1 accelerometer station site. (a) Forward modeling of the observed dispersion curve. (b) V_P and (c) V_S profiles.

The final structure model that resulted from the HVSR curve inversion (Table 4.22) was used as the theoretical model for the numerical simulation of ambient noise. The HVSR of the synthetic recordings were compared with the HVSR of observed ambient noise and (Figure 4.48).

Table 4.22 The final structure model that resulted from the HVSR curve inversion at STL1 accelerometer station site.

Layers	Thickness (m)	VP (m/s)	VS (m/s)	QP	QS
1	2	3804	2186.3	380	218.6
2	3.9	487.1	200	48.7	20
3	1.1	878.6	400	87.9	40
4	485	1490.3	608	149	61
5 (HS)	-	4659.9	2186.6	466	218.7

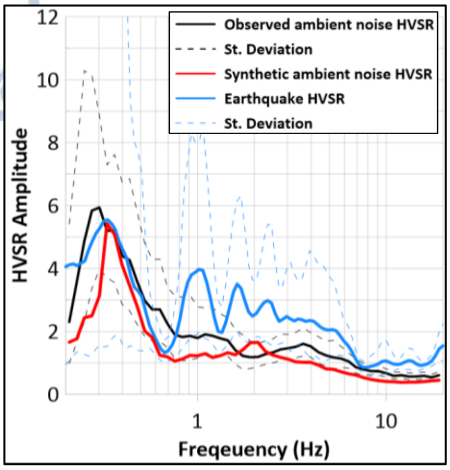

Figure 4.48 The ambient noise HVSR curve (position 1 at Figure 4.45b) (black curve), earthquake HVSR curve (blue curve) and the synthetic ambient noise HVSR curve (red curve). The synthetic ambient noise HVSR has been computed based on the theoretical structure of Table 4.22.

As already has been observed, the ambient noise HVSR measurements at the KLR1 site exhibit a fundamental frequency approximately at $f_0 \cong 0.3$ Hz which relates with a very deep interface between formations with high velocity contrast. This assumption has not been validated by the dispersion curve inversion due to the limited maximum array aperture, but it is validated by the HVSR curve inversion. This high contrast is also recognized by the synthetic HVSR curve which exhibits approximately equal f_0 value and a similar shape. Hence, the synthetic HVSR curve is in satisfactory agreement with the observed HVSR curve as it also exhibits the $f_0 \cong 0.3$ Hz. The earthquake motion HVSR curve exhibits the same $f_0 \cong 0.3$ Hz but also exhibits additional higher mode peaks, excited by the earthquake ground motion with increasing frequency which are not evident in the ambient noise HVSR. The low amplitudes (<1) at the high frequency part of the earthquake motion HVSR (≥5Hz) are possibly attributed to the attenuation of the horizontal and/or the amplification of the vertical motion considering because a possible soil-structure interaction effect due to housing the accelerometer building. Although this assumption is observed at earthquake HVSR curves at every site in this research, it needs further investigation. In any case, for the purpose of this thesis, the satisfactory agreement of the synthetic and observed ambient noise HVSR curves, regarding the f_0 value, can satisfactorily validate the subsoil profile for this site.

The V_{SZ} profile derived from the HVSR inversion (Figure 4.46c) is overestimated compared to the ambient noise array results (Figure 4.47c) at least up to their common depth (80m) and the downhole measurement (Figure 3.19). The V_{S30} parameter was calculated from all available methods and the results are shown in Table 4.23. The results range at the threshold of C-B classes and the site is classified as Ground Type C (Eurocode 8).

Table 4.23 Computation of the V_{S30} parameter from all the available methods at the KLR1 accelerometer station site.

Method	V_{S30} (m/s)
HVSR inversion	437
Ambient noise array	373
Downhole (existing)	337

4.2.4 SEIS accelerometer station – Site 4

The SEIS accelerometer station is considered a reference site and is located on a thin layer of sandy gravel overlain the weathered bedrock formation as is revealed by the provided stratigraphic log from an existing borehole (Figure 3.24). The borehole revealed a thin surficial layer composed of sandy gravel and non-graded sediments down to the depth of 5m. The gneiss-schist formation is detected and considered as the weathered bedrock. Deeper the healthier gneiss formation is detected. The watertable at the time of the downhole measurement was detected at the depth of 8.5m.

The application of the ERT (Figure 4.49a) revealed two main features of the subsurface distribution of the electrical resistivity. The first one is related to the existence of resistive formations of approximately 3m thickness, near the surface, at the south-western part of the tomography (6m – 23m) that are attributed to sandy-gravel formation, while a decrease of the resistivity down to the depth of 10m is related to the weathered and/or intensely fractured gneiss or schist formation. The second feature is the observed decrease of resistivity at the northern part of the ERT (23m – 46m of the tomography) which can be attributed to a local increase in humidity. A possible interpretation might be the existence of a fault zone crossing the ERT line. Finally, the resistivity appears smaller for depths below 10m from the surface. The MASW method was conducted on the same survey line. Two source points were used at the center and the southern edge of the line (outshot). The resulting V_S profile reveals a surficial 5m layer and then a gradual and rapid V_S increase, thus a second layer is considered for the local 1D structure profile.

(a)
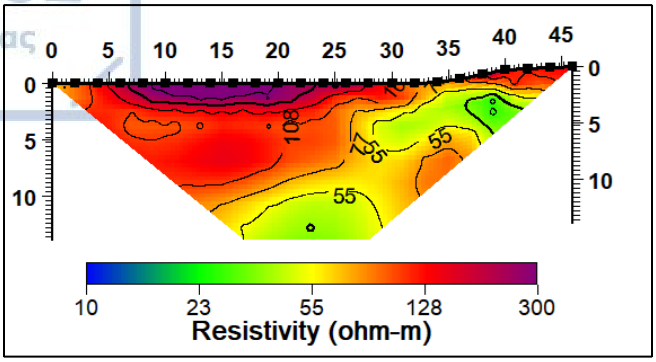

(b)
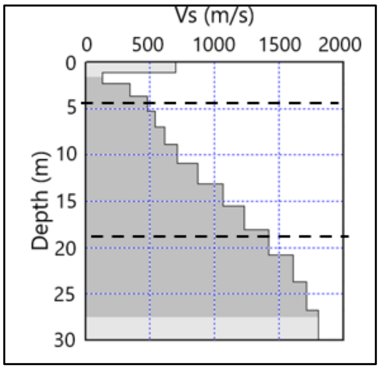

(c)
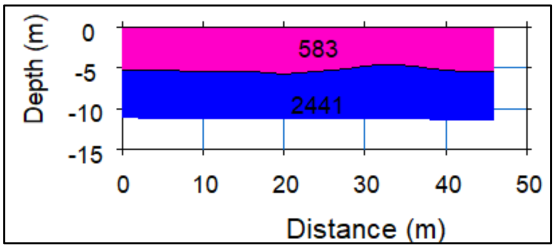

Figure 4.49 Geophysical investigation at the SEIS accelerometer station site. (a) The ERT method result. (b) The 1D V_S profile, generated by the MASW method. (c) P-wave velocity model generated by the seismic refraction.

Table 4.24 Properties regarding the subsurface layers according to the geophysical investigation at SEIS site, including the number of layers, their approximate thicknesses, and the velocity ranges of the seismic waves.

Layers	Thickness (m)	V_P (m/s)	V_S (m/s)
1	5	400 – 1500	150 – 800
2	15	800 – 3000	400 – 1500
3 (HS)	≥10	800 – 3000	≥1500

The HVSR curves computed at all temporary seismometer positions are shown in Figures 4.50b and 4.50c. All HVSR curves are generally flat and 11 out of the 13 exhibit a clear peak at approximately 15-20Hz. The differentiated HVSR amplitudes of the curves are possibly due to ground coupling issues (grass surface) and for this reason, the part 0.2-0.8Hz was omitted. The peak at high frequency(f>10Hz) is undoubtedly related to a very shallow interface with high velocity contrast. This interface possibly corresponds to the boundary between the surface sediments and the underlain weathered schist-gneiss formation.

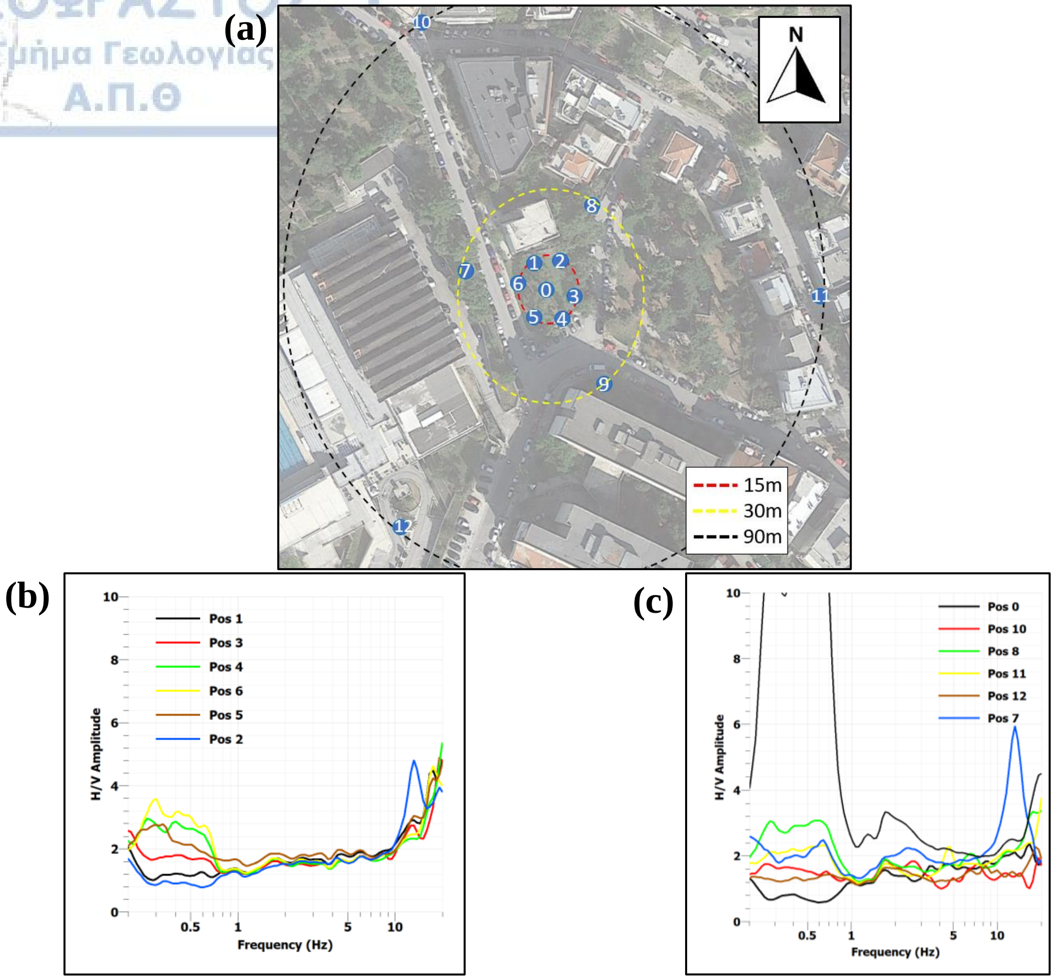

Figure 4.50 HVSR computed at the SEIS accelerometer station site exhibiting a generally flat curve with a clear peak at approximately 20Hz.

To further investigate the origins of the peak at 20Hz, two ambient noise measurements were conducted simultaneously for 1 hour, with one seismometer placed at the basement of the building near the permanently installed accelerometer and the second seismometer placed at the center of the ambient noise array. The HVSR analysis of the measurement conducted at the basement of the building (Figure 4.51a), exhibits a relatively flat HVSR curve possibly because the upper sedimentary formation was removed due to the excavation for the construction of the building and thus no contrast is observed. The HVSR analysis of the measurement conducted at the center of the ambient noise array (Figure 4.51b) exhibits a flat curve up to approximately 10Hz, where the HVSR amplitude starts increasing with frequency. This peak is related to a very shallow interface between the geological bedrock formation and a thin package of overlain sediments.

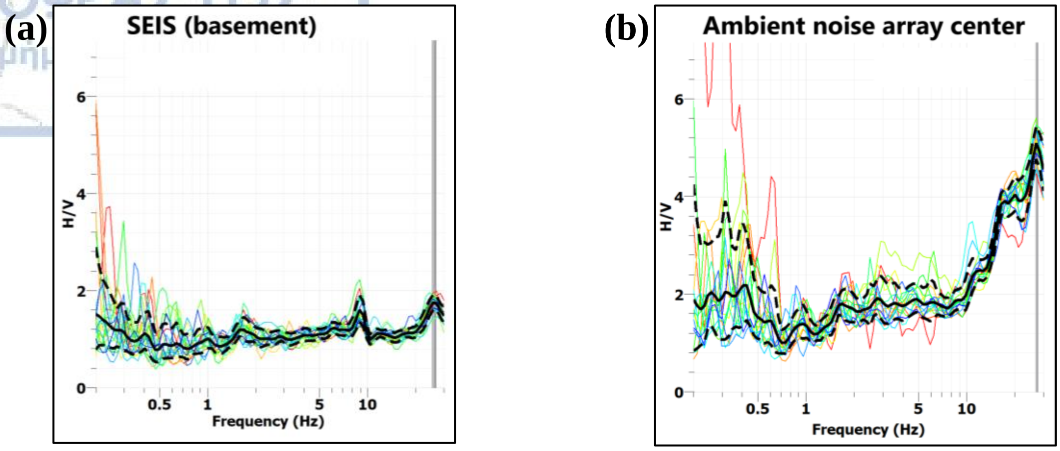

Figure 4.51 HVSR analysis of the two simultaneous ambient noise measurements conducted (a) at the basement of the seismological station on the bedrock and (b) at the center of the ambient noise array.

The HVSR computed at position 4 (Figure 4.50) was selected for inversion as it exhibited the clearest peak at approximately $f_0 \cong 20$Hz. Given the Equation (12) and an average V_S=400m/s for the first layer, the depth of interface related to the f_0 is calculated at approximately 5m. Using this assumption, and the information derived from the application of the geophysical methods, a more elaborated initial model was used for the HVSR inversion (Table 4.25). The HVSR inversion results are shown in Figure 4.52.

Table 4.25 Initial model for the inversion of the HVSR curve at SEIS accelerometer station site.

Layers	**Thickness (m)**	**V_P (m/s)**	**V_S (m/s)**
1	1-5	300-6000	150-800
2	10-30	1000-6000	500-1500
3 (HS)	-	3000-6000	1500-3500

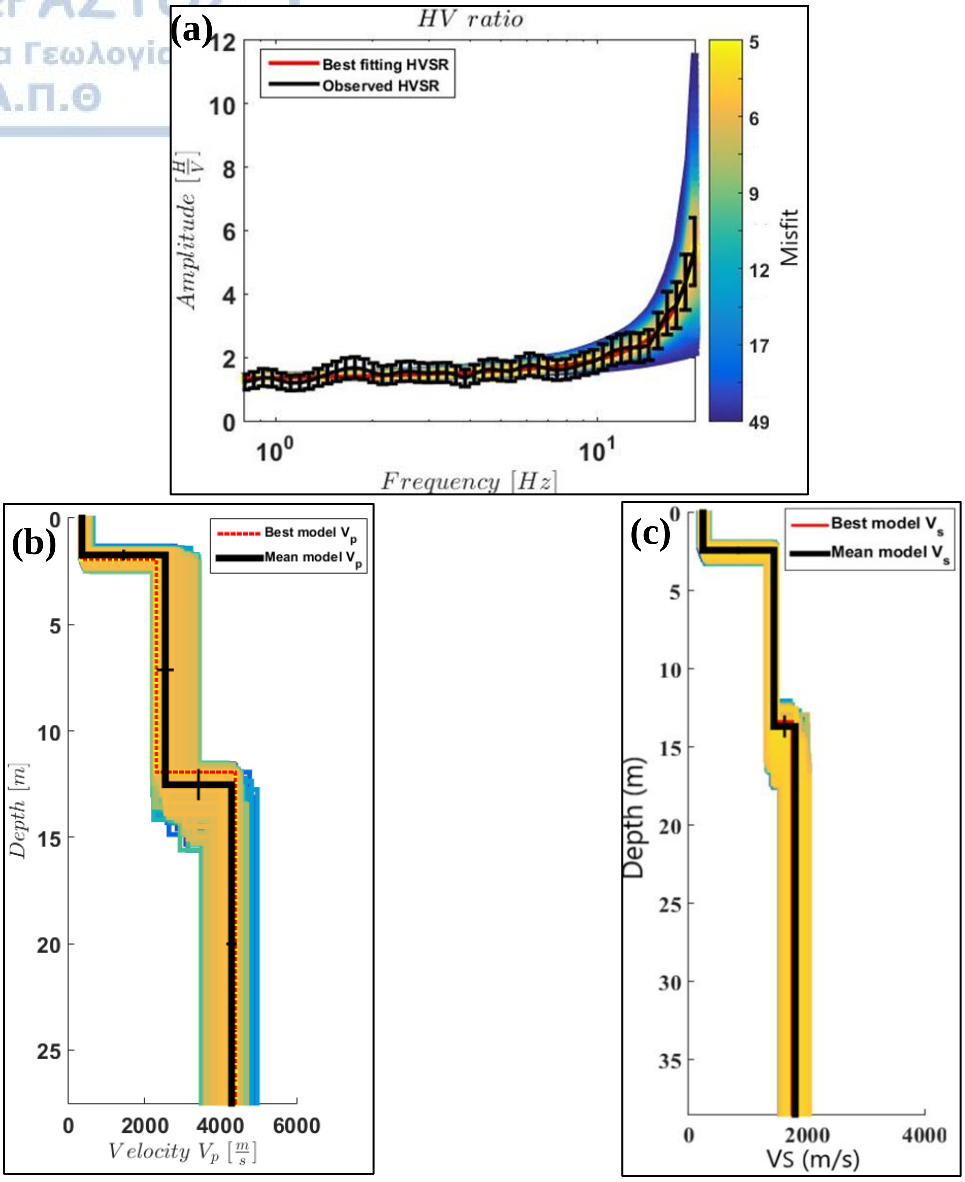

Figure 4.52 Inversion of the HVSR curve (position 4 at Figure 4.50b) for SEIS site. Black line and black error bars in (a) represent the experimental average HVSR curve ±1sd. The colored curves in (a) show the forward calculations for the corresponding velocity models shown in (b) and (c). Red lines show the best fitting model for V_P, V_S, (b and c) and the corresponding theoretical HVSR (a).

The initial model for the dispersion curve inversion is presented at Table 4.26 and the inversion results at Figure 4.53.

Table 4.26 Initial model for the dispersion curve inversion at the SEIS accelerometer station site.

Layers	Thickness (m)	VP (m/s)	VS (m/s)
1	1-5	300-6000	150-800
2	10-30	1000-6000	400-1500
3	50-100	1000-6000	800-3500
4 (HS)	-	3000-6000	800-3500

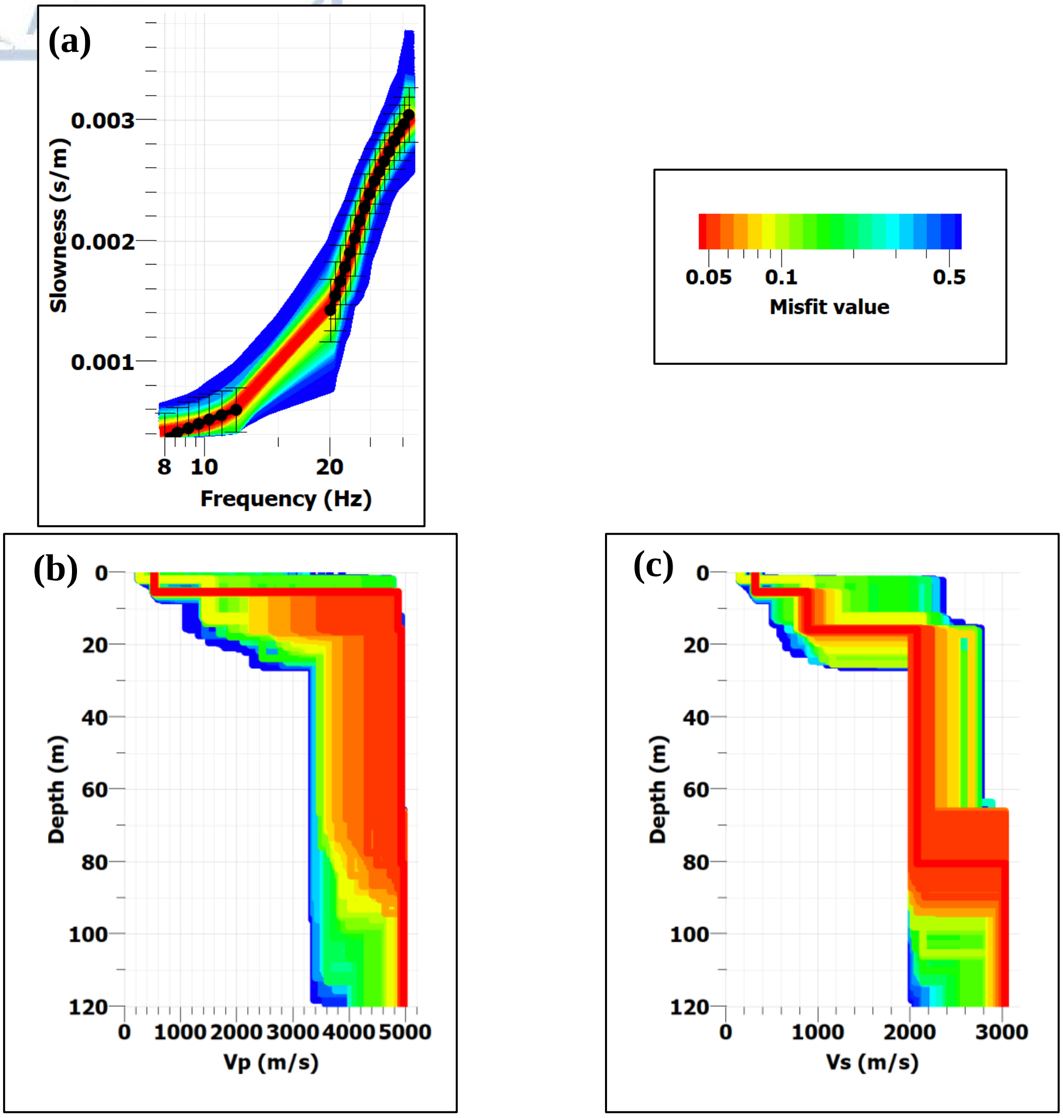

Figure 4.53 Ambient noise array dispersion curve inversion for SEIS accelerometer station site. (a) Forward modeling of the observed dispersion curve. (b) V_P and (c) V_S profiles.

Table 4.27 Final structure model that resulted from the HVSR curve inversion at SEIS accelerometer station site.

Layers	Thickness (m)	VP (m/s)	VS (m/s)	QP	QS
1	2	570	233	57	23
2	11	2451	1415	245	142
3 (HS)	-	4297	1757	576	176

The final structure model that resulted from the HVSR curve inversion (Table 4.27) was used as the theoretical model for the numerical simulation of ambient noise. The HVSR of the synthetic recordings were compared with the HVSR of observed ambient noise and earthquake recordings (Figure 4.54).

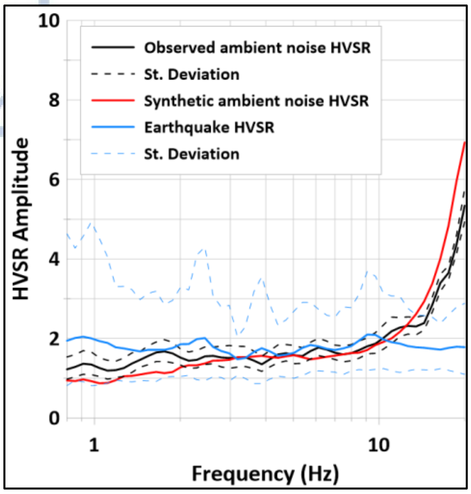

Figure 4.54 The ambient noise HVSR curve (position 4 at Figure 4.50b) (black curve), earthquake HVSR curve (blue curve) and the synthetic ambient noise HVSR curve (red curve). The synthetic ambient noise HVSR has been computed based on the theoretical structure of Table 4.27.

As already mentioned, the SEIS accelerometer is installed at the basement of the seismological station of the Aristotle University of Thessaloniki (AUTH) and is considered as a reference site. Thus, the observed ambient noise HVSR curve is generally flat with a fundamental frequency at the high frequency part (fo~20Hz). This peak is associated with the interface between a very surficial thin sediment layer and the underlying weathered bedrock formation. An outcrop of the bedrock is also observed very close (~50m) to the accelerometer installation location. The synthetic ambient noise HVSR curve is in very good agreement with the observed HVSR curve meaning that the adopted velocity profile is reliable for site characterization. The earthquake motion HVSR curve is also in a very good agreement with the observed ambient noise HVSR curve up to ~10Hz (Figure 4.54). The low amplitudes at the high frequency part (f>10 Hz) of the earthquake motion HVSR curve may be due to two factors: firstly, the accelerometer is installed at the basement of the seismological station on weathered rock conditions, bypassing the surficial thin sedimentary formation that is observed at the ambient noise HVSR measurement point; and secondly, the effect of the building itself, that is a possible soil-structure interaction effect. The later needs further investigation.

The V_{SZ} profile derived from HVSR inversion overestimates the V_S values compared to the ambient noise array and the downhole measurement, although the downhole measurement is limited to 23m (Figure 3.23). The V_{S30} parameter was calculated (Equation 1) from the HVSR inversion and the ambient noise array V_{SZ} profiles and the results are presented in Table 4.28. Hence, the site is classified as Ground Type A (Eurocode-8).

Table 4.28 Computation of the V_{S30} parameter from all the available methods at the SEIS accelerometer station site.

Method	V_{S30} (m/s)
HVSR Inversion	1110
Ambient noise array	850
Downhole	803 (V_{S23})

4.2.5 ITS1 accelerometer station – Site 5

The electrical resistivity distribution of the subsurface (Figure 4.55a) at ITS1 site showed a relatively resistive top layer of an approximate 5m to 8m thickness that corresponds to coarse-grained sediments consisting of sand and clay. At greater depth, resistivity values decrease, probably due to sand gradually being replaced by clay. The gradual increase of the calculated Vs suggests that with increasing depth the geological formations become more cohesive. The 2-layer refraction analysis presents a similar visualization of the subsurface structure with the ERT results. A 5m thickness top layer is depicted with 500m/s P-wave velocity overlain the half-space with higher P-wave velocity (Figure 4.52c). The 1D local structure is presented in Table 4.29. It is noteworthy that shallow heterogeneities in the ERT profile are also visible in the refraction data, hence the thickness of the top layer varies along the cross-section.

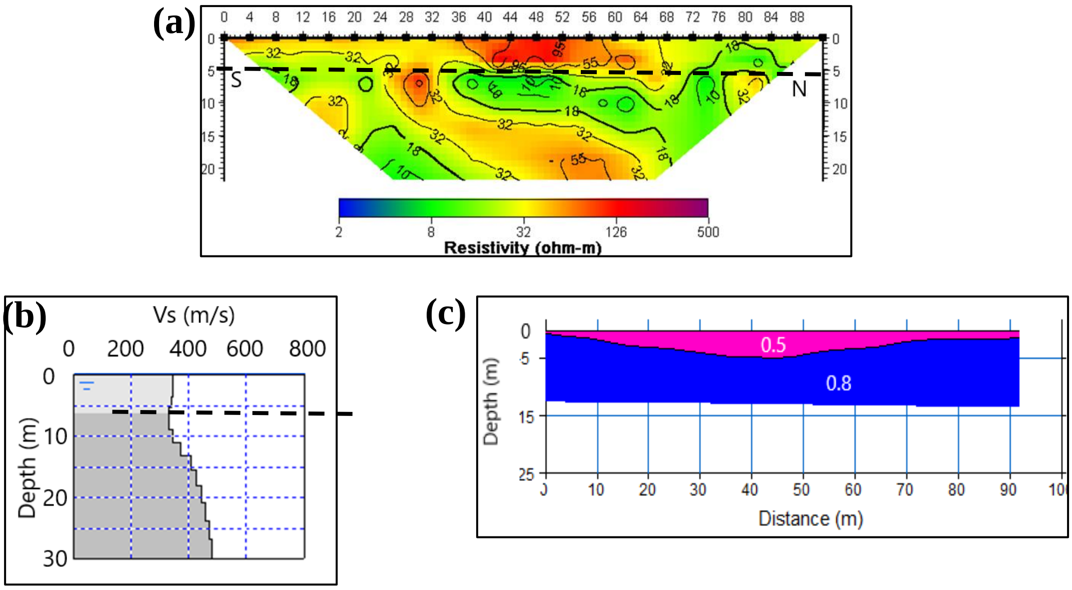

Figure 4.55 Geophysical investigation at the ITS1 accelerometer station site. (a) The ERT method result. (b) The 1D VS profile, generated by the MASW method. (c) P-wave velocity model generated by the seismic refraction.

Table 4.29 Properties regarding the subsurface layers according to the geophysical investigation at ITS1 site, including the number of layers, their approximate thicknesses, and the velocity ranges of the seismic waves.

Layers	Thickness (m)	V_P (m/s)	V_S (m/s)
1	5	400– 500	150– 400
2 (HS)	≥20	800–3000	300–1500

The computed HVSR at the temporary seismometer positions is shown in Figure 4.56 for the small aperture array and in Figure 4.58 for the larger array apertures). The main feature of the HVSR curve is the existence of a peak at approximately 1.5Hz, observable at all locations of the ambient noise array. Another feature is the intense amplitude perturbation at lower frequencies (<1Hz) probably due to strong wind during the time of the measurement. The third feature is a peak around 15Hz – 20Hz which is mostly evident at the positions closest to the building (center of the array) (Figure 4.56). According to SESAME Guidelines (2004), an HVSR peak is related to industrial noise (e.g., machinery operation) if it appears in the spectra of all three components. Figure 4.57 shows that the peak at approximately 18Hz appears at the power spectra of all three components, therefore it is considered to have industrial origins and is not related to subsurface structures.

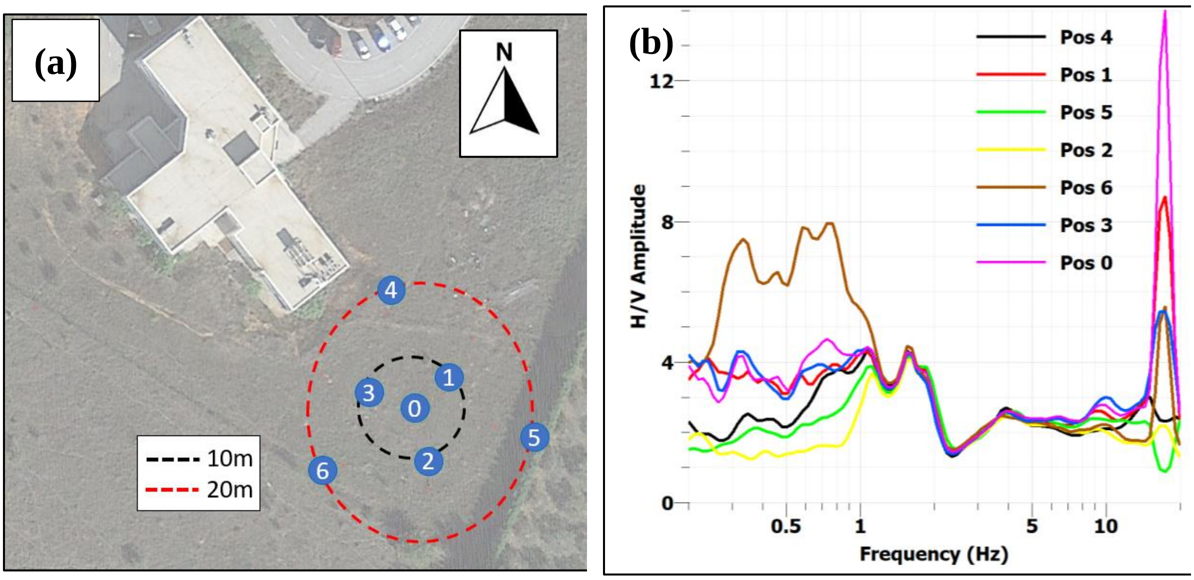

Figure 4.56 (b) HVSR curves computed at the 10m - 20m array of the geometry at (a).

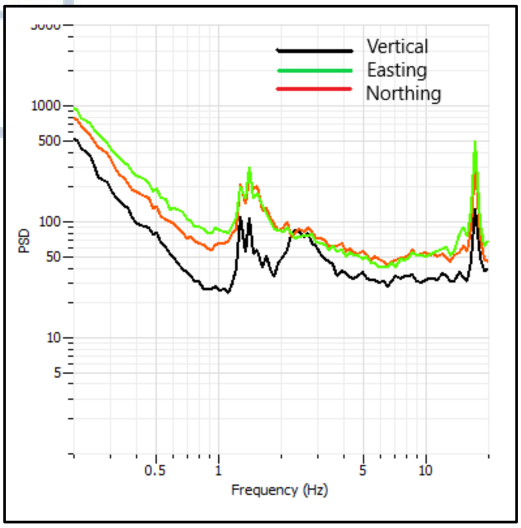

Figure 4.57 Example of the power spectra (seismometer at position 6 at Figure 4.56b) of the Easting (green curve), Northing (red curve) and Vertical (black curve) components of the ambient noise recording at the center of the ambient noise array. The existence of the peak at 18Hz at all three components indicate that it is of industrial origin.

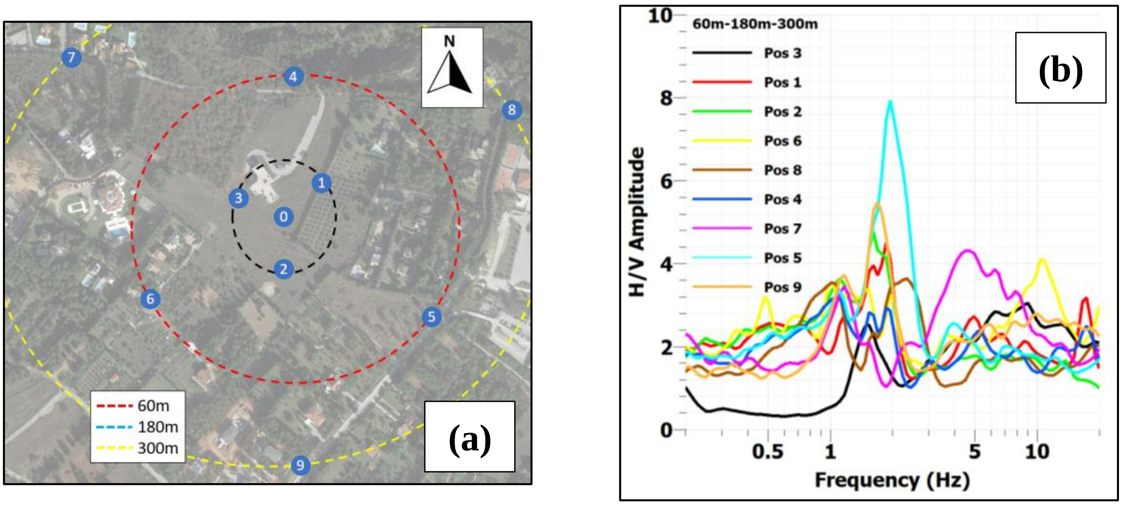

Figure 4.58 (a) The ambient noise array geometry for radii 60m, 180m, and 300m and (b) the computed HVSR curves at each position.

The reliability of the $f_0 \approx 1.5$Hz was also validate by the earthquake HVSR that is also computed up to 15Hz and is shown in Figure 4.59. The ambient noise HVSR curve that was computed at position 5 (Figure 4.56b) of the small ambient noise array (Figure 4.56a) exhibited a very similar shape to the earthquake HVSR curve and thus it was selected for inversion. The >15Hz part of the HVSR curve was omitted to exclude the industrial noise peak that was discussed earlier.

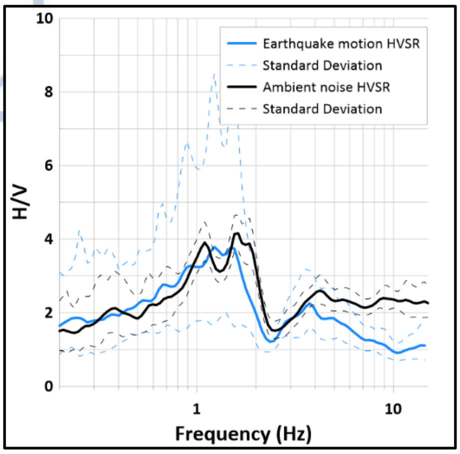

Figure 4.59 The earthquake HVSR curve (blue) and ambient noise HVSR curve (black) up to 15Hz computed at position 5 of the small array in Figure 4.56.

The initial model for the HVSR inversion is presented in Table 4.30 and the inversion results are presented in Figure 4.60.

Table 4.30 Initial model for the inversion of the HVSR curve at ITS1 accelerometer station site.

Layers	**Thickness (m)**	**V_P (m/s)**	**V_S (m/s)**
1	1 – 8	400 – 800	150 – 500
2	20 – 100	700 – 5000	500 – 1500
3	20 – 100	1000 – 5000	600 – 1500
4	50 – 200	1000 – 5000	700 – 3400
5 (HS)	-	1000 – 5000	1000 – 3400

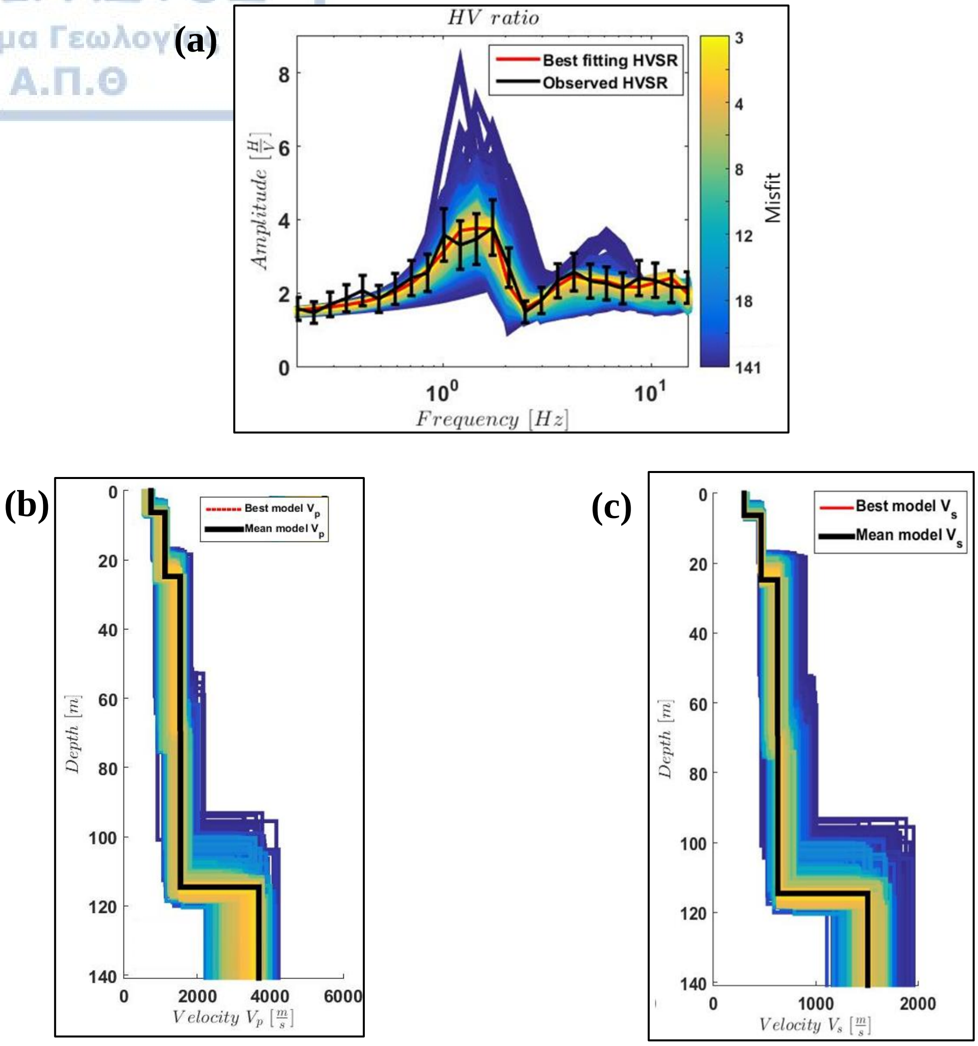

Figure 4.60 Inversion of the HVSR curve (position 5 at Figure 4.53) for ITS1 accelerometer station site. Black line with black error bars in (a) represent the experimental average HVSR curve ±1sd. The colored curves in (a) show the forward calculations for the corresponding velocity models shown in (b) and (c). Red lines show the best fitting model for V_P, V_S, (b and c) and the corresponding theoretical HVSR (a).

The initial model for the dispersion curve inversion is presented in Table 4.31 and the inversion results are shown in Figure 4.61.

Table 4.31 Initial model for the dispersion curve inversion at the ITS1 accelerometer station site.

Layers	Thickness (m)	V_P (m/s)	V_S (m/s)
1	10-20	400 – 800	200 – 500
2	20-50	700 – 5000	150 – 3500
3	50-100	1000 – 5000	150 – 3500
4	50 – 100	1000 – 5000	150 – 3500
5	50 – 100	1000 – 5000	150 – 3500
6 (HS)	-	1000 – 5000	150 – 3500

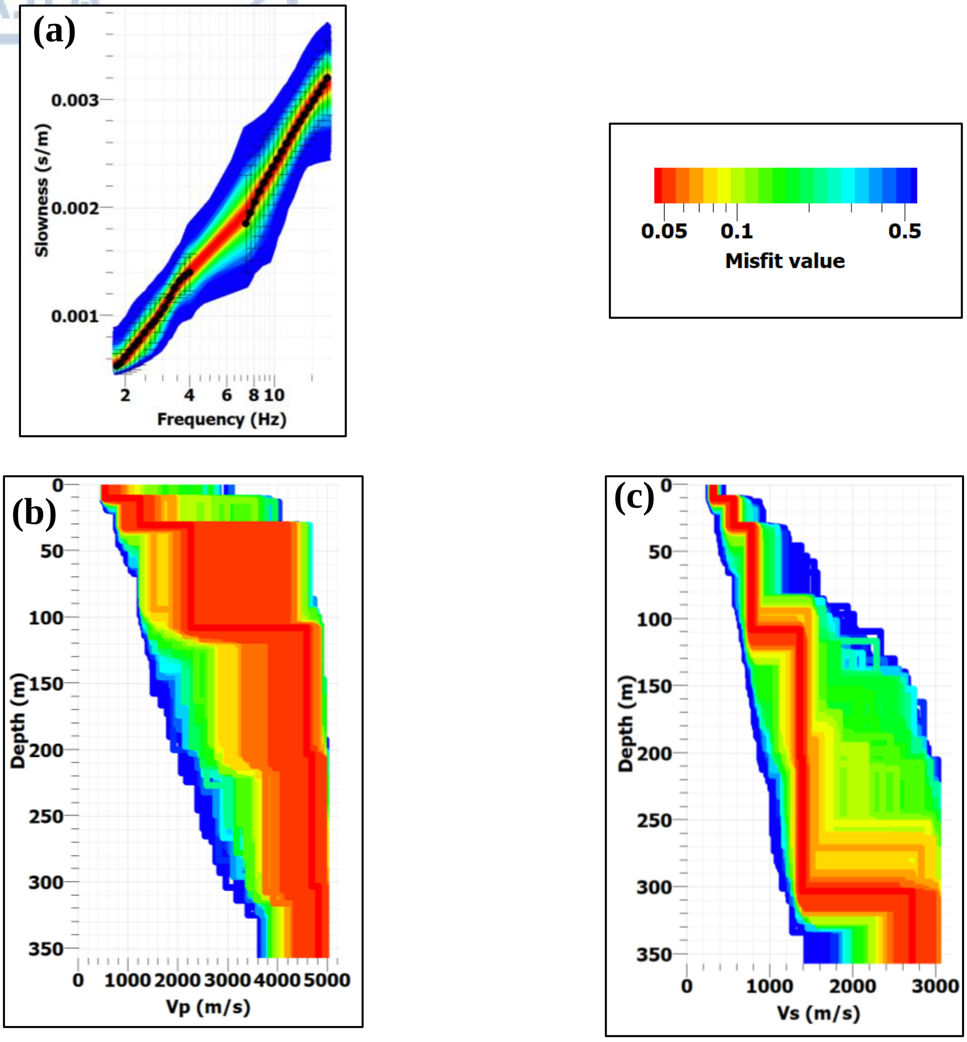

Figure 4.61 Ambient noise array dispersion curve inversion at the ITS1 accelerometer station site. (a) Forward modeling of the observed dispersion curve. (b) V_P and (c) V_S profiles.

Table 4.32 Final structure model that resulted from the HVSR curve inversion at ITS1 accelerometer station site.

Layers	Thickness (m)	VP (m/s)	VS (m/s)	Q_P	Q_S
1	8	864	354	86.4	35
2	25	1464	640	146	64
3	100	1995	815	200	81
4	-	4107	1772	410	177

Figure 4.62 shows the comparison between the ambient noise HVSR curve (black curve), the synthetic ambient noise HVSR curve (red curve) and the earthquake HVSR curve (blue curve). The synthetic HVSR is based on the theoretical subsurface structure of Table 4.32 and

exhibits an f_0=1.5Hz value. The f_0 is in good agreement with the f_0 exhibited by the experimental ambient noise HVSR curve and earthquake HVSR curve

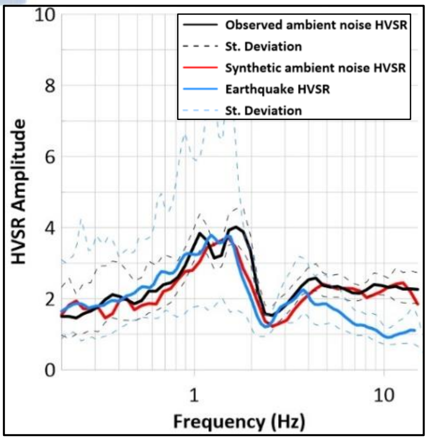

Figure 4.62 The ambient noise HVSR curve (position 5 at Figure 4.56) (black curve), earthquake HVSR curve (blue curve) and the synthetic ambient noise HVSR curve (red curve). The synthetic ambient noise HVSR has been computed based on the theoretical structure of Table 4.32.

Additionally, the V_{SZ} profile derived from the HVSR inversion (Figure 4.60c) is in good comparison with the V_{SZ} derived from the ambient noise array (Figure 4.61c). Therefore, the velocity model derived from the HVSR inversion is reliable for the V_{S30} parameter. Based on the Equation (1), the V_{S30} is estimated for each one of the available methods and are presented in Table 4.33. The V_{S30} values from all methods classify the ITS1 site as Ground Type B (Eurocode-8).

Table 4.33 Computation of the V_{S30} parameter from all the available methods at the ITS1 accelerometer station site.

Method	V_{S30} (m/s)
HVSR Inversion	436
Ambient noise array	441

4.2.6 PLA1 and PLA2 accelerometer stations – Site 6

The electrical resistivity distribution of the subsurface (Figure 4.63a) in this area revealed the existence of a resistive top layer from 60m to 115m, corresponding to sandy coarse-grained materials. At the southern half part of the tomography the materials are replaced by clay. Underneath the top layer, a less resistive layer is revealed. The MASW results show a gradual increase in V_S velocity with depth (Figure 4.63b), probably due to the increasing cohesiveness depicting the same structure as the ERT. The refraction analysis (Figure 4.63c) shows a thin surficial layer with V_P around 550m/sec while at the second layer the V_P increases to values greater than 1500m/s. This velocity range is consistent with a probable shallow water-table depth due to the proximity to the sea (approximately 800m distance to the sea and 14m elevation).

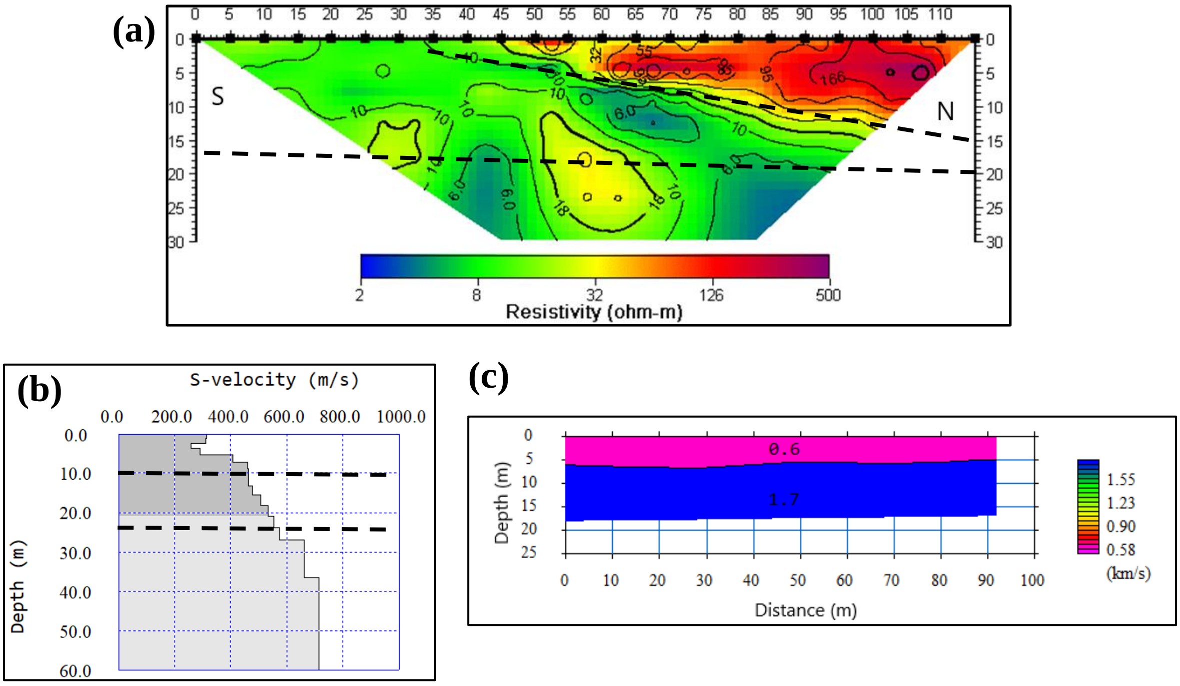

Figure 4.63 Geophysical investigation at the PLA1 accelerometer station site. (a) The ERT method result. (b) The 1D V_S profile, generated by the MASW method. (c) P-wave velocity model generated by the seismic refraction.

Table 4.34. Properties regarding the subsurface layers according to the geophysical investigation at PLA1 site, including the number of layers, their approximate thicknesses, and the velocity ranges of the seismic waves.

Layers	Thickness (m)	V_P (m/s)	V_S (m/s)
1	5	400– 500	200– 500
2	15	800–3000	350-650
3 (HS)	≥10	800– 000	≥600

The computed HVSR at the positions of the temporary seismometers of the small array is shown in Figure 4.64a and for the larger arrays in Figure 4.64b. A clear peak at f_0=0.3Hz is observed which is related to a very deep interface between formations with intense velocity contrast, possibly between the geological bedrock and the overlying sedimentary formations.

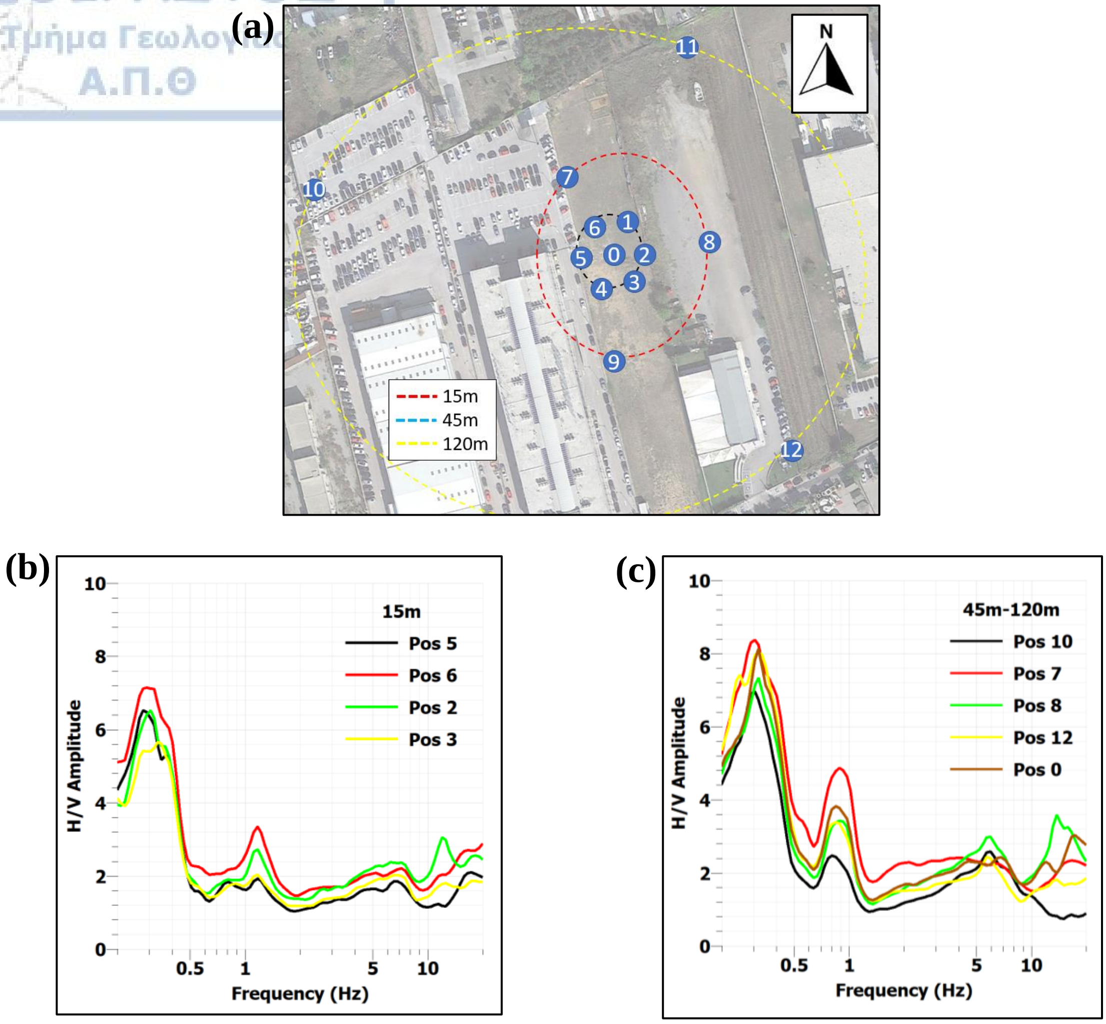

Figure 4.64 The HVSR analysis at the (a) 15m array and (b) at the 45m-120m array for seismometer positions shown in (a).

The earthquake HVSR was computed for the data of two different accelerometers, one installed inside the building (PLA1) and another outside in free-field conditions (PLA2). Both HVSR curves exhibit a very similar shape (blue and green curves at Figure 4.65) and correlate satisfactory with the ambient noise HVSR curve (black curve at Figure 4.65), showing a very clear and unique peak at f_0=0.3Hz and leaving no doubt that the ambient noise HVSR has successfully contributed to the computation of the fundamental frequency of this site. The secondary peak at 5Hz – 6Hz of the PLA2 HVSR curve (green curve) is probably related either to a relatively shallow interface that is not present at the position of the PLA1 accelerometer due to the construction of the installation building or to the soil-structure interaction phenomenon an issue that needs further investigation. Both, earthquake motion HVSR curves exhibit a drop of their amplitudes after ~7Hz up to 20Hz probably due to the higher attenuation of the horizontal motion compared to the vertical one or vise-versa.

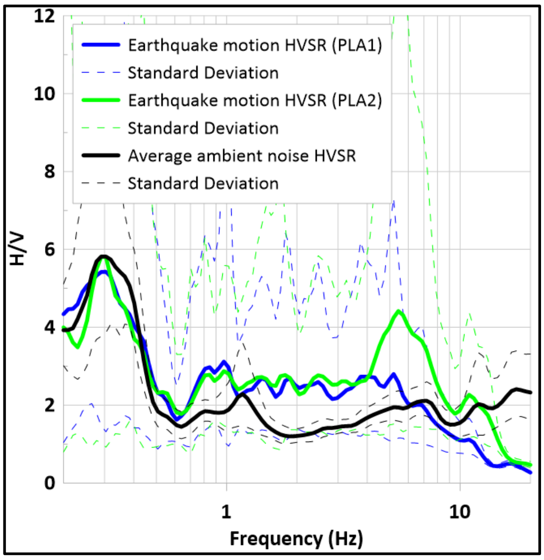

Figure 4.65 The HVSR curves as derived from the analysis of earthquake motion (blue and green curves) and ambient noise recordings.

Due to the very similar HVSR shape at all temporary seismometer positions, the average HVSR curve was computed and was subject to inversion. The initial model for the HVSR inversion is presented at Table 4.35 and the inversion results are presented in Figure 4.66.

Table 4.35 Initial model for the inversion of the HVSR curve at PLA1 accelerometer station site.

Layers	**Thickness (m)**	**V_P (m/s)**	**V_S (m/s)**
1	1 – 5	400-800	200 – 500
2	10 – 25	1400 – 1800	500 – 800
3	100 – 200	1500 – 3500	750 – 900
4	500 – 800	1500 – 6000	800 – 1200
5 (HS)	-	1500 – 6000	1000 – 3400

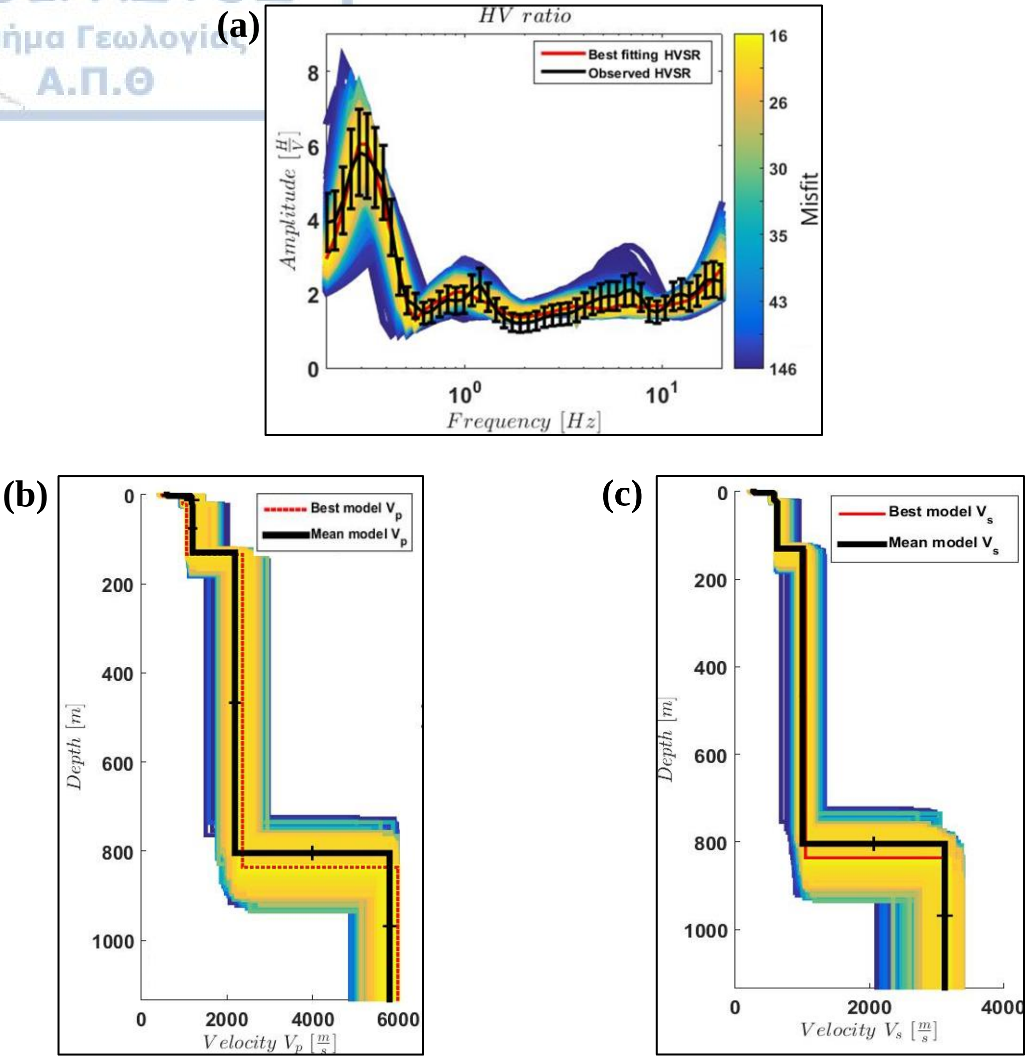

Figure 4.66 Inversion of the HVSR curve for PLA1 accelerometer station site. Black line with black error bars in (a) represent the experimental average HVSR curve ±1sd. The colored curves in (a) show the forward calculations for the corresponding velocity models shown in (b) and (c). Red lines show the best fitting model for VP, VS, (b and c) and the corresponding theoretical HVSR (a).

The initial model of the dispersion curve is presented at Table 4.36. The results of the dispersion curve inversion are presented in Figure 4.67. The gap in the dispersion curve (Figure 4.67a) is due to the data loss in the ambient noise array as has been mentioned in Section 3.3.6.

Table 4.36 Initial model for the dispersion curve inversion at the PLA1 and PLA2 accelerometer stations site.

Layers	Thickness (m)	V_P (m/s)	V_S (m/s)
1	1 – 5	400 – 800	200 – 400
2	10 – 25	1500 – 1800	350 – 600
3	25 – 80	1500 – 3500	500 – 800
4 (HS)	-	1500 – 6000	500 – 3500

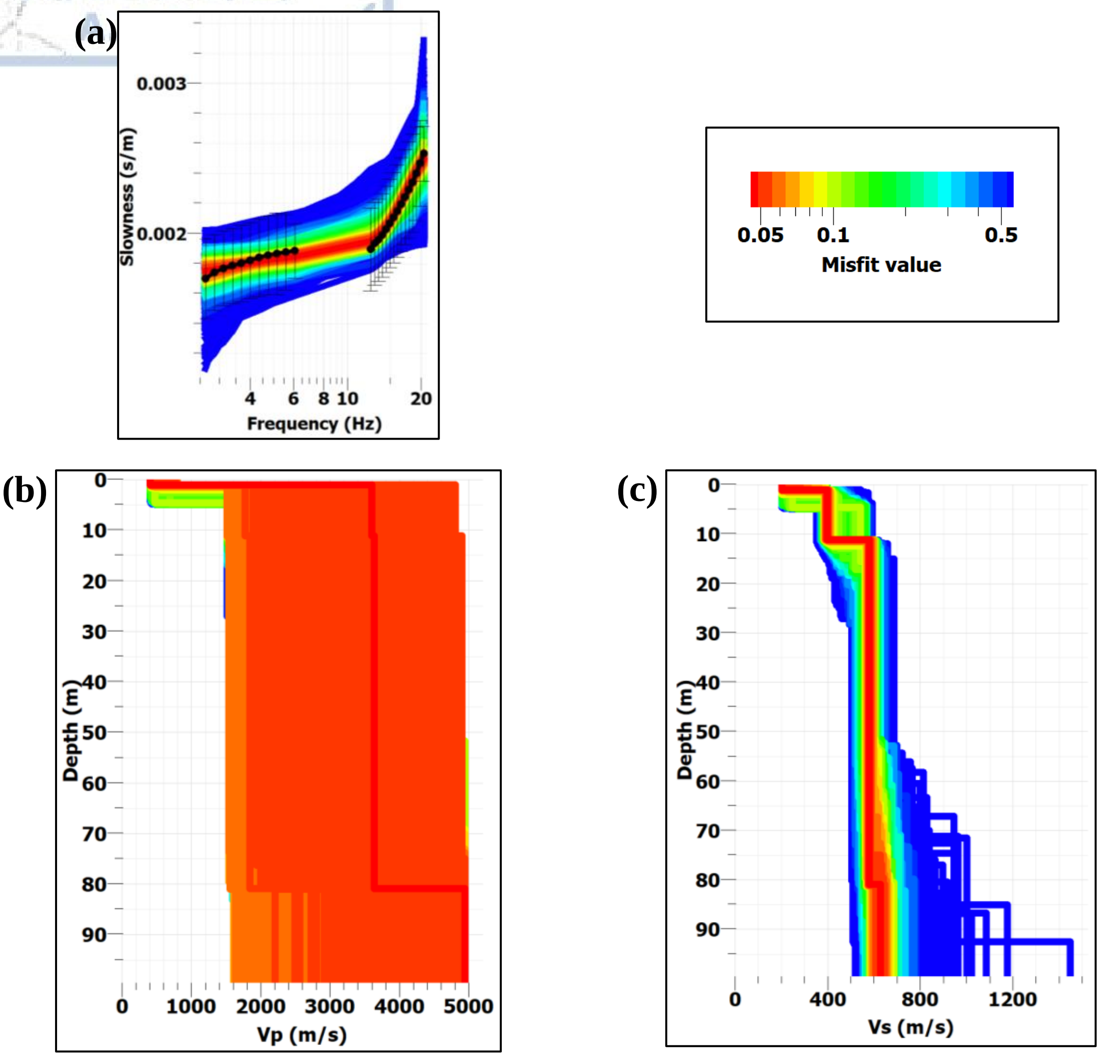

Figure 4.67 Ambient noise array dispersion curve inversion at the PLA1 and PLA2 accelerometer stations site. (a) Forward modeling of the observed dispersion curve. (b) V_P and (c) V_S profiles.

Table 4.37 Final structure model that resulted from the HVSR curve inversion at PLA1 accelerometer station site.

Layers	Thickness (m)	V_P (m/s)	V_S (m/s)	Q_P	Q_S
1	2.2	474	237	47	28
2	19	960	554	96	55
3	113	1054	607	105	60
4	703	2363	1048	236	104
5 (HS)	-	5993	3107	600	310

Figure 4.68 shows the comparison between the synthetic ambient noise HVSR curve (red curve) derived from the theoretical structure at Table 4.37 and the experimental ambient noise HVSR curve (black curve). It is observed that synthetic ambient noise HVSR correlates well

with observed ambient noise HVSR and earthquake HVSR validating the adopted velocity model (from HVSR inversion).

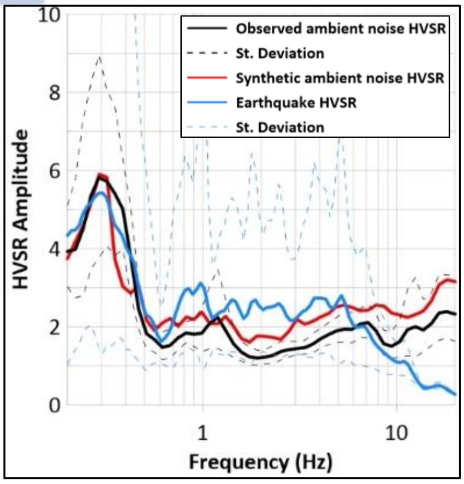

Figure 4.68 The ambient noise HVSR curve (black curve), earthquake HVSR curve (blue curve) and the synthetic ambient noise HVSR curve (red curve). The synthetic ambient noise HVSR has been computed based on the theoretical structure of Table 4.37.

Additionally, the V_{SZ} profile derived from the HVSR inversion (Figure 4.66c) is in good comparison with the V_{SZ} derived from the ambient noise array (Figure 4.67c). Therefore, the velocity model derived from the HVSR inversion is reliable for the V_{S30} parameter. Based on the Equation (1), the V_{S30} is estimated for each one of the available methods and are presented in Table 4.37. The V_{S30} values from all methods classify the PLA1 and PLA2 accelerometer stations site as Ground Type B (Eurocode-8).

Table 4.38 Computation of the V_{S30} parameter from all the available methods at the PLA1 and PLA2 accelerometers station site.

Method	V_{S30} (m/s)
HVSR Inversion	516
Ambient noise array	477

5. Conclusions – Discussion

5.1 Conclusions

The main objective of the present thesis was to propose a new methodology to obtain 1D Vs models for site characterization, considering as a minimum the V_{S30} parameter estimation as well as the engineering bedrock depth where possible. HVSR curves were computed to study the response of the local ground conditions to the seismic motion. Inversion of the HVSR curves was based on the diffuse field assumption (Sanchez-Sesma et al., 2011) which considers all types of elastic waves and uses the relation between the HVSR and elastodynamic Green's function. Inversion of HVSR curves was employed in combination with non-invasive geophysical methods in order to propose a self-restrained methodology in estimating reliable Vsz and V_{S30} values. The acquired geophysical knowledge along with geological information from existing boreholes at some of the test sites was used to facilitate the inversion procedure dealing with the non-uniqueness issue of HVSR inversion.

Applicability of HVSR inversion was tested prior to the employment for site characterization. The testing included inversions with or without a priori information. The results showed that the utilization of a priori certain information is pivotal to tackle the solution non-uniqueness issue of the HVSR inversion to some extent and provide improved V_{SZ} profiles for V_{S30} estimation by comparing the resulting Vsz profiles with a downhole measurement from the existing borehole at the investigation site.

The methodology was implemented and tested at six accelerometric sites with varying geological conditions in the city of Thessaloniki, northern Greece. Geophysical information was acquired at each site attempting at least 30m investigation depth, with the application of small-scale geophysical methods, namely the electrical resistivity tomography (ERT) method and the active seismic methods (source multichannel analysis of surface waves – MASW and Refraction). The length of ERT and seismic survey lines was at average 100m, except for one site with limited space availability which were shorter leading to shallower investigation depth. The ERT method was implemented to identify layers based on their electrical resistivity values. The 2D resistivity imaging of the subsurface contributed to revealing lateral variations (e.g., due to the existence of local heterogeneities in geophysical properties). Active source Rayleigh-wave data was acquired for the P-wave travel-time modeling (seismic refraction) to acquire a pseudo 2D distribution of the P-wave velocities while MASW method provided the shallow 1D S-wave velocity distribution with depth. The ambient noise array provided multiple HVSR curves for each site and the dispersion curve inversion resulted to a statistically more robust 1D Vsz profile for comparison with 1D Vsz profiles from HVSR inversion. The array apertures and therefore the investigation depth was determined depending on the available space and free field restrictions at each test site. Depending on the available space, it was attempted that the middle point of the ERT and MASW investigation lines to be as close as possible to ambient noise array center point.

The ambient noise data were also analyzed with the HVSR technique that provided information regarding the fundamental frequency (f_0) of the surficial sedimentary formations and its corresponding amplitude (A_0). The selection of appropriate HVSR curves for inversion was based on various criteria such as satisfying the criteria proposed by SESAME guidelines (2004), the sharpness of the peak and the smoothness of the curve morphology for the facilitation of the inversion. The acquired geophysical information was used for the mitigation of the solution non-uniqueness problem of the HVSR inversion.

The 1D V_{SZ} profiles that resulted from the HVSR inversion were used for the estimation of the time-averaged S-wave velocity of the topmost 30m (V_{S30}) for each one of the test sites. For the 3 out of the 6 sites, where V_{S30} values were available from downhole measurements (SEIS, KLR1 and PORT sites), the obtained in this study V_{S30} values were in good agreement with the existing ones.

Earthquake motion recordings were acquired from the permanently installed accelerometers at each study site. At the PORT site, where the accelerometer was out of operation, a temporary seismometer was installed for approximately 2 months period. The analysis of the earthquake motion recordings was conducted with the HVSR technique utilizing the most energetic part of the recording corresponding to the window from the arrival of the S-waves to end of coda waves. The results of the HVSR analysis of earthquake motion recordings are comparable with those of ambient noise HVSRs, hence they provide the fundamental frequency (f_0) of the surficial sedimentary layers and its corresponding amplitude (A_0). Therefore, earthquake

HVSR was used to directly validate the observed ambient noise HVSR and indirectly evaluate the derived 1D profile from the HVSR inversion.

The reliability of the subsurface structure models that were derived by the HVSR inversion, was also checked, and validated by one-dimensional (1D) numerical simulation of ambient noise with the generation of synthetic recordings. The subsurface structure that was derived from the HVSR inversion was used as theoretical structure model for the numerical simulation. The synthetic ambient noise recordings were analyzed with the HVSR methods. The comparison of the experimental and synthetic ambient noise HVSR curves reveals the similarity or discrepancy between the theoretical and actual structure 1D model.

Finally, based on the V_{S30} parameter that was derived from the final Vsz models from the inversion of the HVSR curves at each site, the accelerometer station site was characterized according to the provisions of the Eurocode 8.

The conclusions that are deduced from the tests of HVSR inversion with and without a priori information are summarized as follows:

- Application of other geophysical methods (e.g., ERT, MASW) and utilization of a priori information (e.g., geological information from boreholes) can provide a reliable initial model for the HVSR inversion.
- Utilization of this model is pivotal to stabilize the inversion results and to tackle the solution non-uniqueness issue to some extent and to finally lead to unambiguous 1D Vsz profiles for site characterization.
- The very low HVSR amplitudes (<1 - almost flat) at the high frequency range (usually ≥5hz) were rapidly converged during inversion by adding a thin surficial layer of high velocity, interpreted mainly as pavement or cemented area. A possible explanation of this effect could be the damping of the seismic energy mainly through the horizontal components, due to the stiff surficial high velocity layer. Although our approach helped in our cases, it remains an empirical result and needs further investigation.

The conclusions that are derived from the application of the methodology at the six accelerometer station sites are summarized as follows:

- All six investigation sites exhibit HVSR curves with maximum peaks. Both KLR1 and PLA1 sites exhibit very low frequency f_0 (≈ 0.3 Hz). This peak is probably related with a very deep interface probably between the surficial sedimentary layers and the geological bedrock. The PORT and ITS1 sites exhibit maximum peaks at approximately 1Hz and 1 – 1.5Hz respectively. These peaks are also probably related to the sediments – bedrock formation interface. At the STL1 site the maximum peak is exhibited at around 2.5Hz – 3Hz which is probably related to an interface with high impedance contrast between sedimentary formations. The HVSR curve at the SEIS site is a mostly flat curve that exhibits a very high f_0 at 15-20Hz. Though at some positions of the ambient noise array is appears flat across all frequencies. In the case of SEIS site, such structure is related to the shallow geological bedrock since the site is considered as reference site and outcrops of the bedrock formations were observed nearby.
- The computation of HVSR curves resulted in similar results in terms of f_0 for the ambient noise array for most sites (i.e., PORT, STL1, PLA1 , KLR1). This means that the subsurface interface structure that exhibits high impedance contrast is located at the same depth at all positions of the seismometers. Therefore, it is an indication that the test site does not exhibit lateral variations and the subsurface structure is mostly 1D. At sites with varied HVSR results (SEIS, ITS1) from the ambient noise array it is suggested to exclude HVSR curves with perturbed results in the low frequency band and keep the HVSR curves with the sharpest f_0 peaks that exhibit mostly the same curve shape (in accordance with SESAME Guidelines, 2004). It is possible that low frequency perturbations are stabilized using larger time-windows (e.g., ≥100s). Also, in cases of varied HVSR results it is suggested to examine the possible industrial origins of the peaks by computing the power spectra of each component. If a peak is depicted at all three components, then it is of industrial origin. By that rule, some HVSR curves can be omitted. Additionally, HVSR curves that were computed on non-optimal ground (e.g., grass) and exhibit perturbed low frequency results can also be omitted or just the interpretation of the low frequency part can be avoided.
- The V_{SZ} profiles derived from HVSR inversion are comparable to V_{SZ} profiles from the existing downhole measurements (PORT, KLR1) except for the SEIS site where HVSR inversion V_{SZ} profile is slightly overestimated. The HVSR inversion results are in good

comparison with the ambient noise array results at PORT, ITS1 and PLA1 and PLA2 sites at least up to their common depth. At STL1 site the V_{SZ} profile from the HVSR inversion is underestimated compared to the ambient noise V_{SZ} profile. At KLR1 and SEIS site the HVSR inversion V_{SZ} profiles are overestimated compared to the ambient noise array results. The reason for KLR1 might be the low resolution (5 layers) for such a deep V_{SZ} profile (600m deep).

- HVSR analysis of earthquake motion recordings exhibit similar results to HVSR analysis of ambient noise recordings in terms of similar fundamental frequency (f_0) values. As far as the corresponding amplitudes (A_0) little to no similarity is observed as the A_0 derived from ambient noise HVSR is time-depended.
- The HVSR analysis at the PORT and KLR1 sites exhibited very low amplitudes at the high frequency part of the HVSR curves. Such low amplitudes appear to be the effect of pavement or heavily cemented surfaces at the investigation areas (effect of a thin, surficial, high velocity layer) as shown with the results of the HVSR tests. In principle, such layers are also taken into consideration during computation of the V_{S30} parameter because they are part of the propagation of the seismic waves but without a considerable influence. As a matter of fact, layers that exhibit lower V_S velocities are more important than layers with higher velocities in the computation of the V_{S30}. This is due to the V_{S30} being computed in terms of duration of propagation (time-averaged) and the duration of propagation in such a thin layer is negligible compared to the propagation through layers with lower velocity values. It is noteworthy that, the dispersion curve extracted with the ambient noise array did not recognize the high velocity surficial layer. A possible explanation for this might be the large recordable wavelength due to the array apertures. Another possible explanation is that only the horizontal components are affected by such layer (damping of the seismic energy) and not the vertical (only the vertical component is used for the extraction of the Rayleigh waves dispersion curve).
- Synthetic ambient noise HVSR curves derived from the 1D numerical simulation of ambient noise (Hisada 1D), are in satisfactory agreement with the observed ambient noise HVSR and earthquake HVSR curves at each site. In this case also, the agreement concerns the f_0 and not the A_0 values.

5.2 Discussion

The conclusions of the present thesis were based on the results of a methodology that involved a combination of the ERT, active source seismic methods (MASW and seismic refraction) and ambient noise methods as well as methods for the validation of the methodology results such as the HVSR analysis of earthquake recordings and the 1D numerical simulation of ambient noise.

The HVSR inversion method with the utilization of shallow a priori geophysical information for the mitigation of the solution non-uniqueness problem provides satisfactory results for the estimation of the time-averaged S-wave velocity of the topmost 30m (V_{S30}). Therefore, we propose the following methodology for reliable V_{SZ} profiles estimation and the subsequent calculation of engineering parameters such as the V_{S30} and H_{800} (depth at which the V_S surpasses the 800m/s value - engineering bedrock) and the H_{3000} parameter (depth at which the V_S surpasses the 3000m/s value - seismological bedrock) where possible. Constraining the near-surface structure (thickness and number of layers, V_S values) is pivotal to obtain reliable V_{SZ} profiles. For this purpose, ERT is applied to identify layers based on their specific electrical resistivity values and MASW is applied to obtain a shallow V_S structure. A three-component seismometer should be used for the recording of ambient noise. The recording duration depends on f_0 value. If a low f_0 value is expected, then long recording duration is suggested as large time-windows are needed for a reliable HVSR curve (see also SESAME Guidelines). In areas with high anthropogenic noise, it is safer to conduct long duration recording regardless of the expected f_0 value. The HVSR is computed considering the total wavefield (all types of elastic waves) to be compatible with the diffuse field assumption. The shape of the HVSR curve can help to obtain information for a reliable initial model for the inversion. The f_0 value can be utilized and provide information about the deeper related structure using Equation (12) and an average V_S provided by the MASW. Thus, additional layers can be added to reach that depth. If low HVSR amplitudes (<1) are observed at the high frequency part, they are indicative of a possible surficial layer of high velocity (most probably corresponding to anthropogenic activities e.g., cemented area). By this methodology a reliable initial model for the HVSR inversion is constructed.

Different combinations of geophysical methods can be considered to acquire geophysical information for the initial model of the HVSR inversion. Seismic methods for the extraction of the seismic velocities are highly suggested since constraining Vs is the controlling factor of the HVSR inversion. If both active and passive source seismic methods are used it is good practice to generate a combined dispersion curve to achieve good resolution V_S profiles (passive seismic methods provide the dispersion curve part at low frequencies, while active seismic methods provide the high frequency dispersion curve part). However, simultaneous data acquisition should be avoided to prevent cross-contamination of the active and passive wavefields. It is suggested that the methodology is applied at "quiet periods" of the day, avoiding working or high traffic hours (direct body waves of anthropogenic noise) to acquire good quality ambient noise data and possibly less free field restrictions. If the measurements take place in a large metropolitan area, passive measurements during night-time are recommended (see also Foti et al., 2018 for additional guidelines on the good practice of surface wave analysis.

Although HVSR analysis of earthquake recordings offers direct validation of ambient noise HVSR curves and an indirect validation of the final structure model, it is not possible to implement it at investigation sites far away from accelerometric sites or at sites with low seismicity. It is important to validate the results with geotechnical and geological data if available as they are the ground-truth and provide information about the true subsurface structure.

It is suggested that at least two methods for collection of seismic data, or the ERT and a seismic method are applied because a combined approach is also self-restrained, providing a more spherical knowledge of the subsurface structure. Another electrical method that may also be implemented is the Vertical Electrical Sounding (VES) method which is used to reveal the 1D resistivity model. This approach could be useful when the 2D and more spherical approach of the ERT method (e.g., to study shallow lateral variations) is not needed or the relevant information is already known. The advantage of the VES lies in the fact that it already provides 1D subsurface structure in contrast with the 2D ERT method where it is needed to extract or assume the 1D structure introducing possible uncertainties or subjectivity issues.

Although the applicability of ambient noise methods is well established internationally, the HVSR inversion is still in experimental state and cannot fully replace the conventional but costly and time-consuming methods, for the estimation of the V_S profiles with depth as further investigation is required. The main aim of such investigation could be the implementation of the combined methodology to produce Vs profiles of higher resolution for V_{S30} estimation, especially at sites with very low (<1Hz) fundamental frequency. The next step to our work could involve joint HVSR and dispersion curve inversion for 1D V_S profiles, to limit the set of equivalent solutions.

Bibliography

Aki K. 1957. Space and time spectra of stationary stochastic waves, with special reference to microtremors, Bulletin of the Earthquake Research Institute 35, 415–457.

Aki K. and Richards P. 1980. Quantitative Seismology: Theory and Methods, Vol. 1 W. H. Freeman, San Francisco

Aki K. and Richards G. P. 2002. Quantitative Seismology, Second edition, University Science Press, 700p.

Ansary, M. A., Fuse, M., Yamazaki, F. and Katayama, T., 1995. Use of Microtremors for the Estimation of Ground Vibration Characteristics. 3rd International Conference on Recent Advances in Geotechnical Engineering and Soil Dynamics (Saint-Louis, USA), 571-574p.

Anthymidis, M. 2008. Geophysical structure and response of the upper layers of the earth using ambient noise array data and earthquake recordings (in Greek). Master Thesis. Aristotle University of Thessaloniki. 262p.

Anthymidis, M., Theodoulidis, N., Savvaidis, A., and Papazachos, C. 2012. Constraining site response and shallow geophysical structure by ambient noise measurements and 1D numerical simulations: The case of Grevena town (N. Greece). Bulletin of Earthquake Engineering, 10. https://doi.org/10.1007/s10518-012-9378-3

Arai, H. and Tokimatsu, K., 1998. Evaluation of local site effects based on microtremor H/V spectra. Proceeding of the Second International Symposium on the Effects of Surface Geology on Seismic Motion. Yokohama, Japan, pp. 673–680.

Arai, H. and Tokimatsu K., 2000. Effects of Rayleigh and love waves on microtremor H/V spectra. Proceedings of the 12th World Conference on Earthquake Engineering. Auckland, New Zealand, No. 2232.

Arai, H., and Tokimatsu, K., 2004. S-Wave Velocity Profiling by Inversion of Microtremor H/V Spectrum. Bulletin of the Seismological Society of America, 94, 53–63. https://doi.org/10.1785/0120030028

Asten, M., 1978. Geological Control on the Three-Component Spectra of Rayleigh-Wave Microseism, Bulletin of the Seismological Society of America Vol. 68, 1623-1636.

Asten, M., J., Henstridge 1984. Array Estimators and Use of Microseisms for Reconnaissance of Sedimentary Basins, Geophysics 49, 1828-1873.

Bard, P.-Y., 1999. Microtremor Measurement: A Tool for Site Effect Estimation?. The Effects of Surface Geology on Seismic Motion, 1251-1279p. https://doi.org/10.12681/bgsg.16536

Bard P.-Y. and SESAME Participants 2004, "The SESAME Project: An Overview and Main Results", Proceedings of the 13th World Conference on Earthquake Engineering (Vancouver, Canada), Paper No. 2207, 2004.

Bard P.-Y., Cadet H, Endrun B, Hobiger M, Renalier F, Theodulidis N, Ohrnberger M, Fäh D, Sabetta F, Teves-Costa P, Duval A-M, Cornou C, Guillier B, Wathelet M, Savvaidis A, Köhler A, Burjanek J, Poggi V, Gassner-Stamm G, Havenith HB, Hailemikael S, Almeida J, Rodrigues I, Veludo I, Lacave C, Thomassin S, Kristekova M 2010. From non-invasive site characterization to site amplification: recent advances in the use of ambient vibration measurements. Geotech Geological Earthquake Engineering 17, 105–123.

Bonnefoy-Claudet, S., Cornou, C., Kristek, J., Ohrnberger, M., Wathelet, M., Bard, P.-Y., Fah, D., Moczo, P. and Cotton, F., 2004. Simulation of Seismic Ambient Noise: I. H/V and Array Techniques on Canonical Models. Proceedings of the 13th World Conference on Earthquake Engineering (Vancouver, Canada), Paper No. 1120.

Bonnefoy-Claudet, S., C., Cornou, P., Bard, F., Cotton, P., Moczo, J., Kristek, D. Fah 2006a. H/V ratio: a tool for site effects evaluation. Results from 1-D noise simulations, Geophys. J. Int. 167, 827-837.

Bonnefoy-Claudet, S., C., F., Cotton, P., Bard 2006b. The nature of noise wavefield and its applications for site effects studies A literature review. Earth Science Reviews 79, 205-227.

Bonnefoy-Claudet, S., Baize, S., Bonilla, L., Berge-Thierry, C., Pasten, C. R., Campos, J., Volant, P., and Verdugo, R. 2008. Site effect evaluation in the basin of Santiago de Chile using ambient noise measurements, Geophysical Journal International, 176, 925–937.

Borcherdt, R. D. 1970. Effects of local geology on ground motion near San Francisco Bay*. Bulletin of the Seismological Society of America, 60(1), 29–61. https://doi.org/10.1785/BSSA0600010029

Byrd, R. H., Hribar, M. E., and Nocedal, J. 1999. An interior point algorithm for large-scale nonlinear programming. SIAM Journal on Optimization, 9(4), 877–900. https://doi.org/10.1137/S1052623497325107

Capon, J., 1969. High Resolution Frequency-Wavenumber Spectrum Analysis. Proceedings of the IEEE (Vol.57), 1408-1418p.

CEN., Eurocode 8, 2004. Design of Structures for Earthquake Resistance—Part 1: general rules, seismic actions and rules for buildings. EN 1998-1: 2004. Comite Europeen de Normalisation, Brussels.

Chouet, B., De Luca, G., Milana, G., Dawson, P., Martini, M. and Scarpa, R., 1998. Shallow velocity of Stromboli volcano, Italy, derived from small-aperture array measurements of Strombolian tremor. Bulletin of the Seismological Society of America 88 (3), 653–666.

Christopher C. Pain, Jörg V. Herwanger, Michael H. Worthington, Cassiano R. E. de Oliveira, Effective multidimensional resistivity inversion using finite-element techniques, Geophysical Journal International, Volume 151, Issue 3, December 2002, Pages 710–728, https://doi.org/10.1046/j.1365-246X.2002.01786.x

Constable, S. C., Parker, R. L., and Constable, C. G. 1987. Occam’s inversion: A practical algorithm for generating smooth models from electromagnetic sounding data. GEOPHYSICS, 52(3), 289–300. https://doi.org/10.1190/1.1442303

Cornou, C., 2002. Traitement d'antenne et imagerie sismique dans l'agglomération grenobloise (Alpes françaises): implications pour les effets de site. Ph.D. Thesis, University Joseph Fourier, Grenoble, France. (In French with English abstract).

Cornou, C., Bard, P.-Y. and Dietrich, M., 2003a. Contribution of dense array analysis to identification and quantification of basin-edge induced waves. Part I: methodology. Bulletin of the Seismological Society of America 93 (6), 2604–2623.

Cornou, C., Bard, P.-Y. and Dietrich, M., 2003b. Contribution of dense array analysis to identification and quantification of basin-edge induced waves. Part II: application to Grenoble basin (French Alps). Bulletin of the Seismological Society of America 93 (6), 2624–2648.

Pridmore, D. F., Hohmann, G. W., Ward, S. H., and Sill, W. R. 1981. An investigation of finite-element modeling for electrical and electromagnetic data in three dimensions. Geophysics, 46(7), 1009–1024. https://doi.org/10.1190/1.1441239

Douze E. J. 1964, "Rayleigh Waves in Short-Period Seismic Noise", Bulletin of the Seismological Society of America (Vol. 54), 1197-1212p.

Douze, E. J. 1967. Short-period seismic noise. Bulletin of the Seismological Society of America, 57(1), 55–81. https://doi.org/10.1785/BSSA0570010055

Emad K. Mohamed, M.M.F. Shokry, Awad Hassoup, A.M.A. Helal, Evaluation of local site effect in the western side of the Suez Canal area by applying H/V and MASW techniques, Journal of African Earth Sciences, Volume 123, 2016, Pages 403-419, ISSN 1464-343X, https://doi.org/10.1016/j.jafrearsci.2016.07.004.

Field E. and Jacob K., 1993. The theoretical response of sedimentary layers to ambient seismic noise. Geophys. Res. Lett., 20-24, 2925–2928.

Foti, S., Hollender, F., Garofalo, F., Albarello, D., Asten, M., Bard, P.-Y., Comina, C., Cornou, C., Cox, B., di Giulio, G., Forbriger, T., Hayashi, K., Lunedei, E., Martin, A., Mercerat, D., Ohrnberger, M., Poggi, V., Renalier, F., Sicilia, D., and Socco, V. 2018. Guidelines for the good practice of surface wave analysis: a product of the InterPACIFIC project. Bulletin of Earthquake Engineering, 16(6), 2367–2420. https://doi.org/10.1007/s10518-017-0206-7

Gabr, Amir and Murad, Ahmed and Baker, Haydar and Al Bloushi, Khalid and Arman, Hasan and Mahmoud, Saber. (2012). The use of seismic refraction and electrical techniques to investigate groundwater aquifer, Wadi Al-Ain, United Arab Emirates (UAE).

García-Jerez, A., Piña-Flores, J., Sánchez-Sesma, F. J., Luzón, F., and Perton, M. 2016. A computer code for forward calculation and inversion of the H/V spectral ratio under the diffuse field assumption. Computers and Geosciences, 97, 67–78. https://doi.org/https://doi.org/10.1016/j.cageo.2016.06.016

Goffe, W. L., Ferrier, G. D., and Rogers, J. 1994. Global optimization of statistical functions with simulated annealing. Journal of Econometrics, 60(1), 65–99. https://doi.org/https://doi.org/10.1016/0304-4076(94)90038-8

Goffe, W. L., 1996. SIMANN: A Global Optimization Algorithm using Simulated Annealing. Studies in Nonlinear Dynamics andamp; Econometrics, 1(3), 1–9. https://EconPapers.repec.org/RePEc:bpj:sndecm:v:1:y:1996:i:3:n:al1

Gutenberg, P. 1958 Microseisms, Advanced Geophysics (5), 53-92.

Haghshenas, E., Bard, P.-Y. and Theodulidis, N., 2008. Empirical evaluation of microtremor H/V spectral ratio. Bulletin of Earthquake Engineering 6.1: 75-108.

Hastings, W. K. 1970. Monte Carlo sampling methods using Markov chains and their applications. Biometrika, 57(1), 97–109. https://doi.org/10.1093/biomet/57.1.97

Hauksson, E., and P. M. Shearer 2006, Attenuation models (QP and QS) in three dimensions of the southern California crust: Inferred fluid saturation at seismogenic depths, Journal of Geophysical Research, 111, B05302, doi:10.1029/2005JB003947.

Hisada, Y. 1994. An efficient method for computing Green’s functions for a layered half-space with sources and receivers at close depths. Bulletin of the Seismological Society of America, 84(5), 1456–1472. https://doi.org/10.1785/BSSA0840051456

Hisada, Y. 1995. An efficient method for computing Green’s functions for a layered half-space with sources and receivers at close depths (part 2). Bulletin of the Seismological Society of America, 85(4), 1080–1093. https://doi.org/10.1785/BSSA0850041080

Holland, J. H. 1992. Adaptation in natural and artificial systems: an introductory analysis with applications to biology, control, and artificial intelligence. MIT press.

Horike, M. 1985. Inversion of phase velocity of long-period microtremors to the S-wave velocity structure down to the basement in urbanized AREAS. Journal of Physics of the Earth, 33, 59–96.

Horike, M., 1996. Geophysical Exploration Using Microtremor Measurements, Proceedings of the 10th World Conference on Earthquake Engineering (Acapulco, Mexico), Paper No. 2033.

Hunter J-A., Crow H., Brooks G., Pyne M., Motazedian D., Lamontagne M., Pugin A. Pullan S., Cartwright T., Douma M., Burns R., Good R., Kaheshi-Banab K., Caron R., Kolaj M., Folahan I., Dixon L., Dion K., Duxbury A. 2010. Seismic site classification and site period mapping in the Ottawa area using geophysical methods. Geological Survey of Canada, Open File 6273. https://doi.org/10. 4095/286323

Hunter, J.A. and Crow, H. 2012. Shear Wave Velocity Measurement Guidelines for Canadian Seismic Site Characterization in Soil and Rock; Geological Survey of Canada, Open File 7078, 227 p. doi:10.4095/291753

Igboekwe M. U. and Ohaegbuchu H. E. 2011. Investigation into the weathering layer using up-ole method of seismic refraction. Department of Physics, Michael Okpara University of Agriculture, Umudike, Abia State. Nigeria. https://doi.org/10.5897/JGMR.9000042

Iglesias, A., Cruz Atienza, V. M., Shapiro, N. M., Singh, S. K., and Pacheco, J. F. 2001. Crustal structure of south-central Mexico estimated from the inversion of surface-wave dispersion curves using genetic and simulated annealing algorithms. Geofísica Internacional, 40(3), 181–190.https://www.redalyc.org/articulo.oa?id=56840303

Institute of Engineering Seismology and Earthquake Engineering 2008. Sample drilling and borehole installation for the accommodation of triaxonic accelerometers. Central Macedonia Regional Operational Programme (ROP).

Kanai, K. and T. Tanaka 1954. Measurements of microtremor, Bull Earth Res. Inst., Tokyo Univ. 30, 199-209.

Kim, J. H. 2010. DC_2DPro - User's Guide. Korea: KIGAM.

Kim, J.-H., Supper, R., Tsourlos, P., and Yi, M.-J. 2013. Four-dimensional inversion of resistivity monitoring data through Lp norm minimizations. Geophysical Journal International, 195(3), 1640–1656. https://doi.org/10.1093/gji/ggt324

Kirkpatrick, S., Gelatt, C., and Vecchi, M. 1983. Optimization by Simulated Annealing. Science (New York, N.Y.), 220, 671–680. https://doi.org/10.1126/science.220.4598.671

Konno, K. and Ohmachi, T., 1998. Ground Motion Characteristics Estimated from Spectral Ratio Between Horizontal and Vertical Components of Microtremor. Bulletin of Seismological Society of America (Vol.88), 228- 241p.

Kramer, S. 1997. Geotechnical Earthquake Engineering. University of Washington. ISBN 0-13-374943-6

Kritikakis, G. 2010. Surface Waves: Applications to Environmental and Geotechnical Problems (in Greek), PhD Thesis, Technical University of Crete, (Greece), 357p.

Kvaerna, T. and F. Ringdal 1986 Stability of various f-k estimation techniques. NORSAR Scientific Report 1-86/87, 29-40, https://doi.org/10.21348/p.1986.0001

Lachet, C., and Bard, P.-Y., 1994. Numerical and Theoretical Investigations on the Possibilities and Limitations of Nakamura’s Technique, Journal of Physics of the Earth 42, 377–397.

Lacoss, R. T., Kelly, E. J. and Toksoz, M. N., 1969. Estimation of Seismic Noise Structure Using Arrays. Geophysics (34), 21-38p.

Langston, C. A. 1979. Structure under Mount Rainier, Washington, inferred from teleseismic body waves, Journal of Geophysical Research, 84, 4749-4762.

Lay T. and Wallace C. T., 1995. Modern Global Seismology, International Geophysics Series, Vol. 58, Academic Press, pp. 521

Lee, Y. S., Graham, E., Jackson, G., Galindo, A., and Adjiman, C. S. 2019. A comparison of the performance of multi-objective optimization methodologies for solvent design. Computer Aided Chemical Engineering, 46, 37–42. https://doi.org/10.1016/B978-0-12-818634-3.50007-2

Lermo, J., and Chávez-García, F. J. 1993. Site effect evaluation using spectral ratios with only one station. Bulletin of the Seismological Society of America, 83(5), 1574–1594. https://doi.org/10.1785/BSSA0830051574

Lermo, J. and Chavez-Garcia F. J. 1994. Site effect evaluation at Mexico City: dominant period and relative amplification from strong motion and microtremor records, Soil Dynamics Earthquake Engineering 13, 413-423.

Li T. M., Ferguson J. F., Herrin E. and Drham H. B. 1984, High-Frequency Seismic Noise at Lajitas, Texas, Bulletin of the Seismological Society of America 74, 2015-2033.

Lontzetidis K. 1993. “Application of the cross-hole method in the city of Thessaloniki”. Master Thesis (in Greek), Faculty of Engineering, Aristotle University of Thessaloniki.

Loupasakis, C., Tsangaratos, P., Rozos, D., Rondoyianni, Th., Vafidis, A., Kritikakis, G., Steiakakis, M., Agioutantis, Z., Savvaidis, A., Soupios, P., Papadopoulos, I., Papadopoulos, N., Sarris, A., Mangriotis, M.-D., and Dikmen, U. 2015. Cross validation of geotechnical and geophysical site characterization methods: near surface data from selected accelerometric stations in Crete (Greece). Proc.SPIE, 9535. https://doi.org/10.1117/12.2192673

Lozano L., Herraiz M. and Singh S. K. 2008. Site Effect Study in Central Mexico Using H/V and SSR Techniques: Independence of Seismic Site Effects on Source Characteristics, Soil Dynamics and Earthquake Engineering 13p.

Luco, J. E. and Apsel R. J., 1983. On the Green's functions for a layered half-space, part 1, Bulletin of the Seismological Society of. America 73, 909-929.

Martin, A., Yong, A., Stephenson, W. J., Boatwright, J., and Diehl, J. 2017. Geophysical Characterization of Seismic Station Sites In The United States – The Importance Of A Flexible, Multi-Method Approach. 16th World Conference on Earthquake Engineering, Santiago, Chile

McMechan, G. and Yedlin, M. J. 1981. Analysis of dispersive waves by wave field transformation. Geophysics, 46 (6), 869-874.

Moczo P. and Kristek, J. 2002, FD code to generate noise synthetics, SESAME EVG1-CT-2000-00026 project, Deliverable D02.09, 31 p, http://SESAME-fp5.obs.ujf-grenoble.fr, 2002.

Mohamed, E., Farag, M., Hassoup, A., and Helal, A. M. A. 2016. Evaluation of local site effect in the western side of the Suez Canal area by applying H/V and MASW techniques. Journal of African Earth Sciences, 123. https://doi.org/10.1016/j.jafrearsci.2016.07.004

Moisidi M., Vallianatos F., Soupios P., Kershaw S., Rust D., Piscitelli S. 2012. Spatial spectral variations of microtremors and electrical resistivity tomography surveys for fault determination in southwestern Crete, Greece. Journal of Geophysical Engineering 9, 261-270.

Murphy, J. R., and Shah, H. K. 1988. An analysis of the effects of site geology on the characteristics of near-field Rayleigh waves. Bulletin of the Seismological Society of America, 78(1), 64–82. https://doi.org/10.1785/BSSA0780010064

Nakamura, Y., 1989. A Method for Dynamic Characteristics Estimation of Subsurface using Microtremor on the Ground Surface. Quarterly Report of Railway Technical Research Institute 30, 25-33.

Nakamura, Y., 1996. Real-Time information systems for hazards mitigation. Proceedings of the 11th World Conference on Earthquake Engineering (Acapulco, Mexico).

Nakamura, Y. 1997. Vulnerability indexes for surface ground and structures using microtremor, 8th Soil Dynamics Earthquake Engineering ’97, Istanbul, Turkey, 20–24 July 1997.

Nakamura, Y., 2000. Clear Identification of Fundamental Idea of Nakamura’s Technique and its Applications. Proceedings of the 12th World Conference on Earthquake Engineering (Auckland, New Zealand), 8p.

Nakamura, Y. 2014. A modified estimation method for amplification factor of ground and structures using the H/V spectral ratio, Proc. Of the 2nd Workshop on Dynamic Interaction of Soil and Structure ’12, L’Aquila, Italy, 29–30 March 2012, 273–284.

Nakamura, Y. 2019. What Is the Nakamura Method?, Seism. Res. Letters, 90, 4, 1437- 1443.

Nazarian S., Stokoe II, K.H. and Hudson W.R., 1983. Use of spectral analysis of surface waves meth-od for determination of moduli and thicknesses of pavement systems, Transp. Res. Rec. Vol. 930, Washington DC, 38-45.

Nelder, J. A., and Mead, R. 1965. A Simplex Method for Function Minimization. The Computer Journal, 7(4), 308–313. https://doi.org/10.1093/comjnl/7.4.308

Nogoshi, M. and Igarashi, T., 1971. On the Amplitude Characteristics of Microtremor (Part 2) (in Japanese with English Abstract). Journal of Seismological Society of Japan (Vol. 24), 24-40p.

Ohmachi, T. and Umezono, T., 1998. Rate of Rayleigh waves in microtremors. Proceeding of the Second International Symposium on the Effects of Surface Geology on Seismic Motion. Yokohama. Japan, pp. 587–592.

Ohori, M., Nobata, A., and Wakamatsu, K. 2002. A Comparison of ESAC and FK Methods of Estimating Phase Velocity Using Arbitrarily Shaped Microtremor Arrays. Bulletin of the Seismological Society of America, 92(6), 2323–2332. https://doi.org/10.1785/0119980109

Ohrnberger, M., 2004. User manual for software package CAP—a continuous array processing toolkit for ambient vibration array analysis, SESAME report D18.06, pp. 83 http://sesamefp5.obs.ujf-grenoble.fr

Ohrnberger, M., Schissele, E., Cornou, C., Bonnefoy-Claudet, S., Wathelet, M., Savvaidis, A., Scherbaum, F., and Jongmans, D. 2004. Frequency wavenumber and spatial autocorrelation methods for dispersion curve determination from ambient noise vibration recordings.

Okada, H., 2003. The Microtremor Survey Method. Society of Exploration Geophysics (SEG), 135p.

Panou A., 2007. Ambient noise measurements and correlation with seismic damage distribution in the city of Thessaloniki (North Greece). (in Greek), PhD Thesis, Aristotle University of Thessaloniki, p. 238.

Papazachos, C., and Papazachos, B., 2013. Introduction to Geophysics (in Greek), Ziti Publ., Thessaloniki, 581pp., ISBN 978-960-456-121-6.

Park, C. B., Miller R. D., and Xia J., 1998. Ground roll as a tool to image near-surface anomaly, SEG expanded abstracts, 23, 1437.

Park, C. B. and Carnevale, M. 2010. Optimum MASW Survey - Revisit after a Decade of Use. In Fratta, D. O., Puppala, A. J. and Muhunthan, B (editors), GeoFlorida 2010: Advences in Analysis, Modeling and Design (pp. 1303-1312). doi: 10.1061/41095(365)130

Park, C. B., Miller, R. D., and Xia, J. 1999. Multichannel analysis of surface waves. Geophysics, 64(3), 800–808. https://doi.org/10.1190/1.1444590

Permanent Regional Seismological Network operated by the Aristotle University of Thessaloniki, http://dx.doi.org/doi:10.7914/SN/HT

Perton, M., Sánchez-Sesma, F. J., Rodriguez-Castellanos, A., Campillo, M. and Weaver, R. L. 2009.Two perspectives on equipartition in diffuse elastic fields in three dimensions, J. acoust. Soc. Am., 126, 1125–1130.

Piña-Flores, J., Perton, M., García-Jerez, A., Carmona, E., Luzon, F., Molina Villegas, J., and Sánchez-Sesma, F. 2016. The inversion of spectral ratio H/V in a layered system using the Diffuse Field Assumption (DFA). Geophysical Journal International, 208. https://doi.org/10.1093/gji/ggw416

Piña-Flores, J., Cárdenas-Soto, M., García-Jerez, A., Campillo, M., and Sánchez-Sesma, F. J. 2021. The Search of Diffusive Properties in Ambient Seismic Noise. Bulletin of the Seismological Society of America, 111(3), 1650–1660. https://doi.org/10.1785/0120200189

Rhie J, Romanowicz B. 2004. Excitation of Earth's continuous free oscillations by atmosphere-ocean-seafloor coupling. Nature. Sep 30;431(7008):552-6. doi: 10.1038/nature02942. PMID: 15457256.

Richart, F.E., Hall, J.R. and Woods, R.D. 1970. Vibrations of Soils and Foundations. Prentice-Hall Inc., Upper Saddle River.

Roberts, J. C., and Asten, M. W. 2004. Resolving a velocity inversion at the geotechnical scale using the microtremor (passive seismic) survey method. Exploration Geophysics, 35(1), 14–18. https://doi.org/10.1071/EG04014

Robinson, E.S. and Coruh, C. 1988 Basic Exploration Geophysics. John Wiley and Sons, New York, 562p.

Salinas, V., Luzón, F., García-Jerez, A., Sánchez-Sesma, F. J., Kawase, H., Matsushima, S., Suarez, M., Cuellar, A., and Campillo, M. 2014. Using Diffuse Field Theory to Interpret the H/V Spectral Ratio from Earthquake Records in Cibeles Seismic Station, Mexico City. Bulletin of the Seismological Society of America, 104(2), 995–1001. https://doi.org/10.1785/0120130202

Sambridge M., 1999. Geophysical Inversion with a Neighborhood Algorithm I. Searching a Parameter Space, Geophysical Journal International 103, 4839-4878.

Sánchez-Sesma, F. J., Rodríguez, M., Iturrarán - Viveros, U., Rodríguez - Castellanos, A., Suarez, M., Santoyo, M. A., Garcia-Jerez, A. and Luzon, F. 2010. Site effects assessment using seismic noise, in Proceedings of the 9th International Workshop on Seismic Microzoning and Risk Reduction, 2010, February 21–24, Cuernavaca, Mexico.

Sánchez-Sesma, F. J., M. Rodríguez, U. Iturrarán-Viveros, F. Luzón, M. Campillo, L. Margerin, A. García-Jerez, M. Suárez, M. A. Santoyo, and A. Rodríguez-Castellanos 2011. A theory for microtremor H/V spectral ratio: Application for a layered medium, Geophysical Journal International 186, 221–225.

Sánchez-Sesma, F. J., Pérez-Ruiz, J. A., Luzón, F., Campillo, M., and Rodríguez-Castellanos, A. 2008. Diffuse fields in dynamic elasticity. Wave Motion, 45(5), 641–654. https://doi.org/https://doi.org/10.1016/j.wavemoti.2007.07.005

Sánchez-Sesma, F. J., R. L. Weaver, H. Kawase, S. Matsushima, F. Luzón, and M. Campillo 2011. Energy partitions among elastic waves for dynamic surface loads in a semi-infinite solid, Bull. Seismol. Soc. Am. 101, no. 4, 1704–1709.

Sánchez-Sesma, F., Rodriguez, M., Iturrarán - Viveros, U., Luzon, F., Campillo, M., Margerin, L., García-Jerez, A., Suarez, M., Santoyo, M., and Rodríguez-Castellanos, A. 2011. A theory for microtremor H/V spectral ratio: Application for a layered medium. Geophysical Journal International, 186, 221–225. https://doi.org/10.1111/j.1365-246X.2011.05064.x

Sasaki, Y. 1994. 3-D resistivity inversion using the finite-element method. 165 Geophysics, 59(11), 1839–1848. https://doi.org/10.1190/1.1443571

Seo, K. 1997. Comparison of Measured Microtremors with Damage Distribution, In JICA, Research and Development Project on Earthquake Disaster Prevention.

SESAME European research project 2004. Guidelines for the implementation of the H/V spectral ratio technique on ambient vibrations: Measurements, Processing and Interpretation, Deliverable D23.12, 62p. http://sesame.geopsy.org/Papers/HV_User_Guidelines.pdf

Schmidt, R.O., 1981. A signal subspace approach to multiple emitter location and spectral estimation. Ph.D., Thesis, Stanford University, California, USA, Society of America 91 (2), 206–218.

Sheriff, R., and Geldart, L. 1995. Exploration Seismology (2nd ed.). Cambridge: Cambridge University Press. doi:10.1017/CBO9781139168359

Steidl, J. H., A. G. Tumarkin, and R. J. Archuleta 1996. What is a reference site?, Bulletin of the Seismological Society of America 86, 1733-1748.

Stein S. and Wysession M. 2003. An Introduction to Seismology, Earthquakes and Earth Structure, Blackwell Publishing, 498p.

Stephenson, W. J., Odum, J. K., Hartzell, S. H., Leeds, A. L., and Williams, R. 2021. Shear-wave velocity site characterization in Oklahoma from joint inversion of multi-method surface seismic measurements: Implications for central U.S. Ground Motion Prediction. Bulletin Seismological Society America, 111(4), 1693–1712. https://doi.org/10.1785/0120200348

Stokoe K. H., II, Wright G. W., James A. B., and Jose M. R., 1994. Characterization of geotechnical sites by SASW method, in Woods, R. D., Ed., Geophysical characterization of sites: Oxford Publ.

Styles P. 2012. Environmental Geophysics: Everything you ever wanted (needed!) to know but were afraid to ask! European Association of Geoscientists and Engineers (EAGE), Educational Tour Series, no. 7, 220 pp.

Telford, W., Geldart, L., and Sheriff, R. 1990. Applied Geophysics (2nd ed.). Cambridge: Cambridge University Press. doi:10.1017/CBO9781139167932

Tokimatsu, K., Arai H. and Asaka, Y., 1996. Three-Dimensional Soil Profiling in Kobe Area Using Microtremors. 10th World Conference of Earthquake Engineering (Acapulco, Mexico), Paper No. 1764.

Tokimatsu, K., 1997. Geotechnical site characterization using surface waves. Proceedings of the First International Conference on Earthquake Geotechnical Engineering 3,1333–1368.

Toksöz, M. N., and Lacoss, R. T. 1968. Microseisms: Mode Structure and Sources. Science 159(3817), 872–873. https://doi.org/10.1126/science.159.3817.872

Tsourlos, P. I., Szymanski, J., and Tsokas, G. N. 1998. A smoothness constrained algorithm for the fast 2-D inversion of DC resistivity and induced polarization data. Journal of the Balkan Geophysical Society 1(1), 3-13.

Waltz, R. A., Morales, J. L., Nocedal, J., and Orban, D. 2006. An interior algorithm for nonlinear optimization that combines line search and trust region steps. Mathematical Programming, 107(3), 391–408. https://doi.org/10.1007/s10107-004-0560-5

Tsourlos, P. I., and Ogilvy, R. D. 1999. An algorithm for the 3-D inversion of 166 tomographic resistivity and induced polarization data: Preliminary results. Journal of the Balkan Geophysical Society, 2(2), 30–45.

Wathelet, M., D. Jongmans, and M. Ohrnberger 2004. Surface wave inversion using a direct search algorithm and its application to ambient vibration measurements, Near Surface Geophysics **2**, 211--221.

Wathelet M., 2005. Array Recordings of Ambient Vibrations: Surface-Wave Inversion, PhD Thesis, University of Liège (Belgium), 177p.

Wathelet, M., D. Jongmans, M. Ohrnberger, and S. Bonnefoy-Claudet 2008. Array performances for ambient vibrations on a shallow structure and consequences over V_s inversion. Journal of Seismology, 12, 1-19.

Wathelet, M., B. Guillier, P. Roux, C. Cornou and M. Ohrnberger 2018. Rayleigh wave three-component beamforming: signed ellipticity assessment from high-resolution frequency-wavenumber processing of ambient vibration arrays. Geophysical Journal International, **215**(1), 507-523.

Wathelet, M., Chatelain, J., Cornou, C., Giulio, G. di, Guillier, B., Ohrnberger, M., and Savvaidis, A. 2020. Geopsy: A User-Friendly Open-Source Tool Set for Ambient Vibration

Processing. Seismological Research Letters, 91(3), 1878–1889. https://doi.org/10.1785/0220190360

Woods, J. W., and Lintz, P. R. 1973. PLANE WAVES AT SMALL ARRAYS. GEOPHYSICS, 38(6), 1023–1041. https://doi.org/10.1190/1.1440393

Yamamoto, H., 2000. Estimation of shallow S-wave velocity structures from phase velocities of Love- and Rayleigh-waves in microtremors. Proceedings of the 12thWorld Conference on Earthquake Engineering. Auckland, New Zealand.

Yamanaka, H., Takemura, M., Ishida, H. and Niwa, M., 1994. Characteristics of long-period microtremors and their applicability in exploration of deep sedimentary layers. Bulletin of the Seismological Society of America 84 (6), 1831–1841.

Yi, M. J., Kim, J. H., Song, Y., Cho, S. J., Chung, S. H., and Suh, J. H. 2001. Three-dimensional imaging of subsurface structures using resistivity data. Geophysical Prospecting, 49(4), 483–497. https://doi.org/10.1046/j.1365-2478.2001.00269.x

Yilmaz, Öz 2001. Seismic data analysis. Society of Exploration Geophysicists. ISBN 1-56080-094-1.

Yong, A., Martin, A., Stokoe, K., and Diehl, J., 2013, ARRA-funded VS30 measurements using multi-technique approach at strong-motion stations in California and central-eastern United States: U.S. Geological Survey Open-File Report 2013–1102, 59 p. and data files, http://pubs.usgs.gov/of/2013/1102/.

Websites:

http://www.iris-instruments.com/

https://www.geometrics.com/

https://www.guralp.com/

https://www.geopsy.org/

http://geophysics.geo.auth.gr/ss/ - AUTh Seismological Station

http://allshookup.org/quakes/wavetype.htm